Oluwadare Temitope Seun

Investigation of Regional Ionospheric Irregularities over Africa (IRIA)

Scientific Technical Report STR21/05

INVESTIGATION OF REGIONAL IONOSPHERIC IRREGULARITIES OVER AFRICA (IRIA)

vorgelegt von

M.Sc.

Oluwadare Temitope Seun

von der Fakultät VI - Planen Bauen Umwelt

der Technischen Universität Berlin

zur Erlangung des akademischen Grades

Doktor der Ingenieurwissenschaften
- Dr.-Ing.-

genehmigte Dissertation

Promotionsausschuss:

Vorsitzender: Prof. Dr. Jens Wickert
Gutachter: Prof. Dr.-Ing. Dr. h.c. Harald Schuh
Gutachter: Prof. Dr.-Ing Michael Schmidt
Gutachter: Prof. Mahdi M. Alizadeh
Gutachter: Dr. Norbert Jakowski

Tag der wissenschaftlichen Aussprache: 3. November 2020

Berlin 2021

Acknowledgements

ABSTRACT

The Earth's upper atmosphere – a part of it, the ionosphere- is a dynamic partly ionized region with temporal and spatial variations under different phases of solar activity. The ionosphere being a dispersive medium causes signal strength fluctuation, propagation delay, signal attenuation, and signal degradation. These have constituted significant threats to both communication and navigation systems operating in microwave band which is due to the presence of high electron density and its irregularities. The key parameter of the ionosphere which is closely related to most of these delay effects on radio signals is the electron density and density gradients, in particular - its vertical integral, the Total Electron Content (TEC) which can be estimated from the Global Positioning System (GPS) data. The estimated TEC profiles, and TEC perturbation are studied to gain insights into the occurrence of irregular structures in the ionosphere and their distribution.

One of the ionospheric irregularities located within the F region, and E region top side are Traveling ionospheric disturbances (TIDs). TIDs are propagating perturbations in the ionospheric electron density as a consequence of Atmospheric Gravity Waves (AGWs) passage. The AGWs originate in the troposphere or stratosphere, and exhibit neutral wind perturbations propagating to the F region heights (i.e. ionospheric heights), where the neutral wind perturbations interact with the plasma via collisions, carrying it along the magnetic field lines (i.e. ion-neutral collision). This entire process in the ionosphere is manifested as oscillations of the ionospheric electron density, resulting in a TID. However, TIDs vary in scale sizes ranging within a few hundred kilometers (km) to over one thousand km, and based on this, they are categorized as either medium-scale TIDs (MSTIDs) or large scale TIDs (LSTIDs). In this thesis, we focus only on MSTIDs as one of the major and frequent ionospheric irregularity phenomena which may degrade positioning systems and could cause a delay in GPS signal transmission between a satellite and the GPS receiver.

Multiple studies of ionospheric irregularities with the main focus on MSTIDs over different regions and continents around the world have been carried out, but studies of MSTIDs over the African region have neither been carried out nor reported probably due to lack of GPS data set, and the question of what drives its occurrence in the region which is not yet documented.

The objective of this thesis is to study and describe for the first time the occurrence of MSTIDs and its characteristics over the African region under quiet geomagnetic condition (Kp ≤ 3) during the years 2008 – 2016. In addition, this thesis presents novel results of the time series of MSTIDs

percentage occurrence rate (POR) during daytime and nighttime, and seasonal occurrence. Ion-neutral coupling processes like the connection between AGW and MSTIDs are also discussed in the study. Observational TEC data used in this thesis are obtained from ground-based GPS networks within the African region and nearby stations. Additionally, temperature data from COSMIC radio occultation and SABER satellite observations for some case studies were used to validate AGWs passage as a driving source of MSTIDs, especially during the daytime. Consequently, regional MSTIDs distribution maps have been generated to capture the latitudinal, seasonal, and local time extent of the MSTID occurrence. Investigation of regional ionospheric irregularities over Africa (IRIA) gives a novel result of a climatological view of MSTIDs over Northern and Southern hemispheres in the African region.

ZUSAMMENFASSUNG

Die obere Erdatmosphäre - ein Teil davon ist die Ionosphäre - ist eine dynamische und teilweise ionisierte Region mit unterschiedlichen zeitlichen und räumlichen Schwankungen während verschiedenen Phasen der Sonnenaktivität. Die Ionosphäre ist ein dispersives Medium. Sie verursacht Signalstärkeschwankungen, Ausbreitungsverzögerungen, Signaldämpfung und Signalverschlechterungen. Das stellt eine erhebliche Störungsquelle für Kommunikations- und Navigationssysteme dar, die im Mikrowellenbereich arbeiten. Die Störungen sind auf das Vorhandensein einer hohen Elektronendichte und deren Unregelmäßigkeiten zurückzuführen. Der Schlüsselparameter der Ionosphäre, der eng mit den meisten dieser Verzögerungseffekte auf die Signale zusammenhängt, ist die Elektronendichte und der Dichtegradient, insbesondere sein vertikales Integral, der Gesamtelektronengehalt (TEC), der aus den Global Positioning System (GPS) Daten bestimmt werden kann. Die errechneten TEC-Profile und die TEC-Störung werden untersucht, um Einblicke in das Auftreten unregelmäßiger Strukturen in der Ionosphäre und deren Verteilung zu erhalten.

Ein Phänomen innerhalb der F-Region und der Oberseite der E-Region sind wandernde ionosphärische Störungen (TIDs). TIDs sind sich ausbreitende Störungen der ionosphärischen Elektronendichte als Folge des Durchgangs von atmosphärischen Schwerkraftwellen (AGWs). Die AGWs stammen aus der Troposphäre oder Stratosphäre und weisen Störungen des neutralen Windes auf, die sich in der Höhe der ionosphärischen F-Region ausbreiten, wo die neutralen Windstörungen über Kollisionen mit dem Plasma interagieren und es entlang der Magnetfeldlinien zu Interaktionen der neutralen und der ionisierten Bestandteile der Hochatmosphäre kommt. Dieser gesamte Prozess in der Ionosphäre erzeugt Schwingungen der ionosphärischen Elektronendichte, was zu einer TID führt. TIDs variieren jedoch in ihrer Skalengrößen zwischen einigen hundert Kilometern und über tausend Kilometern. Auf dieser Grundlage werden sie entweder als mittelgroße TIDs (MSTIDs) oder als große TIDs (LSTIDs) kategorisiert. In dieser Arbeit konzentrieren wir uns nur auf MSTIDs als eines der wichtigsten und häufigsten Phänomene der ionosphärischen Unregelmäßigkeit, die Positionierungssysteme beeinträchtigen und die GPS-Signalübertragung zwischen einem Satelliten und dem GPS-Empfänger verzögern können.

Eines der häufig auftretenden ionosphärischen Phänomene innerhalb der F-Region oberhalb der E-Region sind die so genannten Medium Scale Traveling Ionospheric Disturbances (MSTIDs). MSTIDs erscheinen häufig als wellenartige Schwankungen der Elektronendichte als Folge von Kopplungsprozessen mit atmosphärischen Schwerewellen (AGWs), die aus der Troposphäre oder

Stratosphäre stammen. Kopplungsprozessen zwischen der neutralen Hochatmosphäre und der Ionosphäre erzeugen Oszillationen in der Plasmadichte. Dieser Prozess führt folglich zu wellenförmigen Strukturen im TEC, was zu einer Verringerung der Genauigkeit der präzisen GPS-Positionierung und Navigation führen kann.

In verschiedenen Regionen und Kontinenten auf der ganzen Welt wurden mehrere Studien zu ionosphärischen Unregelmäßigkeiten mit dem Schwerpunkt auf MSTIDs durchgeführt. Studien zu MSTIDs in der afrikanischen Region sind jedoch rar, wahrscheinlich aufgrund des Fehlens eines geeigneten GPS-Datensatzes. Somit konnte die Frage, was sein Auftreten in der Region antreibt, noch nicht beantwortet werden.

Das Ziel dieser Arbeit ist es, erstmals das Auftreten von MSTIDs und ihre Eigenschaften in der afrikanischen Region unter ruhigen geomagnetischen Bedingungen (Kp ≤ 3) in den Jahren 2008 - 2016 zu untersuchen und zu beschreiben. Darüber hinaus werden in dieser Arbeit neue Ergebnisse von Zeitreihe der prozentualen MSTID-Auftrittsrate (POR) während des Tages und der Nacht sowie das saisonale Auftreten vorgestellt. Kopplungsprozesse zwischen der neutralen Hochatmosphäre und der Ionosphäre wie die Verbindung zwischen AGW und MSTIDs werden hier ebenfalls in der Studie diskutiert. Die in dieser Arbeit verwendeten TEC-Beobachtungsdaten stammen von bodengestützten GPS-Empfängernetzwerken in der afrikanischen Region sowie von nahe gelegenen Stationen. Zusätzlich wurden Temperaturdaten aus COSMIC-Radiookkultation und SABER-Satellitenbeobachtungen für einige Fallstudien verwendet, um das Auftreten von Schwerewellen als hauptsächliche Quelle der MSTIDs zu identifizieren und validieren, insbesondere tagsüber. Folglich wurden regionale MSTID-Verteilungskarten erstellt, um die Verteilung des Auftretens der MSTIDs in Abhängigkeit von der geografischen Breite, der Jahreszeit und der Lokalzeit zu erfassen. Die Untersuchung regionaler ionosphärischer Unregelmäßigkeiten über Afrika (IRIA) liefert ein neues Ergebnis einer klimatologischen Betrachtung von MSTIDs über der nördlichen und südlichen Hemisphäre des afrikanischen Kontinents.

Stichpunkte: Ionosphäre, GNSS Messungen, TEC, Kopplungen der Thermosphäre-Ionosphäre, MSTIDs, AGWs

Contents

LIST OF FIGURES

LIST OF TABLES

LIST OF ABBREVIATIONS

AGW   - Atmospheric Gravity Wave

AMEC   - Annual MSTIDs event count

COI   - Cone of influence

CI   - Confidence interval

COSMIC   - Constellation Observing System for Meteorology, Ionosphere and Climate

CDAAC   - Data Analysis and Archive Center

RO   - Radio occultation

CCF   - Cross-Correlation Function

DT   - Daytime

DoD   - Department of Defense

DCB   - Differential Code Bias

EIA   - Equatorial ionization anomaly

EPBs   - Equatorial plasma bubbles

ETH   - Event threshold

EUV   - Extreme ultraviolet

FFT   - fast Fourier transform

GNSS   - Global Navigation Satellite Systems

GOES   - Geostationary Environment Operational Satellite

GPS   - Global Positioning Systems

GWS   - Global wave spectrum

GLONASS - Russia's Global Navigation Satellite System

GWs   - gravity waves (GWs)

ISUAL   - Imager of Sprites and Upper Atmospheric Lightning

ISR   - incoherent scatter radar

IRNSS   - Indian Regional Navigation Satellite System

IC   - Ionospheric conductivity

QZSS   - Japan and the Asia-Oceania region

LEO   - Low Earth Orbit

LSTIDs   - Large Scale Travelling Ionospheric Disturbances

MSTIDs   - Medium Scale Travelling Ionospheric Disturbances

NAVSTAR- Navigation System with Time and Ranging Positioning

NNSS   - Navy Navigation Satellite System

NH   - Northern Hemisphere

NT   - Nighttime

OR   - Occurrence rate (OR)

POR   - Percentage of occurrence rate

RINEX   - Receiver Independent Exchange

SE   - Southeastward

SH   - Southern Hemisphere

SSA   - Singular Spectrum Analysis

SABER   - Sounding of the Atmosphere using Broadband Emission Radiometry

SW   - Southwestward

TEC   - Total Electron Content

TID   - Travelling Ionospheric Disturbance.

UCAR   - University Corporation for Atmospheric Research

WPS   - Wavelet power spectrum

WVC   - Water vapor content

Chapter   1

INTRODUCTION AND MOTIVATION

1.1   Background

Radio wave-based technologies have made our lives easier and have helped in various aspects of our social interaction. One good attributes of radio wave signals are its ability to propagate over a long distance through the ionosphere. This medium of signal propagation through the ionosphere has brought diverse ways of satellite applications, most especially in Global Navigation Satellite Systems (GNSS) e.g. Global Positioning Systems (GPS). However, the ionosphere is a dispersive medium for GPS signals. GPS signals passing through the ionosphere experience signal strength fluctuation, propagation delay, signal attenuation, signal degradation, and in extreme cases loss of lock. These ionospheric effects have constituted significant threats to both communication and navigation systems (Akala et al., 2010a, 2011, 2012). The ionosphere extends approximately from about 50 to 1000 km, and the main sources of ionization at this altitude are the solar radiations such as extreme ultraviolet (EUV) and X-ray radiations which produce free electrons and ions. Therefore, the ionosphere can be defined as the upper part of the earth atmosphere where free electrons exist in high and sufficient density to influence electromagnetic waves (Hargreaves, 1995). The free electrons in the ionosphere are major impact and influence on the propagation of radio waves which consequently leads to range errors on the GPS signals. The key parameter of the ionosphere which is closely related with most of these delay effects on radio signals is Total Electron Content (TEC), and it represents the total amount of free electrons in a cylinder with a cross section of $1m^2$, and a height that is equal to the slant signal path between the GPS satellite and the receiver, where 1 TECU = 10^{16} electron/m^2. The dispersive nature of the ionosphere allows dual-frequency GNSS receivers to measure TEC; the measured TEC along the signal path is known as slant TEC (STEC) and is often mapped into vertical TEC (VTEC) using a mapping function (M). The structure and properties of the ionosphere depend essentially on processes occurring in the Sun called solar activity (Tinsley et al., 1989) and on variations of Earth's magnetic field called the geomagnetic field effect (Chapman, S. and Ferraro, V.R, 1933), on movements of neutral wind in the upper atmosphere due to Earth's rotation, on the effects of electrical currents and ambient electrical fields, on the density and the atmospheric composition of gas at different altitudes and geographical latitudes. Furthermore, the Earth's ionosphere

continuously changes and it varies with altitude, latitude, longitude, daytime, season, solar cycle, and magnetic activity. The ionospheric medium is highly dynamic where electron density can vary significantly at any given location resulting in temporal and spatial variations. The temporal variation of the ionosphere involves the combination of regular and irregular variations; which are the two categories of ionospheric variations. The regular variation of ionosphere occurs in cycles and it is associated with the diurnal and seasonal changes in the Earth-Sun geometry or in solar zenith angle and it changes in the solar ionizing radiation intensity over 11 years (a solar cycle = 11 years). The irregular variation is majorly due to the irregular behavior of the sun and can't be predicted. One of the major and frequent phenomena of irregular variation of the ionosphere are Travelling ionospheric disturbances (TIDs). TIDs are gravity wave signatures in the ionosphere, and they were first observed by Hines (1960). The wavelike structure of TIDs varies in scale sizes, and they are categorized as either medium-scale TIDs (MSTIDs) or large-scale TIDs (LSTIDs). The MSTIDs are generated and propagated by a continuous spectrum passage of atmospheric gravity waves (AGWs) propagating the neutral atmosphere (Fedorenko et al., 2010). Different studies have reported the regular and dynamic nature of the ionospheric TEC at different latitudes over the African region in previous years to improve the understanding of the dynamic and complex nature of ionosphere (Adewale et al., 2011; Ouattara and Fleury, 2011; Fayose et al., 2012; D'ujanga et al., 2012; Ikubanni and Adeniyi, 2012; Olwendo et al., 2012; Zoundi et al., 2012; Ngwira et al., 2013; Opio et al., 2015; D'ujanga et al., 2016), but these earlier studies have only been confined to short-term basis observation under limited solar activities and in most cases with the consideration of only F10.7 cm and/or SSN as solar indices to specify the level of influence of solar radiation. Besides, majority of the investigations reported to date have mostly focused on the broader or general name of 'ionospheric irregularity' without specifically clarifying the type of the irregularity. In addition, there is yet an important aspect of ionospheric irregularities which is yet to be reported on both local and regional scales over Africa. In recent years, with an improved study of long-term time series of characterization of ionospheric GPS-TEC under different geomagnetic conditions for daytime and nighttime respectively during 2009 - 2016 (Oluwadare et al., 2018), certain wave-like structure of ionospheric TEC was observed to be irregular which vary in time and space has called for further investigation. The characteristics of this irregular phenomenon are mostly associated with MSTIDs as described by ionospheric irregularity theories and experimental results from different authors (e.g: Kotake et al., 2007; Valladares and Hei, 2012; Jonah et al., 2016; Oinats et al., 2016; Figueiredo et al., 2018) who have reported MSTIDs observations from different regions e.g.; North Asia, South America, North America, Europe, and Oceania around the globe except for the African region. These have

created a huge gap of ionospheric irregularity information and in interregional MSTIDs characteristics comparison. Before now, MSTIDs study over the African region has not been reported, probably due to the limitation of ionospheric data availability in the region or none-access to the GPS data and other technical reasons. Hence, for the first time, this study has considered further observation and investigation of the occurrence of ionospheric irregularities with the main focus on MSTIDs from GPS-TEC estimates over the African region. To avoid an incorrect and erroneous interpretation of ionospheric behavior, this study ignored geomagnetic disturbed days, and considered geomagnetic quiet days (i.e. $Kp \leq 3$) during 2008-2016. This study reports and present the result obtained from MSTIDs observations, its characteristics, and excitation mechanisms.

1.2 Research Aim

The main focus of this thesis is to present a long-term time series of irregular variations of the ionospheric TEC measurement from GPS (i.e. GPS-TEC) for both daytime and the nighttime period during geomagnetic quiet days ($Kp \leq 3$), with the goal to derive TEC perturbation (dTEC) associated with MSTIDs, and also estimate its characteristics and excitation mechanisms over Africa region during 2008-2016. To do this, disturbed GPS-TEC exhibiting wave-like structures were identified from the GPS-TEC measurements, TEC perturbation is derived, and MSTIDs were estimated. The measurements used in this thesis span through different phase (solar minimum, solar ascending, solar maximum, and descending solar phase) of solar cycle 24, which therefore allow for different solar activity comparisons. For the purpose of validating AGWs as one of the sources of occurrence of MSTIDs during some selected days, we used temperature as a parameter which is believed to often exhibit AGW signature or passage as it propagates from the lower atmospheric region into the ionosphere, hence causing irregularity. Procedures for AGWs structure observations from temperature data is discussed in chapter 6 and 7 of this thesis. Furthermore, we believe that the global observation and investigation of MSTIDs can be improved by including these novel results and information on MSTIDs over the African region.

Research Objective

- Find wave-like structures in GPS-TEC estimates, and derive the ionospheric TEC perturbation (dTEC).

- Observe and quantify dTEC exhibited to be MSTIDs occurrence.

- Estimate MSTIDs percentage of occurrence rate (POR) and MSTIDs characteristics (e.g. periods, amplitude, and propagation direction) for both daytime and nighttime.

- Investigate AGW as an excitation source for the MSTIDs occurrence for selected events.

- Observation of simultaneous occurrence of MSTIDs across African region and hemispheric conjugacy of MSTIDs for selected events.

1.3   Research Overview

MSTIDs study and investigation will be carried out under the following outline:

Chapter 2: Background description of earth's atmosphere structure- This chapter gives a background description of the Earth's atmosphere in terms of different layers that make the atmosphere, and the photo-ionization process that makes up the ionosphere. It also contains the ionospheric variation description as a function of season, time, latitude, solar/geomagnetic condition, different ionospheric irregular variations, ion-electron transportation processes, and ionospheric conductivity property.

Chapter 3: TIDs background and MSTIDs regional review- Brief description of the background of the TIDs and MSTIDs are discussed followed by the MSTIDs regional study literature reviews. Also, the daytime and nighttime MSTIDs characteristics are briefly discussed, followed by the causes of MSTIDs. Since there is a connection between the ionosphere and AGWs, then we are obliged to also briefly discuss AGWs and its characteristics.

Chapter 4: Instrumentation and measurements- The descriptions of the instruments used in the study are described alongside the data estimated by these instruments. TEC values are estimated, this is followed by the description of the methodology required in filtering out the days with low geomagnetic condition days, and the required mathematical algorithm for deriving TEC perturbation (dTEC) from TEC values. Lastly, criteria for the estimation of MSTIDs and the procedures for estimation of MSTIDs characteristics are stated.

Chapter 5: EIA Observations results- Based on the methodology described in chapter 4, the estimated TEC values were used to study the regular and irregular ionospheric behavior over Africa. The regular nature of the ionosphere needs to be understood before having a proper understanding of MSTIDs as one of the ionospheric irregularities. We started our study on the equatorial ionization anomaly (EIA) zone to have good information about the regular and irregular behavior of the ionosphere. Hence, this chapter discussed the characteristics of the ionosphere over at the EIA zone during daytime and nighttime.

Chapter 6: MSTIDs Observations results at the North African mid-latitude results- Based on the methodology described in chapter 4, MSTIDs occurrence and its characteristics at the African mid-latitude sector are presented. Construction of the 2-D map MSTIDs showing the propagation pattern is presented. Statistical analyses to estimate MSTIDs spread in daytime and nighttime, and seasonal variation during 2008-2016 are described. Possible occurrence mechanism for MSTIDs at the mid-latitude are discussed.

Chapter 7: MSTIDs Observations results at the Equatorial and low latitude (ELL) results- Same procedure as chapter 6 but for ELL at Northern and Southern hemisphere. Regional construction of the MSTIDs map during 2008-2016 is presented. AGWs signatures exhibited from perturbed temperature profile and MSTIDs travel-time plots known as keogram for selective days are presented. There is variability from the hemisphere to the hemisphere in terms of amplitude, MSTIDs percentage occurrence rate (POR), and season. Possible occurrence mechanism for MSTIDs at the equatorial and low-latitude are discussed.

Chapter 8: MSTIDs simultaneous observation and hemispheric conjugacy results – Daytime and nighttime MSTIDs observation at the conjugate hemisphere are presented for the selected day. AGWs signatures exhibited from the perturbed temperature profile as a consequence of convention activities are presented. MSTIDs keogram plots during daytime and nighttime also are presented, with the mechanisms responsible for the mirrored MSTIDs at the conjugate hemisphere discussed.

Chapter 9: Conclusion and suggestions for further research- This chapter highlights the conclusions from chapter 5, 6, 7, 8 and also presents some ideas for research in the future.

Chapter   2

BACKGROUND DESCRIPTION OF EARTH'S ATMOSPHERE

The Earth's atmosphere has been generally accepted to be sub-divided into various regions based on temperature profiles, conductivity, or electron density. As to the ionospheric electrodynamic processes, each area is studied in isolation. Atmospheric structures are organized by a representative temperature profile, and typical midlatitude profiles of temperature and plasma density are given in fig. (2.1). There is an initial decrease in atmospheric temperature profile with altitude from the surface temperature, with a "lapse rate" of about 70° K / km in the troposphere and at about 10 km altitude this temperature begins to increase with altitude at the tropopause and thereafter the stratosphere region begins. This increase is fundamentally due to the absorption, by ozone, of part of the ultraviolet portion of the solar radiation, the increase further maximizes at 50 km, where the temperature trend again decreases at the stratopause. At about 90 km, the temperature experiences a sharp decrease to a minimum in the range 130° - 190° K due to radiative cooling. At the mesopause level (altitude of the temperature minimum), the temperature again increases dramatically due to the absorption of energy solar photons, and this region is referred to as the thermosphere. The temperature increases at the thermosphere due to the absorption of ultra-violet (UV) and extreme UV (EUV) radiation from the sun. However, the EUV radiation is also responsible for plasma production in the atmosphere, since these solar photons have sufficient energy to ionize the neutral atmosphere. In addition, equal numbers of positive ions and electrons are produced during the ionization process. There are several ways to categorize the earth's atmosphere and it is based on the thermal characteristics (temperature changes); the various categories of the Earth's atmosphere are distinct layers /regions and they are four in number: Troposphere, Stratosphere, Mesosphere, and Thermosphere.
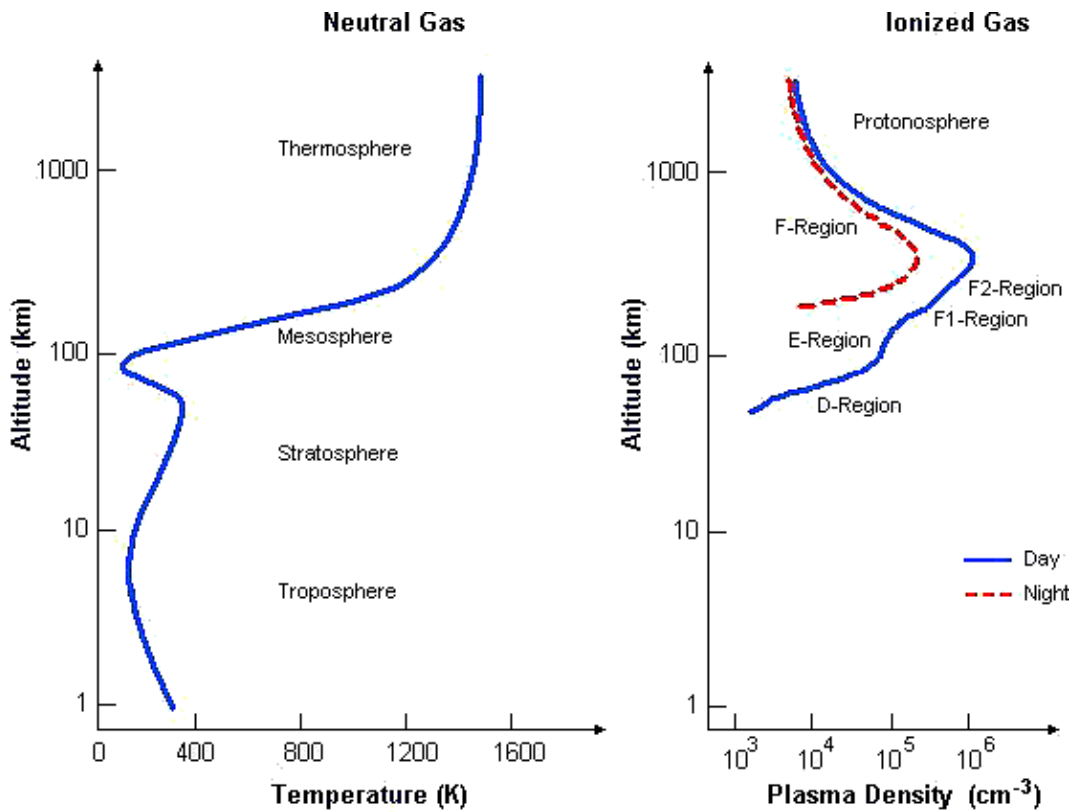
Figure 2.1: Neutral atmospheric temperature profile consisting different layers (left) and the various concentration of ionospheric electron density profile for both daytime and nighttime (right) (Kelley, M.C., 2009).

2.1 Troposphere: In the Greek language troposphere means 'the sphere of change', and it is the most turbulent layer. In fact, most of the atmosphere's water vapor lies in the troposphere (about 99%). It extends from the Earth's surface to about 10 km high and it is the part of the atmosphere that is most dense. Shortly after this layer is stratosphere which means 'sphere of layers' and it contains sub-layers of lighter gases such as helium and hydrogen. In between troposphere and stratosphere is 'tropopause' which means 'end of change'. The tropopause separates the troposphere from the next layer. As you go higher in this layer, the temperature drops from about 290.15 to 221.15 degrees Kelvin at the tropopause. The troposphere has a high concentration of water vapor which varies with latitude but shows high values above the tropical regions and decreases toward the Polar Regions. The entire tropopause and troposphere from the lower atmosphere, and 99% of the lower atmosphere consist of Nitrogen (78% by volume), and Oxygen (21% by volume). Looking from the signal propagation perspective, the troposphere is a non-dispersive medium and the propagation delay is not frequency-dependent. The signal propagation depends mostly on the water vapor content (WVC) and on temperature. It must be noted that the tropospheric region is a common source of atmospheric convection (a consequence of a parcel-

7

environment instability, or temperature difference layer in the atmosphere) which is an important source of gravity waves (GWs); these GWs normally propagate vertically and horizontally away from their source with its amplitudes increase with height as the background density decreases. As the waves propagate upwards, it automatically modifies the structure, dynamics and hence causes perturbation of the other atmospheric regions.

2.2 Stratosphere: It is the second layer of the Earth's atmosphere, above the troposphere. The stratosphere extends from an altitude of about 13 km up to its upper boundary, the stratopause, at about 50 km. Ten kilometres is the upper band beyond which man can't survive without oxygen. Hence, sealed cabins were designed and built, in which pressure and temperature at the Earth's surface were maintained, helping men to get to the stratosphere. Further development of lighter and plastic balloons enabled man to get to a higher height of 18km and helped prolong his stay up there. By the year 1960, manned balloons had gone as high as 34 km and unmanned balloons to almost about 46 km. The atmospheric temperature residing within the stratospheric region increases with altitude up to about 270^0 K. The AGWs also exist within this region due to the transmitted energy and momentum transmitted from the troposphere, and now from the stratosphere, transmits energy from this region up into the next layer above it.

2.3 Mesosphere: It is a region of the upper atmosphere between 50 and 80 km approximately. The temperature at this level decreases as the altitude increases and is regarded as the coldest region of the Earth's atmosphere with the temperature rising to a maximum of 263.15^o K (-10°C) and then again dropped to a low of 183.15^o K (-90°C) at about 80 km altitude. It is the base of the thermosphere; the boundary between the two regions is called the mesopause. The major ionization sources in this region are the solar Layman-alpha radiation, X-ray radiation and the intense auroral particle precipitation. The conductivity at this level increases sharply in this region and the main charge carriers are electrons, positive ions (e.g. N^+_2, O^+_2, NO^+), and the negative ions (e.g. O^-_2). In addition, the mesosphere contains higher percentages of ozone than the lower Earth's atmosphere. Also, it must be noted also that the AGWs dynamical processes and its vertical propagation, transferring energy and momentum influence the mesospheric temperature.

2.4 Thermosphere: It is the outermost region of the Earth's atmosphere; it is called 'thermosphere', i.e. 'the sphere of heat'. It's the region where the temperature increases above the mesosphere. It extends from its base height level of about 80 km (the mesopause) to its top at an

altitude of about 450 km known as the thermopause. The temperature at this region rises from about 178.15º K (-95°C) to about 673.15o K (400°C) because it receives energy directly from the Sun. The thermospheric temperature increases steadily up to about $1000°$ K (726.85º C) and it increases with altitude. The temperature increase in the thermosphere is due to the absorption of UV and EUV radiation from the sun. The EUV radiation is also responsible for the production of plasma in the sunlit hemisphere since these solar photons have sufficient energy to ionize the neutral atmosphere. During the ionization process, equal numbers of positive ions and electrons are produced and one requirement for a gas to be termed plasma is when the number density of ions, n_i, must be nearly equal to the number density of electrons, n_e. In addition, above 480 km is the 'exosphere' which extends to an altitude of 1600 km and gradually merges into interplanetary space. At thermopause, the temperature stops from rising with height which depends on solar activity. Within the thermosphere lies the ionosphere. The ionosphere overlaps the thermosphere from about 60 and extends to about 1000 km in altitude above the Earth's surface. The photo-chemical reactions that take within the ionospheric region shall be explained in the subsequent section.

2.5 Ionosphere: The ionosphere is an upper part of the Earth's atmosphere that extends from about 60 km to 1000 km, which is partially ionized majorly due to photo-ionization from the solar radiation such as extreme ultraviolet (EUV) and X-ray radiations (Rishbeth and Garriott, 1969; Hargreaves, 1995). This section of the atmosphere consisting of several layers (mesosphere, thermosphere, and exosphere) is referred to as the ionosphere, and above the ionosphere is the plasmasphere. The ionosphere is therefore defined as the upper part of the earth atmosphere where free electrons exist in high and sufficient density to influence electromagnetic wave. The free electrons and ions affect the propagation of radio wave signals (electromagnetic waves) and this effect is called ionosphere refraction. It must be noted that the structure of the ionosphere continuously changes, and it varies with day/night, seasons, latitude, solar activity, and solar cycle phase. The ionospheric layer is stratified along with the vertical distance in four main regions; these are D, E, F1, and F2. These layers are distinct due to the recombination process which depends on the density of atmosphere (which changes with altitude). The electron concentration and ionospheric behavior at each region are relatively different from one another due to the presence of density of charged particles in each region.

2.5.1 Formation of the ionosphere

The Earth's atmosphere is made up of a large number of chemical constituents and it is characterized by a high density of free electrons and free ions which are majorly produced by the photo-ionization from solar radiation such as extreme ultraviolet (EUV) and X-ray as stated in the above section. It must be noted that abundant chemical constituents in the ionosphere are the neutral atoms and molecules. Notice in fig.2.2) that even where electron/ion density peaks, it is still well below the density of neutral molecules. That's why the ionosphere is referred to as weakly ionized plasma. However, the dominant constituents in the atmosphere are N_2, O_2, and Ar (fig.2.2), produced by photochemical processes. The photochemical process plays a fundamental role in the ionospheric formation and this process determines the structure, composition, and variability of the ionosphere. These processes are Ionization, Charge transfer, and Recombination process (the reverse phenomenon of ionization).
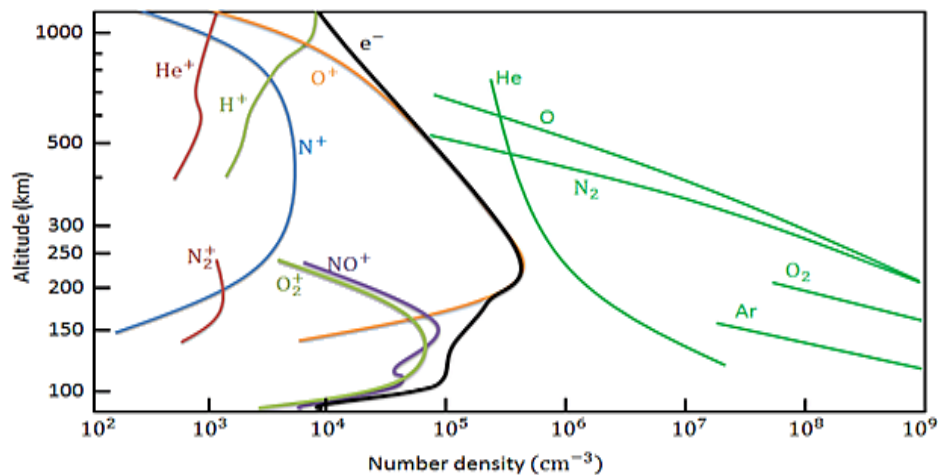
Figure 2.2: Electron density profile chart showing ions and neutral molecules with respect to altitude in the ionosphere. (Kelley, 1989)

2.5.2 Ionization

Ionization production is generally a two-step process. The first step is the ions creation from the neutrals atmosphere by solar photons in the extreme ultraviolet (EUV) and X-ray spectrum, and also to some extent by collisions with energetic particles. The Sun emits hot plasma into interplanetary space from the outer reaches of the Earth's environment as a result of solar corona expansion and so space is filled with ionized gas of an equal number of positively charged ions

and negatively charged electrons which are in constantly mobile due to both internal and external generated force and are incident on neutral atoms (O) and molecules (N_2, O_2) that are present in the neutral atmosphere. At this point, the neutral atoms partially absorbed the radiation, and electrons are detached from the neutral atoms by energetic photo-ionization of EUV and X-rays from the Sun therefore ions and free electrons are produced at both lower and upper atmosphere. The entire process described in this section is called ionization. The below schematic diagram gives a pictorial description of the ionization process.

U V Rays   **Neutral Atoms**   **Positive Ions**   **Free Electrons**
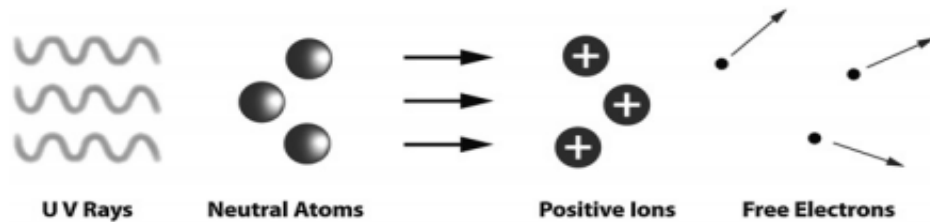
Figure 2.3: Simplified scheme describing ionization process: electrons are detached from their neural atoms by UV ray's energy from the sun, producing ions and free electrons.

2.5.2.1   Ionization photochemical process:

The solar EUV radiation ionizes both molecules (O_2) and atoms (O) in the neutral atmosphere. In this photochemical process, a neutral atom (O) and molecule (O_2) absorbs photon energy hv, to produce a positive atom O^+ and molecule O_2 with a free electron (e^-) respectively in each case. Where h is Planck's constant (6.626 x 10^{-34} Joule. second), and the Greek letter v (nu) is the photon's frequency

e.g

$$hv + O_2 \longrightarrow O_2^+ + e^- \tag{2.10}$$

$$hv + O \longrightarrow O^+ + e^- \tag{2.12}$$

In the case of N_2 molecule,

$$hv + N_2 \longrightarrow N_2^+ + e^- \tag{2.13}$$

Photo-ionization product (N_2^+) rapidly converted into

$$N_2^+ + O \longrightarrow NO^+ + N \tag{2.14}$$

11

2.5.2.2   Charge transfer photochemical process:

It is the first process in the recombination process stage. A neutral particle transfers an electron to an ion. It's an important step in ionization of hydrogen atom (H) and also as a first step in recombination of oxygen molecule (O_2).

e.g

$$H + O^+ \quad \longrightarrow \quad O + H^+ \tag{2.15}$$

$$O_2 + O^+ \quad \longrightarrow \quad O_2^+ + O \tag{2.16}$$

2.5.3   Recombination

The reverse situation of ionization is called recombination. In the recombination process, negative electrons e^-, and positive ions (oxygen ion (O^+)), combine to produce neutral particles. There are two types of recombination processes. These are radiative recombination and dissociative recombination.

2.5.3.1   Radiative recombination photochemical process description:

In this process, an electron (e^-) interacts with positive ions, but in a slow process and produces a neutral atom and a photon hv. Example of this photochemical process is given below.

$$O^+ + e^- \quad \longrightarrow \quad hv + O \tag{2.17}$$

2.5.3.2   Dissociative recombination photochemical process description:

It's a loss process in which electron combines with molecular ions (e.g. NO^+) and thereby reducing it to produce two other neutral atoms, for example Nitrogen atom and Oxygen atom (N and O). e.g

$$NO^+ + e^- \quad \longrightarrow \quad N + O \tag{2.18}$$

$$O_2^+ + e^- \quad \longrightarrow \quad O + O \tag{2.19}$$

As the altitude decreases, the intensity of radiation also decreases and vice –versa, however, there is a certain point where there is a balance in atmospheric neutral gas density and radiation, at this

point the recombination rates balance out the ionization rate and this brings about ionization peak formation layers known as the Chapman layers. It must be noted that photo-ionization by solar radiation is not the only source of plasma in the ionosphere. An ionization source could also be through an energetic particle impact on the atmosphere neutral gas which is an important source that often occurs at high altitudes. Visible light is emitted when the particles strike the atmosphere. These light emissions create visible aurora.

2.6   Variations in the ionosphere

The ionosphere is a complex medium and it varies with some parameters which result in variations. These variations are spatial and temporal in nature, which consequentially influences electron density structure at different ionospheric layers. The major parameters driving the ionosphere are solar activity, geomagnetic conditions, and neutral winds. In addition, the ionospheric variation ranges from little fluctuations to large changes.

2.6.1   Spatial variations

2.6.1.1   Height dependent

The ionospheric regions are overlapping hight-dependent layers. Each layer consists of an altitude of maximum density. These layers are fundamentally three in number and they are: D, E and F. The F layer consists of one layer at night, but in the presence of sunlight (during the day), it divides into two layers, labeled F1 and F2, see fig. 2.4a. The structure and properties of the ionosphere depend essentially on processes occurring in the sun called solar activity (Tinsley et al, 1989) and on variations of Earth's magnetic field called the geomagnetic field effect (Chapman, S. and Ferraro, V.R, 1933), on movements of neutral wind in the upper atmosphere due to Earth's rotation, on the effects of electrical currents and ambient electrical fields, on the density and the atmospheric composition of gas at different altitudes and geographical latitudes. However, as the height decreases, the number of gas atoms and molecules increases (disregarding, for the moment, the diffusive separation of species), hence there are more rooms for energy absorption. The energy from the solar UV radiation is absorbed in higher heights, this consequently leads to smaller radiation intensity at lower altitudes. During these processes, there are instances where the recombination rates balance out the ionization rate and this leads to the formation of ionization peaks and consequently different regions (layers). The generated different regions (layers) is known as the Chapman layers. Each layer has its unique characteristics based on the degree of the

photochemical process. Table 2.1 shows a summary of layers of the ionosphere and characteristics. The characteristics and formation mechanism of these layers are discussed below:
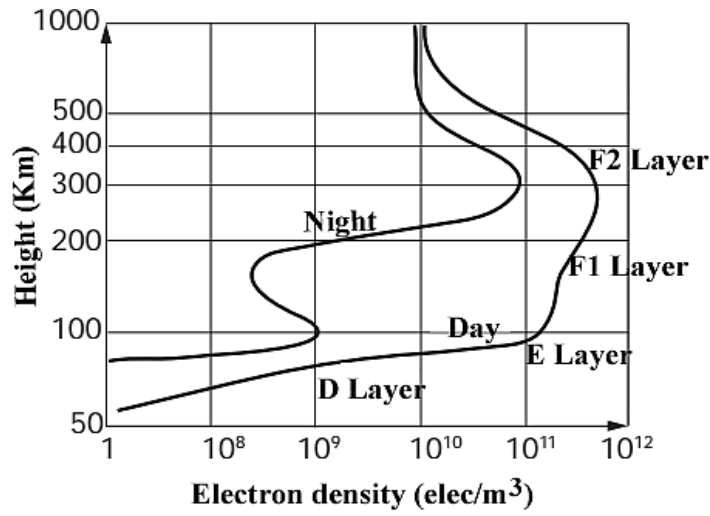
Figure 2.4a: Electron density vertical profile and the ionospheric layers D, E, F1, and F2 for both daytime and nighttime conditions at mid-latitudes.

Table 2.1: Summary of the characteristics of the ionospheric regions

Region		D	E	F1	F2	Topside
Neutral particles		N_2, O_2, NO	N_2, O_2, NO	N_2, O_2, O	N_2, O_2, O	O, H, He
Height-range (km)		< 90	90 - 140	140 - ~ 300	300 - ~600	600 - 1000
Photochem-ical process		Recombination, Photoionization	Recombination, Photoionization	Recombination, Photoionization	Recombination, Photoionization	Recombination, Photoionization
Recombination type		Dissociative recombination	Dissociative recombination	Dissociative recombination	As in F1, but limiting process is charge transfer giving an attachment-like recombination law	Radiative recombination
Electron density [elec/m^3]	Day	10^8 - 10^{10}	10^{11}	5×10^{11}	10^{12}	10^{10}
	Night	-	2×10^9	10^9	3×10^{11}	-
Special features		Negative ions (mostly O_2^-)	Maximum conductivity	-	Peak density	-

Chapman theory

In 1931, Sydney Chapman presented a mathematical model that described the formation of ionized layers. The model described that energetic photons from the sun split air molecules into electrons and positive ions. The model further described the direct relation of the density of free electrons and ions to different heights and daily solar motion. The Chapman layer function produces the ion production rate under the following assumptions: That the ionizing radiation from the sun is monochromatic, the single neutral constituent to be ionized is distributed exponentially (i.e., with a constant scale height), and that there is equilibrium between the creation of free electrons and their loss by recombination. Following Schaer (1999), the ion production rate is given by Chapman layer function

$$q(h, \chi) = q_0 e^{(1-z-sec\chi e^{-z})}, \qquad z = \frac{h - h_0}{H}, \qquad and \quad H = \frac{kT}{mg} \tag{2.20}$$

Where $q(h, \chi)$ is the ion production rate, q_0 is the maximum ion production rate at $\chi = 0$ (i.e. the Sun at zenith), χ is the Sun zenith angle, e is the exponential function base, h_0 is the reference height of maximum ion production at $\chi = 0$, H is the scale height, k is the Boltzman constant, T is the temperature, m is the particle masses, and g is the gravitational constant. The maximum ion production rate is defined as:

$$q_0 = \frac{\vartheta(\psi)\eta}{H\ e} \tag{2.21}$$

Where $\vartheta(\psi)$ is the solar flux destiny outside the atmosphere (photons/area), and η is the number of ion pairs produced per proton. Now, equ. (2.20) is differentiated in order to obtain the height of maximum ion production rate (h_{max}). Hence, we obtain

$$h_{max} = h_0 + H\ z_{max}, \quad and \quad z_{max} = \ln sec\chi \tag{2.22}$$

The ion production maximum is obtained from equ. (2.23)

$$q_{max} = q_0\ cos\chi \tag{2.23}$$

When ions and electrons recombine proportionally to the electron density, then the following equation holds (disregarding electron transportation processes).

$$\frac{dN_e}{dt} = q - xN_e^{1/b} \tag{2.24}$$

15

x is the mean recombination coefficient for molecular ions, and b is a constant as a function of the ionospheric height. Using equ. (2.20), equ. (2.24), and where $dNe/dt = 0$, the electron density is obtained by

$$N_e(h, \chi) = N_0 e^{b(1-z-sec\chi e^{-z})}, \quad and \quad N_0 = \left(\frac{q_0}{x}\right)^b \tag{2.25}$$

Where N_0 is the maximum electron density at $\chi = 0$. This distribution is referred to as the simple Chapman function (Rishbeth and Garriott, 1969). At noontime when $\chi = 0$, the maximum electron density (N_m) reaches its maximum while h_m reaches its minimum. The basic relationship between N_m and when $\chi = 0$ is given in equ. (2.26)

$$N_m = N_0 cos\chi \tag{2.26}$$

Changing N_0 in equ. (2.25) for a general term N_m from equ. (2.26) to produce equ. (2.27).

$$N_e(h) = N_m e^{b(1-z-e^{-z})} \tag{2.27}$$

Figure (2.4b) is a typical example of electron density profile constructed with Chapman function (equ. 2.25) for different solar zenith angle. There is a huge amount of ion production at the height between 200 and 500 km. More details about Chapman can be found in Alizadeh (2013).
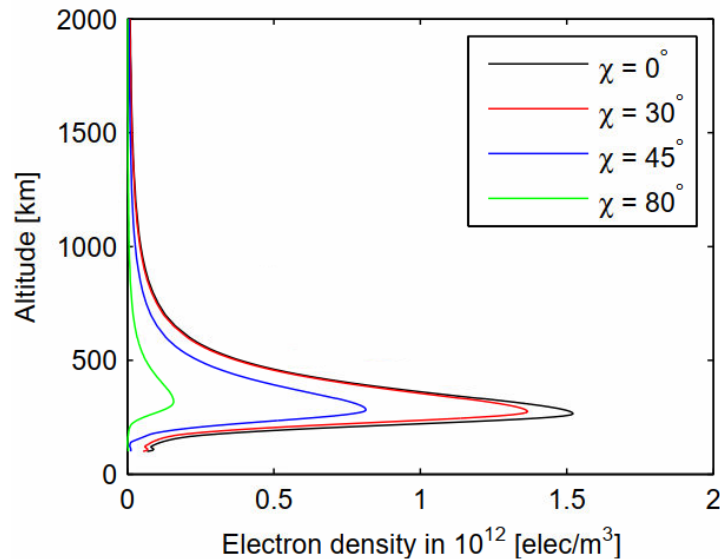
Figure 2.4b: Electron density profile for different solar zenith angles. (Alizadeh, 2013)

D layer: This is the lowest layer of the ionosphere and it is about 50 km to 90 km in altitude above the Earth's surface. This layer absorbs the most energetic part of solar radiation and it must

be noted that the daytime ionization sources in this layer are three; X-rays, cosmic rays and Lyman-α radiation but the most significant one is the Lyman-α which ionize mainly the nitric oxide (NO). The recombination process is high in the D layer; thus, the net ionization effect is very low and as a result high-frequency (HF) radio waves are not reflected by the D layer. The frequency of collision between electrons and other particles in this region is high during the daytime. The absorption is small at night and greatest about midday. The D layer disappears at night after sunset.

E layer: This is the next layer after the D layer and it starts from about 90 km to 140 km in altitude above the Earth's surface but the production peak starts from 90 to 110 km. The major source of ionization is due to X-ray (1-10 nm) and extreme ultraviolet (UV) solar radiation ionization (90-103 nm) ionizing molecular oxygen (O_2). At this layer, electron recombines with molecular ions oxygen (O_2) and (NO^+) (i.e. electron loss). At night the E layer begins to weaken gradually because the primary source of ionization which is the Sun is no longer there, but does not totally disappear. However, due to different mechanisms that interplay at this layer, an unsteady thin and dense layer called sporadic E layers (Es) is being developed. The sporadic E layer could be exhibited within an altitude of about 90 to 120 km or even more. The Es layers do occur at mid and low-latitudes as well as the polar region but with different mechanism sources respectively.

F layer: This is layer is located in about 140 to 1000 km altitude, It is the topmost layer of the ionosphere and it is also known as the Appleton layer. Its electron concentration peak is around 250-300 km in altitude and its major sources of ionization are Extreme Ultraviolet (EUV) solar radiation (20-90nm). The dominant ion in this region is O^+. The F layer consists of one layer at night, but in the presence of sunlight (during the day); it is divided into two layers, labeled F1 and F2 (fig. 1.4). The F1 layer is the lower part of the daytime F layer, and it extends from about 140 to about 300 km above the Earth. It exists only during daytime and disappears at nighttime. Maximum density of the F1 layer occurs shortly after noon, local time, when the sun is directly overhead. It is composed of a mixture of molecular ions O_2^+ and NO^+, and atomic ions O^+. Above the F1 region, atomic oxygen makes up the dominant constituent because lighter particles tend to occupy higher altitudes. This atomic oxygen provides the O^+ atomic ions that make up the F2 layer. The F2 layer is located near the peak electron density (about 300 to 400 km), and it is the

region with a higher ionization density of the ionosphere. The rate of ion production is maximized in this layer and this is due to a little number of the neutral particles. The major and dominant ionization source in the F2 region is the photo-ionization of atomic oxygen. The electron density peak varies with solar cycle activity. The highest concentration of free electrons can be observed in the daytime, and at nighttime, the concentration decreases.

Topside ionosphere: This is the region above the F2 peak which extends from about 600 to 1000 km. Atomic Oxygen ion is still the major and dominant ion here and the density of the topside ionosphere decreases exponentially with height. The ionization and recombination processes are not really important again at this point in the formation mechanism of the topside region. Moreover, above the topside region, is a region where there is dominance of lighter ions such as Hydrogen ion H+ and Helium ion He+. The dominance of the named ions made this region of topside to be totally ionized and the region is referred to as the plasmasphere or the protonosphere. However, from about 1000 km altitude, the density of Oxygen ions starts to fade and the Hydrogen ions turn to be the dominant ion particle as the primary ion constituent. The crossing point between the topside ionosphere and protonosphere regions is known as the transition height and this height varies in altitude. The protonosphere is often considered as part of the ionosphere for radio and navigation applications.

 Peak parameters of the ionospheric regions: Electromagnetic waves undergo a modification effect during its passage through the ionosphere and consequentially change the wave amplitude, propagation direction, velocity, and delay in signal arrival time at the receiving end, most especially in communication and navigation systems. However, these effects on the other hand reveal information about the state and properties of the ionospheric region. As we have known that the ionosphere is a dispersive medium and its interaction with radio waves is a function of frequency. If the frequency of the radio wave (from kHz to GHz) is less than the plasma frequency, the ionosphere acts as a metallic mirror, and if the situation is in the opposite way then the wave penetrates into the ionosphere without reflections. It must be noted that the electron density in the ionosphere depends on the height, and due to this fact, the transmitted radio wave signal from the ground station is reflected back to earth when the signal reaches the ionospheric height where the local plasma frequency reaches the wave frequency (see fig. 1.5). Two of the major instruments used in probing the ionosphere in order to measure maximum frequency where radio waves are reflected at each ionospheric region is known as the critical frequency or peak plasma frequency of the region. The critical frequency is therefore defined as the limiting

frequency at or below which a radio wave signal is reflected by an ionospheric layer at vertical incidence. As stated earlier, the ionosphere is composed of separate layers (D, E, F1, and F2) at all latitudes. Typically, the E, F1, and F2 layers are described by critical frequencies foE, foF1, and foF2 and corresponding peak heights hmE, hmF1, and hmF2. Associated with each critical frequency is a peak or maximum electron density of each ionospheric layer denoted by NmE, NmF1, and NmF2. The maximum or peak electron density (NmE, NmF1, and NmF2) is proportional to the squared peak plasma frequencies (foE, foF1, and foF2). Electron density decreases with height on both sides of peak height. Equation (2.28) is applied to compute critical frequency or maximum or peak electron density depending on the given parameter. The general term for electron density and critical frequency are Ne and fc respectively.

$$f_c^2 = 80.5 * N_e \tag{2.28}$$
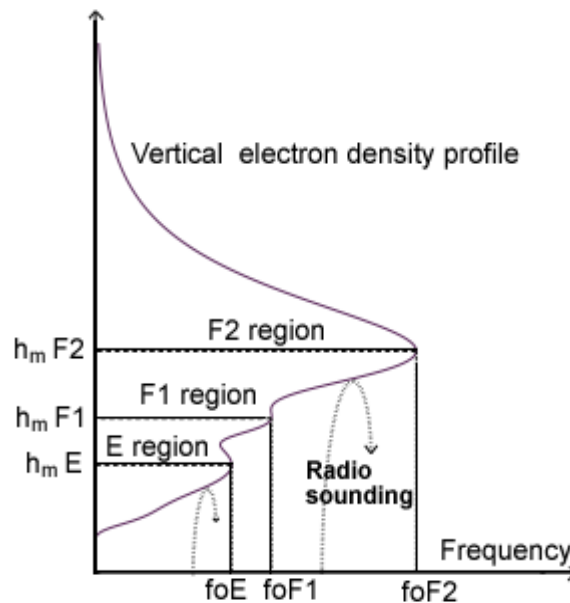
Figure 2.5: Peak plasma frequency and the peak height illustration

2.6.1.2   Latitude dependent

The ionosphere can be divided into three latitudinal regions: low latitude (equatorial), mid-latitude, and high latitude (see fig. 2.7). The boundary between the regions varies according to local time, geomagnetic condition, and solar activity.

Low latitude region

This region absorbs a high proportion of energy photons and it contains the highest ionospheric TEC values compared to other regions as well as a high rate of ionization. The ionosphere around this zone has a peculiar anomaly behavior known as the equatorial ionization anomaly (EIA) or geomagnetic anomaly or Appleton anomaly, it is the most common feature at low and equatorial latitude. The EIA-TEC is majorly a daytime ionospheric phenomenon near the equatorial region. It starts to develop after the sunrise and decays after the sunset during the low solar activity epoch and persists late into the night during the solar maximum. The ionosphere over the EIA zone is quite dynamic and it is characterized by a latitudinal distribution of ionization density showing a trough at the magnetic equator and two peaks (crest) of density near the geomagnetic latitudes 15ºN and 15ºS (Kelley, 1989; Balan and Bailey, 1992). In the equatorial F region, the EIA phenomenon basic mechanism is due to electric field configuration, which is eastward during the day and produces an upward drift (E x B drift) leading to a plasma fountain (i.e. fountain effect) then the plasma diffuses along the magnetic field lines under the influence of gravity and pressure gradient forces. The net result is the ionization enhancement on both sides of the magnetic equator at ±20º latitude (see fig. 2.6). Consequently, the upward plasma movement induced by the electrodynamics during the daytime generates a peculiar ionospheric anomaly behavior known as the equatorial ionization anomaly (EIA), and it must be noted that the fountain effect is the major driver of the EIA (Martyn, 1955; Kelley, 1989; Balan and Bailey, 1995). The EIA perseveres into the nighttime hour periods depending on the season and solar activity and it is known to be produced by the post-sunset enhancement in the eastward electric field produced by the F-region dynamo action (Kumar et al., 2013). The EIA is responsible for the global maximum values of ionospheric TEC over tropical latitude as well as enhancing ionospheric scintillation effects produced by spread-F/plasma bubble irregularities on transionospheric radio wave (GPS signal) propagations (Abdu, 2005). Klobuchar et al. (1991) showed that the effects of day-time E x B drift on TEC were more pronounced at the crests of the equatorial anomaly than at the equator. There is an asymmetric pattern exhibited between the northern and southern ionization crests as a result of an inter-hemispheric wind blowing from the summer to the winter hemisphere. Previous ionospheric studies over this region show that there is major high TEC amplitude over the geomagnetic equator during daytime and becomes decay at post-daytime and then another minor peak during nighttime (Ngwira et al., 2013; Opio et al., 2015; D'ujanga et al., 2016; Oluwadare et al., 2018).
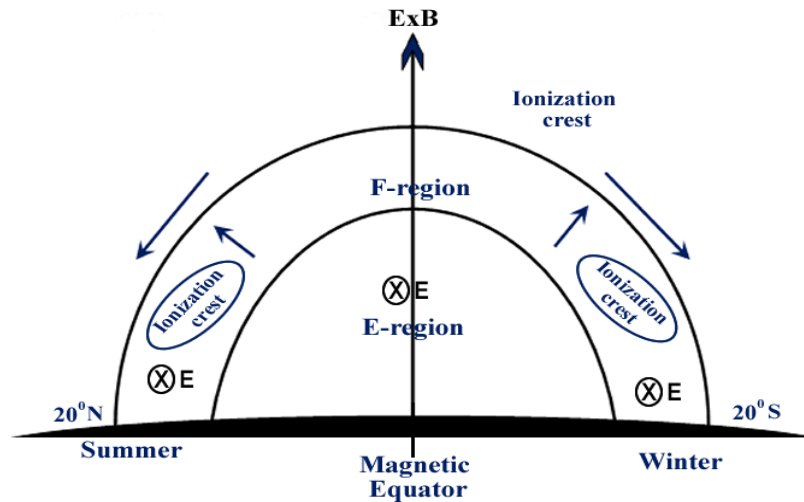
Figure 2.6: Asymmetry of the equatorial ionization anomaly. **E** denotes an eastward electric field and **B** is the northward geomagnetic field Scheme. Source: Anderson and Roble (1981)

There are several electrodynamic processes that causes disturbances over this region. At summer hemisphere, plasma moves upward along the geomagnetic field lines but moves downward in the winter hemisphere, this implies that there is plasma transport from the summer hemisphere to the winter hemisphere, the consequence of this processes makes the equatorial anomaly crests in winter hemisphere to be larger than in the summer hemisphere

Mid-latitude region

The mid-latitude region of the ionosphere includes geographic latitudes from 30° to about 60°. This region has a low TEC variability compared to the low latitude region. The TEC in this region is relatively regular. Only solar photon radiation is responsible for the ionization process and there is no direct influence from phenomena associated with the fountain effect. The mid-latitude ionosphere is to some extent well understood of all regions. The day to day changes in the E, F1, and F2-regions exhibit regular variations and some few irregular variations associated with changes in the neutral atmosphere density and thermospheric winds.

High latitude region

The geomagnetic field lines at high latitudes are nearly vertical and thus guide the charged particles (energetic protons and electrons) from the magnetosphere descending to the Earth's atmosphere. These particles collide with the neutral atmospheric particles causing local enhancements in the electron concentration. Moreover, the accelerating particles lose their energy after collision.

21
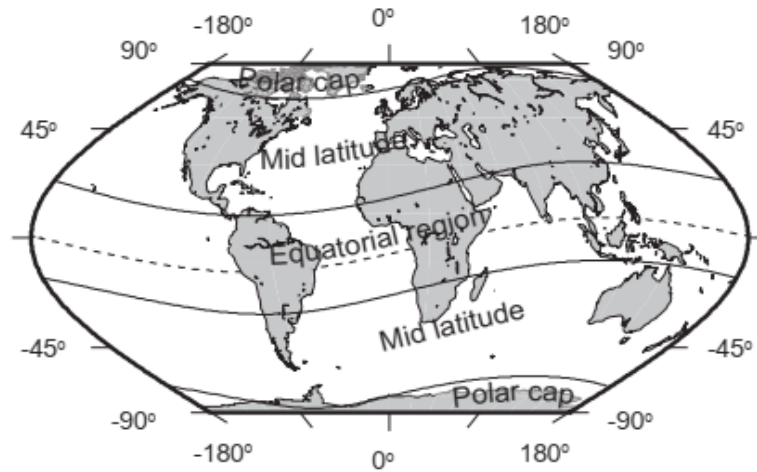
Figure 2.7: Major latitude dependent regions of the ionosphere. (Alizadeh, 2013)

This phenomenon is associated with the auroral activity. The aftermath effect of the particle-collision interaction is that intense electromagnetic waves named Auroral Kilometric Radiation (AKR) are generated. In addition, some atmospheric elements are excited to higher energy levels and this leads to emission of visible lights, called the auroral lights. This activity occurs mainly within the auroral oval. The auroral zones are relatively narrow rings situated between the northern and southern geomagnetic latitudes of about 64° - ~70°. The effect intensity of the auroral ovals is related to geomagnetic disturbances, and this effect is extended towards the equator with increasing levels of geomagnetic disturbance (McNamara, 1991).

2.6.2   Temporal variations

The temporal variation of the ionosphere is categorized into regular and irregular variations. The regular variation of the ionosphere is associated with the daily, seasonal, and longer variations controlled by solar activity. There is daily regular variation in ionospheric TEC at a given location due to the earth's rotation, but there are significant differences from day to day also due to other effects. The irregular variations literally mean ionospheric variation that is not regular (opposite of regular variations), typical examples of this are Ionospheric storms, Ionospheric scintillation, and Traveling Ionospheric Disturbances (TID) among others.

2.6.2.1   Regular variations

Seasonal variations: The seasonal variations of ionospheric TEC are due to the earth's tilt and rotation around the Sun; the relative position of the Sun moves from one hemisphere to the other

with the seasonal variation of solar zenith angle and radiation intensity at any given geographical location. Months in a year conventionally often grouped into four seasons, these are December solstice (November, December, and January), March equinox (February, March, and April), June solstice (May, June, and July) and September equinox (August, September, and October). Some studies also often grouped them into three seasons based on space-oriented seasons; Equinox season (March, April, September, October), Summer season (May, June, July, August) and Winter season (November, December, January, February) following Karia, S.P and Pathak, K.N, 2011; Oron et al, 2013. In general, the maximum electron density and the TEC of the daytime F region are higher in March equinox at low latitude while in mid-latitude; the summer season exhibited a high electron density and high TEC values. The ionosphere over African EIA region sometimes exhibits winter anomaly, it is one of the phenomena peculiar to years with the high solar phase of solar cycle 24 (Oluwadare et al., 2018). The winter anomaly behavior observed has been attributed to the increase in [O]/[N2] ratio in the F2 layer whish results into a higher electron density (Torr and Torr, 1973; Kherani et al., 2013) caused by the meridional wind which changes the neutral composition.

Diurnal variations: The daytime and nighttime variation of the ionosphere is basically due to the Earth's rotation. The daytime TEC is higher at noon than the nighttime due to solar radiation from the sun (increase ionization) and the TEC experience a decrease when the solar radiation from the sun is not in view again. In principle, the amount of ionization of the Earth's atmosphere depends solely on the amount and intensity of radiation it receives during the day. At noontime, when the Sun is at its zenith (solar zenith = 0), the electron density exhibits its maximum. During sunset, the amount of radiation responsible for the ionized plasma decreases considerably and the recombination processes dominate, therefore ionosphere experiences depletion (Campbell, 1997).

Solar-Terrestrial and Geomagnetic Indices: The temporal variations in the ionosphere are linked to the solar activity which is linked to the 11-year solar cycle. Major indicators (i.e. Solar-Terrestrial Indices) for the solar activity level are sunspot numbers (SSN), solar radio flux (F10.7 cm), and extreme ultraviolet (EUV). Sometimes F10.7 cm solar radio flux is often used as a proxy for the solar EUV. During the period of maximum sunspot number, the solar radiation intensity is high and thus the ionosphere exhibits an enhancement in electron concentration and vice-versa during solar minimum. Other indicators for studying ionospheric behavior are geomagnetic indices like disturbance storm time index (Dst) and Kp-index (Kp). These two geomagnetic indicators monitor different (or combinations of responses) responses to solar activities. Most

physics-based ionospheric models need solar and/or geomagnetic indices to specify the solar and geomagnetic disturbance level and to investigate ionospheric behavior. Unglaub et al., (2012), in their research measured global TEC from 2002 to 2010 with corresponding EUV and solar flux F10.7cm. The plot pattern in their result shows a better correlation using EUV data with TEC than the solar flux F10.7cm.

Sunspot Number (SSN): This is the number of dark spot areas as seen on the Sun visible surface and it's a commonly used index of solar activity. The Sun visible surface is known as the photosphere. Counting the sunspot is through the use of a sophisticated space-based telescope, but it is not as straightforward as it sounds. These spots mostly appear as pairs and are caused due to concentrations of magnetic flux (i.e. intense magnetic activity) that occurs in groups. The spots appear visibly as dark spots because they are cooler compared to the surrounding photosphere. As these SSN spots increase, so also the magnetic complexity grows and they eventually become likely sources of large eruptive energy release which is known as the solar flares (Dieminger et al., 1996). The relative sunspot number is defined as:

$$R = K (10g + s) \tag{2.29}$$

R is sunspot activity (R), *K* is an observatory scaling factor (usually <1), *g* is the number of sunspot groups on the solar disk, and *s* is the total number of individual spots / distinct spots.

Solar radio flux (F10.7 cm): The solar radio flux at 10.7 cm (2800 MHz) along with sunspot number is one the most used solar activity monitor indices and it's mostly referred to as the F10.7 index. It is mostly applied as a proxy for solar activity in ionospheric models like International Reference Ionosphere (IRI). F10.7 cm is one of the longest-running records of solar activity as well as a better proxy than SSN as revealed by a solar research scientist (Ouattara and Fleury, 2011; Zoundi et al., 2012; Ngwira et al., 2013; Opio et al., 2015; D'ujanga et al., 2016). This is simply because it gives a better representation of solar EUV fluxes intensity and due to its track record, it has been proven to be very useful in space weather event prediction. In today's space research, it is still been used as a proxy to quantify solar EUV variability.

Solar Extreme Ultraviolet (EUV): EUV is solar radiation that covers the wavelengths 10 – 120 nm of the electromagnetic spectrum. It is absorbed by the upper atmosphere. EUV heat up and ionize the upper atmosphere and thus create the ionosphere. It is been measured by rockets and satellites. Solar EUV radiation changes by a factor of ten over the course of a typical solar cycle.

This variability creates similar variations in the ionosphere and upper atmosphere. Solar EUV variation is a major driver of ionospheric variability. Over the years, scientists have relied on proxies for solar EUV such as the Sunspot Number or the F10.7 cm radio flux due to the fact that solar EUV measuring sensor is hard to build and maintain.

Disturbance storm time: The Dst index is a measure of geomagnetic activity used to assess the degree or severity of magnetic storms. It also gives information about the intensity of the ring current around the Earth which is caused by solar protons and electrons. The ring current around the Earth produces a magnetic field that is directly opposite Earth's magnetic field. Dst is expressed in nanoteslas (nT). A negative Dst value means that Earth's magnetic field is weakened, this is a case during solar storms. Table (2.2) shows the geomagnetic storm classification and its corresponding storm type.

Table 2.2: Geomagnetic classification

Dst value	Storm type
Minimum Dst below -20 nT	Weak storm
Minimum Dst below -50 nT	Moderate storm
Minimum Dst below -100 nT	Strong storm
Minimum Dst below -200 nT	Severe storm
Minimum Dst below -320 nT	Great storm

Kp index: The geomagnetic three-hourly Kp index was introduced by J. Bartels in 1938 and is derived from the standardized K index (Ks) of 13 magnetic observatories. It is the most and widely used of all geomagnetic indices. It is designed to express the degree of geomagnetic activity or disturbance for the whole Earth, at intervals of three hours in Universal Time (UT) (Mayaud, 1973). The Kp index measures the irregular variations of standard magnetograms, and gives an indicator of the general level of geomagnetic disturbance at a given observatory for each three-hour interval based on the largest value of the3-hr ranges in X, Y, D or H. Where the vector components of the Earth's magnetic field can be represented in two ways; either by X, Y, and Z (XYZ-component) or by H (horizontal), D (declination) and Z (into the Earth) (HDZ-component) (Campbell, 1997). The Kp index quantifies disturbances in the horizontal component of Earth's

magnetic field with an integer in the range zero (0) to nine (9), where a value of 0 means that there are very little geomagnetic activity and a value of 9 means extreme geomagnetic storm.

Table 2.3: The Geomagnetic storm scale according to Kp- index.

Kp index	Storm remark
0	Quiet
1	Quiet
2	Unsettled
3	Unsettled
4	Active
5	Minor geomagnetic storm
6	Moderate geomagnetic storm
7	Strong geomagnetic storm
8	Severe geomagnetic storm
9	Extreme geomagnetic storm

2.6.2.2   Irregular variations

Ionospheric storms: Ionospheric storms are huge disturbances that appear in the ionosphere associated with geomagnetic storms. The storm is often excited by huge solar flare then followed by multiple Coronal Mass Ejection (CME) from the sun. This phenomenon influences the behavior of the ionosphere and its structure. At mid-latitudes, F2-region responses to the geomagnetic storm in main three phases: The first phase is known as a positive ionospheric storm; in this situation, the positive phase where the peak electron density increases with respect to pre-storm conditions and this would last for few hours during the first day of the storm event (Hunsucker and Hargreaves, 2003). The second phase is known as a negative ionospheric storm; the negative phase of the peak electron density decreases relative to pre-storm conditions. The third phase is known as the recovery phase; in this condition, the ionosphere gradually returns to normal conditions over a period of 24hrs to several days. The ionospheric storm can cause a depletion of ionospheric electron densities, and consequentially increase the electron density or TEC (Feltens et al., 2009).

Ionospheric small-scale irregularities: Small-scale irregularities in the ionosphere causes rapid fluctuations in the amplitude and phase of radio signals. This observed phenomenon is known as scintillation. When sufficiently strong, it can cause degradation of GPS signal quality and also can reduce its information content. During the high solar activity, strong scintillation could affect GPS receiver stations in the equatorial and low-latitude regions and in some cases at the mid-latitude. Equinox months often exhibit a high scintillation effect in the African region, most especially in the equatorial and low-latitude. The severity of amplitude scintillation is quantified by the scintillation intensity index S4, and it is defined as follows:

$$S_4 = \sqrt{\frac{\langle I^2 \rangle - \langle I \rangle^2}{\langle I \rangle}} \qquad\qquad (2.30)$$

where I is the signal intensity, the angle brackets <...> represent the average values of signal intensity over a 60-second interval and S_4 is the ratio of the signal intensity standard deviation by the signal intensity mean (Ackah et al., 2011).

Traveling Ionospheric Disturbances (TIDs): are wavelike perturbations of ionospheric plasma that are observed in the upper atmospheric region (ionosphere) due to the continuous spectrum passage of internal AGWs propagating the neutral atmosphere (Hines, 1960; Fedorenko et al., 2010). TID can cause degradation of radio signals propagation and consequently lead to a change in TEC value in the range of several percents (Schaer, 1999). The wavelike structure of TIDs varies in scale sizes ranging within few hundreds of kilometers (km) to over one thousand km (Grocott, A. et al., 2013) and they are categorized as either medium-scale TIDs (MSTIDs), which has wavelengths between 50 and 500 km, periods of 12 mins to 60 mins and the phase speed of the order of 50–400 m/s or large-scale TIDs (LSTIDs) characterize with a wavelength greater than 500 km, phase speeds of 400–1000 m/s and the periods of 30 minutes to 3 hours, (Samuel H. Francis., 1974, Ogawa et al., 1987, Jacobson et al., 1995, Hocke and Schlegel, 1996, Grocott, A. et at., 2013). More about MSTIDs which is the main focus of this thesis is discussed in the next chapter.

2.7   Transport and dynamic processes in the ionosphere

It is important to give a brief description of the equation of the dynamic process that takes place during electron/ion transport processes in the ionosphere when steady force is applied. Both E and

F regions of the ionosphere exhibit robust dynamic processes due to the influence of various forces such as gravitational ($\rho_j g$), electric ($n_j q_j E$), magnetic $n_j q_j (V_j \times B)$ and pressure. Where q_j is the charge of the jth species, while E and B are the electric and magnetic fields respectively. The frictional force is exerted on each species by collisions with all of the other species. For instance, electrons will collide with neutrals as well as with the various ions. It must be noted that the charged particles are moved by ionospheric forces. The following forces move charged particles: collisions with neutral particles ($- m_i v_{in} (V_i - U)$), partial pressure gradients ($- (N_i k T_i)/N_i$), gravity force ($m_i g$), electric fields (qE), Lorentz force: $q (V_i \times B)$. These forces are characterized by ratio

$$k = \frac{\Omega}{v_i} \tag{2.31}$$

The forces are designated by ratio index k, where Ω is the gyro-frequency, and v_{in} are the collision frequencies ((i.e. ion-neutral, electron-neutral, and ion-ion collision frequencies)). It must be noted that both E and F regions are categorized based on k_i and k_e. In E region, $k_i \ll 1$, F region: $k_i \geq 1$, while in both regions $k_e \gg 1$. Throughout the E and F region, k_e for the electrons is very large, and consequently, the electrons always move in the direction that is perpendicular to the force and magnetic field and as for the ions, the direction of motion changes as a function of altitude. At higher altitudes the ions gyro-frequency becomes dominant and diffusion processes also play a significant role in the dynamics of the ionosphere. The equation governing the dynamics of the charged particles is called the momentum equation and it is given as:

$$m_i \frac{\partial \vec{V}_i}{\partial t} = -\frac{1}{N_i} \nabla N_i k T_i + m_i \vec{g} + q(\vec{E} + \vec{V}_i \times \vec{B}) - m_i v_{in}(\vec{V} - \vec{U}) \tag{2.32}$$

The motion of a charged particle in magnetic and electric fields is described by the Lorentz term (the third term on the right-hand side of equ. (2.32)) (Walt, 1994).

$$\vec{F} = m_i \frac{\partial \vec{V}_i}{\partial t} = q(\vec{E} + \vec{V}_i \times \vec{B}) \tag{2.33}$$

Where F is the force in Newton, m is the mass of the ions, q is the charge in Coulomb, E is the electric field in Volt/m, B is the magnetic field induction in Tesla, V is the ion velocity in m/s, U is velocity of neutral wind. Charged particles are subject to collisions, with neutrals and ions which are considerably more susceptible to these collisions. Equation (2.33) can be separated into different components parallel and perpendicular to the magnetic field giving as:

$$\vec{F}^{\|} = m_i \frac{\partial \vec{V}_i^{\|}}{\partial t} = q\vec{E}^{\|} \tag{2.34}$$

$$\vec{F}^{\perp} = m_i \frac{\partial \vec{V}_i^{\perp}}{\partial t} = q(\vec{E}^{\perp} + \vec{V}_i^{\perp} \times \vec{B}) \tag{2.35}$$

Equation (2.34) is conventionally used to describe the motion of a charged particle in an electric field, valid as well for neutral gas particles, and can be directly integrated if the external forces are not time-dependent. In equ. (2.35), both magnitude and direction of the magnetic force is a function of the velocity and critically depend on magnetic field configuration. Thus, it makes the solution of equ. (2.35) complex in a situation where the magnetic field is not uniform. However, for simplicity, we consider a situation where the magnetic field is uniform, therefore equ. (2.35) is resolved and the solution is described only for two conditions: The first case; in the absence of an external electric field (i.e. E = 0), the velocity along the magnetic field lines is constant according to equ. (2.34), the acceleration $(\frac{\partial \vec{V}^{\perp}_{i}}{\partial t})$ in equation (2.35) is perpendicular to $(\vec{V}^{\perp}_{i})$ and $\|\vec{V}^{\perp}\|$ = constant. Hence, the trajectory of the charged particle in a uniform magnetic field with no electric field is a helix (Helical Orbit), see fig. (2.8). The angular frequency of the motion of the charged particle in a magnetic field (gyration motion) is called angular gyro-frequency. The magnetic force direction depends on the electric charge type, hence, the positively charged particles move in a circular motion while the negatively charged particles move in the opposite direction see fig. (2.8). The second case; the presence of an external electric field (i.e. E ≠ 0), results in a drift motion of the charged particles in the magnetic field. If $\vec{E}^{\parallel} \neq 0$ and it is constant, in which the particle is accelerated along the magnetic field line. The force $q\vec{E}^{\perp}$ which is perpendicular to $\vec{B}$, consequentially results in drift charged particles in a direction that is perpendicular to both $\vec{B}$ and $\vec{E}$. In this situation, both ions and electrons move together with the same velocity and in same direction perpendicular to both magnetic and electric fields. Hence, drift velocity is obtained by:

$$\vec{V}_{drift} = \frac{\vec{E}^{\perp} \text{x} \vec{B}}{\|\vec{B}\|^2} \tag{2.36}$$
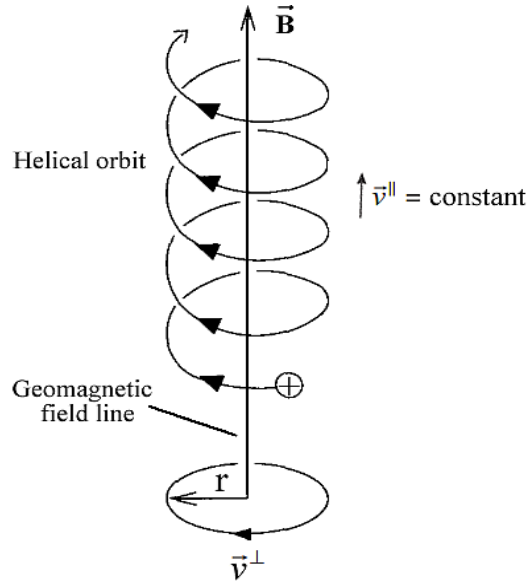
Figure 2.8: Charge particle motion in a uniform magnetic field ($\vec{E} = 0$, $\vec{v}^{\cdot\cdot}$ = constant)

2.8 Ionospheric Conductivity based on altitude

Ionospheric conductivity (IC) varies with altitude and it is mostly active at the E-region (i.e. E-region dynamo). The conductivity is due to the high collision frequency of charged particles related to the gyro-frequency around the magnetic field. IC plays a major role in electric fields development and it could be influenced by space and time, and solar activity. There are three types of IC; the Specific, Pedersen, and Hall conductivities, and are denoted with σ0, σP, and σH, respectively (Kelley, M.C., 2009). The specific (i.e. parallel conductivity (σ0)) is composed of high electron mobility and is equal to ne^2/m$_e$v$_e$ to a good approximation. Controlling of ion motion by magnetic field and collisions is significant and thus, requires an assessment of ionospheric electrical conductivity. In a situation where the electric field and collision terms are engaged in the force balance, then the steady state momentum equation of electrons and ions would be given as:

$$-eE = m_e v_{in} u_e \text{ and } qE = m_i v_{in} u_i \tag{2.37}$$

In the presence of magnetic field, the velocities (u_e and u_i) are no longer expressed, but expressed in terms of E. But in a situation where we solve for velocities (u_e and u_i), the magnetic field (B) has to be taken to be parallel to the z-axis solved (Christopher, T R., 2016). Thus, for this simple medium, j is related to the electric field and it is expressed through a tensor relationship:

$$\vec{J'} = \sigma.\vec{E'}$$

(2.38)

Where conductivity (σ) is a scalar quantity which depends on collision frequencies and magnetic field (B) has been taken to be parallel to the *z*-axis. The conductivity tensor (σ) is given as:

$$\sigma = \begin{pmatrix} \sigma_P & -\sigma_H & 0 \\ \sigma_H & \sigma_P & 0 \\ 0 & 0 & \sigma_0 \end{pmatrix}$$

(2.39)

Where:

$$\sigma_0 = \frac{n_e}{B}(k_i - k_e)$$

(2.40)

$$\sigma_P = \frac{n_e}{B}\left(\frac{k_i}{1+k_i^2} - \frac{k_e}{1+k_e^2}\right)$$

$$\sigma_H = \frac{n_e}{B}\left(\frac{k^2{}_e}{1+k_e^2} - \frac{k^2{}_i}{1+k_i^2}\right)$$

Where *n* is the ionospheric density and other parameters of equ. (2.40) have been defined in the earlier of this section and section (2.7). Parallel conductivity is in the direction parallel to the magnetic field line. At high altitudes when electron-neutral collisions do not happen often, σ_0 is independent of density above ~400 km, hence there is variation above that height (see fig. 2.9). Above ~ 75 km, the electrons only move perpendicular to the forces that act on them. At this time, the Pedersen conductivity may be written in the form:

$$\sigma_P = \frac{n_e^2}{(mv_{in}(1+k_i^2))}$$

(2.41)

For $k_i \gg 1$ (above 130 km) this expression becomes simpler:

$$\sigma_P = \frac{n_e^2 v_{in}}{(m\Omega_i^2)} = \frac{nmv_{in}}{B^2}$$

(2.42)

The Pedersen conductivity is splitted into E and F regions. The E region is much larger than F region during daytime. Pedersen conductivity is the conductivity in the direction of the applied electric field.
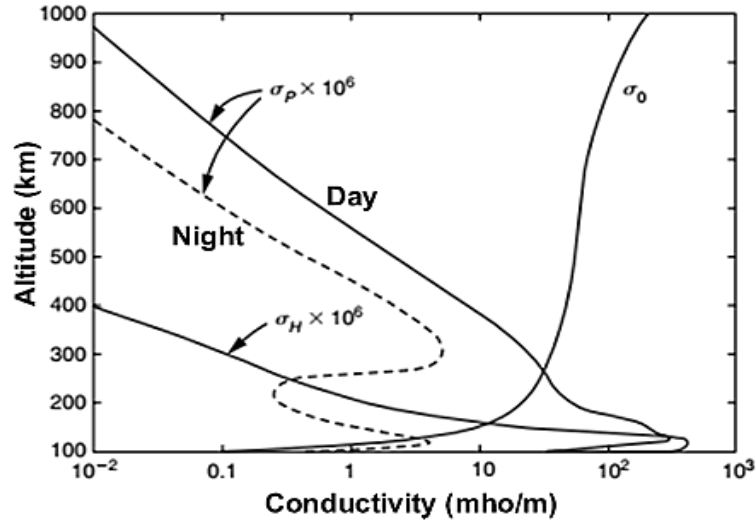
Figure 2.9: Height profile of ionospheric conductivities (Parallel (σ_0), Pedersen (σ_P) and Hall (σ_H) conductivities). Source: Kelley (2009)

The Hall conductivity is a significant layer at about 110 km in the E region of the ionospheric layer, and it is removed during nighttime. It is in the direction perpendicular to both the magnetic and electric fields. fig. (2.9) exhibit a common conductivity values for the mid latitude daytime ionosphere. In fig. (2.9) note that there is a change of scale for σ_P, and σ_H and the dashed curve line is a typical nighttime profile of σ_P also multiplied by 10^6. After several calculations in the neutral reference frame, $\vec{J}' = \sigma.\vec{E}'$ in equ. (2.38) is modified to include neutral wind (U) and electric field E in the earth-fixed frame in order to obtain effective electric field. Nevertheless, since $\vec{E}' = E + UxB$ and $\vec{J}' = J$, we write the conventional form of current equation:

$$J = \sigma.(E + UxB) \tag{2.42}$$

Electric fields thus play a huge role in the dynamics of the ionosphere. The ionospheric plasma is dependent on electromagnetic forces in addition to those felt by the neutral atmosphere. The charge difference (i.e. dipole nature) of the magnetic field is not much affected by ionospheric currents and the consequence is that the magnetic field creates different magnetic latitudes geometric constraints on the plasma behavior and on the contrary, the electric field put the plasma constituents in a motion perpendicular to the magnetic field (B) (Christopher, T. R., 2016).

Chapter 3

TIDs BACKGROUND

As far back as 1920, radio signal/communication engineers were already facing some challenges regarding fading signals reflected from the ionosphere (Mimno, 1937), this effect already gave a clue that the ionosphere is an inhomogeneous medium. Further investigations showed that fading signal as a consequence of focusing and defocusing of radio waves by ionospheric irregularities. Munro, (1958); Georges, (1968); Davis and Jones, (1971) and a host of other researchers investigated the irregularities and described it as quasi-sinusoidal propagating density waves in electron content measurement which is known as Travelling Ionospheric Disturbance (TID). Investigations and studies in more than six decades have established that ionospheric motions and irregularities such as TIDs are attributed to disturbances of the neutral gas associated with the continuous spectrum passage of internal atmospheric gravity waves (AGWs) propagating the neutral atmosphere (Martyn, 1950; Hines, 1960; Hines and Reddy, 1967; Fedorenko et al., 2010). In previous years, researchers studied TID structures using ionograms and it is mostly observed at or near the F-region and the upper side of E-region of the ionosphere in form of propagating wave-like motions of electron density in the neutral atmosphere. Concisely, TIDs are a wavelike perturbation of ionospheric plasma and they are regarded as the plasma manifestation of AGW passing or propagating in the ionosphere from the lower atmospheric regions into the ionosphere (Hines 1960). The wavelike structure of TIDs varies in scale sizes ranging within a few hundreds of kilometers (km) to over one thousand km (Grocott, A. et al., 2013). Different atmospheric excitation mechanisms could cause gravity wave perturbations in the atmosphere which consequentially lead to TIDs occurrence. In general, TIDs are associated with sudden local changes resulting in sudden energy and momentum transfer to the ionospheric plasma. TID is classified into different category based on their disturbance scales, but we only focus on the medium scale in this study.

3.1 Atmospheric Gravity Waves

Atmospheric waves are usually classified into three main categories based on scale and sources (Schunk and Nagy, 2000). The waves which propagate on a global scale are atmospheric tides category, the wave with the smallest scale are acoustic waves category but do not play a major

role in atmospheric dynamics, and the third category of waves produced by atmospheric buoyancy forces are referred to as AGWs. AGWs are the most impactful waves that contribute to the dynamical nature of the upper atmosphere amongst many waves present in the atmosphere. They are divided into three groups depending on the period and wavelength (Hunsucker and Hargreaves, 2003). The large-scale AGWs have horizontal wavelengths of ~ 1000 km, wave periods (> 60 mins), and horizontal velocities of ~250-1000 m/s. The medium-scale AGWs have horizontal wavelengths of several hundred kilometers, wave periods (~ 15 - 60 mins), and horizontal velocities of ~ 90 - 250 m/s. The small-scale AGWs have wave periods (2 - 5 mins), with horizontal velocities (< 300 m/s), and wavelengths are less than medium-scale AGWs wavelengths. It must be noted that AGWs have a localized source and propagate vertically as well as horizontally, but with a minimal wavelength range. Its amplitude grows exponentially with height (which means that the wave source is from below) in order to enable a constant energy flux through the atmosphere with density decreasing with height (Clark et al., 1971). AGWs could be generated below the turbopause height (i.e. turbopause lies near an altitude of roughly 100 km, near the base of the thermosphere) and then propagate into the ionosphere or get generated in the lower ionospheric heights. Studies have indicated that AGWs have many source mechanisms. They can be generated in the auroral regions from Joule heating caused by geomagnetic storms (Hunsucker, 1982). They can be excited/created through orographic means; winds blowing over irregular terrain (e.g. mountains, hills) (Hines, 1960; Hooke, 1968) below the turbopause, but with small amplitudes. However, studies have it that orographic source effect (stationary or modulated waves) is not enough to account for MSTIDs (Koekkoek, 1997). Another source is wind shears; they are mostly present in jet streams which can be observed in the zonal direction during the winter and summer season in the middle atmosphere. AGW can also be generated by the vertical irradiance gradient associated with the Solar Terminator (ST) (i.e. sunset and sunrise terminators) at a given ionospheric region and its magnetic conjugate (MacDougall et al., 2009a; Afraimovich et al., 2002). According to MacDougall et al. (2009b), AGWs could also be driven (i.e. source) by wind component along the magnetic field direction. The most reported common source of AGWs is the meteorological processes like atmospheric winds and convection activities in the troposphere and stratosphere (Somsikov, 1995; Scotto 1995). The AGWs passage involves vertical displacement of air parcels from the troposphere (lower atmosphere) into the ionosphere, and it is characterized by upward propagation of energy and downward propagation of phase (see fig.3.1). During this transport process, energy, momentum, and chemical and atmospheric constituents are transported beyond an unstable region of the atmosphere into a stratified, stable region and then may penetrate into the ionosphere (Vedas, 2007). On penetrating the ionosphere,

the electron density would be perturbed via ion-neutral collisions (i.e. collision with the plasma), and then the charged ions are set in motion but are constrained to move along the magnetic field lines. The transportation of the charged molecules/ions along the magnetic field lines leads to electron density enhancement in certain places along the wavefront and also depletions in some other places. The continuous and regular enhancement and depletion (i.e. oscillations) of the plasma density consequently lead to TIDs occurrence (Hooke, 1968; Hocke and Schlegel, 1996).
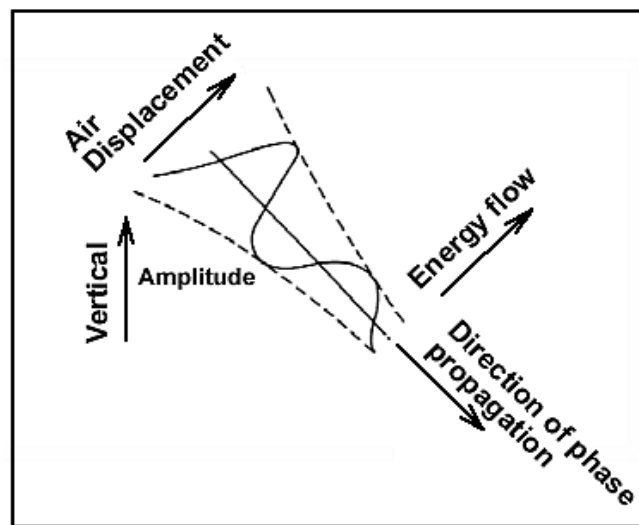
Figure 3.1: Illustration of gravity wave showing the energy
and phase propagations. Source: Hargreaves (1992)

The main features and the measuring parameter of AGWs are temperatures, vertical velocity fluctuations, density, and horizontal winds in a stably stratified environment (Holton, 1992). The atmosphere consists of different density layers and it is well arranged under the influence of gravitational force. However, its density varies and more than two layers of different densities interact with each other in such a way that the vertical propagation of internal gravity waves (i.e. gravity waves that oscillate within a fluid medium, rather than on its surface) becomes possible with their interfaces interacting with each other. A continuously stratified fluid in the neutral atmosphere supplies a restoring force, in the form of buoyancy, resulting in the propagation of internal gravity waves. The equation that describes the effect of dispersion of the properties of a wave traveling within that fluid medium is known as the dispersion relation equation. The dispersion relation of these internal gravity waves is stated under the following assumptions that the atmosphere is non-rotating, stationary, horizontally stratified, isothermal, single-species, and windless, the AGW obeys the dispersion relation (Hines, 1960) see equation (3.1). Follow Hines (Hines, 1960) for a more detailed equation derivation.

35

$$\omega^4 - \omega^2 c_s^2(k_x^2 + k_z^2) - i\gamma g\omega^2 k_z^2 + (\gamma - 1)g^2 k_x^2 = 0 \qquad (3.1)$$

where ω is the wave angular frequency, c_s is the speed of sound, k_x is the horizontal wave number (i.e. $k_x = 2\Pi/\lambda_x$), k_z is the vertical wave number, γ is the ratio of specific heats, g is the force of gravity. If g is equal to zero and equ. (3.1) is resolved, then it is acoustic wave (i.e. dispersion relation for pure sound waves) (see equ. 3.2).

$$\omega^2 = c_s^2(k_x^2 + k_z^2) \qquad (3.2)$$

If we substitute $\omega_a = \frac{\gamma g}{2c_s}$ and $\omega_a = \frac{(\gamma-1)^{1/2}g}{c_s}$ into equation (3.1), then the dispersion relation equation reduces to equation (3.3).

$$k_z^2 = \left(1 + \frac{\omega_a^2}{\omega^2}\right)\frac{\omega^2}{c_s} - k_x^2\left(1 - \frac{\omega_B^2}{\omega^2}\right) \qquad (3.3)$$

where ω_a is the acoustic cutoff frequency and frequency ω_B is the Brunt–Väisälä frequency also called the stratification or buoyancy frequency. A graphical representation of the dispersion relation (equ.3.3) is given in fig. (3.2), signifying the regimes of AGW in terms of frequency (ω) and the horizontal wave number (k_x) in which the consequences of the two waves coupling in a compressible stratified medium leads to their separation into gravity-modified acoustic and compressibility-modified gravity waves (Koekkoek, 1997). Acoustic waves propagating horizontally are non-dispersive. For vertical propagation of a wave, its angular frequency (ω) must be greater than the Brunt–Väisälä frequency (ω_B) or angular frequency (ω) must be greater than acoustic cut-off frequency (ω_a). The shaded areas in fig. (3.2) are regions of propagation within the gravity branch and the acoustic branch (Hines, 1960). The vertical axis shows the angular frequency, while the horizontal axis gives the horizontal wave number. The solid curve represents the propagation boundaries obtained from the non-isothermal cutoff frequencies, while the dashed lines are the effects of neglecting gravity and compressibility, respectively. There exists a wave between the acoustic and gravity regimes called the evanescent waves which do not propagate but whose energy is spatially confined in the vicinity of the source.
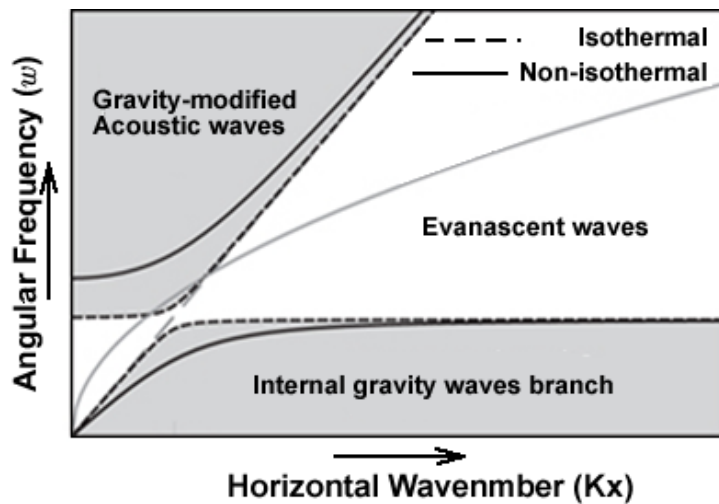
Figure 3.2: Schematic diagram showing different regimes of acoustic, evanescent, and gravity of acoustic-gravity wave's propagation in a compressible, gravitationally stratified medium for a given height in the atmosphere. Source: Vigeesh, Jackiewicz, and Steiner (2017).

AGWs play a major role in the upper atmosphere dynamics because of their interaction and influence on the ionospheric plasma, hence causing wavelike fluctuations of electron density in the ionosphere. Vigeesh, Jackiewicz, and Steiner (2017), Koekkoek, (1997) gave a detailed information on AGWs.

3.2 Medium Scale Travelling Ionospheric Disturbances (MSTIDs)

MSTID is one of the major and frequent ionospheric irregularity phenomena at the F region Mid-latitude which may degrade positioning systems and it has been studied to have the ability to propagate over long distances (Frissell et al., 2014). MSTIDs could cause a delay in GPS signal transmission between a satellite and the GPS receiver, and produce ionospheric disturbances that can degrade communication and navigation signals where the amplitude of MSTIDs is typical of tenth of a TECU (1 TECU = 10^{16} electrons/m^2) (Wanninger, 2004; Husin et al., 2011; Hernandes-Pajares et al., 2006). The MSTIDs frequently appear as oscillating waves in electron density induced by the passage of AGWs propagating upward from the lower atmospheric regions (Fedorenko et al., 2010). The statistical study of MSTIDs has shown that it does occur more frequently than LSTIDs (Husin et al., 2011), and the excitation mechanisms have not been well established as it has been attributed to many phenomena.

3.3 MSTIDs regional study review

Within the last six decades, several MSTIDs studies have been carried out by various researchers and many MSTIDs detailed features of nighttime or daytime of different regions have been reported around the globe using different techniques. To mention a few amongst many are: Ogawa et al. (1987) who investigated MSTIDs occurrence frequency using the U.S. Navy Navigation Satellite System (NNSS) in polar region at a 1000 km altitude during the disturbed geomagnetic condition. The authors concluded that there was no increase in MSTIDs occurrence under disturbed condition. Most researches that used GNSS for their respective investigation of MSTIDs adopted the GPS-TEC methodology. Hernández-Pajares et al. (2006, 2012), Tsugawa et al. (2007), and Kotake et al. (2007), respectively carried out independent research of MSTIDs using GNSS receiver network at different location of North America region and, they all reported nearly the same results in terms of seasonal occurrences, but with slight differences in the propagation directions. Jonah et al. (2016) examined the daytime MSTIDs over equatorial and low latitude regions of Brazil in the southern hemisphere of the South America region using GNSS network, digisonde, Geostationary Operational Environmental Satellite - 13 (GOES-13), and COSMIC satellite data. They reported a strong summer daytime MSTIDs occurrence during the selected days of the year 2011 using the detrended TEC parameter. The observed daytime MSTIDs during summer have not been reported before over Southern hemisphere, as other past studies in this region have only reported a winter daytime MSTID occurrence. They also stated that both the nighttime MSTIDs in the Northern and Southern hemispheres propagate in the same direction which is due to the geomagnetic conjugate dynamics (Otsuka et al., 2004). Guanyi Chen et al. (2019) carried out a statistical analysis of MSTIDs during 2014 - 2017 over the East Asia region by using the Hong Kong GNSS network. They reported that MSTIDs activity shows a major peak during June solstice at nighttime (2200-0200 LT) and minor peak during December solstice. Tsugawa et al. (2006) used the GNSS receiver network to carry out an MSTIDs study over the South-East Asian sector (Japan) and reported that the nighttime MSTIDs within the time range of 0001 - 0200 LT are positively correlated with solar cycle activity behavior. Ding et al. (2011) studied MSTIDs' climatology over the mid-latitude of central China in the South-East Asian region during the 2010 solar minimum and reported that the annual MSTIDs event count (AMEC) is high at nighttime only during solar minimum. Oinats et al. (2016) studied and investigated the statistical observation of MSTIDs during 2013 - 2014 using radar over East Asia (Hokkaido-F region) and European-Asian region during solar maximum and reported high AMEC values, and most especially found out that MSTIDs occurrence rate is dominantly high at daytime, the result is

in a close agreement with Fukushima et al. (2012). Mendillo et al. (1997) and Candido et al. (2008) respectively also reported the observation of MSTIDs using optical imager. Oinats et al. (2016) used Super Dual Auroral Radar Network (SuperDARN) high frequency (HF) radar data and reported that MSTIDs increases with solar activity, while Jacobson et al. (1995) used satellite – beacon radio interferometer and concluded that daytime MSTIDs propagate mainly equatorward, while the nighttime MSTIDs propagate southwestward.

3.4 Characteristics of daytime and nighttime MSTIDs

Daytime MSTIDs

Daytime (DT) MSTIDs occurrence rate (OR) is high and frequently occurs during winter and sometimes equinox season at the Northern hemisphere, with propagation direction mostly southeastward, and with time rotates from southeastward to southwestward (Kotake et al., 2007), with wavelength ranging between 100 - 250 km. They further stated that daytime MSTIDs tend to rotate clockwise from 90° to 240° as observed over southern California in North American. Whereas, Evans et al. (1983) have reported that the day time OR is high only in winter with wavelength ranging between 200 - 250 km. However, Evans at al. (1983), Oliver et al. (1997), and Kotake et al. (2007) all reported that daytime MSTIDs over Europe region are observed during winter and tend to propagate towards south (equatorward). There have been theories for supporting the propagation direction. For instance, Heisler, (1963) stated that the dominant propagation direction of TIDs is towards the ionospheric part where it is mostly illuminated by the Sun (from the Northern hemisphere), but the most supported theory is still in the direction of the geomagnetic field lines (Thome, 1964). At the F-regions, the ions move and travel along the geomagnetic field lines through neutral-ion collision, with velocity the same as the velocity of the neutral motion along the geomagnetic field caused by the gravity waves (Hines, 1960; Hooke, 1968). However, the motion of the ions across the magnetic field line is constrained to move along the magnetic field lines because the gyro-frequency of the ions are much higher than the frequency of the ion-neutral collisions. The direction of the motion of the ions consequentially leads to directivity in the response of the electron density variations to the gravity waves. This kind of directivity phenomenon could be responsible for the daytime MSTIDs Southward propagation direction. Besides, an anisotropic frictional ion drag force has been thought to also contribute to the Southward tendency of the daytime MSTID propagation direction (Liu and Yeh, 1969; Kelley and Miller, 1997).

Nighttime MSTIDs

It is noteworthy to state that nighttime MSTIDs were previously found to be associated with increases in the F-region peak electron density altitude by Behnke (1979), and its source was conventionally thought to be generated by electrodynamical forces such as Perkins instability (Perkins, 1973; Kelley and Miller, 1997) at mid-latitude. Studies have shown that the nighttime MSTIDs propagate southwestward in the Northern hemisphere and northwestward in the southern hemisphere (Afraimovich et al., 1999, Ding et al., 2011) with seasonal dependence in summer (i.e. June solstice). Generally, the wavelike structure of MSTIDs for both daytime (DT) and nighttime (NT) are characterized by a wavelength, period and phase speed of 50 - 500 km, 12 - 60 mins and 50 - 400 m/s, respectively (Ogawa et al., 1987; Hocke and Schlegel, 1996; Grocott et al., 2013), but phase speed at NT is often higher DT period (Husin et al., 2011).

3.5 Causes of MSTIDs

The exhibition of different characteristics during the DT and NT of MSTIDs is an indication that a different excitation mechanism controls its occurrence (Kotake et al., 2007). The daytime MSTIDs have been reported to be primarily due to the passage of AGW (Hines, 1960; Hooke, 1968; Otsuka et al., 2013; Jonah et al., 2016; Oinats et al., 2016; Figueiredo et al., 2018). The nighttime MSTIDs are commonly thought to be generated by electrodynamical forces known as Perkins instability in the mid-latitude MSTIDs electrodynamical process (Perkins., 1973; Kelley and Miller., 1997, Garcia et al., 2000; Tsugawa et al., 2007). Further studies have also revealed that nighttime MSTIDs are most likely to be related to the development of plasma instabilities in the F region (Kelley and Miller., 1997). The instability is often strong in the nighttime and can generate local polarization electric field (**Ep**) that can move the plasma upward (downward) via E x B drift, which consequently causes a perturbation in the plasma density. More details of nighttime MSTIDs is discussed in chapter 6 and 7 in this thesis.

Chapter   4

INSTRUMENTATION AND MEASUREMENTS

This chapter gives a brief overview of instruments used in the study, such as the GNSS, and the Constellation Observing System for Meteorology, Ionosphere, and Climate (COSMIC) satellite mission. This study focuses on one of the major examples of GNSS; GPS for probing the ionosphere. Also discussed are the estimated data derived from the instrument, like TEC from GPS, observed temperature profile from COSMIC satellite, and MSTIDs estimation technique.

4.1   GNSS general concept

The GNSS is an official and acceptable generic name for satellite navigation which comprises the constellation of satellites that provides global coverage of radio signals from space to earth, transmitting data containing geo-spatial positioning and corresponding timing stamp. GNSS example are USA's NAVSTAR GPS, Europe's Global Navigation Satellite System (Galileo), Russia's Global Navigation Satellite System (GLONASS), Chinese navigation satellite system (BeiDou), Indian Regional Navigation Satellite System (IRNSS) and the navigation satellite system that provides service to Japan and the Asia-Oceania region (QZSS).

GPS background

GPS is a space-based navigation system designed and developed by the military Department of Defense (DoD) in the United State in 1973. The purpose is to provide global coverage of radio signals on a 24 hours basis for the military to accurately determine their position, velocity in 3D (latitude, longitude, and altitude), and time on or near Earth. The GPS consists of a minimum of constellations of 24 satellites network that orbits the earth. The satellites orbit at an altitude of approximately 20,200 kilometers, or about half the altitude of a geostationary satellite. The satellites are distributed into six orbital planes inclined 55° up from the equator and are spaced 60° degrees apart. With this kind of constellation geometry and an orbital period of about 12 hours, 4 to 10 GPS satellites are visible anywhere in the world at any given time. Each GPS satellite completes two full orbits each 24-hour day. GPS consists of three major segments, they are Space Segment, Control Segment, and User Segment. The space and control segments are controlled by

the United States Military. The control segment maintains both the integrity of the satellites and the data that they transmit. The space segment is comprised of satellite constellation in orbit, as well as operations and backup. The user segment is simply all the end users (civilians and military) making use of GPS receivers for various applications.

4.2   Ionospheric effects on GPS signals

The ionosphere is the ionized part of the earth's atmosphere as discussed in section 2.5 of chapter 2 of this thesis. The interaction of the radio wave with the ionospheric plasma is a major effect for the limited accuracy and vulnerability in satellite-based positioning or time estimation. The effects have a quantifiable impact on radio wave signals. When a radio wave instruments transmit signal at a frequency below ~30MHz, the ionosphere acting as a medium change the traveled path of the signal back towards the Earth, this particular effect gives room for long-distance communication. On the contrary, when instrument operating at higher frequencies such as GPS transmit signals through the ionosphere (Jonah, 2016), there is a fluctuation in signal strength, propagation delay, signal attenuation, signal degradation and in extreme cases loss of lock, and these have constituted significant threats to both communication and navigation systems (Akala et al., 2010a, 2011, 2012) due to the presence of ionospheric plasma. The density of electrons present along the signal propagation path is a major effect on the signal in terms of the signal propagation speed. A higher density of electrons will imply a greater speed of the carrier phase. The interaction of these propagating radio waves with the electrons causes a first-order propagation delay. The quantification of the entire radio wave signal effect is obtained by integrating the electron density along the path that a signal follows from a satellite to a receiver, and it is expressed as TEC. TEC is defined as an integral of electron density along the path between the GPS satellite and the receiver, where 1 TECU = 10^{16} electron/m^2. The TEC is a function of the amount of incident solar radiation. On the nighttime, the free electron recombines with the ions and hence TEC is reduced. TEC can also change depending on the ionospheric dynamics, but one of the major phenomena that can cause a change in TEC is the TID. Brief details about TID have been discussed in section 3.0 of chapter 3, and sub-section (2.6.6.3) of chapter 2 respectively. In this thesis, TEC from GPS data is referred to as GPS-TEC. In section 4.4, GPS-TEC exhibiting wave-like structures depicting to be MSTIDs are selected and detrended to obtain TEC perturbation (dTEC).

Electromagnetic wave propagation parameters

An electromagnetic wave propagating in space is expressed in terms of frequency (f) and wavelength (λ), and the relation between them is the velocity (v), given as:

$$v = \lambda \cdot f \tag{4.10}$$

where the unit for v, λ, f are metre/seconds, metre and Hertz respectively. In a dispersive medium like the ionosphere, the propagation wave is represented using a sinusoidal wave as an analogy, the propagation velocity of a wave with an unvarying wavelength is termed as phase velocity (vph) while the propagation velocity of the wave group is termed as the group velocity (vgr). It is noteworthy to mention that we followed the approach of Alizadeh et al. (2013) in this section. The phase and group velocities are the same within the vacuum but contrary in a real-life scenario. Following Wells (1974), equ. (4.10) is rewritten in equ. (4.11). Following Hofmann-Wellenhof et al. (1993), the group velocity is given as (see equ. (4.12)).

$$v_{ph} = \lambda . f \tag{4.11}$$

$$v_{gr} = -\left(\frac{df}{d\lambda}\right)\lambda^2 \tag{4.12}$$

By forming a differential equation using equ (4.11) and resolve we obtain equ (4.13)

$$dv_{ph} = fd\lambda + \lambda df \tag{4.13}$$

$$\frac{df}{d\lambda} = \frac{dv_{ph}}{\lambda d\lambda} - \frac{f}{\lambda}$$

Substituting equ (4.13) into equ (4.12) produce the group and phase velocities relationship.

$$v_{gr} = -\left(\lambda \frac{dv_{ph}}{d\lambda} - v_{ph}\right) \tag{4.14}$$

It must be noted that phase and group velocities are the same and equal in a non-dispersive media, or less than light speed (i.e. c= 299,792,458 metres per second) in a vacuum. In a dispersive medium, the propagation velocity of waves depends on the refractive index (n) of that medium (see equ (4.15)) and rewriting equ (4.15) in terms of phase and group velocities yields equ (4.16).

$$v = \left(\frac{c}{n}\right) \tag{4.15}$$

$$n_{ph} = \left(\frac{c}{v_{ph}}\right), n_{gr} = \left(\frac{c}{v_{gr}}\right) \tag{4.16}$$

Differentiating phase refractive index (n_{ph}) in equ. (4.16) w.r.t wavelength (λ) yields

$$\frac{dv_{ph}}{d\lambda} = -\frac{dn_{ph}}{d\lambda}\frac{c}{n^2_{ph}} \tag{4.17}$$

Substituting equations (4.16) and (4.17) into equ. (4.14) we obtain

$$\frac{1}{n_{gr}} = \left(\lambda.\frac{1}{n^2_{ph}}\frac{dn_{ph}}{d\lambda} + \frac{1}{n_{ph}}\right) \Rightarrow n^{-1}_{ph}\left(\lambda.\frac{1}{n_{ph}}\frac{dn_{ph}}{d\lambda} + 1\right) \tag{4.18}$$

Resolving equ (4.18) by applying a mathematical approximation identity: $(1+x)^{-1} = 1-x$, we obtain

$$n_{gr} = n_{ph} - \lambda\frac{dn_{ph}}{d\lambda} \tag{4.19}$$

$$n_{gr} = n_{ph} + f\frac{dn_{ph}}{df} \tag{4.20}$$

Equation (4.19) is the group refractive index, a modified Rayleigh equation (Hofmann-Wellenhof et al., 1993), while equ. (4.20) is another form of group refractive index obtained by differentiating equ. (4.10) w.r.t λ and f. More details about the derivations of equations (4.19 and 4.20) can be found in Hofmann-Wellenhof (2001).

4.3 Ionospheric Refraction

The ionosphere is a dispersive medium. Hence radio signals propagation is affected when passing through the medium. In order to budget for this ionospheric effect, the refractive index of the ionosphere must be accounted for. Following Budden (1985), the radio signal propagation through the ionosphere in the Earth's magnetic field is described by the Appleton-Lassen equation. The Appleton–Lassen equation, sometimes also referred to as the Appleton–Hartree equation is a mathematical expression (see equ. 4.21) which gives a vivid description of the refractive index (n)

for electromagnetic wave propagation in magnetized plasma. Equation (4.21) is the phase ionospheric refractive index when electron-ion collision effects are ignored.

Ionosphere refractive index

$$n_{ph}^2 = 1 - \frac{X}{1 - \frac{\frac{1}{2}Y^2\sin^2\theta}{1-X} \pm \frac{1}{1-X}\left(\frac{1}{4}Y^4\sin\theta + Y^2\cos\theta(1-X)^2\right)^{0.5}}$$

(4.21)

where

$$X = \frac{\omega_0^2}{\omega^2}, \quad Y = \frac{\omega H}{\omega},$$

$$\omega_0 = 2\pi f_0 = \sqrt{\frac{N_e e^2}{\varepsilon_0 m_e}}, \quad \omega H = 2\pi f H = \frac{B_0 |e|}{m_e},$$

θ is the angle between the radio waves propagation direction and the Earth's magnetic field, n is the complex refractive index, ω is the radial frequency ($\omega = 2\pi f$), ω_0 is the electron plasma frequency, ε_0 is the permittivity of free space, Ne is electron density, e is the electron charge, f is the wave frequency, ω_H is the electron gyro frequency, B_0 magnitude of the magnetic field vector $\mathbf{B}_0$, m_e is the electron mass. GPS signal range error from the ionosphere (i.e. ionospheric effects) is computed from the refractive index equation in equ. (4.21). However, for easy computation, assumptions and approximations were put into consideration to obtain a suitable approximate expression for the ionospheric refractive index. For instance, Hartmann and Leitinger (1984) assume the magnetic field is assumed to be negligible (i.e. $\sin \theta \approx 0$) and the refractive index is reduced to:

$$n_{ph}^{ion} = 1 - \frac{X}{2} \pm \frac{XY}{2}\cos\theta - \frac{1}{2}\left(\frac{X}{2}\right)^2$$

(4.22)

For convenience, C_X and C_Y are constants defined in equ. (4.23a) and equ. (4.23b), following Brunner and Gu (1991).

$$C_x \equiv \frac{e^2}{4\pi^2\varepsilon_0 m_e} = 80.62$$

(4.23a)

$$C_Y \equiv \frac{e}{2\pi m_e},$$

(4.23b)

The constants are substituted into equ (4.22) and can be rewritten in orders of $1/f^n$, to yield equ (4.24)

$$n_{ph}^{ion} = 1 - \frac{C_X}{2f^2}N_e \pm \frac{C_X C_Y}{2f^3} N_e B_0 cos\theta - \frac{c^2_X}{8f^4}N_e^2$$

(4.24)

where μ_o is the permeability in vacuum. The first two terms in equ. (4.24) are expressed as the first and second order refractive index. The second and third order delays are often referred to as the ionospheric higher-order terms. The higher order terms in equ. (4.24) are ignored here due to their negligible impact, most especially on higher frequencies in the terrestrial ionosphere. Hence the first two terms of equ. (4.24) are reduced after substituting the necessary variables from equ. (4.23a) and equ. (4.23b). Hence equ. (4.24) is reduced to

$$n^{ion} = 1 - \frac{C_X}{2f^2}N_e$$

(4.25)

Resolving the constant in (4.25), we obtain

$$C_2 = \frac{C_X}{2} = \frac{e^2}{8\pi^2\varepsilon_0 m_e} \approx 40.31 \ [m^3 s^{-2}]$$

(4.26)

Now we substitute equ. (4.26) into equ. (4.25) to obtain first order refractive index (equ. (4.27)). We regard equ. (4.25) as a phase measurement, so it is denoted as phase refractive index.

$$n_{ph}^{ion} = 1 - C_2\frac{N_e}{f^2} = 1 - 40.31\frac{Ne}{f^2}$$

(4.27)

To obtain group refractive index, equ. (4.27) is differentiated.

$$n_{gr}^{ion} = 1 + C_2\frac{N_e}{f^2} = 1 + 40.31\frac{Ne}{f^2}$$

(4.28)

Equations (4.27 and 4.28) reveal the same answer except for the mathematical operator sign of negative and positive. When $n_{gr} > n_{ph}$ then, it implies that $v_{gr} < v_{ph}$. As a result of this, the group

velocity is delayed and the phase velocity is advanced. That is to say when radio signal passes through the ionosphere, the GPS carrier waves' phases is advanced and the code measurement is delayed. Following Fermat's principle as published in Hofmann-Wellenhof et al. (2001), the signal delay (or advance) due to the ionosphere, denoted as $\Delta\rho^{ion}$ (m) is given as the difference between the actual signal path and the geometrical distance between the satellite and the receiver.

$$\Delta\rho^{ion} = \int_r^s n\,ds - \int_r^s ds_0 = \int_r^s (n-1)\,ds_0 \tag{4.29}$$

This is called the ionosphere delay. For simplification, the delay is integrated along the geometric straight path thus ds changes to ds_0. Substituting the phase refractive index in equ (4.27) into equ (4.29) and group refractive index in equ (4.28) to yield phase delay (Δ_{ph}^{ion}) and group delay (Δ_{gr}^{ion}) respectively. The parameter that described the integral of the electron density (Ne) along the ray path from the satellite (s) to the receiver (r) in the ionosphere is termed Total Electron Content (TEC).

$$\Delta\rho_{ph}^{ion} = -\int_r^s \frac{40.3Ne}{f^2}\,ds_0 = -\frac{40.3}{f^2}\int_r^s Ne\,ds_0 \tag{4.30}$$

$$\Delta\rho_{gr}^{ion} = \frac{40.3}{f^2}\int_r^s Ne\,ds_0 \tag{4.31}$$

TEC is the total number of free electrons in a slant column with a unit-squared cross-section in the ionosphere along the signal path. Conventionally, TEC is measured in TEC units (TECU) where 1 TECU = 10^{16} electron/m^2. Usually, slant TEC (STEC) parameter is used as a measure of the total electron content of the ionosphere along the ray path from the satellite to the receiver, and it is given as:

$$STEC = \int_r^s Ne\,(l)dl \tag{4.32}$$

where Ne indicate the varying electron density along the signal path. Taking equ. (4.30) and equ. (4.31) into consideration, we obtained carrier phase and group delay measurements to be:

$$\Delta\rho_{ph}^{ion} = -\frac{40.3}{f^2}STEC \tag{4.33}$$

$$\Delta\rho_{gr}^{ion} = \frac{40.3}{f^2}STEC \tag{4.34}$$

Ionospheric Mapping Function

For absolute TEC mapping using ground-based GPS over a given area, the TEC along the vertical should be considered. Therefore, the slant distance of TEC known as slant TEC (STEC) is projected to the zenith distance at the ionospheric pierce point (IPP). Thus, STEC is converted to vertical TEC (VTEC) using the mapping function (M) equation. Mapping function (M) is based on a single layer model (SLM) (see fig. (4.1)). The model assumes a homogeneous distribution of free electrons that are concentrated in a thin shell of infinitesimal thickness at about 350km to 500km height (H) above the Earth's surface (Schaer, 1999). In addition, it describes the overall ionization of the ionosphere over a given location (Horvath and Essex, 2000). The height is slightly above the height where electron density is considered the highest, above F2 layer peak. The GPS signal is transmitted from the satellite passes through the ionospheric shell point called the IPP to the receiver. The signal crosses the zenith angle at the IPP (X') and arrives at the ground station with zenith angle X, (see fig. (4.1)).

$$Sin\,X' = \frac{R_e}{R_e+H}\,Sin\,X \tag{4.35}$$

where R_e is the mean Earth radius (6,371 km), X' is the zenith angle at IPP, X is the zenith angle at receiver position, H is the altitude of the thin single layer above the surface of the Earth, taken to be 350km in this study.
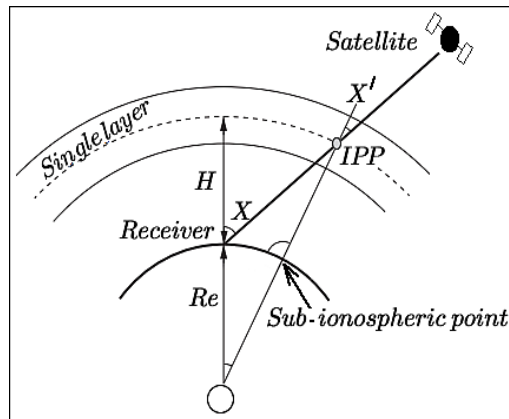
Figure 4.1: Geometry of the ionospheric single-layer approximation

The relationship between STEC and VTEC in relations to the zenith angle (X') at the ionospheric piercing point (IPP) and the zenith angle (X) at the receiver position is given in equ. (4.36)

$$VTEC = STEC\,(Cos\,X')\tag{4.36}$$

where

$$X' = arcsin\left(\frac{R_e}{R_e + H}SinX\right)$$

The SLM mapping function (M) is given as:

$$M(X) = \frac{1}{Cos(X')} = \frac{1}{\sqrt{1 - Sin^2\,X'}}\tag{4.37}$$

$$STEC = M(X).VTEC$$

However, following Dach et al. (2007) a modified single-layer mapping functions (MSLM) was given as:

$$Mf(X) = \frac{1}{\sqrt{1 - \left(\frac{R_e}{R_e + H}.sin(\alpha X)\right)^2}}\tag{4.38}$$

$$STEC = Mf(X).VTEC\tag{4.39}$$

Where α = 0.9782 and H = 506.7 km and the difference between MSLM and SLM is called the heuristic factor α.

4.4   GPS Observation equation.

GPS receivers are of two types: single frequency receiver and dual frequency receiver. The single-frequency receivers only operate on L1 signal and cannot remove the error introduced by the ionosphere. On the contrary, the dual-frequency GPS receiver consists of both code (pseudorange) and carrier phase observations on L1 (1575.42 MHz) and L2 (1227.60 MHz) frequencies, each encoded with two digital codes, and navigation messages (El-Rabbany, 2006). The navigation message can be found on the L1 frequency channel and it carries information on the broadcast Ephemeris (satellite orbital parameters), satellite health status, satellite clock corrections, and almanac data (a crude ephemeris for all satellites). The new generation GPS satellites now transmit on an additional third frequency, L5 which was developed for a better performance application.

The GPS transmits two types of measurements as observables, these are phase (of the carrier frequency) and code (digital code) measurements. Phase measurement is the number of cycles at the corresponding carrier frequency between the satellite and the receiver. The phase measurements are biased by an unknown number of phase cycles, coupled with other errors. When a GPS receiver is switched on or tracks a newly risen satellite, it cannot determine the total number of complete cycles between the receiver and the satellite. Hence the initial number of complete cycles remains ambiguous; this is known as phase ambiguity bias (Arora et al., 2015). Furthermore, the GPS code measurements have two types of code observables, namely the C/A-code (Coarse/Acquisition code, modulated only on the L1 carrier, denoted as C1) and P-code (Precise code, modulated on both L1 and L2 carriers, denoted as P1 and P2, respectively). It must be noted that code modulation varies for a different GPS satellite. A code signal is sometimes referred to as PRN (Pseudo Random Noise) (Arora et al., 2015). The C/A-code measurement is less precise than the P-code (Langley, 1993). The P-code is modulated on both the L1 and L2 frequencies (GPS dual frequency) and is used in the estimation of TEC in this study. Detail description of GPS system operations can be found in Jin et al. (2008), and Arora et al. (2015). The GPS observation equations for code (pseudorange) and carrier phase observables are expressed as below, following Jin et al. (2008).

Code or pseudorange observation equation

A code (pseudorange) P_i measurement is a measurement of the geometric distance between GPS receiver (r) and GPS satellite (s). Following Teunissen and Kleusberg (1998), GPS code (pseudorange) P_i observable can be given as:

$$P_i = \rho + c(\Delta t_r - \Delta t_s) + T + I_i + b_{ir}^P + b_{is}^P + m_i^P + \varepsilon_i^P \tag{4.40}$$

where

Subscripts *r, s*, and *i* implies receiver, satellite and GPS frequency number, respectively

P_i slant range between satellite and receiver, as observed at *i* frequency (*i* =1, 2)

ρ geometric range (distance) between receiver and satellite

$\Delta t_r, \Delta t_s$ receiver and satellite clock error with respect to GPS time (s)

$I_i,$ ionospheric delay (frequency dependence)

T   signal delay due to the troposphere

b_{ir}^P, b_{is}^P receiver and satellite hardware delay/biases expressed in time (nsec) unit respectively

$m_i^P,$ multi-path effect (m)

ε_i^P measurement noise (m)

Carrier phase observation equation

As for the GPS carrier phase observable, it is obtained by finding the phase difference between the carrier signal produced by the GPS receiver's internal oscillator and the carrier signal transmitted from a GPS satellite. The Carrier phase observable is more accurate than the code observable, but it also gives an ambiguous measurement of the geometric distance between a satellite and the receiver (Schaer, 1999). The phase-psuedorange (Li) is expressed as:

$$L_i = \rho + c(\Delta t_r - \Delta t_s) + T - I_i + \lambda_i N_i + m_i^L + \varepsilon_i^L \tag{4.41}$$

where λ_i is the wavelength of the GPS signal on Li frequency, the term λN at each frequency indicates a constant bias expressed in cycles, which contains the initial carrier phase ambiguity N.

4.4.1 Ionospheric observable

In order to filter out the information about the ionosphere from the GPS observations, a linear combination is formed. This approach eliminates the geometric term. Here the ionospheric linear combination of the carrier phase of the signal and the pseudo-range measurements is formed. This helps in reducing the effect of the ionosphere. The equations are formed from signal measurements on L1 and L2 frequencies. Recalling the observation equation for the GPS code (pseudorange) in equ (4.1).

$$P_1 = \rho + c(\Delta t_r - \Delta t_s) + I_1 + T + b_{1r}^P + b_{1s}^P + m_1^P + \varepsilon_1^P$$
$$P_2 = \rho + c(\Delta t_r - \Delta t_s) + I_2 + T + b_{2r}^P + b_{2s}^P + m_2^P + \varepsilon_2^P \tag{4.42}$$

After all geometric range terms, clock error and tropospheric delay cancelled out then we obtain.

$$P_4 = P_1 - P_2 = (I_1 - I_2) + (b_{r1}^P - b_{r2}^P) + (b_{s1}^P - b_{s2}^P) \tag{4.43}$$

Ionospheric delay (I) as is also expressed as $\Delta\rho^{ion}$, therefore we rewrite equ (4.41) as:

$$P_4 = P_1 - P_2 = (\Delta\rho_1^{ion} - \Delta\rho_2^{ion}) + \Delta b_{s1,2}^P + \Delta b_{r1,2}^P \tag{4.44}$$

where $(\Delta b_{s1,2}^P) and (\Delta b_{r1,2}^P)$ are differential code biases (DCB) of the satellites and differential code biases of the receivers, between P1 and P2. The ionospheric term ($\Delta\rho^{ion}$) is equivalent to the group delay in equ (4.34). The same procedure is followed to obtain ionospheric-free linear combination for carrier phase, starting from equ (4.41).

$$L_1 = \rho + c(\Delta t_r - \Delta t_s) + T - I_1 + \lambda_1 N_1 + m_1^L + \varepsilon_1^L$$
$$L_2 = \rho + c(\Delta t_r - \Delta t_s) + T - I_2 + \lambda_2 N_2 + m_2^L + \varepsilon_2^L \tag{4.45}$$

The difference between the L1 and L2 carrier frequency of the GPS signal forms L4-combination which could remove all frequency independent components.

$$L_4 = L_1 - L_2 = (I_1 - I_2) + (\lambda_1 N_1 - \lambda_2 N_2) + \Delta b_{r1,2}^L + \Delta b_{s1,2}^L \tag{4.46}$$

where $(\Delta b_{s1,2}^L)$ and $(\Delta b_{r1,2}^L)$ are differential code biases (DCB) of the satellites and differential code biases of the receivers, between L1 and L2 frequencies. It is well known that code (pseudorange) observations is much noisy due to the inbuilt noise in the frequency channel, so the carrier phase observations are used to smooth the pseudorange, this is known as carrier phase leveling (Rui Jin., et al 2012). However, cycle slips and gross errors in the carrier phase observations must be removed before using the carrier phase observations to smooth the pseudorange observations. The phase and group delays obtained in equ. (4.33) and equ. (4.34) are substituted into equ. (4.47) and equ. (4.48) respectively.

$$L_4 = \left[\frac{1}{f_2^2} - \frac{1}{f_1^2}\right] STEC_{ph} + (\lambda_1 N_1 - \lambda_2 N_2) + \Delta b_s^L + \Delta b_r^L \tag{4.47}$$

$$P_4 = \left[\frac{1}{f_2^2} - \frac{1}{f_1^2}\right] STEC_{gr} + \Delta b_{s1,2}^P + \Delta b_{r1,2}^P \tag{4.48}$$

Equation (4.48) is the he ionospheric observable smoothed code measurement. Resolve equ. (4.48) and make STEC subject of the formula.

$$STEC = \frac{f_1^2 f_1^2}{40.3(f_1^2 - f_2^2)}(P_4 - \Delta b_{s1,2}^P - \Delta b_{r1,2}^P) \tag{4.49}$$

The STEC can be translated into the vertical total electron content (VTEC) using the single layer model (SLM) mapping function (M) or modified single-layer model (MSLM) mapping function (Mf).

$$VTEC = \frac{STEC}{M(X)} \tag{4.50}$$

$$VTEC = \frac{STEC}{Mf(X)} \qquad\qquad (4.51)$$

Rui Jin., et al (2012) and Ciraolo L., et al (2006) discuss more details about ionosphere observables.

4.5 COSMIC Satellite data

The Constellation Observing System for Meteorology, Ionosphere, and Climate (COSMIC). The COSMIC satellites are a low Earth orbit (LEO) satellite that provides both upper and lower atmospheric products for different altitude observations of temperature, the electron density of the ionosphere, pressure, refractivity, and water vapor. The satellite is a constellation system which comprises of six low-earth-orbiting (LEO) microsatellites assigned mainly for the Global Positioning System Radio Occultation (GPS RO) remote sensing of the atmosphere and ionosphere at different altitudes with global coverage. COSMIC data is processed by the COSMIC Data Analysis and Archive Center (CDAAC) located at the University Corporation for Atmospheric Research (UCAR) in the United States of America. The COSMIC data product is made available to download free for the atmospheric research community through their online archive[4.1]. In this study, we extracted and observed some perturbed temperature profiles which may be due to the vertical propagation of AGWs from the COSMIC data (Grant et al., 1998) for MSTIDs study.

4.6 Methodology

4.6.1 Quiet day's selection process for TEC estimate

In this study, different geomagnetic day conditions were considered using K planetary (Kp) index. The Kp index data were obtained from the GFZ German Research Centre for Geosciences, Indices of Global Geomagnetic Activity, Potsdam, Germany[4.2]. For regular ionospheric behavior which would be discussed in chapter five, we considered days where Kp ≤ 1 (extreme quiet days) and 1 > Kp ≤ 4 (averagely active days) during 2008-2016 for daytime and nighttime period. The presented set of equations (4.32 - 4.50) in section 4.4 - 4.5 of chapter four described the procedures used in developing the GPS-TEC files processing scripts package which gives the estimated VTEC as the output alongside with other parameters (Seemala, 2011; Seemala and

Valladares, 2011; Oluwadare et al., 2018). The corresponding Receiver Independent Exchange (RINEX) format navigation and observation files are obtained from the International GNSS Service (IGS) data site[4.3], while the receiver and satellites biases (Differential Code Bias (DCB)) files are obtained from the Data Centre of the Bern University, Switzerland[4.4]. The DCB files are available for the same durations as the RINEX files. To eliminate tropospheric effects, water vapor scattering and multipath effects from the data, an elevation cut-off angle greater than 30° was adopted (Bagiya et al., 2009; Adebiyi et al., 2016; Oluwadare et al., 2018). Subsequently in this study, we refer VTEC to as TEC. The ionospheric irregularities study with a focus on MSTIDs would be discussed in chapter six. In addition, we considered only geomagnetic quiet conditions days with Kp $\leq$ 3 (quiet days) during 2008 - 2016 for the daytime and nighttime period. TEC exhibiting wave-like structures depicted to be MSTIDs are investigated. The background trends of the TEC time series were obtained by using singular spectrum analysis (SSA) with a sliding window duration of 60 mins and thereafter the output is subtracted from the original TEC time series resulting in TEC perturbation (dTEC).

4.6.2   Singular spectrum analysis (SSA)

Different order of polynomial fittings as a band-pass technique have been deployed to obtain TEC perturbations associated with MSTIDs in previous studies (Ding et al., 2004; Wang Min et al., 2007; Valladares and Hei, 2012; Jonah et al., 2016). However, most of these techniques have some limitations because the direction of the trend of the fitness line and degree of smoothness/resolution cannot be controlled due to imposition of predetermined function. However, in this study we adopted singular spectrum analysis (SSA) algorithm as a detrending tool for TEC. Our choice of SSA among other things is because it is a nonparametric spectral estimation method for time series which cannot be affected by the limitations described above and most importantly due to its ability to find trends of different degrees of resolutions. SSA technique consists of two complementary stages: Decomposition and Reconstruction, and both of which include two separate steps.

[4.1] `https://cdaac-www.cosmic.ucar.edu/cdaac/tar/rest.html`

[4.2] `ftp://ftp.gfz-potsdam.de/pub/home/obs/kp-ap`

[4.3] `ftp://cddis.gsfc.nasa.gov/pub/gps/data/`

[4.4] `ftp://ftp.unibe.ch/aiub/CODE/`

Decomposition

At this first stage, we map the original one-dimensional TEC time series (i.e. F_N) of length N (N>2) into a multi-dimensional series of lagged vectors of size L. The output of this stage gives a trajectory matrix (F) with L rows. The matrix uses an L-element vector obtained from the time series by sliding a window of size L. Equations (4.52) to (4.54) gives a mapping description of the original one- dimensional TEC time series. F_N implies the TEC time series which formed a trajectory matrix (F), f_i implies TEC values at each epoch of each PRN as time increases, f_i must not be series of zeros, and $i= 1,2\ 3.... L$. The trajectory matrix (F) is a Hankel matrix, which means that all the elements along the diagonal are constant and equal.

$$\overbrace{f_1,\quad f_2,\quad f_3,\ ....,f_L,}^{window}\ f_{L+1},\ ....,\ f_N,\ implies\ F_1{}^T=(f_1,\quad f_2,\quad f_3,\ ....,f_L) \qquad (4.52)$$

$$f_1,\quad \overbrace{f_2,\quad f_3,f_4\ ....,f_L,\ f_{L+1},}^{window}\ ....,\ f_N,\ implies\ F_2{}^T=(f_2,\quad f_3,\quad f_4,\ ....,f_{L+1}) \qquad (4.53)$$

$$F=[F_1,F_2,F_3,F_4,.......F_K]=\begin{pmatrix} f_1 & f_2 & f_3 & .....f_K \\ f_2 & f_3 & f_4 & .....f_{K+1} \\ f_3 & f_4 & f_5 & .....f_{K+2} \\ \vdots & \vdots & \vdots & \vdots \\ f_L & f_{L+1} & f_{L+2} & f_N \end{pmatrix}\ ,\ \begin{cases} 1<L<K \\ K=N-L+1 \end{cases} \qquad (4.54)$$

The next step involves decomposing the trajectory matrix (F) by using singular value decomposition (SVD). SVD described different degree of ways a multi-dimensional matrix (F) columns correlate to its rows, by re-presenting the original matrix in a lesser (lower) dimensional matrix such that the lower dimension can convey an estimate of information as the original matrix. It also gives number of times required to describe different groups of correlated values in a multi-dimensional matrix/data. SVD is employed to factorize F in the form $U\Sigma V^T$ so that the principal components (PC) are obtained.

$$F= U\ \Sigma\ V^T \qquad (4.55)$$

where U and V are the left and right singular vectors respectively, and Σ is a diagonal matrix consisting of singular values of (F) which reflect the significance of each corresponding pair of left–right singular vectors. The decomposition step can be performed using calculation of eigenvalues and eigenvectors of the matrix $S=FF^T$ and it is represented in the form $FF^T = (U\Sigma V^T)$ $(U\Sigma VT)^T = U\Sigma^2 U^T = U \Lambda U^T$, where $\Lambda = diag\ (\lambda_1, \lambda_2......, \lambda_L)$ is the diagonal matrix of eigenvalues of S. The diagonal matrix is in a decreasing order so that $\lambda_1 \geq \lambda_2 \geq ... \geq \lambda_L \geq 0$, and $U = (U_1, U2...$ UL) is the corresponding orthogonal matrix of eigenvectors of FF^T $(S=FF^T)$. S is also called scatter matrix, while U_i is called "factor empirical orthogonal functions (EOF)" of F. The right singular vectors of F are eigenvectors of F^TF calculated by:

$$V_i = \frac{F^T U_i}{\sqrt{\lambda_i}}, \begin{cases} i = 1,2...d \\ d = max\ (i, such\ that\ \lambda_i > 0) = rank\ F \end{cases}$$

(4.56)

Consequently, the SVD of the trajectory matrix F can be rewritten as:

$$F = F_1+F_2+F_3......+ F_d, \ F_i = \sqrt{\lambda_i}.\ U_i.\ V_i^T$$

(4.57)

The collection of ($F_i = \sqrt{\lambda_i}.\ U_i.\ V_i^T$) is called eigentriple of SVD.

Reconstruction

This stage involves grouping steps, which corresponds to partitioning/splitting of the matrices F_i (equ.4.57) into several m disjoint subset groups $I_1, I_2, ..., I_m$. Let $I= \{i_1, i_2, i_3...i_p\}$ be a group index. Then the resultant matrix F_I corresponding to the group I is defined as $F_I = F_{i1}+ F_{i2}+......$ F_{ip}. The resultant matrices computed for the groups $I = I_1, I_2..., I_m$. The decomposition form of equation (4.57) is given as:

$$F = F_{I1}+F_{I2}+F_{I3}......+ F_{Im}$$

(4.58)

The last stage of the reconstruction process is the known as the diagonal averaging. Diagonal averaging transfers each matrix I (equ.4.58) into a time series with length N, which is an additive component of the initial series of trajectory matrix (F). The output of this procedure gives a more/nearest representative trend of the original trajectory matrix (F). The smoothness and degree of resolution of the trend depends on the choice of the principal component (PC). The formula (equ.4.59) describes how diagonal averaging can be applied to the reconstructed trajectory matrix (F*). Let G be a L×K matrix, where elements g_n are the elements of G so that G can be transferred into series of $g_1, g_2, g_3 .... g_N$, (i.e. $G=g_1, g_2, g_3 ....g_N$).

$$
g_i = \begin{cases}
\dfrac{1}{i} \displaystyle\sum_{m=1}^{i} \mathbf{f}^*_{m,i-m+1} & 1 \leq i < L \\[4mm]
\dfrac{1}{L} \displaystyle\sum_{m=1}^{L} \mathbf{f}^*_{m,i-m+1} & L \leq i < K \\[4mm]
\dfrac{1}{N-i+1} \displaystyle\sum_{m=i-K+1}^{N-K+1} \mathbf{f}^*_{m,i-m+1} & K \leq i \leq N
\end{cases}
\qquad (4.59)
$$

In a nutshell, the following processes were performed in using SSA to form a smooth TEC background with the choice to select the desired degree of resolution and trend; select window length (L) considering the dominant periods of the time series, form trajectory matrix (F) using L, compute the SVD of F, reconstruct F, and calculate the trend by applying diagonal averaging. Check Golyandina et al. (2001) for more details about singular spectrum analysis (SSA).

4.6.3   Estimation of Detrended TEC

An SSA fit is determined for each TEC time series (TEC$_{\text{SSA-fit}}$) of the corresponding PRN. The dTEC is obtained by subtracting the TEC$_{\text{SSA-fit}}$ from the TEC estimate. The approach to obtain dTEC in equ. (4.60) is known as detrending and it can be done using several methods

$$
dTEC = [\text{ TEC}] - [\text{ TEC}_{\text{SSA-fit}}] \qquad (4.60)
$$

We determine that an MSTID event is detected whenever the dTEC points fall above the event threshold (ETH) value of 0.07 TECU (Husin et al., 2011). The choice of ETH value was based on computing the standard deviation of the dTEC of all epochs per observed satellite (Warnant, 1998; Warnant and Pottiaux, 2000). We iterated the entire standard deviation process for several satellites for different days and then found an approximate value of the most dominant standard deviation value which we set as the ETH point value. Points above the ETH in fig. (4.2) are regarded as occurrence of MSTIDs. The RABT GPS station is located in Morocco in North Africa.
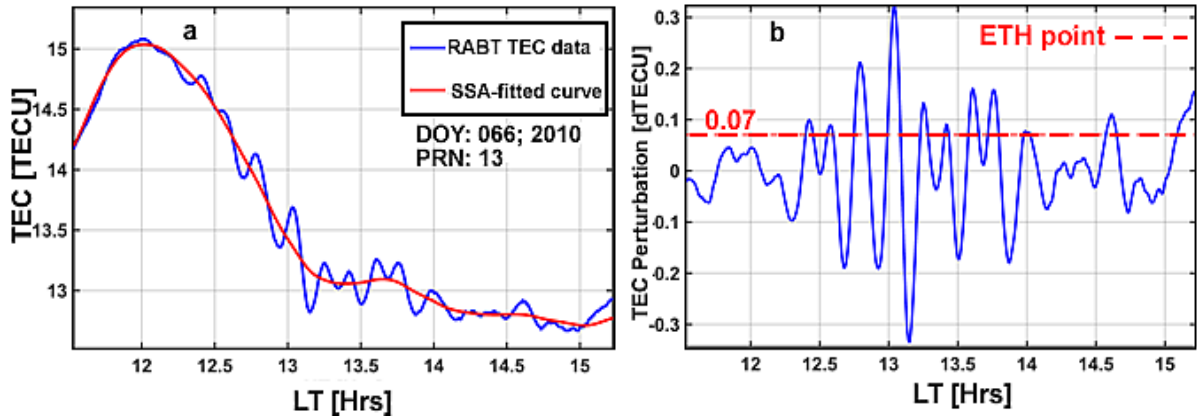
Figure 4.2 (a) TEC time series in PRN 13 as observed at RABT GPS station exhibiting wave-like structures depicting to be MSTIDs. The red line fitted curve (TEC$_{SSA-fit}$) is the background trend while (b) is the corresponding detrended TEC time series known as dTEC.

4.6.4 Estimation of MSTIDs Characteristics

In this study, we define MSTIDs as the dTEC that satisfy the following criteria: (1) the dTEC has as amplitude exceeding 0.07 TECU (1TECU=10^{16} Electron/m^2) as shown in (fig. (4.2)); (2) the horizontal wavelength is described as the distance between peak to peak of each wave event using visual assessment of dTEC signals (Jonah et al., 2016) and estimated to be less than 500 km; (3) the dTEC series after transformation from the time domain to the frequency domain in order to determine the MSTIDs event frequencies and most especially the dominant frequency using a fast Fourier transform (FFT) method following Husin et al. (2011) and Arikan et al. (2017), and the event period must be less than 60 mins; MSTIDs periods determination using FFT is discussed in chapter six of this study; (4) the propagation velocity does not exceed 450 m/sec. For the estimation of MSTIDs propagation direction and velocity, we configured geometry of sub-network of GPS receivers, see fig. (4.3). We assume that the TID's wavefront propagates along the Earth's spherical surface and crosses point positions X, Y, and Z with speed *v* and propagation azimuth (ɸ). The azimuth is measured from the north (**N**) towards the east along the horizon. The phase fronts propagation velocity and direction satisfy the equations below (Ding et al., 2007).
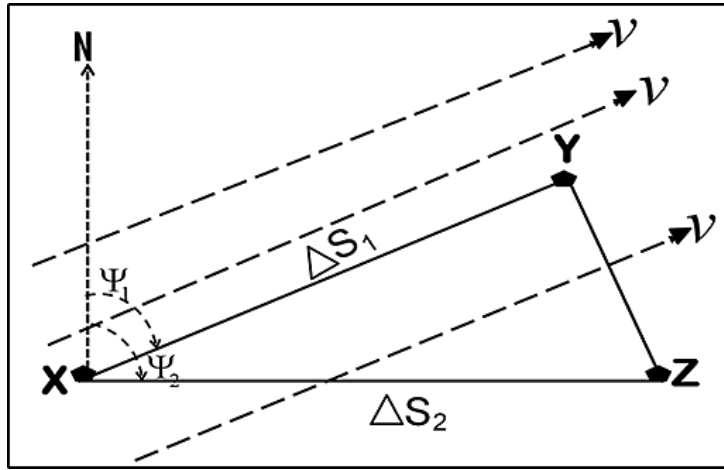
Figure 4.3: Network geometry illustrating a GPS sub-network
(X-Y-Z) used for obtaining the MSTIDs propagation direction and velocity.

$$V\Delta t_1 = \Delta S_1 \cos(\Phi - \psi_1), \; V\Delta t_2 = \Delta S_2 \cos(\Phi - \psi_2) \tag{4.61}$$

where Δt_1 and Δt_2 are time delays for dTEC to move from point X to Y and Z respectively along the Earth spherical surface and computed using cross-correlation function (CCF) (Valladares and Hei, 2012). $\Delta S1$ is the spherical distances between X and Y, $\Delta S2$ is the spherical distance between X and Z, while $\psi1$ and $\psi2$ are the azimuths of spherical paths XY and XZ.

$$\Phi = \arctan\left(\frac{\Delta t_1.\Delta S_2.\cos\psi_2 - \Delta t_2.\Delta S_1.\cos\psi_1}{\Delta t_2.\Delta S_1.\sin\psi_1 - \Delta t_1.\Delta S_2.\sin\psi_2} \right) \tag{4.62}$$

Phase velocity of the TIDs was computed using

$$V = \frac{\Delta S_1}{\Delta t_1}\cos(\Phi - \psi_1) \tag{4.63}$$

Different observation points of X, Y, and Z were chosen to compute absolute values of V and Φ; thereafter we take the average value of V and Φ as the MSTIDs propagation velocity and azimuth. One important criterion that must be noted for computation of azimuth using equation (4.62) is that each of the GPS receiver stations within a sub-network must see the same satellite per observation time. Hence, the same satellite that could be seen by a sub-network is filtered for computation of propagation velocity and azimuth while other satellites are discarded.

Chapter 5

COMPUTATION RESULTS

This chapter presents and discusses the regular behavior of the ionosphere over the equatorial ionospheric anomaly (EIA) region of Africa. It is expedient that the regular behavior of the ionosphere is investigated in order to have general overview knowledge of the ionosphere when there is no external perturbation, thereafter we can have a better understanding of ionospheric irregularity behavior in the subsequent chapter. This chapter includes the study of characterization of ionosphere over the African EIA zone, different regular variations, time series of TEC within EIA of the ionosphere on a long-term time basis from 2008 – 2016 under different geomagnetic conditions (Kp ≤ 1) and (2 > Kp ≤ 4).

5.1 Characterization of ionosphere over African EIA

The ionosphere over the equatorial latitudes is a dynamic plasma region in the Earth's upper atmosphere with variation in solar and geomagnetic activities, as well as temporal and spatial variation. As it has been discussed in the previous chapter that the key parameter that closely describes the ionosphere is TEC. The temporal and spatial variations of ionospheric TEC at the equatorial and low latitude regions are important and sensitive to be monitored owing to its dynamic nature due to EIA phenomenon that is associated with it. The EIA-TEC is majorly a daytime ionospheric phenomenon near the equatorial region. It starts to develop after the sunrise and decays after the sunset during the low solar activity epoch and persists late into the night during the solar maximum. The ionosphere over EIA zone is quite dynamic and it is characterized by a latitudinal distribution of ionization density showing a trough at the magnetic equator and two peaks (crest) of density near the geomagnetic latitudes 15°N and 15°S (Kelley, 1989; Balan and Bailey, 1992). In the equatorial F region, the EIA phenomenon basic mechanism is due to electric field configuration, which is eastward during the day and produces an upward drift (E x B drift) leading to a plasma fountain (i.e. fountain effect) then the plasma diffuses along the magnetic field lines under the influence of gravity and pressure gradient forces. Consequently, the upward plasma movement induced by the electrodynamics during the daytime generates a peculiar ionospheric anomaly behavior known as the EIA, and it must be noted that the fountain effect is the major driver of the EIA (Martyn, 1955; Kelley, 1989; Balan and Bailey, 1995). The EIA is

responsible for the global maximum values of ionospheric TEC over tropical latitude as well as ionospheric irregularities on trans-ionospheric radio wave (GPS signal) propagations (Abdu, 2005). The African region has the largest landmass under the equatorial anomaly zone, with characterized complex and dynamic ionospheric structures that are yet to be fully understood and explored. This might be due to low ionospheric observations and studies from the region as well as sparse GPS Continuous Operating Reference Stations (CORS). A lot of studies have been done in the recent years to improve the understanding of the dynamics and complex nature of ionosphere especially at the equatorial and low latitude over African region (Adewale et al., 2011; Ouattara and Fleury, 2011; Fayose et al., 2012; D'ujanga et al., 2012; Ikubanni and Adeniyi, 2012; Olwendo et al., 2012; Zoundi et al., 2012; Ngwira et al., 2013; Opio et al., 2015; D'ujanga et al., 2016). However, these earlier studies have been confined to short-term time basis observation under limited solar activity variations and in most cases with the consideration of only F10.7 cm and/or SSN as solar indices to specify the level of influence of solar radiation and to use as a proxy to extreme ultraviolet (EUV) irradiance. Earlier, Libo et al. (2011) reported that neither SSN nor F10.7 cm index is ideal for representing solar EUV variability accurately. The ionospheric TEC is computed from the ground-based GPS dual-frequency L1 (1.575 GHz) and L2 (1.228 GHz) pseudoranges and carrier phase measurements. The GPS receiver network stations are listed in the table (5.1), also see fig. (5.1).

Table 5.1: GPS receiver network station names and their corresponding location details.

GPS stations	Town	Country	Geographic coordinates	Geomagnetic Latitudes
ADIS	Addis Ababa	Ethiopia	9.04°N, 38.77°E	0.17°N
YKRO	Yamoussoukro	Côte d'Ivoire	6.87°N, 5.24°W	2.57°S
MAL2	Malindi	Kenya	3.00°S, 40.19°E	12.42°S
NKLG	Libreville	Gabon	0.35°N, 9.67°W	8.04°S

We studied daily, diurnal, monthly, seasonal and long-term time series variation of ionospheric TEC over the EIA during the study period.
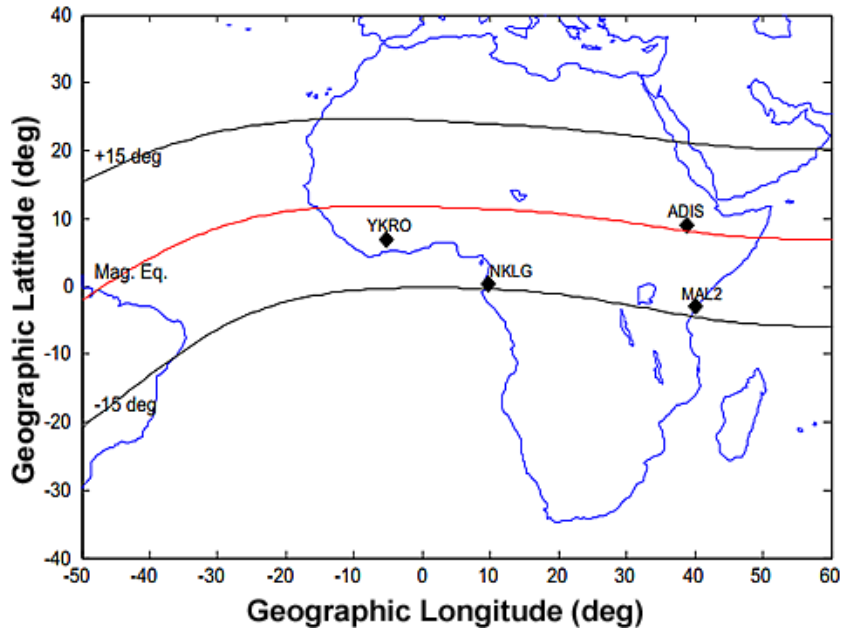
Figure 5.1: A map showing the four African equatorial/low-latitude GPS stations

Furthermore, to study the influence of the solar activity dependence of ionospheric TEC, we have considered using solar index parameters; EUV irradiance (mw/m^2), solar flux F10.7 cm and SSN data since the inception of solar cycle 24 up to 2016 (i.e. 2008-2016) different geomagnetic conditions (Kp ≤ 1) and (1 > Kp ≤ 4) for daytime and nighttime respectively (Oluwadare et al., 2018).

5.2 Daily variation of ionospheric TEC

Daily variation of ionospheric TEC is investigated. Figure (5.2) in panel (a – d) shows a daily-annual variation of TEC. The plotted TEC points are daily VTEC average spread throughout the year. As reflected from the figures, there are data gaps in every station within the period investigated. From the figures, months of March, April, and October have consistently recorded a high daily average of TEC during 2009 - 2016 and in some cases in November also high TEC values.
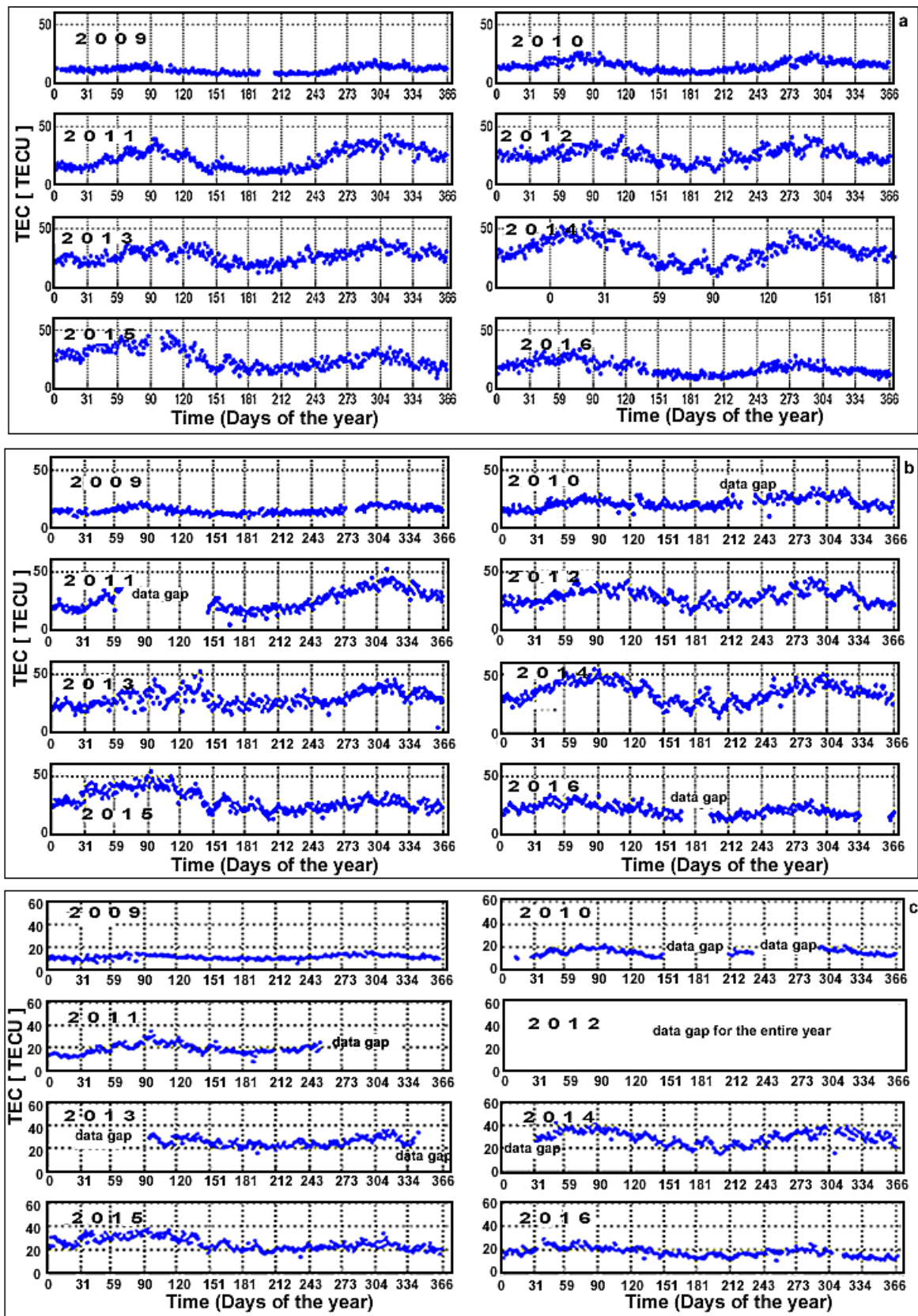
Figure 5.2(a-c): The mean daily TEC time series during the period of eight years (2009 - 2016) over MAL2 station (panel a: Geomag. Lat: 12.4ºS), NKLG station (panel b: Geomag. Lat: 13.5ºS) and YKRO station; (panel c: Geomag. Lat: 2.6ºS).

63
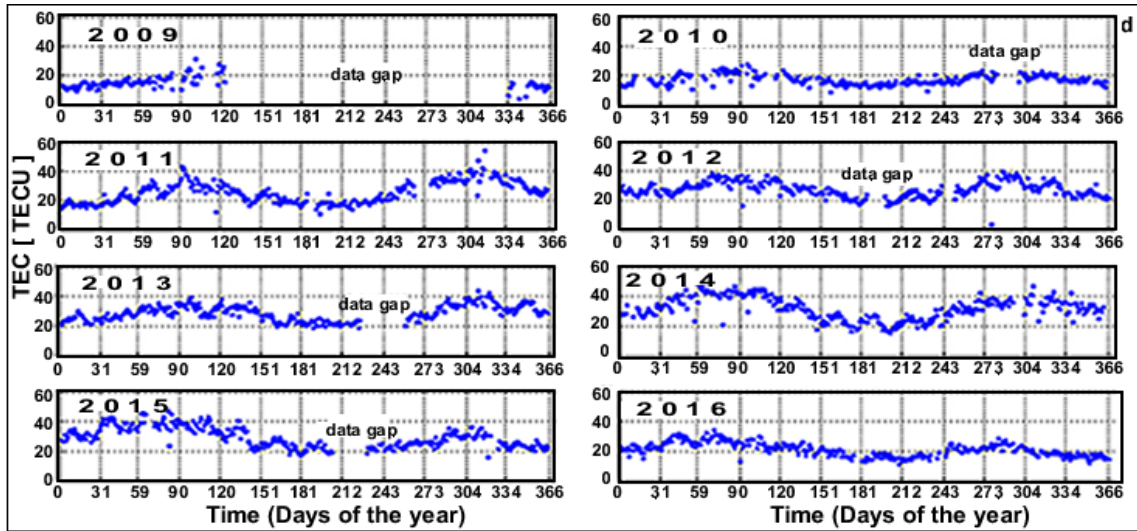
Figure 5.2(d): The mean daily TEC time series during the period of eight years (2009 - 2016) over ADIS station (panel d: Geomag. Lat: 0.2ºN),

5.3 Diurnal variation of ionospheric TEC

In investigating the diurnal variation of ionospheric TEC features, a daily spread of TEC estimate was used. The daily spread normally gets congested, highly variable, and, consequently, hard to interpret (Opio et al., 2015) as we can see in fig. (5.2a-d). We, therefore, resolve to make use of the average of daily TEC measurement of every epoch bin of a given set of TEC data of each year. This method gives a single data set comprising 2880 epochs (24 hr) which represent average diurnal TEC data (Akala et al., 2013; Oryema et al., 2015). The 24 hr dataset was obtained and plotted against Local Time (LT) for every station (ADIS, MAL2, YKRO, and NKLG) as shown in figs. 5.3–5.5. This approach gives a better way to compare, interpret, and analyze the diurnal behavior of ionospheric TEC. However, not every month in each year at different stations was considered. A month whose data gap is more than half of that month was not considered. The stations are grouped together based on their respective local time (LT) of the same time zone. LT in East African time (EAT) = UT + 3hrs; (ADIS and MAL2), LT in West African time (WAT) = UT + 1hr; (NKLG) and LT in Greenwich Mean Time (GMT) = UT + 0hr; (YKRO). To monitor the TEC changes in relation to the solar cycle activity condition, the mean diurnal TEC variations over the four stations been grouped into four different phases, namely: solar minimum; 2009–2010, ascending solar phase; 2011–2012, solar maximum; 2013–2015 and descending solar phase; 2016 (Oluwadare et al., 2018).
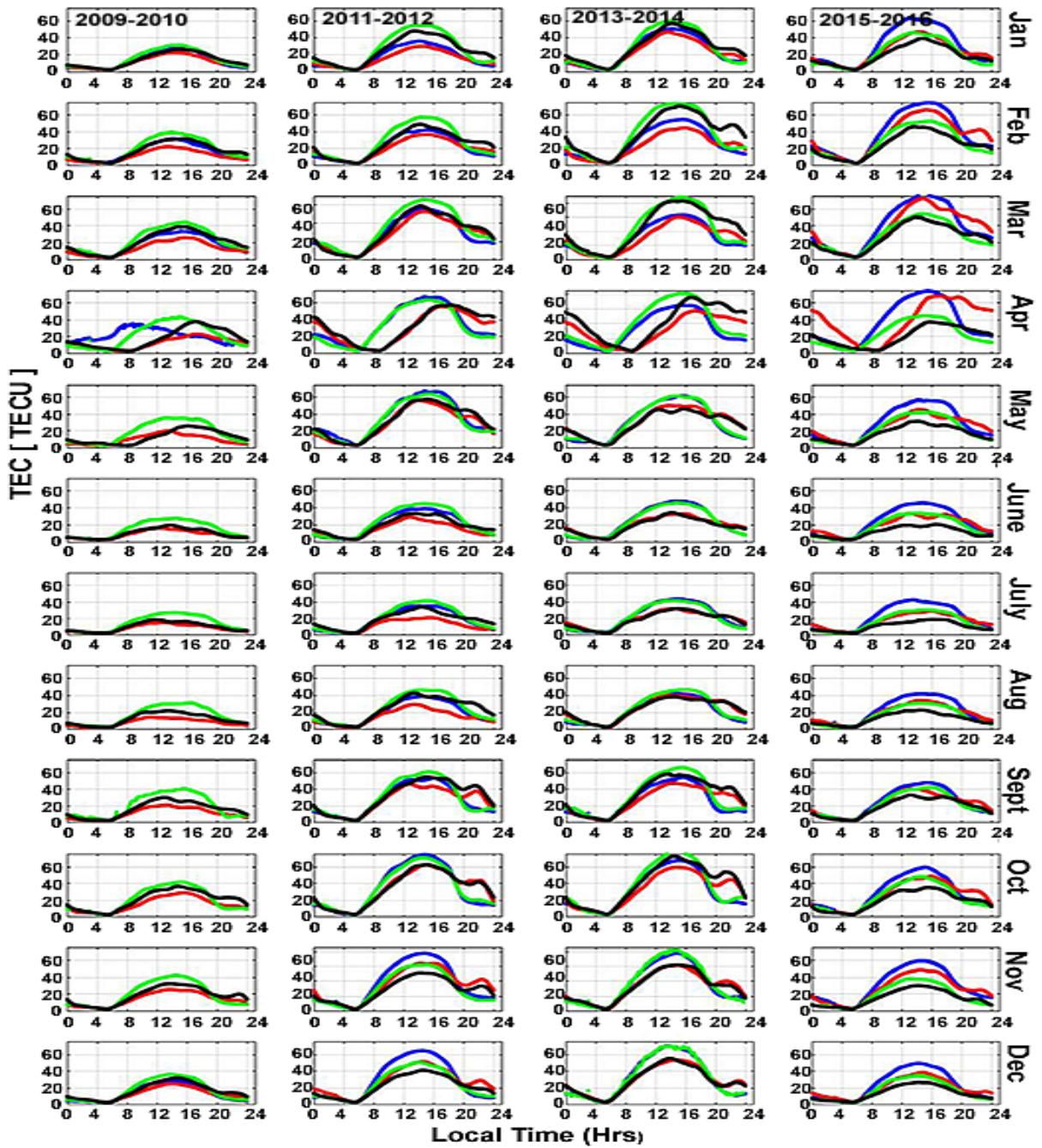
Figure 5.3: Diurnal variation of TEC for 98 months (2009 - 2016). The bold blue line shows diurnal TEC variation at ADIS station for odd years (2009, 2011, 2013, and 2015). The bold green line shows diurnal TEC variation at ADIS station for the even years (2010, 2012, 2014, and 2016). The bold red line shows diurnal TEC variation at MAL2 station for odd years while the bold black line shows diurnal TEC variation at MAL2 station for the even years.
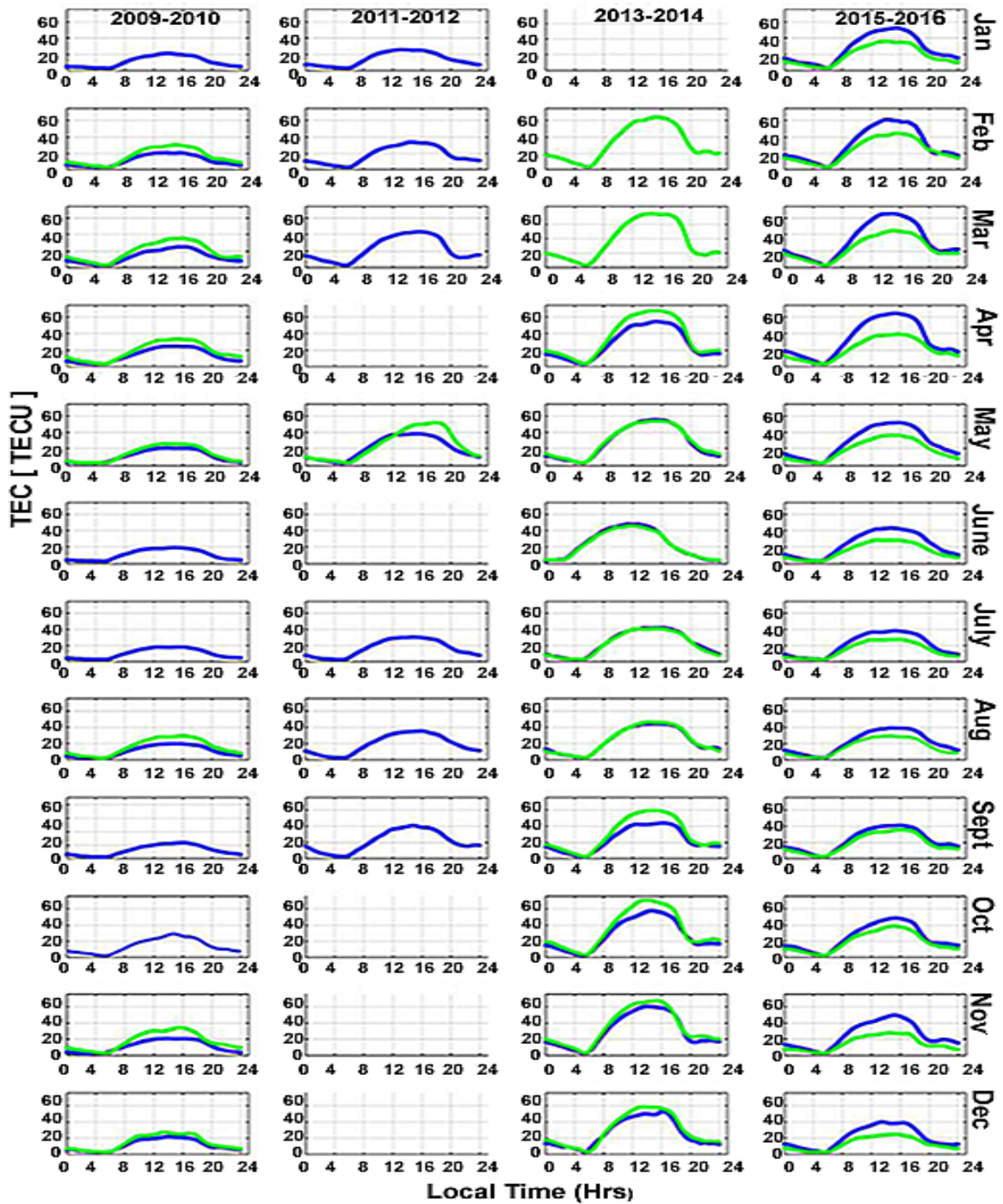
Figure 5.4: Diurnal variation of TEC for 98 months (2009 - 2016). The bold blue line shows diurnal TEC variation at YKRO station for odd years while the bold green line shows diurnal TEC variation at YKRO station for the even years.
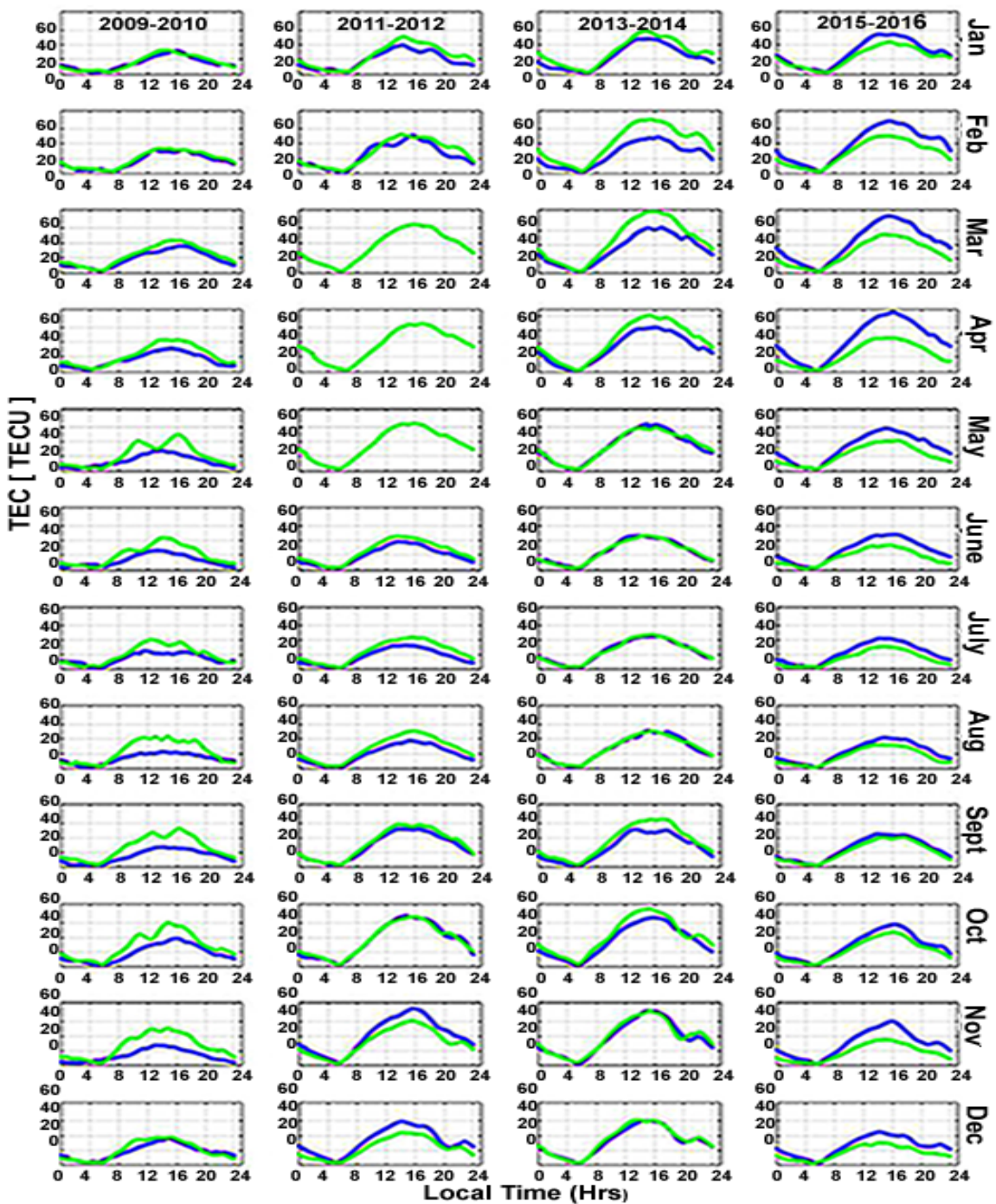
Fig. 5.5: Diurnal variation of TEC for 98 months (2009 - 2016). The bold blue line shows diurnal TEC variation at NKLG station for odd years while the bold green line shows diurnal TEC variation at NKLG station for the even years.

According to fig. (5.3 - 5.5), the mean diurnal variation of TEC at all stations exhibited about the same behavior as all stations exhibited a steady increase starting at ~ 0600 LT and the afternoon maximum is at ~ 1300 - 1600 LT which is the major TEC peak. ADIS and MAL2 stations experienced a minor peak at about 2100 LT, while NKLG experiences its minor peak between

67

2200 - 2300LT also NKLG station shows a longer duration in decaying period relative to other stations within the same EIA zone. During the solar minimum activity years (2009 and 2010), ADIS recorded its highest TEC values (38 TECU and 43 TECU) during March equinox, respectively. MAL2 recorded its highest TEC values (30 TECU and 38 TECU) in equinox season (September and March), YKRO station recorded peak TEC values (25 TECU and 35 TECU) during March equinox, and NKLG station recorded peak TEC values (38 TECU and 58 TECU) both values were recorded in October (equinox season). During the ascending solar phase (2011) and (2012), ADIS and MAL2 exhibited their highest TEC values (70 TECU and 62 TECU) both in October respectively, YKRO recorded 43 TECU in March, while NKLG station recorded (76 TECU) as the highest TEC values in November of 2011. During the solar maximum phase (2013 - 2015), ADIS station recorded TEC peak values; 81 TECU (November), 88 TECU (March), and 77 TECU (March) during 2013, 2014, and 2015, respectively. MAL2 station recorded its peak values to be: 60 TECU, 82 TECU, and 72 TECU during March month of 2013, 2014 and 2015, respectively. In 2013, YKRO and NKLG stations, recorded their TEC peaks values in November to be 60 TECU and 73 TECU respectively, but in 2014 (YKRO: 74 TECU, NKLG: 86 TECU) and 2015 (YKRO: 64 TECU, NKLG: 80 TECU), both stations exhibited TEC peak in March. Towards the descending solar phase (2016), ADIS, MAL2, YKRO, and NKLG station recorded their peak TEC values to be (53 TECU, 50 TECU, 44 TECU, and 54 TECU) during March equinox, respectively.

5.4   Seasonal variation of ionospheric TEC

We used the associated three months of data for each season for the seasonal grouping: March equinox (February, March, and April), June solstice (May, June, and July), September equinox (August, September, and October), and December solstice (November, December, and January) following the methods of Akala et al., 2010b; Chauhan et al., 2011; Fayose et al., 2012; Oluwadare et al., 2018. The monthly mean TEC variation computed for different seasons during 2009 to 2016 is shown in fig. 5.6. From 2009 to 2014, all stations exhibited higher TEC peak values during equinox season than in winter and summer. In 2015 ADIS and YKRO stations exhibited a high TEC peak value during the winter season, while MAL2 and NLLG stations exhibited the same TEC peak value in both equinox and winter season, respectively.
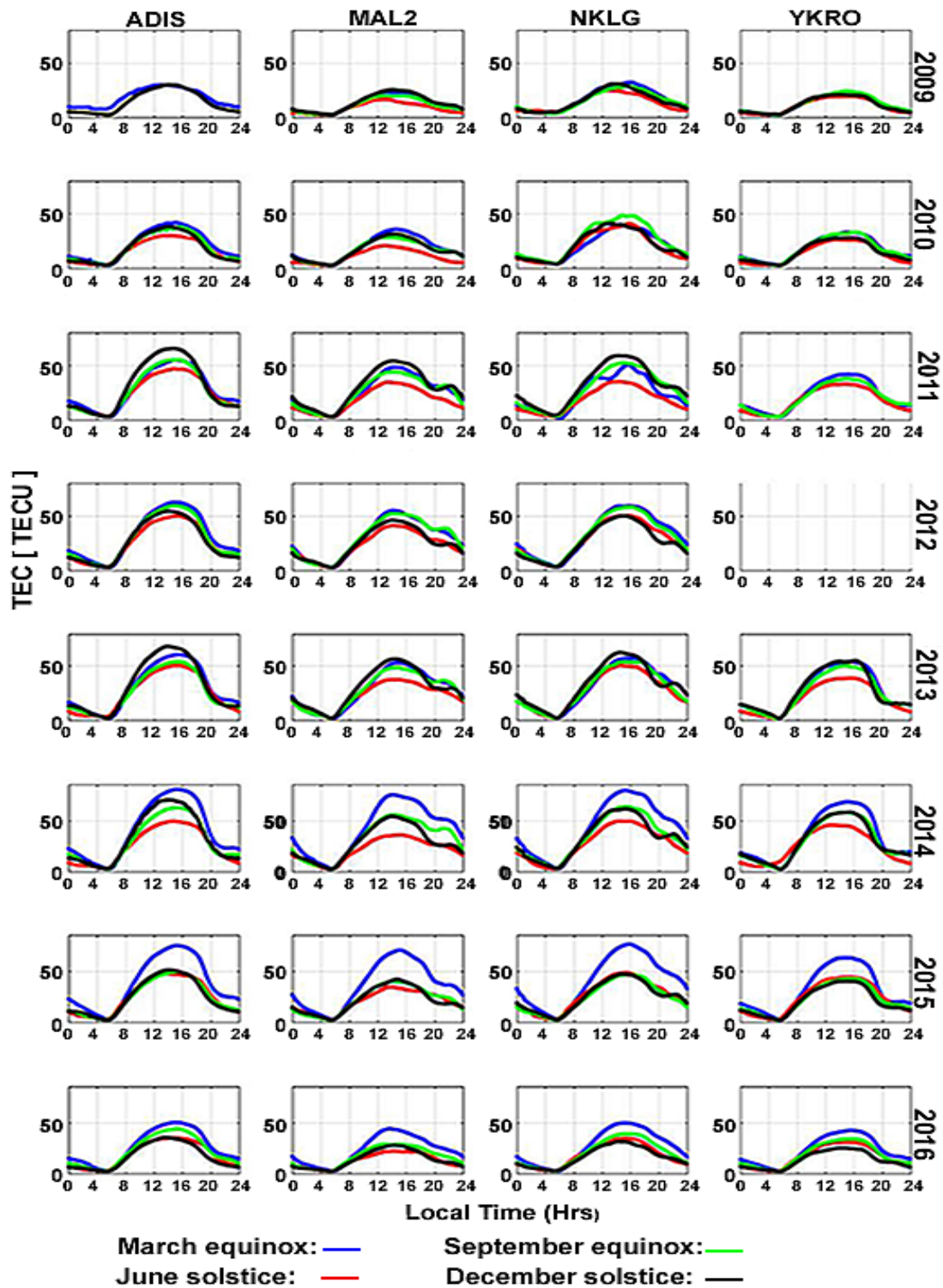
Figure 5.6: Seasonal variation of ionospheric TEC for different seasons from solar minimum (2009), up to solar maximum (2013–2015) and descending phase (2016). Check the above legend for interpretation of preference to color. Note that there is no data for June solstice and September equinox for 2009 at ADIS station and also no data at all for the entire YKRO station in 2012.

In 2016, all stations exhibited a higher slightly TEC peak value in winter than in equinox and summer. Also, all stations exhibited the lowest TEC value during the summer season except for 2010 and 2011 during which summer TEC peak is higher than winter for YKRO and NKLG. The mean seasonal daily TEC peak values from 2009 to 2016 for the entire stations are as follows: For stations located near EIA-trough (geomagnetic equator), ADIS has the following values: equinoxes ~ 51 TECU. YKRO: equinoxes ~46 TECU, summer ~35 TECU, and winter ~39 TECU. As for stations located near EIA- Southern crest; MAL2: equinoxes ~49 TECU, summer ~30 TECU, and winter ~43 TECU while NKLG: equinoxes ~57 TECU, summer ~42 TECU and winter ~49 TECU. We consider TEC behavior in each month with respect to solar activity conditions as one of the main ionospheric drivers.
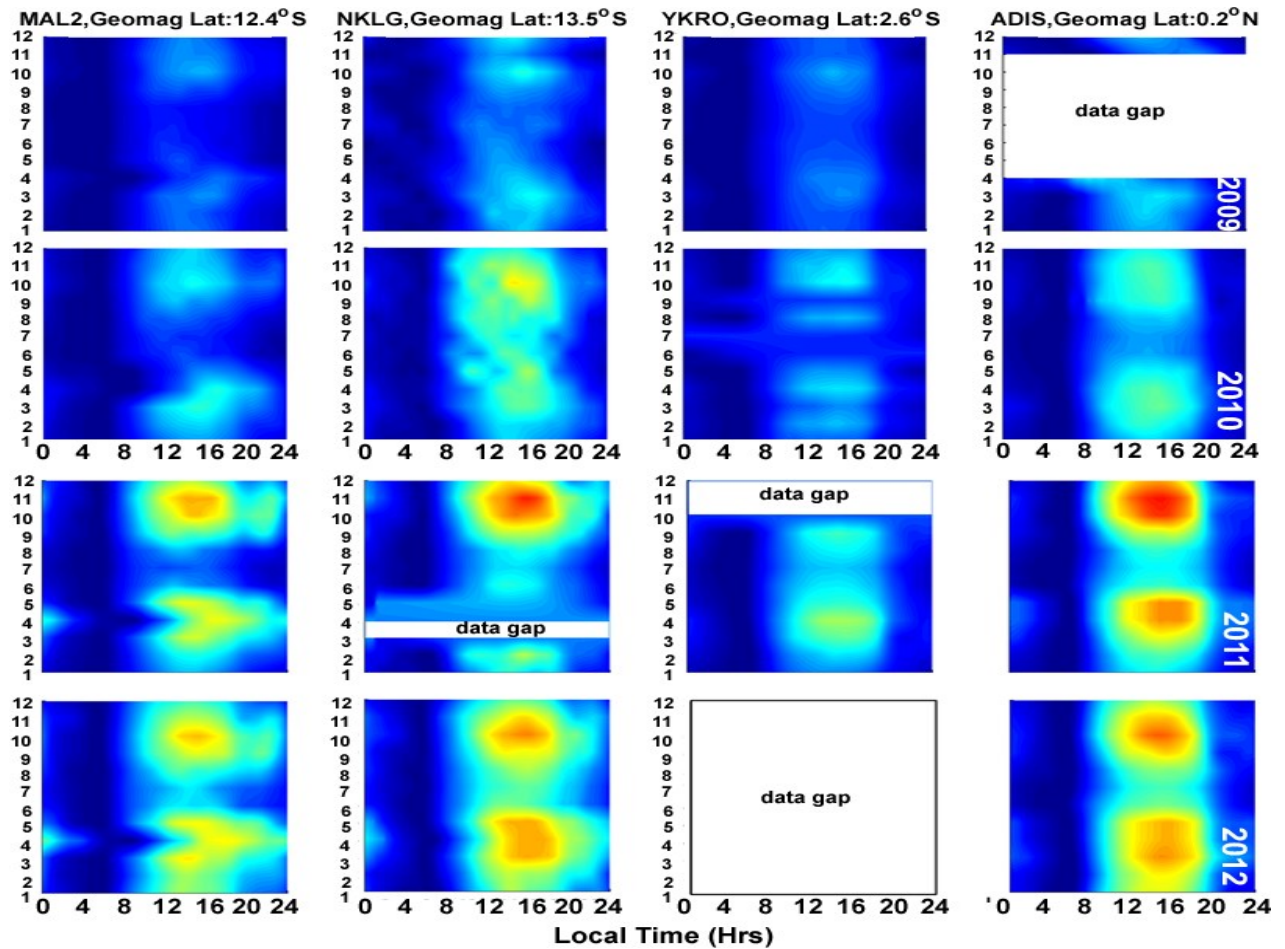
Figure 5.7a: Contour plots of the monthly average of TEC during 2009 to 2012, clearly showing the feature of seasonal, spatial and temporal variation in ionosphere. The number 1 to 12 on the vertical axis indicate the twelve months in a year, starting from January (1) to December (12).
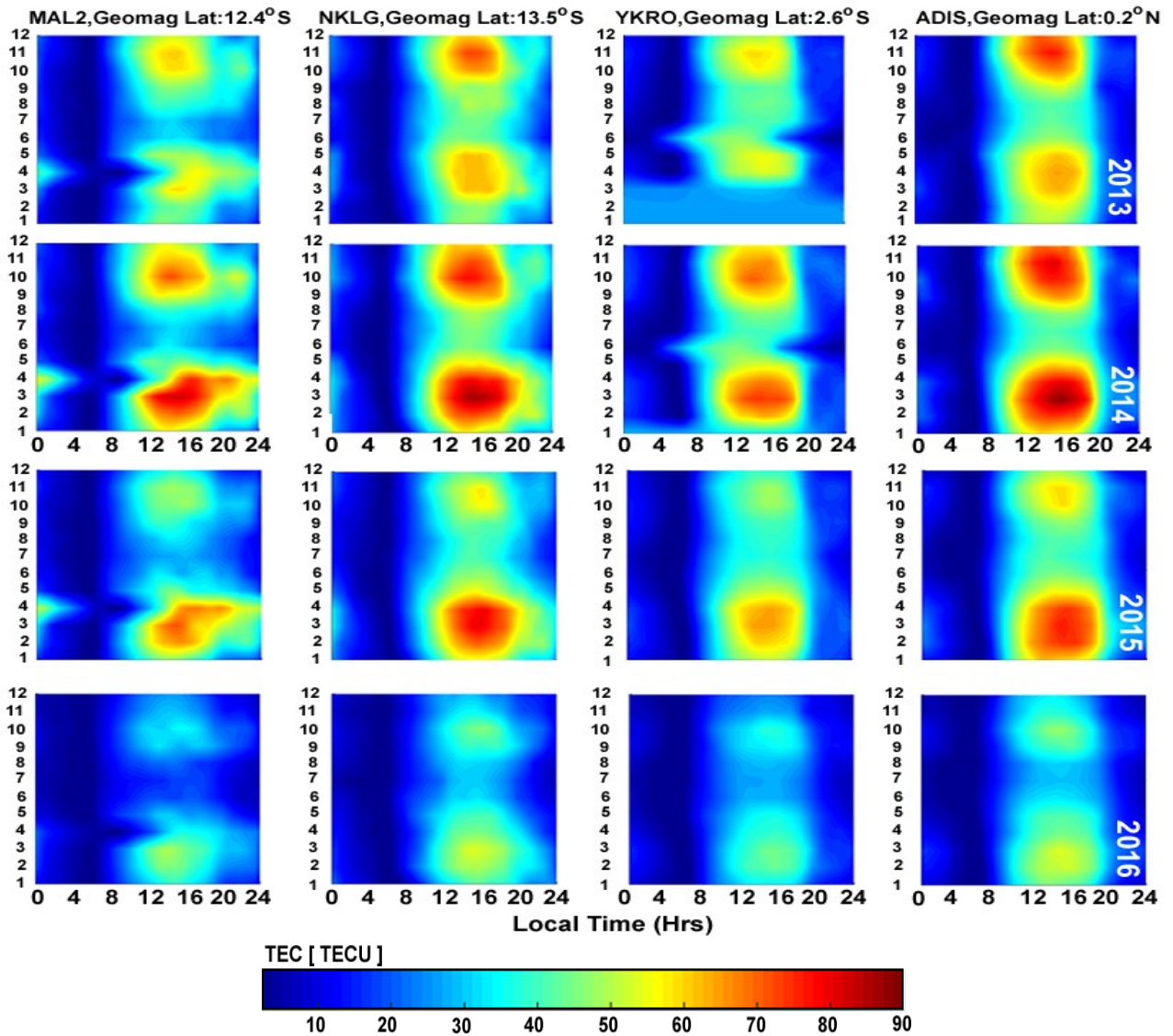
Figure 5.7b: Contour plots of the monthly average of TEC during 2013 to 2016, clearly showing the feature of seasonal, spatial and temporal variation in ionosphere. The number 1 to 12 on the vertical axis indicate the twelve months in a year, starting from January (1) to December (12).

Thus, fig. (5.7a-b) shows the contour plots of the monthly average diurnal variation of TEC at the four stations within the EIA region of Africa. The portion on the contour plots is where data are not available (i.e. data gap). The contour plots graphically describe the influence of solar activity conditions on ionospheric TEC. The result is in agreement with Liu et al. (2007) who studied solar activity impact on ionosphere along EIA region using CHAMP satellite data, and they found that electron density along the EIA-crest region increases linearly from solar minimum to the solar maximum also agrees with Akala et al. (2013) who observed an increase in TEC with solar activity during 2011 solar ascending phase on longitude to longitude comparison between African and American region using GPS data of the year 2009 to 2011.

5.5   Long term time series of ionospheric TEC within EIA

This section allows us to examine the behavior of the ionosphere on a long-term time series basis by considering the maximum TEC value per day from each GPS receiver station. The most interesting fact in this section is the geomagnetic latitudinal influence within the EIA zone on the TEC results which is independent of the solar cycle phase impact, see fig. (5.8).
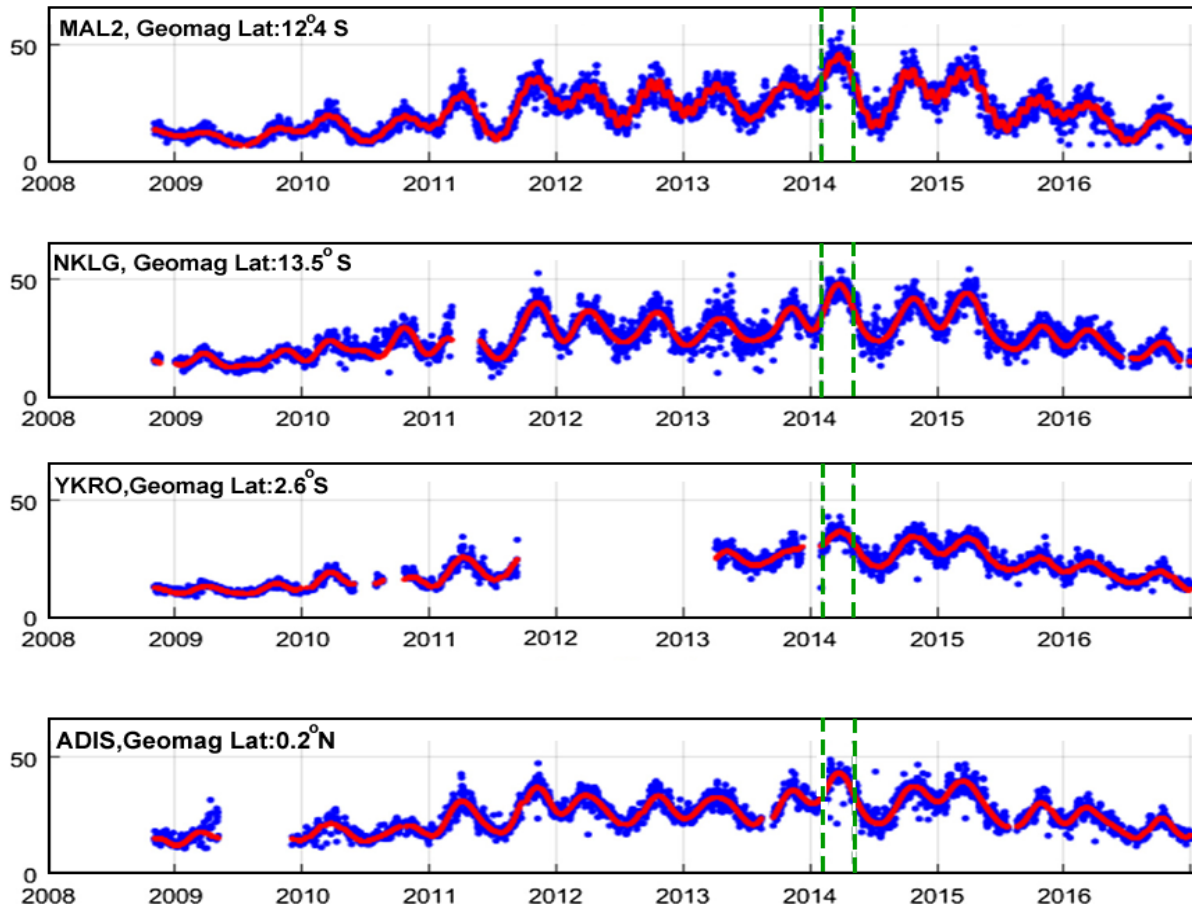
Figure 5.8: Long term TEC time series for stations at EIA zone from Nov., 2008 to 2016. The solid dashed line in the figure indicates the year with the highest TEC within the period under consideration. The red line denotes the TEC trend line.

5.6   Solar indices dependence of ionospheric TEC

The ionosphere is primarily influenced by solar radiation. A wide spectrum of radiation is emitted from the Sun and these solar radiations are measured in terms of three solar indices, i.e. EUV flux, solar radio flux (F10.7), and SSN, for the entire period (2009- 2016). To further investigate the effect of solar activity on the ionosphere, we carried out a correlation analysis between TEC

values within EIA zone and the three solar index parameters, see equ. (5.10) for the computation of the correlation coefficient. The solar EUV flux data from the Solar Heliospheric Observatory (SOHO) is taken from website[5.1] while Solar flux F10.7 cm and SSN data were taken from the data archive of NASA/Goddard Space Flight Centre, space physics data facility website[5.2]. We classify the entire data of this section into two categories; solar indices data and TEC data estimated on days when Kp ≤ 1 (extreme quiet condition) and data estimated on days with moderately active geomagnetic conditions (2 > Kp≤ 4) for the entire 2009-2016, respectively. In order to find the day period with the most solar influence, each day is categorized daytime and nighttime period with respect to SSN, F10.7 cm and EUV index and also because most stations within the EIA zone exhibits second TEC peak at the nighttime period. This approach would help us to compare and estimate the actual impact of solar activity. The correlation results are shown in the table (5.2a-d).

$$r_{xy} = \frac{\Sigma(x_i - \bar{x})(y_i - \bar{y})}{\sqrt{\Sigma(x_i - \bar{x})^2 (y_i - \bar{y})^2}} \tag{5.10}$$

where

r_{xy} is the correlation coefficient of the linear relationship between the variables x and y. x is the daily maximum value of TEC from 2009-2016, y is the EUV flux or solar radio flux (F10.7) or and SSN, $\bar{x}$ and $\bar{y}$ are the mean value of x and y.

Table. 5.2a: ADIS, Latitudinal location: EIA-trough

TEC peak period	SSN		Solar Flux F10.7		EUV flux	
	2 > Kp≤ 4	Kp ≤ 1	2 > Kp≤ 4	Kp ≤ 1	2 > Kp≤ 4	Kp ≤ 1
Daytime	0.68	0.80	0.63	0.86	0.52	0.89
Nighttime	0.35	0.45	0.34	0.49	0.37	0.50
Mean	0.52	0.62	0.49	0.68	0.45	0.70

Table. 5.2b: MAL2, Latitudinal location: EIA-Southern crest

TEC peak period	SSN		Solar Flux F10.7		EUV flux	
	2 > Kp≤ 4	Kp ≤ 1	2 > Kp≤ 4	Kp ≤ 1	2 > Kp≤ 4	Kp ≤ 1
Daytime	0.66	0.78	0.62	0.83	0.53	0.86
Nighttime	0.65	0.76	0.60	0.80	0.63	0.81
Mean	0.66	0.77	0.61	0.81	0.58	0.83

Table. 5.2c: NKLG, Latitudinal location: EIA-Southern crest

TEC peak period	SSN		Solar Flux F10.7		EUV flux	
	2 > Kp≤ 4	Kp ≤ 1	2 > Kp≤ 4	Kp ≤ 1	2 > Kp≤ 4	Kp ≤ 1
Daytime	0.66	0.82	0.62	0.85	0.52	0.85
Nighttime	0.63	0.75	0.58	0.78	0.60	0.79
Mean	0.64	0.79	0.60	0.82	0.56	0.82

Table. 5.2d: YKRO, Latitudinal location: EIA-trough

TEC peak period	SSN		Solar Flux F10.7		EUV flux	
	2 > Kp≤ 4	Kp ≤ 1	2 > Kp≤ 4	Kp ≤ 1	2 > Kp≤ 4	Kp ≤ 1
Daytime	0.80	0.88	0.72	0.92	0.87	0.94
Nighttime	0.72	0.77	0.63	0.79	0.78	0.82
Mean	0.76	0.82	0.68	0.86	0.82	0.88

[5.1] http://www.usc.edu/dept/space_science/sem_first.htm

[5.2] https://omniweb.gsfc.nasa.gov/form/dx1.html

5.7 Discussion

All results show that TEC increases yearly from solar minimum to maximum which is in good agreement with Chauhan et al. (2011), Oron et al. (2013) Oluwadare et al. (2018). The equinoctial months exhibited higher TEC values than solstice months which also confirms the research done by Opio et al. (2015), but this study further quantifies the level of ionospheric disturbances by computing the percentage of the occurrence. The computation result shows a high ionospheric TEC disturbance by 76% and 24% for equinoctial and solstice months, respectively, during eight years within the solar cycle 24. Figures (5.2 a-d) show the ionospheric TEC asymmetry patterns on the annual scale, except for the years with the data gap. In addition, the figures also show the existence of equinoctial asymmetry (Bailey et al., 2000; Chakraborty and Hahra, 2007). The peak amplitude of the equinoctial asymmetry depends upon the condition of the next in-coming solar phase condition, and the asymmetry feature has been attributed to neutral atmospheric and [O]/[N2] ratio composition (Kherani et al., 2013). The yearly change of the TEC values is dependent on the solar activity for each month or year, and that is why 2009 recorded the least TEC value because it is a deep solar minimum year. There is an increase within 2013 - 2015, with 2014 having the highest TEC amplitude attributed to solar maximum year. The long-term time series of TEC at all latitudes within EIA zone in fig. (5.8) clearly reveals 2014 as the most disturbing year. During the years 2015 - 2016, the TEC values began to decrease again because the Sun is approaching another solar minimum phase. On average, stations located at the EIA-South crest showed the highest TEC variability relative to equatorial stations and this could be attributed to the upward vertical E x B drift of plasma during the daytime (Bolaji et al., 2012) at the F-region which is associated with crest region. In figs. (5.3 - 5.5), the peak TEC values vary due to influence from solar activity conditions, and the daytime TEC peak is majorly controlled by solar photoionization processes. Also, we observed a nighttime TEC enhancement which agrees with previous studies (Mukherjee et al., 2010; Aggarwal, 2011; Adewale et al., 2012; D'ujanga et al., 2012; Oron et al., 2013; Oryema et al., 2015), most especially in MAL2 and NKLG stations where the nighttime TEC enhancement is irrespective of the solar condition and this may have been as a result of the fountain effect. The highest TEC value was recorded in 2014 which we considered the year with the highest solar activity. The TEC peak observed at the daytime in this study has been attributed to the solar photo-ionization process which is caused by solar EUV radiation which consequently enhances the electron density in that region (Huang and Cheng, 1996, Wu et al., 2004) in addition to the upward E x B drift at the equatorial ionosphere driven by F-region electrodynamics processes

(Schunk and Nagy, 2000). At every station, TEC values experienced a significant decrease at the post solar maximum of 2014; towards the solar minimum of 2016. Another interesting feature is the noontime ionospheric TEC bite-out that was observed at the EIA-South crest during the low solar activity condition of 2010 (NKLG) in fig. (5.5). However, Opio et al. (2015) had earlier reported ionospheric TEC bite-out at equatorial stations during the ascending phase of solar activity. Noontime bite-out with a larger afternoon peak has been reported to be mostly found during low solar activity (Rajaram and Rastogi, 1977; Radicella and Adeniyi, 1999; Adeniyi et al., 2003; Lee et al., 2008; Lee and Reinisch, 2012). This feature is majorly a result of the upward plasma drifts in the F-region during the daytime, which is driven by a complex interaction of E- and F regions electrodynamics processes (Schunk and Nagy, 2000). In section 5.4, the high and low seasonal variation of TEC values observed in March equinox and June solstice, respectively, are as a result of the conventional enhancement in zonal plasma drift variation at the F-region during March equinox and then diminishes during the June solstice (Fejer et al., 2008, Fejer, 2011), the changes in the Sun's position (Adewale et al., 2012) which makes the temperature at the equator in equinoctial months to be higher than the pole because the Sun is overhead the equator, and Millward et al. (1996) have ascribed the seasonal changes to the heating due to solar radiation as well as the energy generated by the solar wind which he regarded as the driving force behind the seasonal change. The winter anomaly is one of the phenomena peculiar to years with the high solar phase of solar cycle 24 in which 2011 (ascending solar cycle year) 2013 and 2014 are grouped to be among such years. Rishbeth and Gariott (1969) explained that the anomaly is due to TEC dynamical nature at EIA zone during high solar activity in the daytime. The winter anomaly behavior may also be attributed to the increase in [O]/[N2] ratio in the F2 layer which results in higher electron density (Torr and Torr; 1973, Kherani et al., 2013). Traditionally, TEC exhibits a major high value along the EIA-crest regions near $\pm 15^o$ geomagnetic latitude and most especially at the nighttime period as observed in fig. (5.7a-b). The equatorial station (ADIS) exhibited the highest TEC peak at daytime, while the two stations at the EIA-crest near ± 15 geomagnetic latitude (NKLG and MAL2) exhibited a second TEC peak of contour structure in the nighttime period. In addition, the figure also shows the existence of equinoctial asymmetry which conform to result of Bailey et al. (2000), and Chakraborty and Hahra, (2007), in which the TEC contour peak in March equinox is relatively larger than in September equinox (2014 - 2016) and vice-versa (2009 - 2013). The high amplitude of electron density exhibited during equinox has been attributed to the optimized effect of the thermospheric composition and solar zenith angle at the equinoxes when the thermospheric circulation is most symmetric (Balan and Otsuka, 1998). This kind of behavior of the asymmetry has been reported to depend on location and solar

activity (Essex, 1977; Titheridge and Buonsanto, 1983). In addition, Fuller-Rowell (1998) reported that the asymmetric phenomena are due to the global thermospheric circulation during solstices period which gives rise to the molecular nitrogen and oxygen densities and, consequently, reduces the atomic oxygen density compared with the equinoxes period, and since the molecular gases and atomic gases control the loss and production rate of the plasma, respectively, a low atomic/molecular ratio gives rise to low electron densities in the ionosphere. It is noteworthy to know which of the solar radiation parameters (SSN, F10.7 cm, and EUV indices) from different solar atmospheric regions is the best proxy for TEC or has more influence on the behavior of the ionosphere. Tables (5.2 a-d) shows that TEC exhibits a strong correlation with all the three solar indices during the nighttime period at both stations of EIA-southern crest and YKRO station, but shows a low correlation with ADIS station during the same night time period. The correlation coefficient result also shows that correlation of TEC with both F10.7 and EUV flux (24 - 36 nm) index is good, but the higher degree of correlation is on EUV flux (24 - 36 nm) with the mean highest correlation coefficient (R) value of 0.70, 0.83, 0.82 and 0.88 at stations ADIS, MAL2, NKLG, and YKRO respectively. The EUV flux gives a remarkable representation of ionospheric TEC behavior. This consequently means that SSN and solar flux F10.7 index might not be an ideal index as a proxy for EUV flux as well as to measure the variability of TEC strength within the EIA zone. Furthermore, the EUV flux index being the index with a higher degree of correlations with TEC suggest that it's a major influence in the photoionization and dynamics of the ionosphere.

Chapter 6

MSTIDs COMPUTATION RESULTS AT NORTH AFRICAN MID-LATITUDE

The mid-latitude ionospheric event is generally considered to be mild when compared to low latitude ionosphere, but still not absolute void of ionospheric disturbances. This chapter presents and discusses the results of long-term time series observation of MSTIDs over the mid-latitudes of the North African region. Also, this chapter discusses MSTIDs as it is driven by propagating AGWs which perturb the ionospheric electron density. In addition, MSTIDs characteristics such as period, propagation velocity, wavelength, seasonal variation, and parentage occurrence rate are discussed.

6.1 North Africa GPS receiver stations description

MSTIDs have been observed and estimated during 2008-2016 using seven ground-based dual-frequency GPS receiver network stations majorly situated in the mid-latitude region. Table (6.1) shows the station names and their corresponding coordinates.

Table 6.1: The GPS receiver station names and corresponding coordinates

GPS stations	Town	Country	Geographic Coordinates	Geomagnetic Latitudes
RABT	Rabat	Morocco	33.99°N, 6.85°W	23.88°N
TETN	Tetouan	Morocco	35.56°N, 5.36°W	26.18°N
IFR1	Ifrane	Morocco	33.51°N, 5.13°W	23.03°N
ALX2	Alexandria	Egypt	31.20°N, 29.91°E	23.31°N
NOT1	Noto	Italy	36.88°N, 14.91°E	28.74°N
NICO	Nicosia-Athalassa	Cyprus	35.14°N, 33.40°E	28.64°N
RAMO	Ramon	Isreal	30.60°N, 34.76°E	23.36°N
MAS1	Maspalomas	Spain	27.76°N, 15.63°W	15.75°N

It must be noted that four out of seven GPS stations at the mid-latitude are from the African region (RABT, TETN, IFR1, ALX2), and three GPS stations are from the European region (NOT1, NICO, RAMO). There are not many GPS receiver stations in the North African region; hence we

made use of the GPS stations that are very close to the African region for better observation and result. We also added a low latitude station (MAS1) for the comparison of results. Thus, we used a total number of eight GPS network stations for MSTIDs study in this section (see fig. (6.1a)).
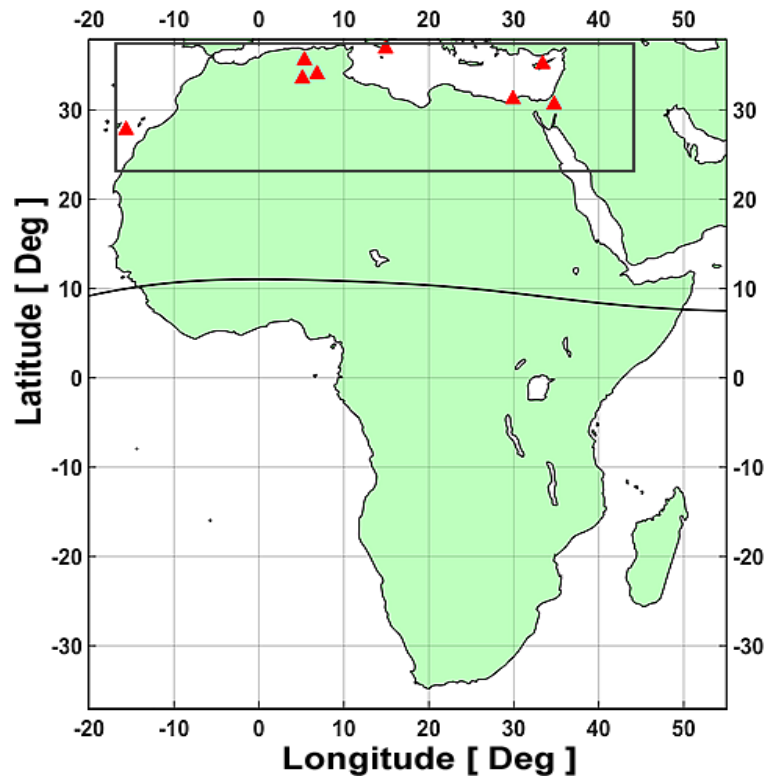
Figure 6.1a: A map showing the eight GPS stations used in this study.

The GPS stations are indicated with red triangle points enclosed in a black rectangle shape box on the Africa map replotted in fig. (6.1b) for clarity.
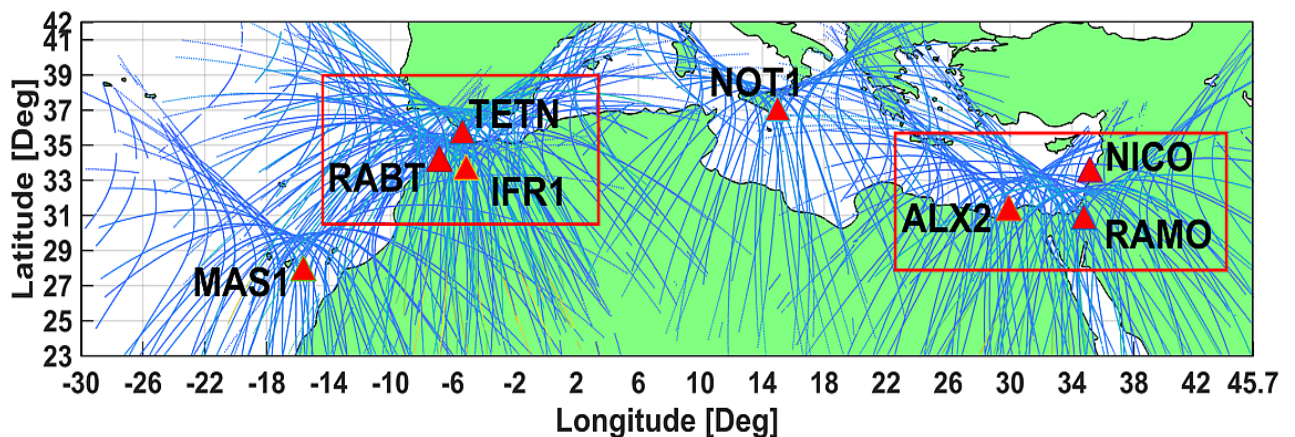
Figure 6.1b: Location of the GPS receiver stations (red triangles) with IPP tracks of all GPS satellites observed. GPS geometric networks were formed by choosing minimum of three stations (enclosed in red box) to form new sub networks.

6.2 Perturb and Unperturbed TEC profile depicting MSTIDs

It is important to understand TEC time series structure that could depict MSTIDs, when the TEC looks perturb and unperturbed, figure (6.2) shows a typical example of such instance.
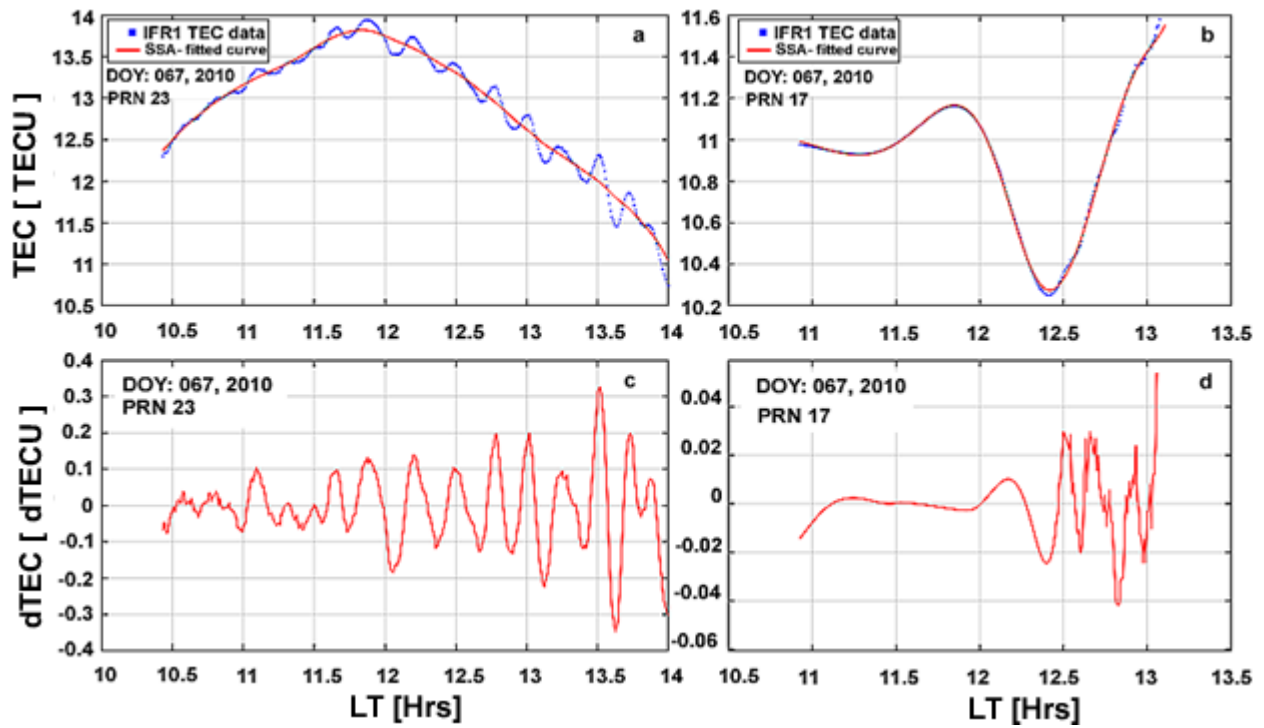
Figure 6.2: (a) TEC time series showing wave-like structure in a perturbed situation, (b) TEC time series profile structure in an unperturbed situation, (c) detrended TEC time series of a perturbed situation and (d) detrended TEC time series of an unperturbed situation

The blue curve line is the TEC time series and the red line fitted curve is the unperturbed background trend of TEC referred to as $TEC_{SSA-fit}$ as established in chapter 4. In fig. (6.2a and b), despite same day and nearly same local time range in hours (hrs), the TEC time series exhibit different structure on different satellite (i.e. PRN). Recall that MSTIDs event threshold (ETH) value of 0.07 TECU has been computed, and set as a criterion to record MSTIDs event in section (4.7.3 - 4.7.4) of chapter 4. This thus means that there is no MSTIDs event exhibited by PRN 17 of day 067 in fig. (6.2b, d).

6.2.1 Estimation of MSTIDs Period using FFT

In this study, we define the MSTIDs period to be ~11 - 60 mins following (Ogawa et al., 1987; Grocott et al., 2013). The dominance period is estimated using the FFT method. The method involves transforming the detrended TEC (i.e. dTEC) time series from the time domain to the

frequency domain. The FFT algorithm determines the frequencies, and most importantly the predominant frequency of the dTEC spectrum of a given GPS satellite.

$$P(f) = \int_{-\infty}^{\infty} \vec{P}(t)\, e^{2\pi i f t}\, dt \tag{6.10}$$

$$\vec{P}(t) = \int_{-\infty}^{\infty} P(f)\, e^{-2\pi i f t}\, df \tag{6.20}$$

The spectral analysis provides important information on the fundamental frequency of the signal; hence the frequency is converted to determine the periods and most importantly the predominant periods of dTEC time series of the given satellite, following Husin et al. (2011), and Arikan at al. (2017). The Fourier transform (F $\{\vec{P}\}$) representation of a dTEC time series in the frequency domain is hence defined in equation (6.10) (Hernandez-Pajares et al. (2012)) and its time domain can be written in equation (6.20). For more details on FFT see Press et al. (1992). Figure (6.11) shows the plot of dTEC time series using FFT algorithm. We only focus on the satellite (PRN 23, DOY 067) that exhibited MSTIDs occurrence (see fig. (6.3)) and disregarded satellite (PRN 17) since PRN 17 is without evidence of disturbances as we can observe fig. (6.2b, 6.2d).
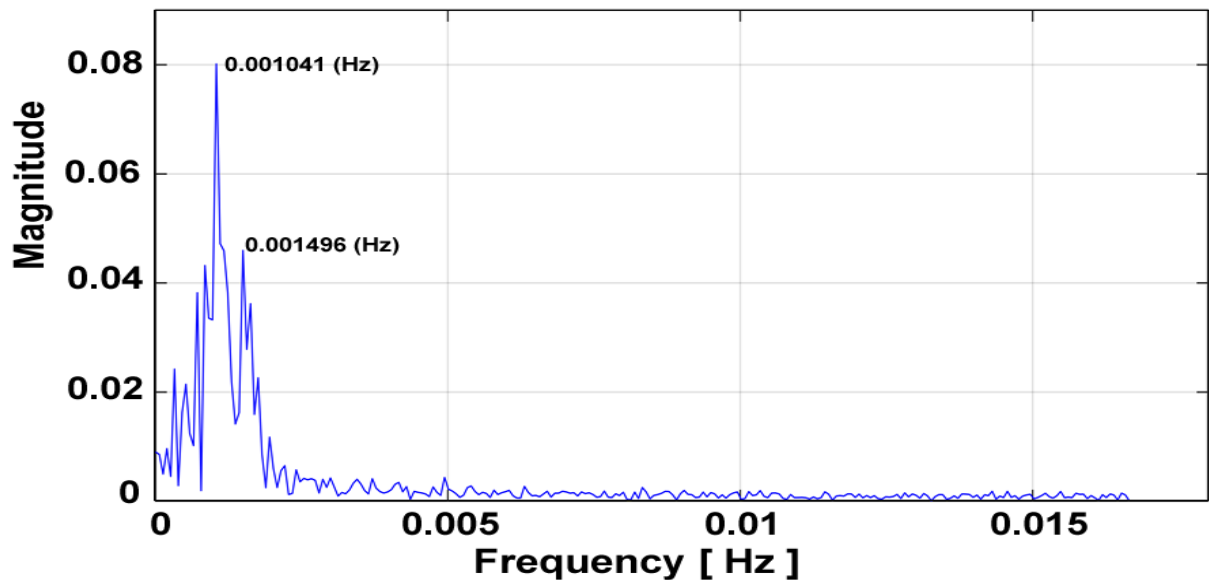
Figure 6.3: FFT plot of dTEC time series showing the magnitude of the frequencies and the dominant frequency.

As observed from fig. (6.3), the dominant MSTIDs occurrence period is between 11.14 mins (0.001496 Hz) and 16.01 mins (0.001041 Hz). It must be noted that only the PRN TEC time series with a wave-like structure as a form of disturbance is considered in this study.

6.2.2   Two-dimensional observation of MSTIDs over North Africa

MSTID has been studied to have the ability to propagate over long distances (Frissell et al., 2014), this long-distance characteristic is observed in fig. (6.4) as shown on a two-dimensional map over the North Africa region during the daytime of day 066 at 1019 to ~1200 UT in 2010. PRN 20 is observed in all the eight stations. With careful observation of fig.6 (a-b), MSTIDs propagates towards the equator and south-east (SE) with a maximum amplitude of 0.3 TECU.
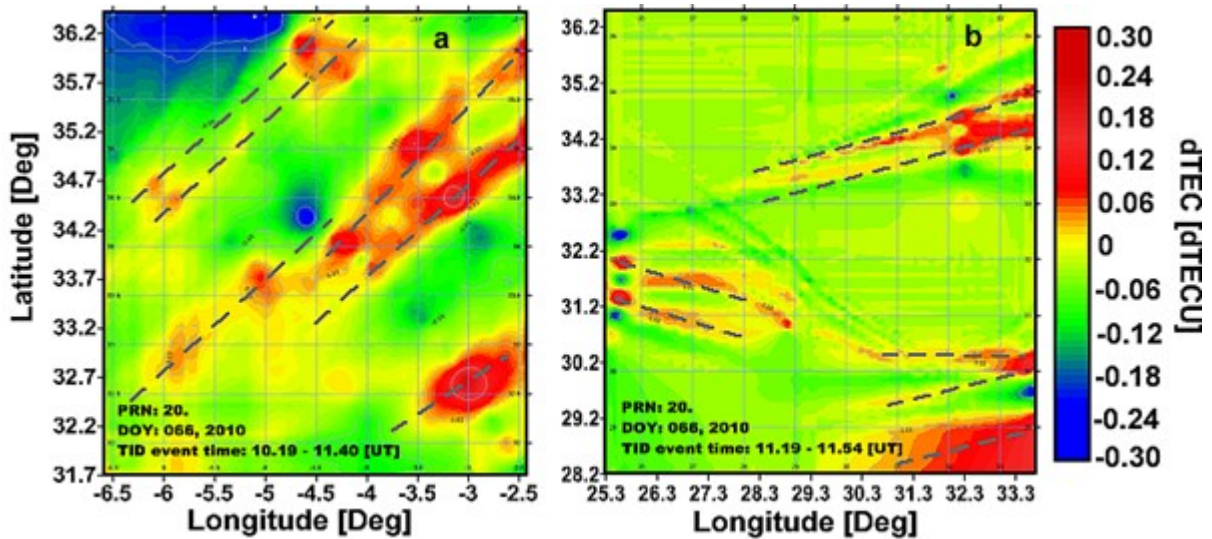
Figure 6.4: Two-dimensional maps of MSTIDs over North Africa at 1019 to ~1200 UT on 7th March, 2010 (DOY 066).

Figure (6.4) was split into two (6.4a and 6.4b) to increase the map resolution due to the absence of GPS receiver stations within certain longitudes. To avoid complex interpretation and for better analysis we converted local time (LT) of each station to universal time (UT).

6.2.3   Observation of MSTIDs on DOY 066, March 2010

In this sub-section, we determine the MSTIDs characteristics on the 7th March 2010 (DOY 066). We use equations (4.56 - 4.58) to determine the MSTIDs propagation azimuth and velocity. One important criterion that must be noted for computation of azimuth is that a sub-network that

comprises a minimum of three GPS receiver stations must be created, and each of the receiver stations must be able to see the same satellite per observation time (see fig. (6.5a)).
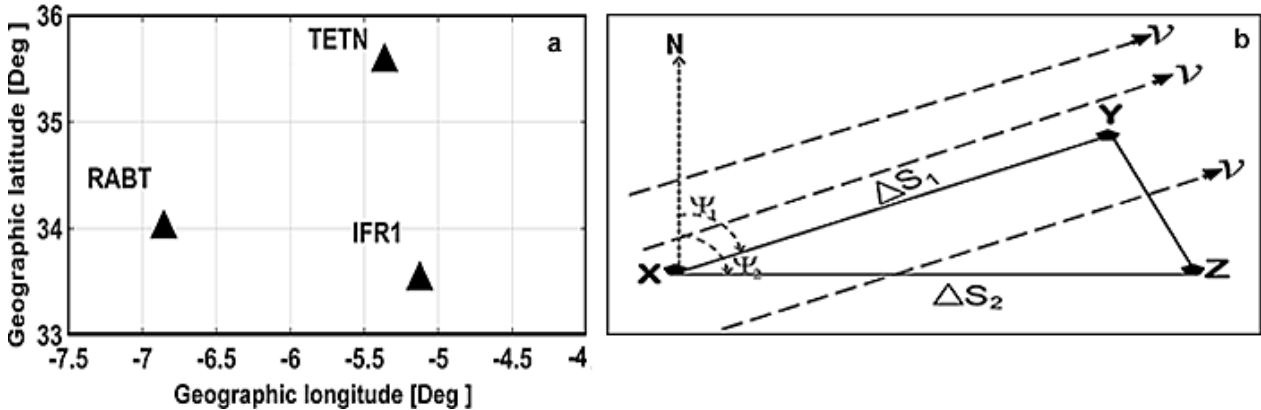
Figure 6.5a: An example illustrating one of the sub-networks (N1: RABT-TETN-IFR1) used in studying MSTIDs characteristics. (b) The configured network geometry for obtaining the MSTIDs propagation direction and velocity.

The GPS receiver stations RABT, TETN and IFR1 are represented by X, Y, and Z respectively in fig. (6.5b). We assume that the TID's wavefront propagates along the Earth's spherical surface and crosses point positions X, Y, and Z with speed v and propagation azimuth (ϕ), see the speed and propagation azimuth computation details in sub-section 4.7.4 of chapter four. The DOY 066 daytime phenomenon in fig. (6.5c) has majorly been assumed to be caused by AGW as stated in the introductory section. Temperature profile is one of the parameters use in studying AGW which is why we obtain temperature profile from COSMIC-RO satellite[6.1] in this study.

[6.1] https://cdaac-www.cosmic.ucar.edu/cdaac/tar/rest.html
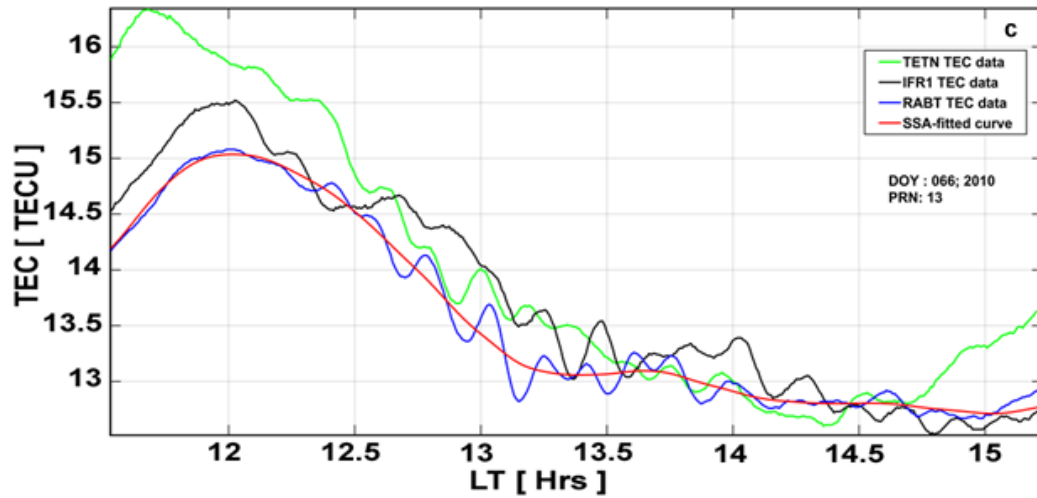
Figure 6.5c: TEC versus local time (LT) measured by the GPS receivers; color green, black, and blue signal traces represent TEC values from the three receivers. The red line represents the estimated background/unperturbed TEC values. The procedure for obtaining the background/unperturbed TEC is performed for the three stations to obtain fig. (6.5d).
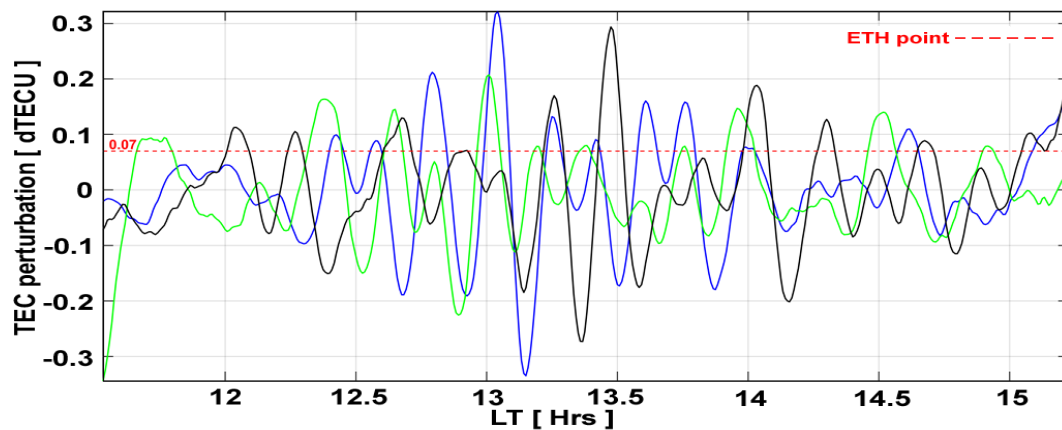
Figure 6.5d: Corresponding detrended TEC time series of fig. (6.5c)

It must be noted that the Constellation Observing System for Meteorology, Ionosphere, and Climate (COSMIC) radio occultation (COSMIC-RO) observation points do not always coincide with the geographical study area of interest and this fact is a limitation of the COSMIC satellites. We therefore made use COSMIC temperature profile measurement within the geographic coordinate (lat: 31.4º N - 32º N, long: 1.7º E - 1.8º E) that is most aligned or close in distance to the geographic area of interest. The DOY 066 daytime phenomenon in fig. (6.5c) has majorly been thought to be caused by AGW as stated in the introductory section, and the perturbed temperature profile in fig. (6.5e) characterizes a possible passage of AGWs from the troposphere to the ionosphere, and which eventually propagate above 50 km into the ionosphere (Azeem and Barlage, 2017). One of the important atmospheric parameters that exhibit the AGWs passage is

the cloud top brightness temperature which ranges (i.e. threshold) between -65°C and -20°C during convection activities (Figueiredo et al., 2018). Having set the threshold for convection activities, we may then state that the temperature within this threshold on this day (DOY 066) is due to convection activities, and hence a possible source of MSTIDs (Figueiredo et al., 2018). Following Jonah et al. (2016), the plotted fig. (6.5e) indicates how the perturbed temperature profile exhibits the AGWs passage from the troposphere to the ionosphere. The wave on reaching the mesosphere (above 50 km) breaks and release momentum where some waves travel further into the thermosphere (Tsuda et al., 2015), this brief process suggests a possible source of the MSTIDs during the selected day. Following Wang et al. (2009) in fig. (6.5f), the temperature profile is detrended, and the output structure exhibited a vertical signature of upward AGW propagation, which shows an increase in amplitude with height. It is a major characteristic of AGWs (Jonah et al., 2016).
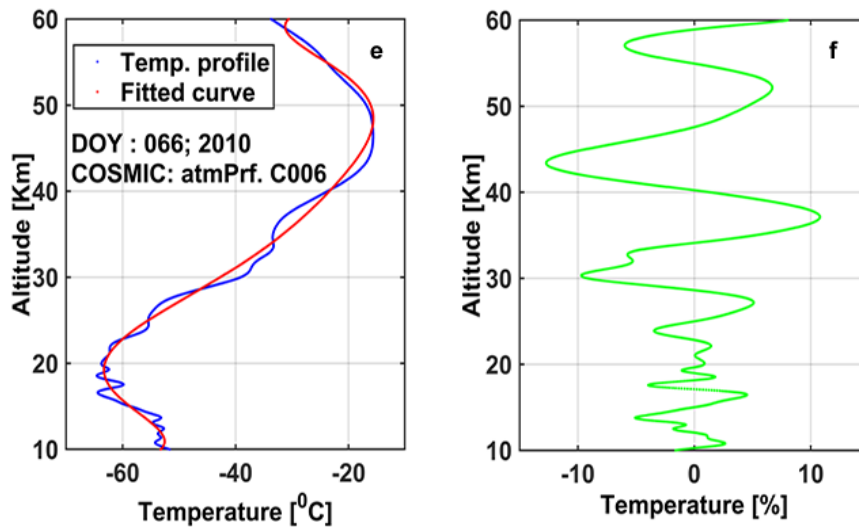
Figure 6.5e: Perturbed temperature profile from COSMIC satellite (blue color) and its curve fit (red color). Fig. (6.5f): Signature of upward AGW propagation obtained from the detrended temperature profile in fig. (6.5e).

Unfortunately, the COSMIC satellite could not capture temperature measurements above 60 km altitude, and this is one of the limitations of the COSMIC satellites for temperature measurement. In order to validate the possibility that the AGWs propagated beyond 60km as shown in fig. (6.5e), temperature data from SABER satellite is plotted in fig. 6.5 (g-i). We filtered and obtained three temperature profile measurement within the geographic coordinate (lat: 28.07° N – 37.07° N, long: 4.00° E - 4.22° E) that is most aligned or close in distance to the geographic area of interest during 1440 to 1445 UT.
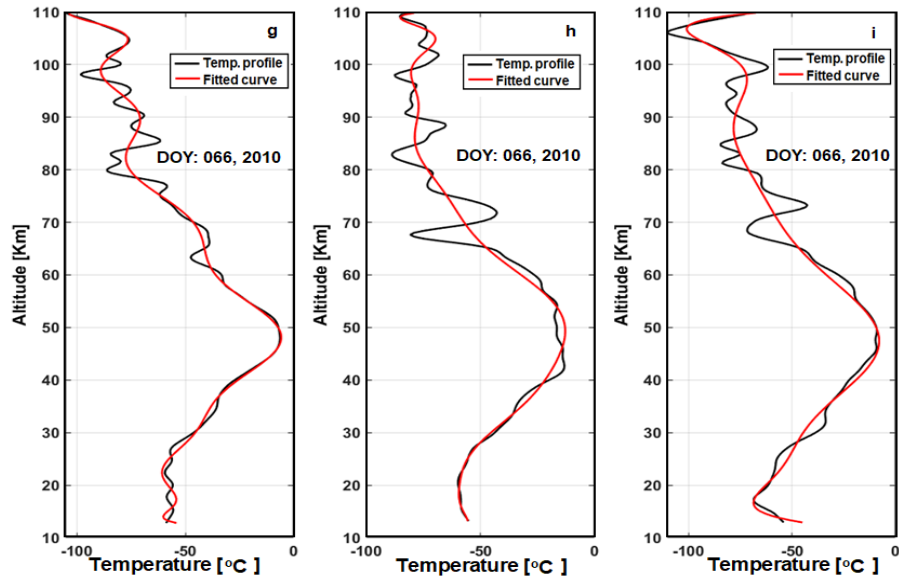
Figure 6.5 (g-i): Perturbed temperature profile from SABER satellite (black color) and its fit (red color).

Recently, Figueiredo et al. (2018) reported cloud top brightness temperature which ranges between -65°C and -20°C corresponds to deep or strong convection activities as an important atmospheric parameter that exhibit the AGWs passage, and this temperature range feature could be observed in fig. 6.5 (g-i), the temperature changes as the height increases and the perturbed temperature profile structure (black line curve) shows an indication of vertical propagation of the AGWs (Jonah et al., 2018). We observed a considerable dynamic variation at a height between ~30 and 100 km in each of the temperature profiles, indicating that the AGWs propagation survived up to 110 km altitude. Hence, it is possible that the observed AGWs during the selected day is responsible for MSTIDs generation. Figure (6.5j) shows the FFT plot of dTEC time series of PRN 13 on DOY 066, 2010 as observed from the three stations (RABT, TETN, IFR1). MSTIDs variations in local time (LT) are analyzed by sorting the data into one-hour bins. Figure (6.5k) shows that MSTIDs propagates towards the equator (southward) but indicated a higher percentage towards the south-east (SE). Following Jayawardena et al. (2016), we considered the daytime (DT: 0600 - 1800 LT) as dawn to dusk while the nighttime (NT: 1800–0600 LT) as dusk to dawn. However, for easy analysis and convenience, we converted the LT to universal time (UT) in a case where MSTIDs event is being observed simultaneously at more than one station in different regions of the time zone.
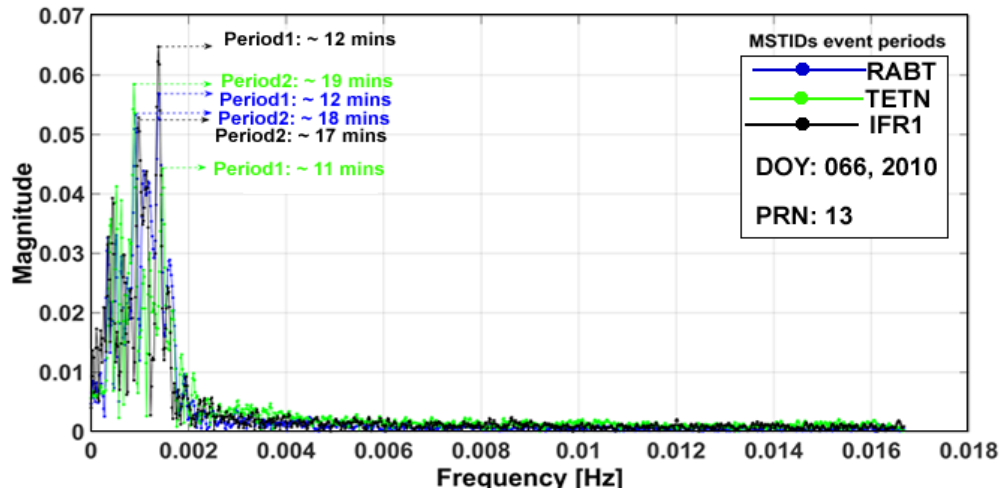
Figure 6.5j: FFT plot of dTEC time series showing frequency magnitude and the dominant frequency. The first-two prominent periods are referred to as period 1 and period 2.

For the speed v and propagation azimuth (ϕ) estimation, we formed a sub-network; N1 (RABT-TETN-IFR1) as seen in fig. (6.5a). The dominant period of MSTIDs on day 066 (fig. (6.5g)) is computed to be within an average of ~15 mins and ~18 mins. Figure (6.5h) shows that both daytime and nighttime of MSTIDs propagates southward (equator) and the MSTIDs velocity is faster at the daytime than nighttime.
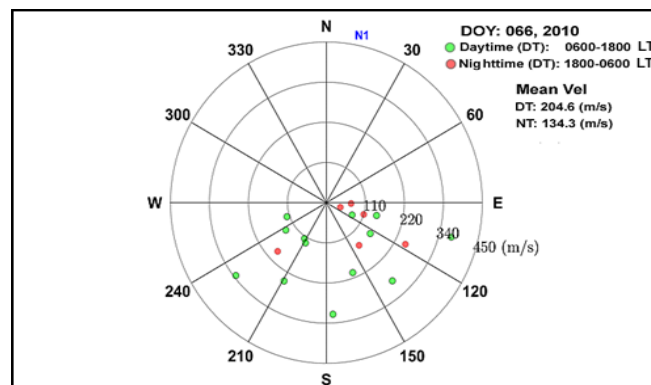
Figure 6.5k: N1 polar plot representing MSTIDs velocities and azimuth for daytime during DOY 066, 2010.

Table 6.2: The mean value of MSTIDs daytime characteristics during DOY 066, 2010.

Event/Parameters	Daytime
	N1
Velocity	204.6 m/sec
Period	~15 - ~18 mins
Azimuth	Southward

6.3   Local observation of MSTIDs over the North African region

Having observed MSTIDs occurrence of daytime for one day (DOY 066), we continue by observing the entire year using multiple stations located in the North African region. Using the network geometry approach in sub-section 4.7.4 of chapter four, we formed another sub-network; N2 which comprises of ALX2, NICO, and RAMO station respectively. Now we have sub-networks N1 (RABT-TETN-IFR1) and N2 (ALX2-NICO-RAMO). The sub-network was formed with minimum of three stations following the approach of Afraimovich et al. (1998); Hernández-Pajares et al. (2012); Valladares and Hei, (2012); and Habarulema et al. (2013a). We also calculated the MSTIDs percentage occurrence rate (POR) of every MSTIDs event using equation (6.30).

$$\text{POR} = \left[\frac{\alpha}{\omega}\right] x \ [100] \tag{6.30}$$

where α is the total count number of dTEC estimation above ETH per epoch, ω is the total count number of dTEC estimation per epoch. Figure (6.6a-b) exhibits local diurnal and seasonal variations of MSTIDs occurrence at the different GPS receiver's stations located at mid-latitude stations. Data gap are indicated by the white portions on figure. Each station in each panel exhibited a similar contour structure but clearly shows different occurrence rate in terms of season and local time. In fig. (6.6 a), the MSTIDs occurrence shows a strong dependence on the season (June solstice) and local times but with a major peak around the (nighttime) 2100 - 0200 LT (~40 % to ~50%). Also, the daytime MSTIDs exhibited some minor peaks in December solstice around 1200 - 1600 LT. In figure (6.6b), the nighttime MSTIDs occurrence exhibited similar seasonal (June solstice) and local times features as figure (6.6a), but during 1900 - 0200 LT (~30 % to ~40%). In addition, the daytime (09000–1600 LT) MSTIDs exhibited some peaks but not as pronounced as figure (6.6a) during 2011 - 2015. Nighttime MSTIDs seems to decrease with an

increasing solar activity. All stations exhibited an increasing MSTIDs POR consistently with the solar cycle. The highest MSTIDs POR at the Mid-latitude is consistently observed in June solstice during 2008-2016. The POR density shows that the occurrence rate varies with time of the day and season. This result seems to reveal occurrence variation and a level of inconsistency during day and night time from year to year. At low latitude fig. (6.6c), the major peak is around 2000-0100 LT (nighttime) in March equinox and June solstice but got extended to December solstice in 2011 and solar maximum years (2013-2014).
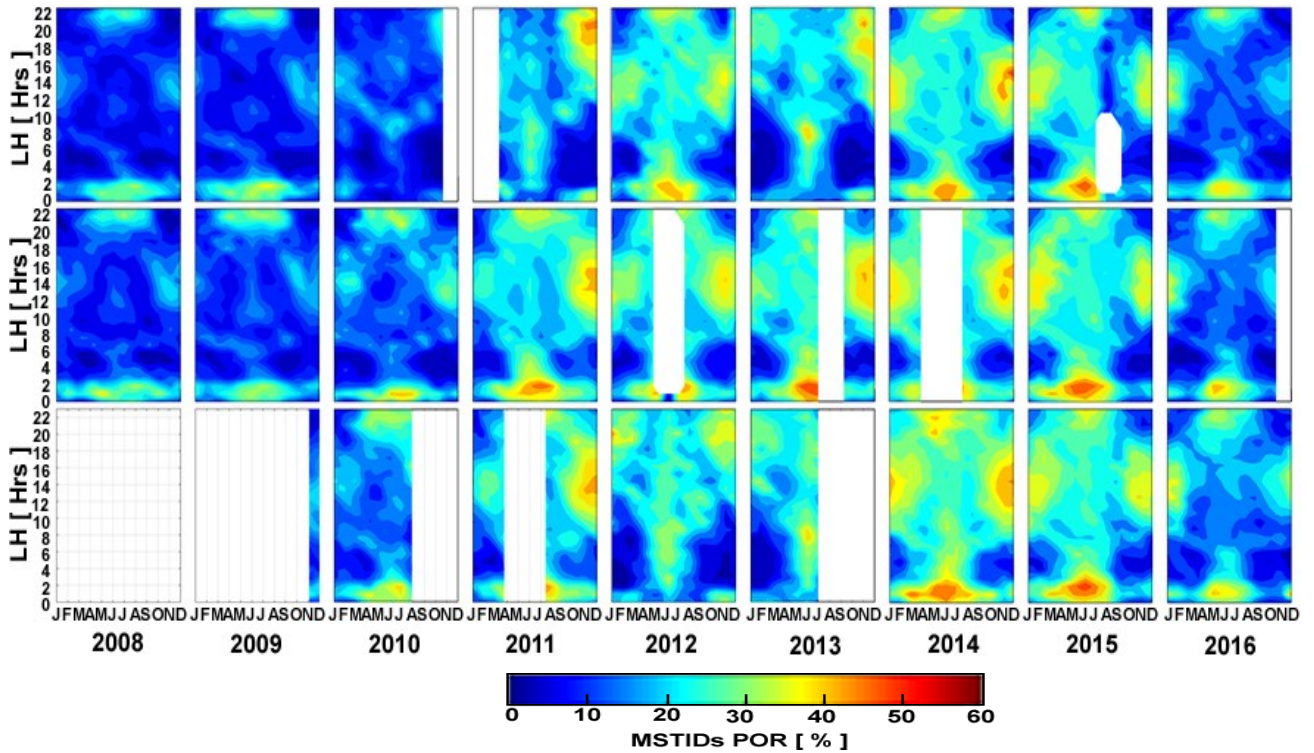
Figure 6.6a: Local diurnal and seasonal variations of MSTIDs occurrence at sub-network N1 at Mid-latitude. (top panel: TETN, middle panel: RABT, bottom panel: IFR1).
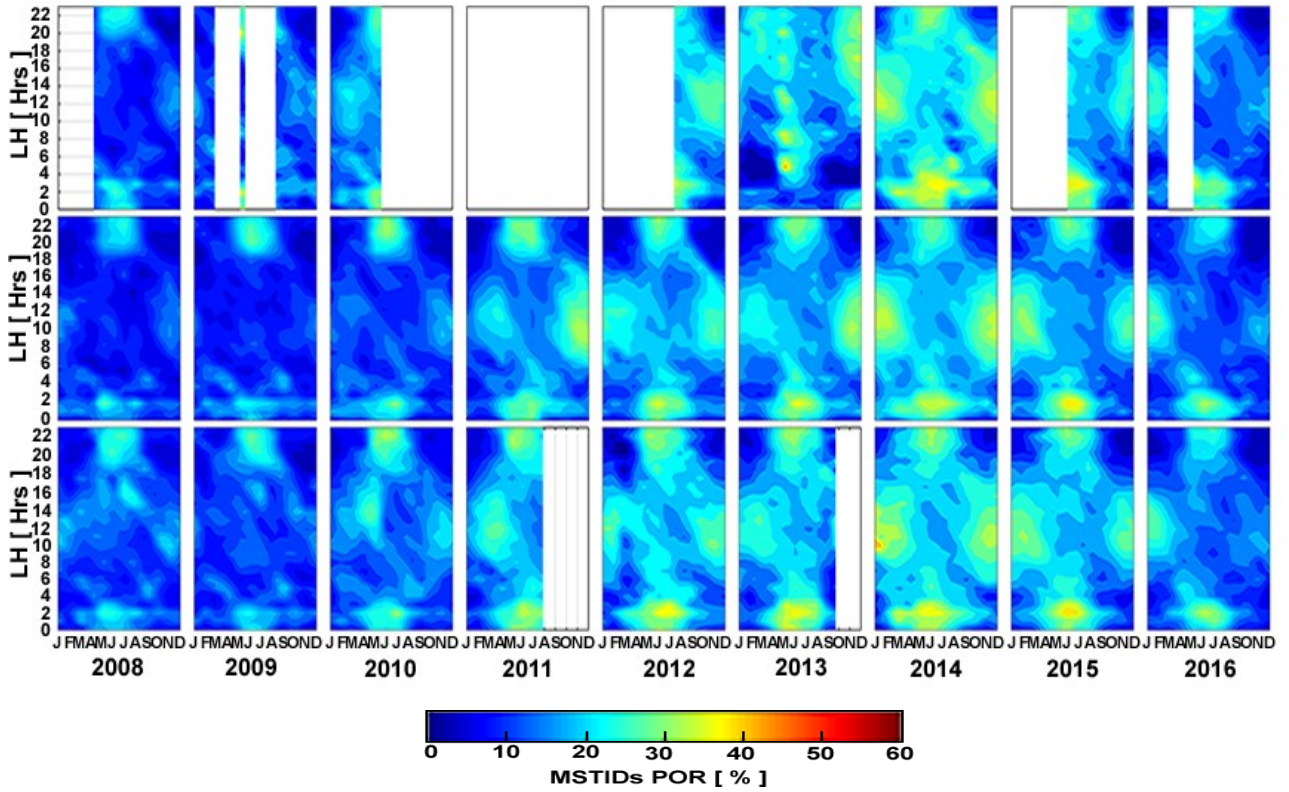
Figure 6.6b: Local diurnal and seasonal variations of MSTIDs occurrence at sub-network N2 at Mid-latitude. (top panel: ALX2, middle panel: NICO, bottom panel: RAMO)
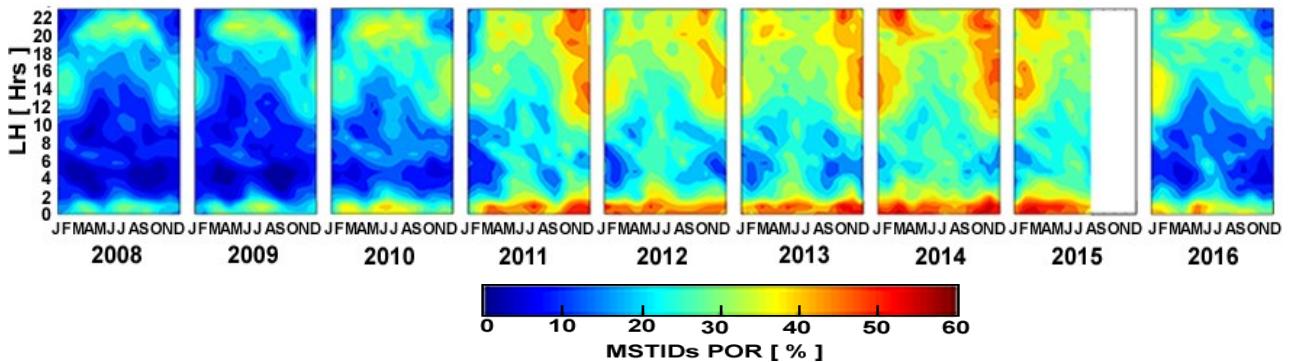
Figure 6.6c: Local diurnal and seasonal variations of MSTIDs occurrence at low latitude station (MAS1)

The maximum MSTIDs POR is observed to be between ~40% to ~50%, and ~30% to ~40% at June solstice in mid-latitudes, while it is observed to be between ~45% to ~60% during the December solstice, and equinox months at low latitude. There is an increase in occurrence rate with different intensity during nighttime at both Mid-latitude and low latitude. However, more stations need to be incorporated in the investigation in order to ascertain low latitude result. All stations exhibited an increasing MSTIDs POR consistently with the solar cycle. High MSTIDs

POR at the Mid-latitude is consistently observed in June solstice during 2008-2016, while that of low latitude is predominantly observed in December solstice, June solstice, and March equinox during 2011-2015. The POR density shows local time, season and latitudinal variation for both day and night. Hence, in subsequent sections, we analyze the daytime and nighttime amplitudes, and further separate them to make a statistical count during different periods.

6.4   Local and seasonal dependence of MSTIDs amplitudes

Figure 6.7 shows an interannual and seasonal dependence of MSTIDs amplitudes. The MSTIDs daily maximum amplitudes for all stations at Mid-latitude (N1 and N2) only were merged, and further separated into daytime and nighttime. For better visual analysis and to observe slightest changes in the multiple scatter plots, we introduced a mathematical function (simple moving average) which estimates the average value to determine the trend line-curve for both day and night (red and blue line). The contour structure in fig. (6.6c) already gave the idea that low latitude stations would seems to have a higher amplitude than mid-latitude. Hence, to avoid erroneous results in the amplitude analysis, we focus only on mid-latitude amplitude merging.
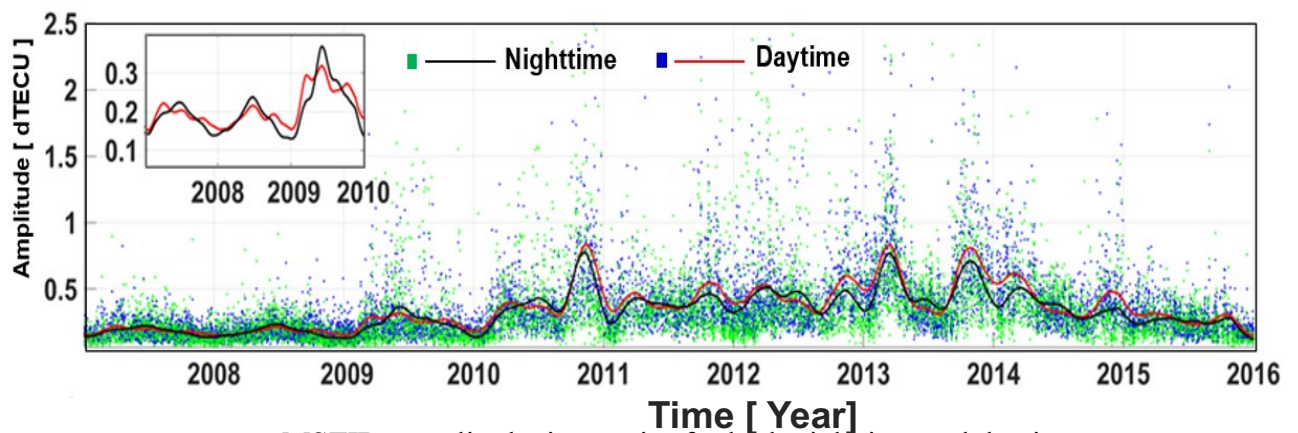
Figure 6.7: MSTIDs amplitude time series for both nighttime and daytime

Both nighttime and daytime exhibited similar pattern of trend curve but different amplitude variability. For instance, the nighttime amplitude consistently and dominantly higher than daytime during the solar minimum year (2008 - 2010), having a high peak around (0.22 - 0.37 TECU) in June solstice. The high peak amplitudes switched from nighttime to daytime, exhibiting major peaks around (0.45 - 0.94 TECU) in September equinox during 2011 - 2015, and March equinox of 2014. The nighttime amplitude consistently exhibits higher peak during the June solstice, while the daytime consistently exhibits higher peak during the equinox months during 2008 - 2016. The

dominant major higher peaks are observed in solar maximum year of 2014. By considering the solar minimum and maximum years, the nighttime amplitude seems to be slightly decreasing with increase in solar activity during June solstice. The daytime amplitude values increase with solar activity. However, it must be noted that the high background TEC experienced during high solar activities in equinox season also could influence the high MSTIDs amplitude, in that whenever the TEC background is large, the amplitude of TEC perturbation is also large. Hence, this has in a way shown a correlation between background TEC and MSTIDs (Jonah et al., 2020).

6.5   MSTIDs occurrence count

In order to statistically estimate the quantity of MSTIDs occurrence rate at daytime and nighttime, we computed the annual MSTIDs event count (AMEC).

$$AMEC = \left[\frac{\text{total count No. of } (\alpha) \text{ at DT during the year}}{\text{total count No. of } (\omega)}\right] x \ [100] \tag{6.40}$$

Figure (6.8) shows the annual MSTIDs event count (AMEC) during 2008-2016 for which daytime (DT) and nighttime (NT) were estimated using equation (6.40).
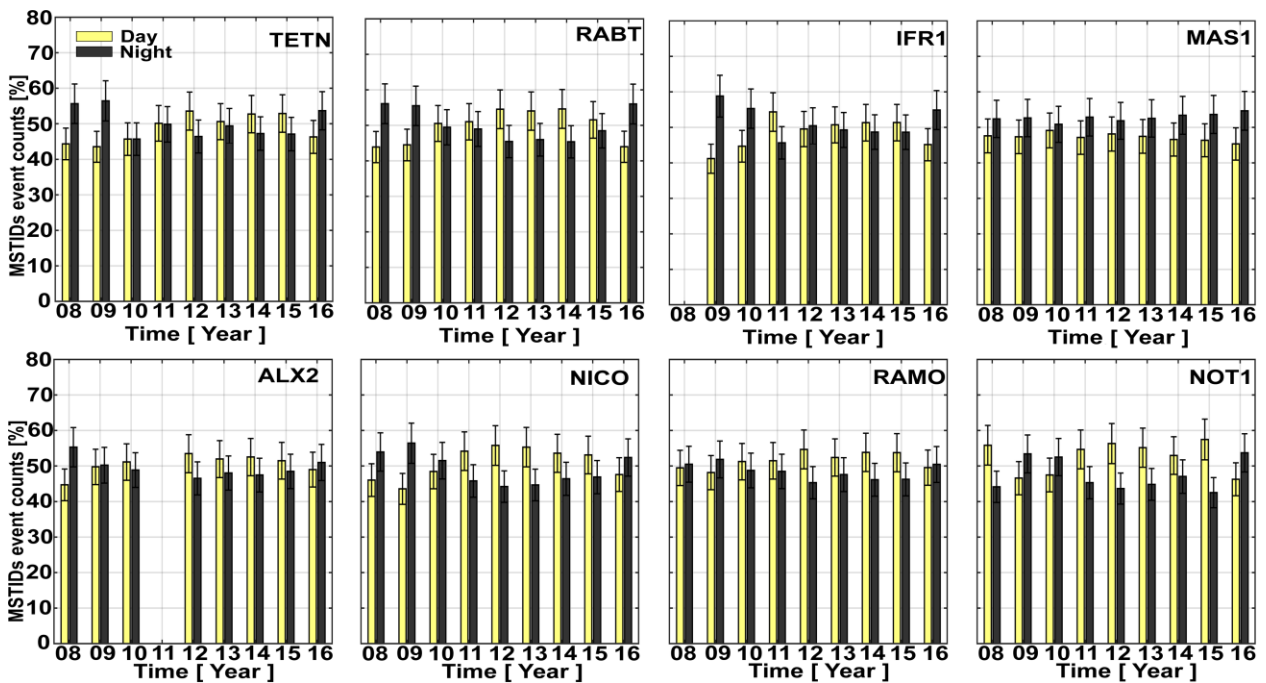
Figure 6.8: MSTIDs daily maximum amplitudes for day and night time for sub-network N2 (N2: top three panels). The fourth (last) panel is the low latitude station (MAS1)

At low latitude, the event is consistently high at nighttime which is dominantly above 50%, compared to mid-latitudes cases where the same nighttime period was dominantly below 50% except during the solar minimum of 2008, 2009, 2010, and 2016. On the contrary, at mid-latitudes, the figure shows that MSTIDs at daytime are dominantly high above 50% during 2011 – 2015 while at low latitude the daytime is consistently below 50% during daytime in 2008-2016.

6.6   Estimation of MSTIDs characteristics

In this section, we estimated the MSTIDs characteristics such as; propagation direction, velocity, period, and wavelength. The propagation azimuth during the daytime and nighttime is emphasized most especially the dominant directions. In order to avoid erroneous result in MSTIDs azimuth and velocity estimation, we selected GPS receiver stations with a closer intra-distance such as (N1: RABT-TETN-IFR1) which have an estimated intra-distance of 206 km, while other stations have their intra-distance more than 600 km. Figure 6.9a (top panel) shows polar plots representing MSTID velocities (in m/s) and azimuths during 2008 - 2016 for March equinox, June solstice, September equinox, and December solstice. In other to estimate a discrete propagation direction as a function of percentage since the polar measurements looks clustered, and for clearer analysis, we further divided the azimuth measurements into daytime and nighttime and get it plotted on a bar-chart (fig. 6.9 (bottom panel)). The bar-chart shows discrete cardinal directions; North (N), North-East (NE), East (E), South-East (SE), South (S), South-West (SW), West (W), and North-West (NW) following Otsuka et al. (2013) approach, the bar chart also shows the daytime and nighttime mean velocity for each of the seasons. The MSTIDs propagation velocity is within 50 - 450 m/s, with velocity dominance of 200 - 300 m/s for every season except September equinox which has a dominance velocity value between 100 - 200 m/s.
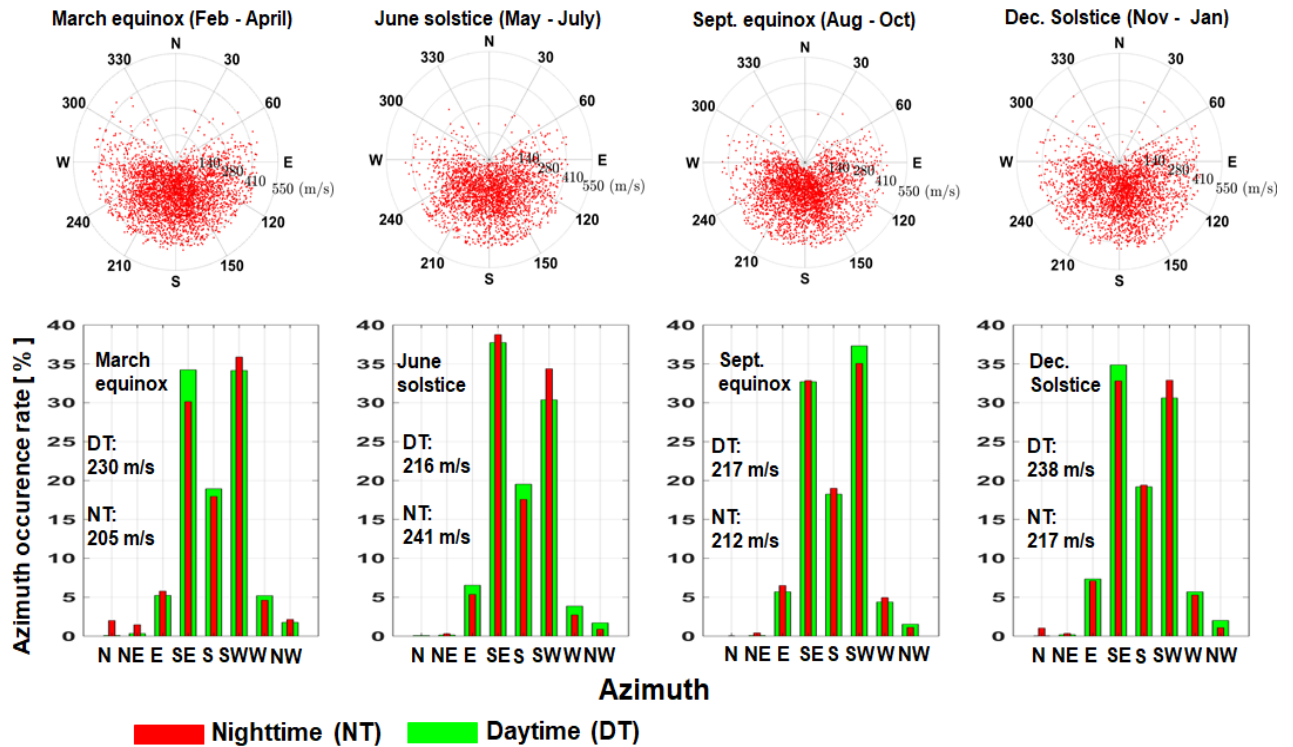
Figure 6.9a (top panel) shows polar plots representing MSTID velocities (in m/s) and azimuths for different seasons. (bottom panel) Bar chart showing cardinal directions of MSTIDs propagation having the percentage azimuth occurrence rate on the vertical axis, while the corresponding cardinal directions are on the horizontal axis.

Generally, the entire MSTIDs dominantly propagates southward (equatorward) as seen in fig. 6.9 (top panel), dominantly between $120°$ - $230°$. However, there are slight variations in propagation direction during daytime and nighttime as seen in Fig. 8 (bottom panel) which reveals the preferred propagation direction. Some few MSTIDs are observed to propagate northward, but most observation are seen to be dominantly southeastward and southwestward for both daytime and nighttime MSTIDs in all the seasons but with slight exceptional cases in March equinox, June solstice and December solstice, where the nighttime MSTIDs propagation towards the southwest is slightly higher than the daytime by ~1.80 %, 4.01 %, and 2.01 %, respectively. Furthermore, both daytime and nighttime discretely propagated southward within 17% - 19% (azimuth occurrence rate) in all seasons, with the daytime slightly higher than the nighttime during the March equinox, and June solstice, respectively. On the other hand, the nighttime is slightly higher than the daytime during the September and December solstice, respectively. In addition, the daytime MSTIDs propagates towards the southeast, and slightly higher than the nighttime which also propagates in the same direction by ~ 4.0 %, and ~ 3.0 % during the March equinox, and December solstice, respectively. The nighttime MSTIDs percentage of propagation direction is

higher in both southeast and southwest direction during June solstice, and during the September equinox the daytime MSTIDs percentage of propagation direction is higher southwest direction while the nighttime is slightly higher than the daytime in southeast direction. There are certain exceptions where the percentage of the southeastward propagation of daytime MSTIDs is comparable with that of the southwestward propagation during March equinox, the same thing also applies to nighttime MSTIDs but during December solstice.
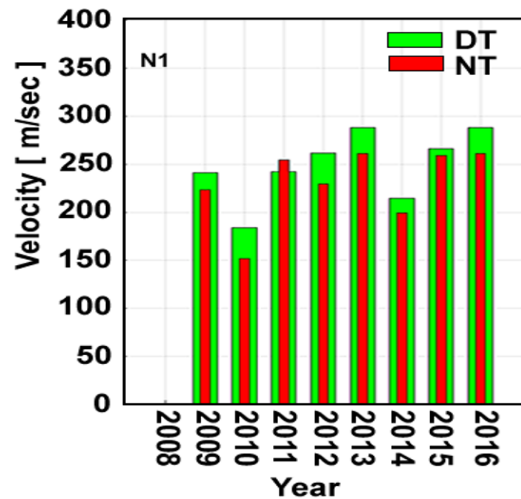
Figure 6.9b: Annual mean velocity of MSTIDs occurrence during daytime and nighttime for N1.

During the study period (2008-2016), the annual mean values of the velocity of MSTIDs at daytime and nighttime were computed and plotted as seen in fig. (6.9b). Figure (6.9b) again shows that daytime velocity is dominantly larger than nighttime, this indicates that MSTIDs is faster during daytime than the nighttime. The MSTIDs wavelengths were estimated from the distance the TEC wave-like structure traveled in space (latitude or longitude) by using the criterion in sub-section 4.7.4, following (Jonah et al., 2016), see table (6.3). Furthermore, having followed the procedure in sub-section 6.2.1, we obtained the MSTIDs periods during (2008 - 2016) following the approach of Husin et al. (2011) and Arikan et al. (2017). Periods estimated with less than 6 minutes were regarded as noise fluctuations and therefore eliminated (Valladares and Hei, (2012)). The minimum and maximum values of the MSTIDs wavelength are within ~54 km, and ~450 km respectively, and the dominant wavelength is this order: 150 - 250 km (~49 %), 50 - 150 km (~24 %), 350 - 450 km (~15 %), and 250 - 350 km (~12 %) for both daytime and nighttime, respectively. However, we computed for the mean minimum and maximum values (table (6.3))

Table 6.3: The mean value of the period and wavelength of MSTIDs at daytime and nighttime.

Year	Period (minutes)		Wavelength (kilometre)	
	N1		N1	
	Daytime	Nighttime	Daytime	Nighttime
2008	11.50 - 37.27	11.39 - 37.15	78 – 217	79 - 213
2009	15.76 - 33.65	16.73 - 33.40	85 – 241	87 - 236
2010	12.60 - 36.80	12.99 - 36.10	80 – 215	81 - 228
2011	14.55 - 34.10	13.99 - 33.88	77 – 216	75 - 223
2012	13.30 - 36.00	13.40 - 36.58	77 – 217	81 - 221
2013	14.15 - 34.10	14.19 - 33.85	75 – 223	75 - 228
2014	12.90 - 36.70	13.68 - 36.75	75 – 222	76 - 228
2015	16.10 - 34.03	14.13 - 34.70	82 – 229	81 - 235
2016	14.66 - 36.38	13.14 - 36.70	75 – 232	80 - 234

The period and wavelength estimated results in N1 sub-network fall within the ranges that are typically associated with MSTIDs. However, the daytime period results seem higher than the nighttime results. Based on the count of higher MSTIDs periods in the table (6.3a) during daytime and nighttime, the estimate of the quantity of the MSTIDs occurrence periods during daytime in N1 is ~55.5%, this indicates that the daytime MSTIDs is slightly higher than the nighttime.

6.7 Regional distribution of MSTIDs on a spatio-temporal map

Figure (6.9c) shows a regional distribution of MSTIDs on a spatio-temporal map over the North Africa region (mid-latitude).
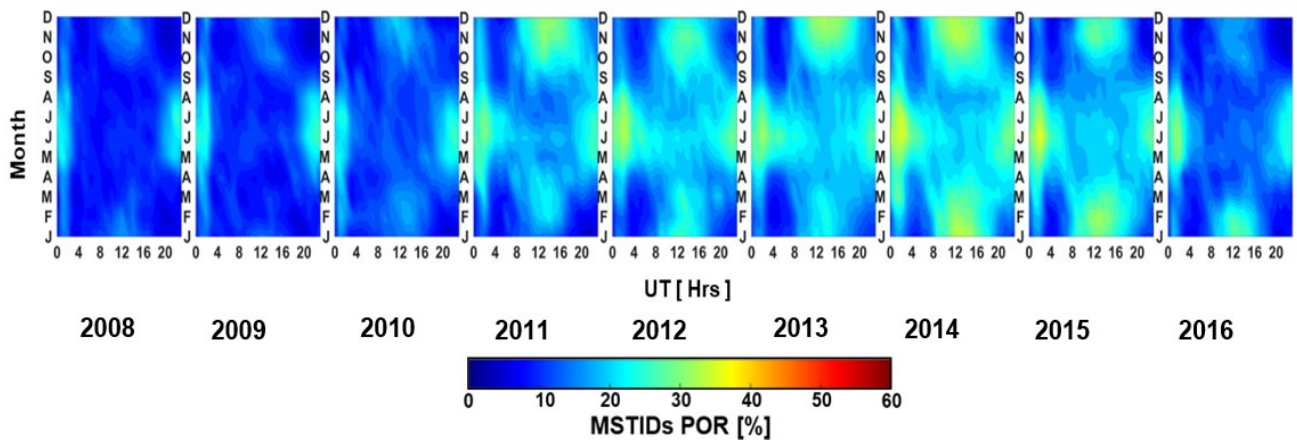
Figure 6.9c: Universal time and seasonal variations in MSTIDs POR at mid-latitudes
$(42^0N \leq GL \geq 30^0N)$; 2008 – 2016

MSTIDs maps from different sectors or local regions at mid-latitude were superimposed. The local times (LT) was converted to UT to avoid complexity in interpretation, for time uniformity,

easy analysis and most importantly to observe the dominant event time of MSTIDs occurrence for each year covering geographic latitudes (GL) 30°N to 42°N and longitude 18°W to 42°E following the approach of Otsuka et al. (2013). The distribution of dominant MSTIDs occurrence in fig. (6.9c) shows a semiannual variation with the major primary peak at June solstice (i.e. summer) during the NT (2100 - 0300 UT) and a secondary peak at December solstice (i.e. winter) during the DT (1000 - 1500 UT). The maximum MSTIDs POR was observed to be ~45% in 2014 and 2015.

6.8 Discussion

We have investigated statistically dTEC variations observed by GPS receivers located in the Northern African region at mid-latitudes to reveal MSTIDs occurrence rate at local time, seasonal, latitudinal variations, and propagation direction at daytime and nighttime, respectively, during 2008-2016. Our statistical results show a distinct difference between the observed MSTIDs activities.

Our statistical results show a distinct difference between the observed MSTIDs activities. Figures (6.2a) and (6.5c) shows daytime TEC measurement exhibiting wave-like structures depicting to be MSTIDs due to the passage of AGW (Hines, 1960; Hooke, 1968; Jonah et al., 2016; Oinats et al., 2016; Valladares et al., 2012), this hypothesis is validated in fig. 6.5(g-i). Figueiredo et al. (2018) reported that cloud top brightness temperature which ranges (i.e. threshold) between -65°C and -20°C during convection activities is an indication of AGWs passage. Therefore, we may deduce from the Figueiredo et al. (2018) report that the observed MSTIDs during the selected day (DOY 066) is possibly generated by AGWs which is as a consequence of convection activities. The AGWs passage involves vertical displacement of air parcels originating in the troposphere (Hines (1960)) and which causes perturbation in the ionospheric electron density. Temperature and wind perturbations are the two parameters that oscillate for a freely propagating wave which transport energy and momentum from their source into certain height in the ionosphere. The neutral air wind perturbation collides with the plasma at F region, and then the charged ions are set in motion but are constrained to move along the magnetic field lines. The transportation of the charged molecules/ions along the magnetic field lines leads to electron density enhancement in certain places along the wave-front and also depletions in some other places. The continuous, and regular enhancement and depletion of the

plasma density consequently leads to TIDs occurrence (Hooke, 1968). Figure (6.5e) shows the disturbed temperature profile obtained from COSMIC satellite and fig. (6.5f) shows the signature of upward AGW propagation as obtained from the detrended temperature profile. Our result in fig. (6.5c-h) is similar with the results obtained by Jonah et al. (2016) who reported MSTIDs occurrence and causative mechanism in the Southern hemisphere of the Brazilian sector. The MSTIDs 2-D map in fig. (6.4) shows TEC perturbations during the passage of MSTIDs, which seems to stretch from the Northwest (NW) towards the Northeast (NE) with a maximum amplitude peak value of 0.30 dTECU, this elongation from NW to NE confirms the MSTIDs feature of long-distance travel or one of propagation hypothesis of MSTIDs (Frissell et al., 2014). Figure (6.6a) and figure (6.6b) consist of GPS receiver stations located at NW and NE, respectively, and they show different characteristics between daytime and nighttime MSTIDs occurrence, such as local time, seasonal, and solar activity dependence. These facts indicate that different mechanisms initiate MSTIDs occurrence during daytime and nighttime period, and at different seasons. A high occurrence rate of MSTIDs was observed in the daytime during 1100–1600 LT, and 0900–1400 LT at NW and NE, respectively during the March equinox and December solstice, respectively. However, the nighttime MSTIDs exhibited highest occurrence rate observed in June solstice during ~2100 - 0200 LT and ~1900 - 0200 LT at NW and NE, respectively. Both daytime and nighttime MSTIDs occurrence at NW seems to be more pronounced during 2011 - 2015, than NE stations. Both the daytime and nighttime MSTIDs POR increases with increase with solar activity. Our MSTIDs seasonal occurrence results show a good agreement with the MSTIDs investigation conducted by Tsugawa et al. (2006a) who reported MSTIDs occurrence over South-East Asian sector (Japan). In their investigation, they reported nighttime (2100 - 0300 LT) MSTIDs to be the highest activities in every year during summer (May–August). They also observed on the contrary that the daytime (0900 - 1500 LT) MSTIDs occurrence is high during the winter, but there is no clear indication of solar activity dependence of the daytime activities. The slight difference between this current study and Tsugawa et al. (2006a) is that the current study shows a clear increase in daytime MSTIDs occurrence as solar activity increases, and the nighttime MSTIDs seems to be decreasing specifically during 1900 - 2300 LT as solar activity increases. Furthermore, the seasonal results in this current study is similar to the result obtained from with MSTIDs study over the North American sector (California) conducted by Hernández-Pajares et al. (2012), they reported daytime MSTIDs occurrence during winter (November–January) and fall (August–October), and nighttime during summer (May–July) and spring (February–April), whereas this current study reported daytime and nighttime occurrence during December solstice and June solstice, respectively. However, the

nighttime (0001 - 0200 LT) slightly extends to March equinox season during the solar maximum of 2014. Figure 6.6 (a-c) shows time (daytime and nighttime), seasonal, and latitude, and solar activity dependence of MSTIDs. These facts indicate that mechanisms causing MSTIDs could be different between daytime and nighttime period, and from location to location. A high occurrence rate of MSTIDs was observed during the daytime 1100–1800 LT at MAS1 station, and there is variability in the nighttime activities due to latitudinal dependency. However, the highest MSTIDs occurrence rate was observed during June solstice (May–July) every year at mid-latitude. There is different MSTIDs occurrence behavior as seen fig. (6.6c- low latitude), where the nighttime activities (2000-2300 LT) oscillate between March equinox (February, March, and April) and June solstice during 2008-2010. In addition, the nighttime activities become weaker in June solstice, but become high in December solstice (November, December, and January) during 2011-2015. However, in 2016 the high occurrence rate at the nighttime switch back to June solstice. It must be noted that the increase in MSTIDs occurrence rate from year to year is relative, and the occurrence rate of MSTIDs increases with the solar activity. Our results show good agreement with the MSTIDs nighttime results over the South-East Asian sector (Japan) reported by Tsugawa et al. (2006), although there is little difference in the level of occurrence in the nighttime within the local time range of 0001-0300 LT. The nighttime MSTIDs seem to decrease with increase in solar activities during 2011-2015. The latitudinal difference of the MSTIDs could be due to the different occurrence of electrodynamics mechanisms during daytime and nighttime. The MSTIDs occurrence rate at low latitude in fig. (6.6c) is obviously higher than the MSTIDs occurrence rate at mid-latitude in fig. (6.6 a-b), and this could possibly do with the TEC background that is generally large at low latitude than mid-latitude. In addition, one important factor responsible for the high TEC background at the low latitude station (MAS1) is the fact the station is situated within the EIA zone. Details of TEC behavior over EIA zone is reported in Oluwadare et al. (2018). In fig. (6.7), each year of the MSTIDs amplitude time series exhibited an asymmetric structure, and most especially during the daytime period. The MSTIDs occurrence exhibited a significant increase in the year 2011 relative to 2009 - 2010, and 2012 - 2013, during September equinox, possibly due to the increase in solar activity as expressed by an increase in sunspot numbers. The mean sunspot numbers in September equinox in 2009, 2010, 2011, 2012, and 2013 are 4.9, 33.2, 104, 88, and 87, respectively (see. http://www.sidc.be/sunspot-data/) (Tariku (2015)). Generally, the MSTIDs amplitude increase with an increase in solar activity, most especially the daytime period, this result agrees with Oinats et al. (2016) who investigated MSTIDs observation over Hokkaido East during 2007 - 2014, and over European-Asian sector during the 2013-2014 using radar data. They reported an increase in amplitude with an increase in

solar activity, and that the amplitude tends to increase with increasing auroral electrojet (AE) index, and also found that MSTIDs amplitude is dominantly high at daytime. In fig. (6.8), the annual MSTIDs event count (AMEC) at nighttime in low latitude is high and it's consistent irrespective of solar cycle phase condition, and this might indicate that there are more electrodynamics processes within this region as discussed above. On the contrary, the AMEC is high at nighttime only during solar minimum at mid-latitude; the result is in close agreement with Ding et al. (2011) who studied MSTIDs climatology over central China in South-East Asian sector during the 2010 solar minimum. The high AMEC results at daytime during solar maximum at mid-latitude are in close agreement with Oinats et al. (2016), who studied MSTIDs statistical characteristics using radar data over East Asia (Hokkaido-F region) and European-Asian sector during the 2013-2014 solar maximum and found that MSTIDs occurrence rate is dominantly high at daytime. The figure also shows that there were more daytime events than nighttime events at mid-latitude. Statistically, the figure has revealed that daytime MSTIDs is a major ionospheric irregular phenomenon at Mid-latitude. In estimating the MSTIDs propagation direction, we grouped the azimuth of the MSTIDs propagation direction into daytime, nighttime and seasons. The propagation direction of MSTIDs for both DT and NT are dominantly Southward (equatorward) as observed from the Northern hemisphere in fig (6.5k), and fig. (6.9-top panel), while fig. (6.9-bottom panel) show the azimuth occurrence rate expressed in percentage following Otsuka et al. (2013) approach. The percentage azimuth occurrence rate is observed to spread into different cardinal directions (see fig. 6.9-bottom panel). Certain MSTID propagating towards the N, NE, E, W, and NW, having the percentage of azimuth of the propagation direction below ~6.2% are considered insignificant, and hence we focused on the azimuth occurrence rate higher than 19%. However, our propagation direction results do not completely similar with some previous studies of MSTIDs propagation direction. For instance, Jacobson et al. (1995) investigated MSTIDs occurrence using a very long baseline interferometer (VLBI) array over New Mexico (35.9º N, 106.3º W), and they reported different seasonal variations in terms of occurrence rate and they further showed that the preferred daytime MSTIDs propagation direction is southward during winter and equinox seasons, respectively, while the nighttime MSTIDs often occur during summer solstice and autumn equinox and propagate toward the west/northwest. In addition, Kotake et al. (2007) reported the MSTID over Southern California using GPS network, and reported that the azimuth during the daytime is southeastward (90º to 240º) in equinox and in winter (120º to 240º) season, respectively, and also reported the nighttime MSTIDs to be southwestward and westward propagation (between 210º and 300º in azimuth) in equinox and summer seasons. While Ding et al. (2011) reported a dominant propagation of daytime MSTIDs

towards the equator, they added that the nighttime MSTIDs dominantly propagated southwestward in the Northern hemisphere at all seasons, with highest propagation occurrence in June, around the summer solstice. In the current study, the daytime MSTIDs dominantly propagates southeastward during March equinox and December solstice, even though the daytime exceeded the nighttime by ~ 4%. This result shows a slight similarity with the seasonal propagation dominance obtained by both Jacobson et al. (1995) and Kotake et al. (2007) discussed earlier, but differs in terms of propagation direction with the latter. The nighttime MSTIDs dominantly propagates southwestward during March equinox, June solstice, and December solstice. This also exhibits a slight similarity with the seasonal propagation dominance obtained by to Kotake et al. (2007), and Ding et al. (2011), except for December solstice. Distinctively in the current study, the dominant nighttime MSTIDs propagation direction during June solstice is observed to exhibit the highest peak of percentage azimuth occurrence rate but propagated southeastward, and also noticeable is the dominant daytime MSTIDs propagation direction during September equinox is observed to be southwestward, and about 17% to 19% of the daytime and nighttime MSTIDs discretely propagts southward in all seasons. These propagation direction behaviors are not similar with Kotake et al. (2007) and Ding et al. (2011). However, similar unconventional propagation direction behavior of MSTIDs have been reported. For instance, Figueiredo et al. (2018b) investigated the nighttime MSTIDS morphology over Cachoeira Paulista at Brazil in Southern hemisphere using Optical Thermosphere Imagers, and they reported certain class of nighttime MSTIDs to have propagated towards the northwestward direction in which they explained its mechanism as a consequences of PI theory, and another class of nighttime MSTIDs to have mainly propagated towards the north-northeastward direction. Also, in the same vein, Paulino et al. (2016) observed that nighttime MSTIDs over "São João do Cariri" in the Southern hemisphere exhibited a wide propagation direction towards the north, northeast, northwest, and southeast. Comparison of the nighttime MSTIDs propagation direction results from Kotake et al. (2007), Figueiredo et al. (2018b), Paulino et al. (2016), and the current study shows an indication that location of the different MSTIDs source could possibly influence propagation direction, and in addition, Perkin instability theory does not play out in nighttime propagation direction since not all of the nighttime MSTIDs observed in the Northern hemisphere are heading in the Perkins phase front normal direction. Several studies have been done to investigate the mechanisms responsible for the daytime and nighttime propagation direction of MSTIDs. Thome (1964) stated that the most supported theory for propagation direction is that TIDs propagates in the direction of the geomagnetic field lines. Hooke, (1968, 1970) in his investigation on ionospheric response to internal gravity waves stated that at F-region heights, the ions move and travel along the

geomagnetic field lines through neutral-ion collision, with a velocity the same as the velocity of the neutral motion along the geomagnetic field caused by the gravity waves, during this process some azimuthal directions of wave propagation are preferred as a function of the ionospheric response that are evoked. However, the motion of the ions across the magnetic field line is constrained to move along the magnetic field lines because the gyro-frequency of the ions is much higher than the frequency of the ion-neutral collisions. The direction of the motion of the ions consequentially leads to directivity in the response of the electron density variations to the gravity waves. This kind of directivity phenomena could be a contributor to daytime MSTIDs southward propagation direction (Kotake et al., 2007). Besides, an anisotropic frictional ion drag force has been thought as a possible candidate responsible for the southward propagation of the daytime MSTID direction (Liu and Yeh, 1969; Kelley and Miller, 1997). The nighttime MSTID were previously found to be associated with increases in the F-region peak electron density altitude by Behnke (1979), and its source was conventionally assumed to be generated by electrodynamical forces such as Perkins instability (Perkins, 1973; Kelley and Fukao, 1991; Kelley and Miller, 1997; Garcia et al., 2000; Tsugawa et al., 2007; Otsuka et al., 2007). The main concept of the Perkins instability (PI) is that when a perturbation of Pedersen conductivity (Σ) has a structure extended from Northwest to Southeast, and electric current **J** flowing Northeastward traverses the Pedersen conductivity perturbation. In this condition, the polarization electric field which is Northeastward (Southwestward) in the regions of low (enhanced) Pedersen conductivity is generated to maintain a divergence-free current. The generated polarization electric field (∂E) moves the plasma upward (downward) via the E x B drift, which consequently causes perturbation in the plasma density (Otsuka et al., 2013), and the mechanism for generating polarization electric field (∂E) is mostly consistent with an ionospheric instability mechanism introduced by Perkins (1973). This process is a possible mechanism for generating the nighttime MSTIDs with phase fronts elongated from Northwest-Southeast in the Northern hemisphere. Therefore, the nighttime MSTIDs observed to be propagating southwestward over North Africa region could be possibly caused by the electrodynamical force processes discussed above. However, it is noteworthy to add that the growth rate of the generative mechanism of Perkins instability at mid-latitudes is very low, and therefore would require additional seeding mechanism such as gravity waves (Huang et al., 1994) as well as electrodynamic coupling processes between F- and E- regions to boost the low Perkins growth rate to allow for the nighttime MSTIDs development (Cosgrove, 2004; Otsuka et al., 2007). The estimated results of N1 during the daytime and nighttime MSTIDs event in the table (6.3) are typical properties of MSTIDs (Samuel, 1974; Ogawa et al., 1987; Grocott et al., 2013). The mean propagation velocity of MSTIDs varies from 205 - 241 m/s, with the daytime

propagation velocity mostly higher than nighttime, which is similar with previous study (Husin et al., 2011; Hernandez-Pajares et al., 2012) except during June solstice where the nighttime is higher than the daytime which agrees with Oinats et al. (2016). The major contrast between present study and Oinats et al. (2016) is that, the nighttime MSTIDs propagation velocity is higher than the daytime only in June solstice, on the contrary Oinats et al. (2016) reported higher daytime velocity values over in the nighttime during 2007- 2014, using HF radar data. Often times, the nighttime MSTIDs have propagation direction to southwestward (northwestward) in Northern (Southern) Hemisphere (Garcia et al. 2000; Kotake et al. 2007), and for this reason Perkins instability (Perkins, 1973) is assumed to be responsible for the generation of nighttime MSTIDs (Figueiredo et al., 2018). Moreover, the dominant nighttime MSTIDs propagation direction during June solstice in the current study is observed to exhibit the highest peak of percentage azimuth occurrence rate but propagated southeastward, while the dominant daytime MSTIDs propagation direction during September equinox is observed to be southwestward. The wavelengths show a high wavelength dominance during the daytime than the nighttime. The MSTIDs distribution map is developed in fig. (6.9c), the map gives a general view of MSTIDs in the North Africa region, and most importantly its occurrence dominance. The regional distribution has similar features such as season and time (Hrs) of occurrence as fig. (6.6a-b) but with a major difference in occurrence time rangeacti. The high MSTIDs occurrence level observed during daytime and nighttime are 0900–1600 UT (December solstice (winter)) and 2000–0400 UT (June solstice (summer) respectively, in each year but the seasonal peak got extended to March equinox during in 2011, 2014, and 2015, but more pronounced in 2014. The same occurrence mechanism discussed above for local sector is also responsible for the regional distribution. The figure shows a consistent increase in MSTIDs occurrence with increase solar activity. The MSTIDs distribution map is developed in fig. (6.9c), the map gives a general view of MSTIDs in the North Africa region, and most importantly the MSTIDs occurrence dominance. The regional distribution has similar features such as season and time (Hrs) of occurrence as fig. (6.6a-b) but with little difference in occurrence time range, and solar activity dependence. The high MSTIDs occurrence level observed during daytime and nighttime are 0900–1600 UT (December solstice (winter)) and 2000–0400 UT (June solstice (summer) respectively, in each year but the seasonal peak got extended to March equinox during in 2011, 2014, and 2015, but more pronounced in 2014. The same occurrence mechanism discussed above for local sector is also responsible for the regional distribution. The figure shows a consistent increase in MSTIDs occurrence with increase solar activity.

Chapter 7

MSTIDs COMPUTATION RESULTS AT AFRICAN EQUATORIAL AND LOW LATITUDE

The equatorial and low latitude ionospheric event is generally considered to be dynamical in nature with a high electron density when compared to the mid-latitude ionosphere. Disturbance occurrence at this latitude is high, mostly due to solar flux and geomagnetic activities around the region. However, previous studies report that MSTID structures are commonly found in the middle latitude ionosphere, during June solstice (summer). Previously, MSTIDs has not often been reported to occur within the EIA zone ±20°, most especially within the African sector. Here, we present observational evidence of MSTIDs derived from TEC perturbation obtained from GPS network receivers within and outside the EIA zone. We discuss the implications of this observation in terms of the development and propagation of MSTIDs. For the first time, we report and discuss MSTIDs observation during the geomagnetic condition of kp ≤ 3 during 2008-2016 in the African region. This chapter reports MSTIDs causative mechanism at daytime and nighttime, seasonal variation, as well as MSTIDs characteristics (period, wavelength, dominant propagation direction) in both Northern hemisphere (NH) and Southern hemisphere (SH).

7.1 A brief overview of Equatorial and low latitude MSTIDs previous result

For about three decades or more, authors like Hernández-Pajares et al. (2006, 2012), Valladares and Hei (2012) and Jonah et al. (2016) in recent times among others have investigated, and reported the ionospheric irregularities phenomena with main focus on MSTIDs around the low latitude of different regions. These authors and several others have discussed the use of GPS as a technique in monitoring and investigating ionospheric disturbance such as MSTIDs. For instance, Hernández-Pajares et al. (2012) reported MSTIDs occurrence during 1998 - 2011 through the use of GPS networks at mid-north hemisphere (California), mid-south hemisphere (New Zealand), high and low latitudes (Alaska and Hawaii) during different solar cycle conditions. The results revealed that MSTIDs occurrence at mid-latitude also extends to low and high latitudes. Each sector investigated exhibits different MSTIDs characteristics mostly as a function of local time

and latitude. Valladares and Hei (2012) measured and investigated MSTIDs occurrence characteristics using a GPS receiver network located at a low latitude in South America during selected campaign days of 2008. The study reported the possibility of using small and long baselines of GPS networks for TEC perturbation investigation. They concluded that disturbances propagate towards the equator. Jonah et al. (2016) also reported TEC perturbation associated with MSTIDs, and possible causative mechanisms around the low latitude of Brazil in the southern hemisphere during the daytime of selected days in 2011. They reported AGWs to be responsible for daytime MSTIDs, and that the disturbance propagates towards the equator. Different studies have reported many interesting MSTIDs occurrence results around the globe. However, no studies have been done to report the MSTIDs occurrence in Africa. Exclusion of MSTIDs results or reports from Africa would create a gap in global modeling of ionospheric disturbances and consequently create a deficiency in the estimation of ionospheric disturbances budget. Hence, this chapter focuses on MSTIDs observation, characteristics, and occurrence mechanism in low latitude over the Africa region during the daytime and nighttime period in both NH and SH.

7.2 Equatorial and low latitude Africa GPS receiver stations description

MSTIDs have been observed and estimated during 2008-2016 using ground-based dual-frequency GPS receiver network stations situated at the equatorial and low latitude region in both the NH and SH. Table (7.0) shows the station names and their corresponding coordinates. We used a total number of twenty-seven (27) GPS network stations for MSTIDs study in this section (see figure (7.2a)). The geographic coordinates were transformed to geomagnetic coordinate using the altitude adjusted corrected geomagnetic (AACGM) coordinates[7.1].

[7.1] `https://ccmc.gsfc.nasa.gov/requests/instant/`
`instant_aacgm.php?model=AACGM&type=1`

Table 7.0: The GPS receiver station names and corresponding coordinates

GPS stations	Town	Country	Geographic Coordinates	Geomagnetic Latitudes
ABUZ	Zaria	Nigeria	11.15°N, 7.65°E	-0.13°
ACRA	Accra	Ghana	5.56°N, 0.20°E	-3.49°
ADIS	Addis ababa	Ethiopia	9.04°N, 38.76°E	0.16°
ARMI	Arba Minch	Ethiopia	6.06°N, 37.56°E	-3.03°
BETH	Bethlehem	South Africa	28.24°S, 28.33°E	-38.23°
BJCO	Cotonou	Benin Rep.	6.38°N, 2.45°E	-3.08°
BJKA	Nord Benin	Benin Rep.	11.12°N, 2.93°E	-0.23°
CGGN	Toro	Nigeria	10.12°N, 9.11°E	-0.78°
DAKR	Dakar	Senegal	14.72°N, 17.44°W	2.34°
EMLO	Ermelo	South Africa	26.50°S, 29.98°E	-36.81°
HARB	SAC, Hartebeesthoek	South Africa	25.88°S, 27.71°E	-36.31°
HRAO	HartRAO, Hartebeesthoek	South Africa	25.89°S, 27.69°E	-36.32°
KRUG	Krugersdorp	South Africa	26.08°S, 27.77°E	-36.48°
KSTD	Kroonstad	South Africa	27.66°S, 27.24°E	-37.77°
MAL2	Malindi	Kenya	2.99°S, 40.19°E	-12.42°
MAS1	Maspalomas	Spain	27.76°N, 15.63°W	15.75°
MBAR	Mbaraba	Uganda	0.60°S, 30.74°E	-10.22°
MOIU	Eldoret	Kenya	0.28°N, 35.29°E	-9.17°
NAMA	Namas	Saudi Arabia	19.21°N, 42.04°E	11.49°
NAZR	Nazret	Ethiopia	8.56°N, 39.29°E	-0.25°
NKLG	Libreville	Gabon	0.35°N, 9.67°E	-8.04°
PRET	Pretoria	South Africa	25.73°S, 28.28°E	-36.18°
RCMN	Nairobi	Kenya	1.22°S, 36.89°E	-10.69°
TANZ	Tanzania	Tanzania	6.77°S, 39.21°E	-16.59°
UNEC	Enugu	Nigeria	6.42°N, 7.50°E	-3.23°
WIND	Windhoek	Namibia	22.57°S, 17.09°E	-33.16°
YKRO	Yamoussoukro	Côte d'Ivoire	6.87°N, 5.24°W	-2.57°
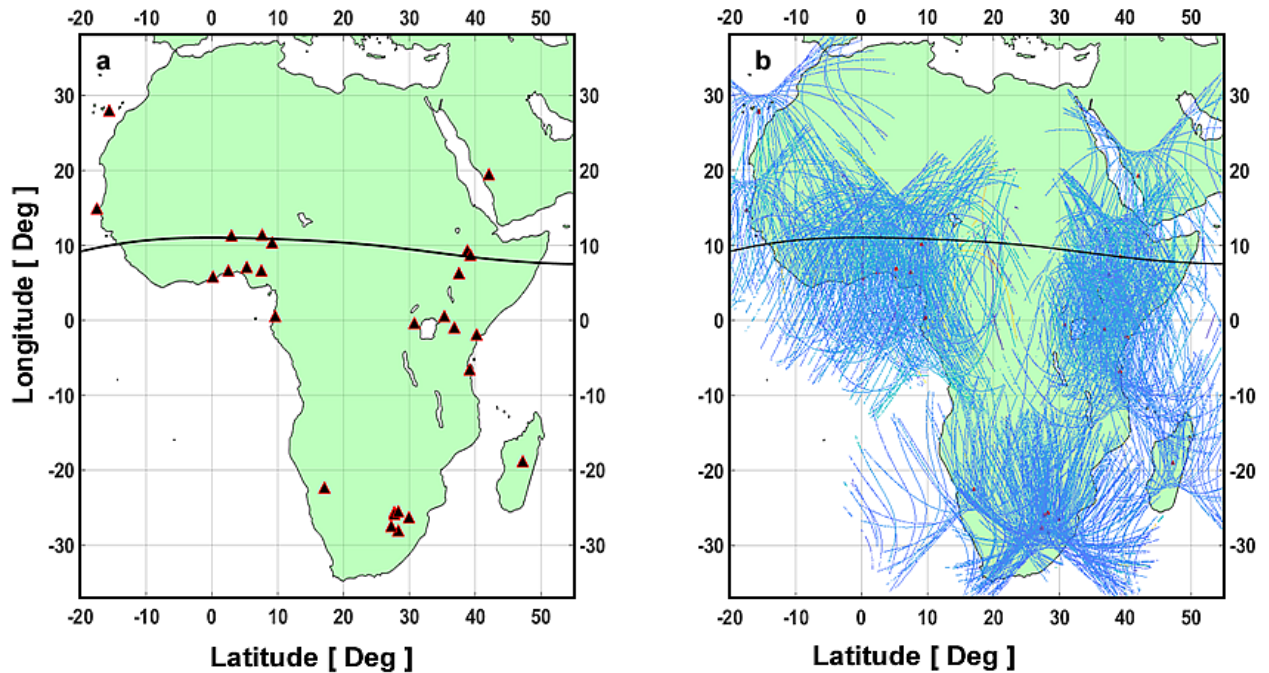
Figure 7.1a: A map showing the GPS stations (red triangles) used in this study at equatorial and low latitude. Figure 7.1b: Location of the GPS receiver stations with IPP tracks of all GPS satellites observed.

7.3 Wave-like structures depicting MSTIDs along the Equatorial and low latitude on selected days

It is important to observe the TEC time series structure that depicts MSTIDs when the TEC looks perturb at some selected days in the equatorial and low latitude. Figure (7.2a) and (7.2b) show typical examples of such instances during DOY 364 of 2009 (30th December 2009) and 351 of 2009 (17th December 2009). The top panel of fig. (7.2a) and fig. (7.2b) has majorly been assumed to be caused by AGW as discussed as validated by the temperature profile. The AGW passage evidence could be seen in the temperature profile which shows some perturbation effects which eventually get propagated into the ionosphere (Azeem and Barlage, 2017) above 50 km. We converted local time (LT) to universal time (UT) in a situation where at least two GPS stations from a different region with more than 1hr local time difference observe a particular satellite (i.e. unique PRN), in order to prevent ambiguity and wrong interpretation of MSTIDs during concurrent or simultaneous observation.
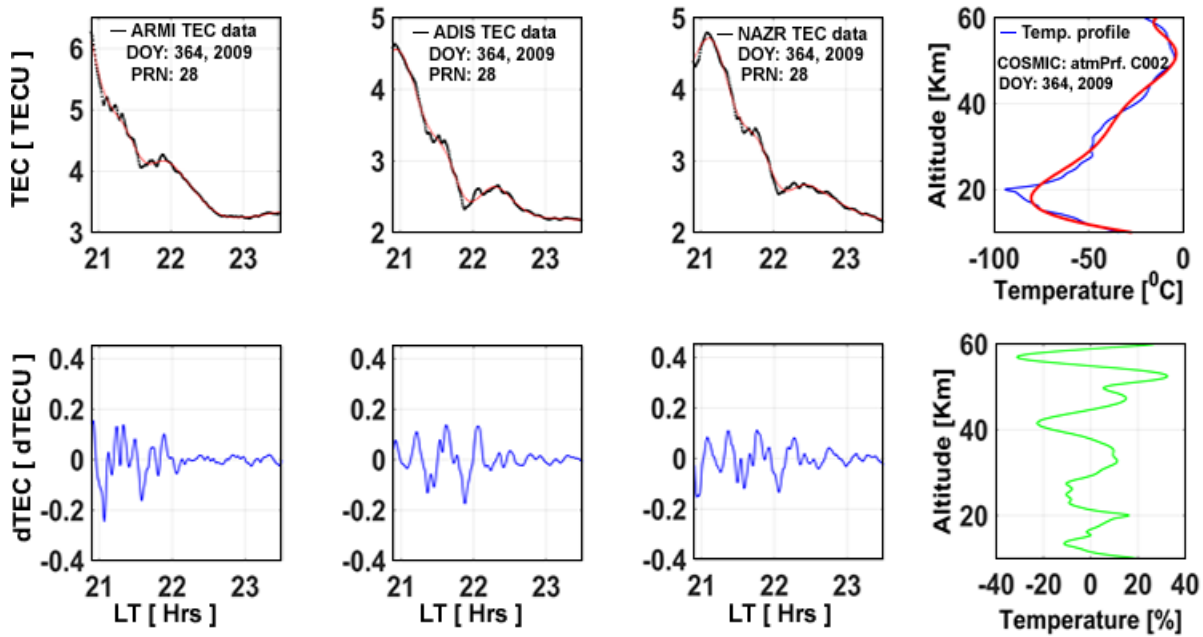
Figure 7.2a: (Top panel): TEC time series of PRN 28 as observed at ARMI, ADIS and NAZR GPS station exhibiting different wave-like structures depicting to be MSTIDs during nighttime. The red line fitted curve (TEC$_{SSA-fit}$) represents the estimated background/unperturbed TEC values. Top panel-extreme right: Perturbed temperature profile from COSMIC satellite (blue color) and its curve fit (red color). Bottom panel: The corresponding detrended TEC time series known as TEC perturbations (dTEC). Bottom panel-extreme right: Signature of upward AGW propagation obtained from the detrended temperature profile during 30th December 2009
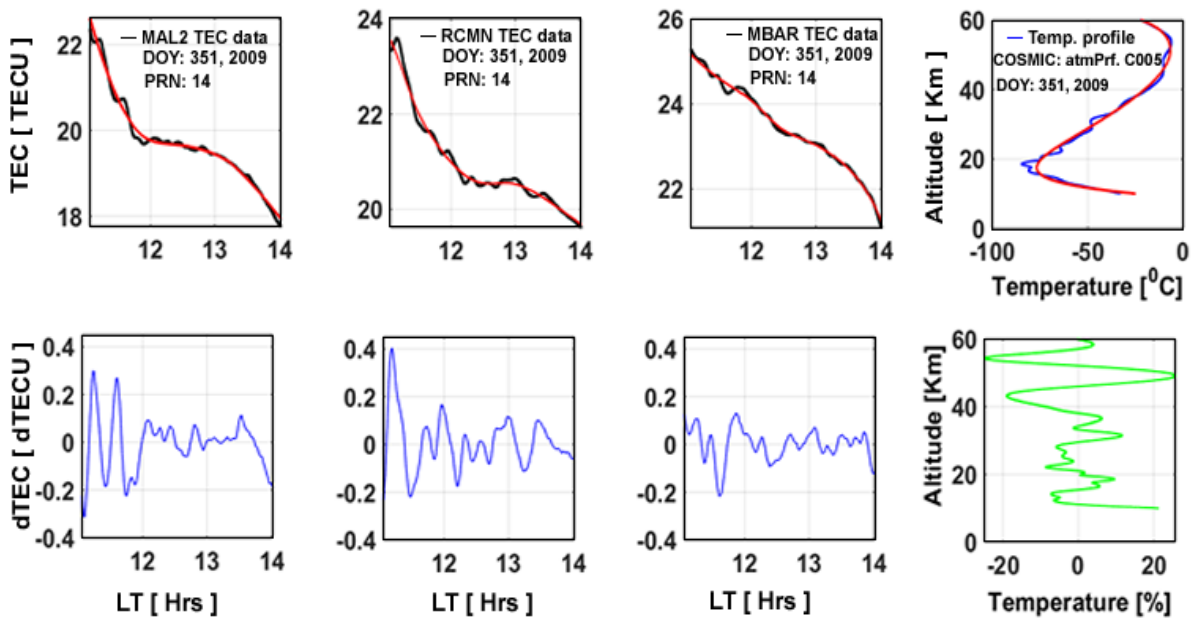
Figure 7.2b: Same as fig. (7.2a) but for PRN 14 as observed at ARMI, ADIS and NAZR GPS station during 17th December 2009.

7.3.1 Perturb TEC profile at selected stations depicting MSTIDs at NH and SH

TEC perturbations (dTEC) were measured at different stations to estimate the variation of MSTIDs at different latitudes during DOY 264 (21st September; 2011). The top panel of fig. (7.3a) displays a maximum perturbation that reaches about 5 TEC units majorly between during the nighttime ~1800 – 2300 LT and 0001 – 0300 LT at NH. The top panel of fig. (7.3b) displays a maximum perturbation that reaches about 4 TEC units majorly between ~1800 – 2300 LT and 0001 – 0300 LT at SH. In this sub-section (7.3.1), the MSTIDs are parameterized by analyzing the amplitude of TEC perturbation (dTEC).
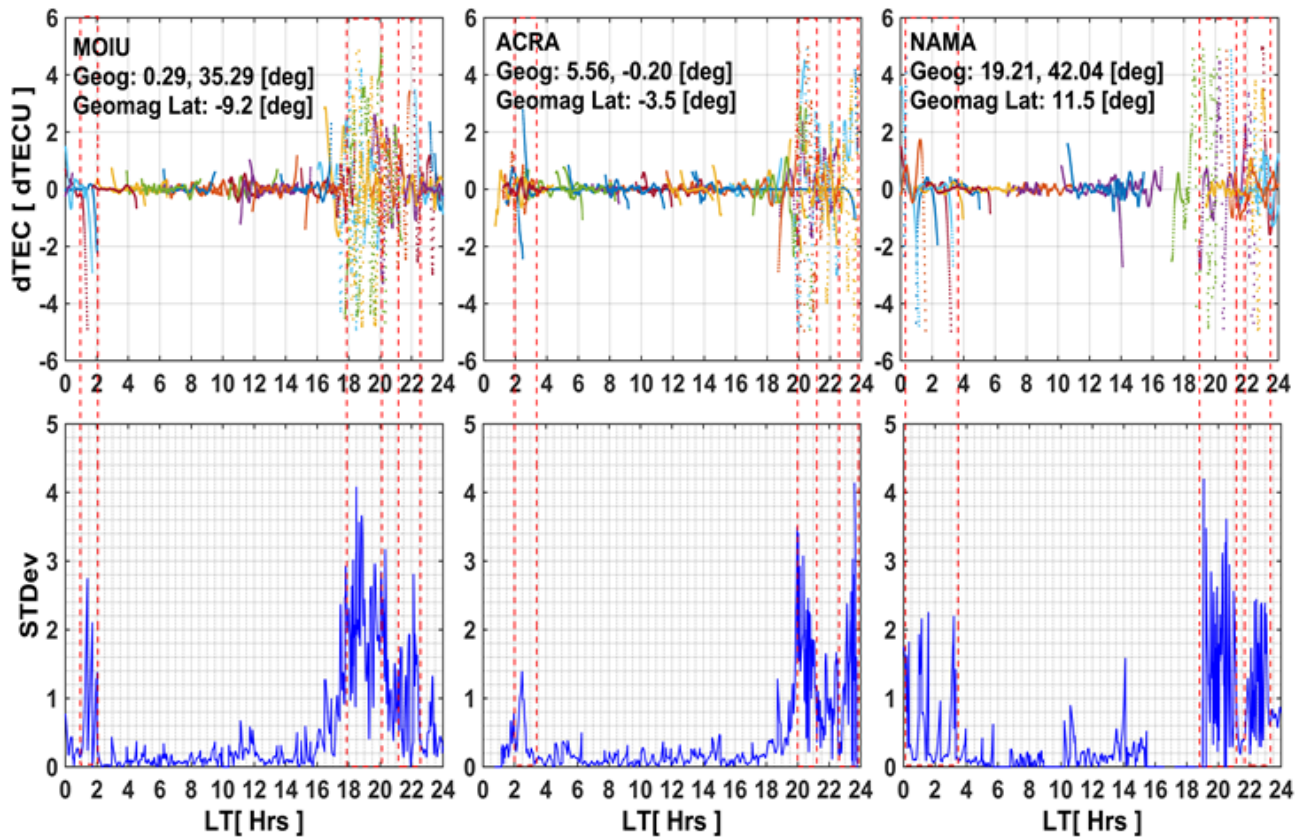
Figure 7.3a: (Top panel) TEC perturbation at various stations (MOIU, ACRA and NAMA) along NH for 21st September, 2011. The dTEC estimate from various GPS satellite signals are plotted; each satellite is distinguished by a different color. Bottom panel: The standard deviation of every TEC perturbation at every epoch. The red dash line is used to mark the high amplitude of TEC perturbation with the corresponding high value of standard deviation at the bottom panel.
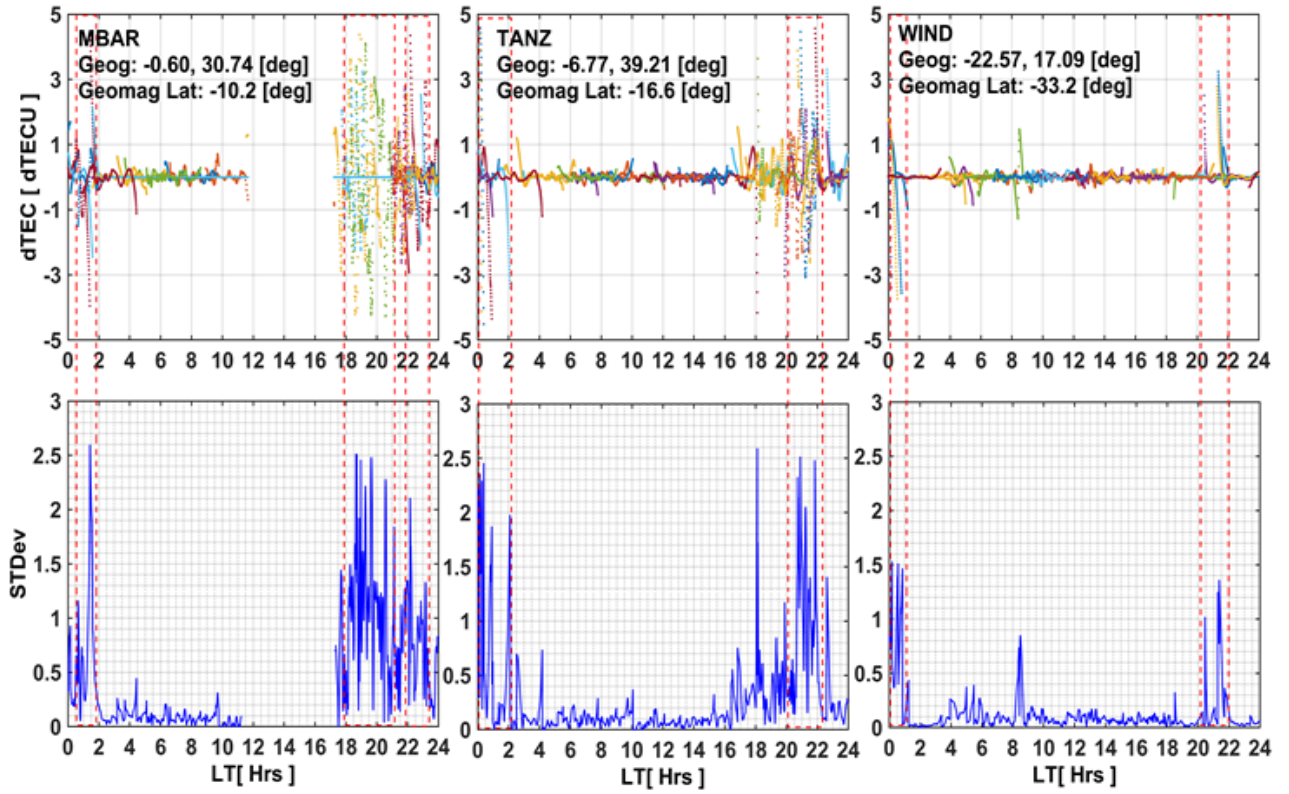
Figure 7.3b: Same as fig. 7.3a but for various stations (MBAR, TANZ and WIND) along SH for day 264 of 2011.

Figures (7.3a) and (7.3b) reveals MSTIDs often occur more at nighttime than daytime. It is obvious that the amplitude of the TEC perturbation (dTEC) at NH is higher than SH, most especially at the nighttime. The high nighttime amplitude varies in terms of local time and latitude. Due to the fluctuation variation in the dTEC amplitude, we calculated the standard deviation (STDev) of dTEC in every satellite in every epoch (see equation (7.2)) in order to estimate the magnitude of the MSTIDs (see figures (7.3a-b) bottom panel).

$$\bar{X}_{epoch1} = \frac{1}{n}\sum_{i=1}^{i=n} dTEC_{sati} = \frac{dTEC_{sat1} + dTEC_{sat2} + \ldots\ldots + dTEC_{satn}}{n} \qquad (7.1)$$

$$STDev_{epochi} = \sqrt{\frac{1}{n-1}\sum_{i=1}^{i=n}(dTEC_{sati} - \bar{X}_{epochi})^2}$$

$$STDev_{epoch1} = \sqrt{\frac{(dTEC_{sat1} - \bar{X}_{epoch1})^2 + (dTEC_{sat2} - \bar{X}_{epoch1})^2 + \ldots\ldots + (dTEC_{satn} - \bar{X}_{epoch1})^2}{n-1}} \qquad (7.2)$$

$dTEC_{sat1}$: estimate value of TEC perturbation of satellite 1 in epoch 1,

dTEC$_{sat2}$: estimate value of TEC perturbation of satellite 2 in epoch 1,

n: total count number of dTEC estimate in epoch1, $\bar{X}_{epoch1}$: dTEC sample mean in epoch1

dTEC$_{sati, i}$: 1, 2,….n are the number of available satellite per epoch,

STDev$_{epoch1}$: Standard deviation of epoch1.

In addition, each station exhibited a variation of dTEC amplitude with a corresponding high magnitude of standard deviation, most especially during the nighttime. Equation (7.1) and (7.2) formulas are a typical example of estimating the standard deviation of epoch 1. The same procedure is applied to estimate the entire 2880 epochs within one day. Interesting observation results in fig. (7.3a), and fig. (7.3b) is that dTEC amplitude with corresponding high magnitude is observed at stations whose geomagnetic latitude coordinate value is closeer to the EIA crest (± 15º). In general, the NH dTEC amplitudes are higher than the SH during the observed day.

7.3.2   Two-dimensional observation of MSTIDs

Figure (7.4a) shows the two-dimensional maps of MSTIDs of fig. (7.4b) over the equatorial and low latitude of Africa region during the daytime of day 264, 2011 at the NH.
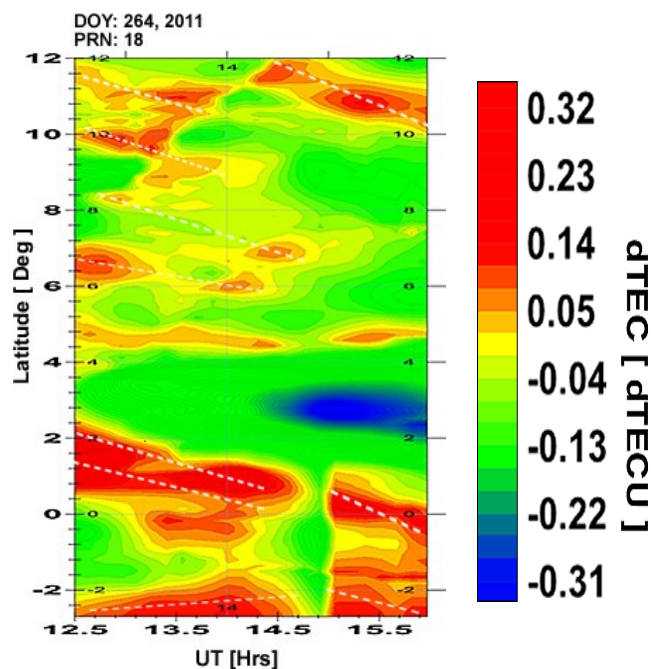
Figure 7.4a: Two-dimensional propagation map of MSTIDs over the Equatorial and low latitude in NH of African region during daytime (1250 to ~1600 UT) on 21st September, 2011 (DOY 264).
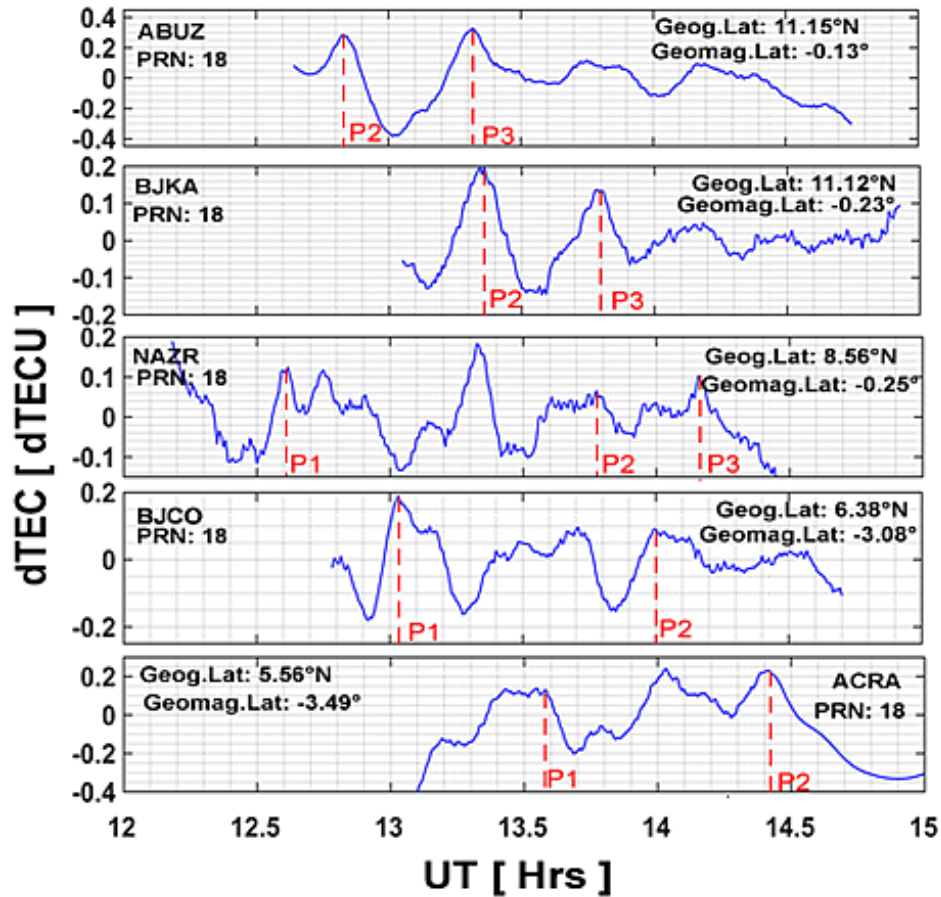
Figure 7.4b: TEC perturbations values exhibiting MSTIDs measured in the NH at different location of GPS receivers. Note that the perturbation amplitudes peaks propagate downward (equatorward).

The observed perturbation in fig. (7.4a) seems to be travelling from low latitude 11.15°N (ABUZ) to the near equator 5.56°N (ACRA). The line plot of the two-dimension propagation map (fig. (7.4a)) is presented in fig. (7.4b). A similar procedure is done at the SH with nearly the same time range period. Red dashed lines with assigned tags (P1, P2, and P3) in fig. (7.4b) and fig. (7.4d) indicates TEC perturbation peaks. The tags allow us to visually observe the peaks as it travels either southward or northward. Parallel alike perturbation wave peaks are carefully selected as they travel south-poleward. Meanwhile, there have been a record of M-class solar flare[7.2] eruption associated with EUV and X-ray, which started around 1204 UT, and ends at about 1245 UT, with peak round 1223 UT during 21st September, 2011. We further investigated to check if there is a relationship between the MSTID observations in the current study and solar flare (SF).

[7.2] ftp. swpc. noaa. gov/pub/warehouse/2011/2011_plots/

Solar flare is referred to as a sudden and intense brightness in active regions on the Sun surface in the photosphere. It is one of the important phenomena which can suddenly affect the dynamics of the ionosphere. It has been categorized as a function of intensity level, in W/m^2 from 1 to 8 A˚ (0.1 - 0.8 nm). It is measured by the X-ray instrument on board the GOES satellite. Studies have shown that EUV and X-ray flares can cause an enhancement in D, E, and F regions ionization at a very short time interval (Mitra, 1974; de Abreu et al., 2019). Further details about ionospheric response to SF can be found in de Abreu et al. (2019). Figure (7.4c) shows the X-ray flux of the solar flare of class M 1.87 during day 264, 2011.
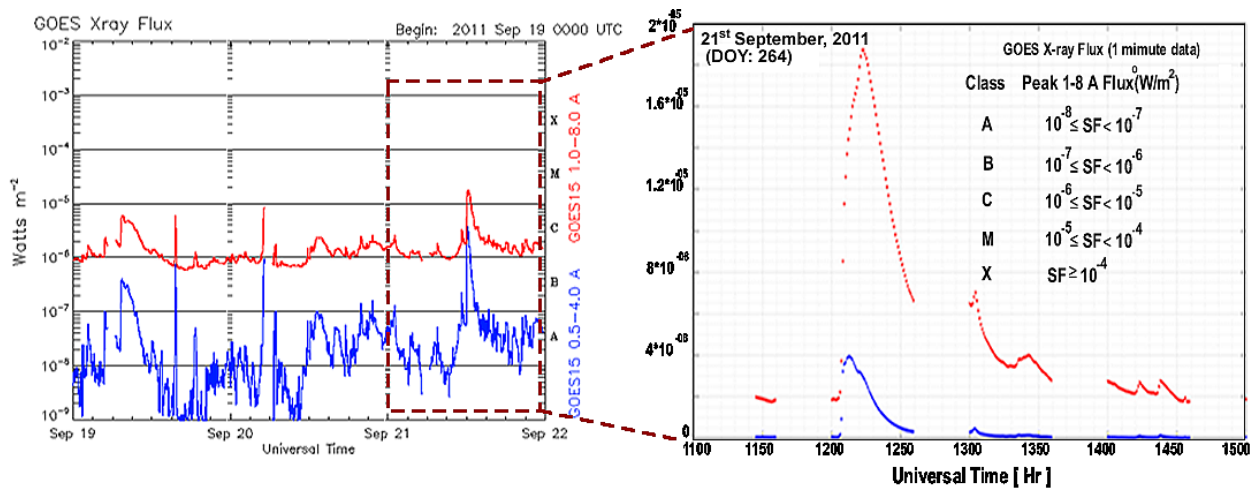
Figure 7.4c: The X-ray flux of the solar flare which is class of M 1.87 on 21st September, 2011.

The data points[7.3] within the 1100 to 1500 UT time series of X-ray flux of the solar flare were extracted to have a clearer view, and a visual observation of fig. (7.4b) and fig. (7.4c) time frame. Hence the time frame reveals that the solar flare does not correlate with MSTID. The solar flare exhibited its maximum around 1223 UT, while MSTIDs exhibited its dominance maximum between 1250 UT and 1400 UT. The same procedure used in NH is also applied to obtain in SH MSTIDs two-dimensional propagation map (fig. (7.4d)) at SH. Figure (7.4e) is the line plot of fig. (7.4d).

[7.3] http://darts.isas.ac.jp/pub/solar/sswdb/goes/xray/20110921_Gp_xr_1m.txt
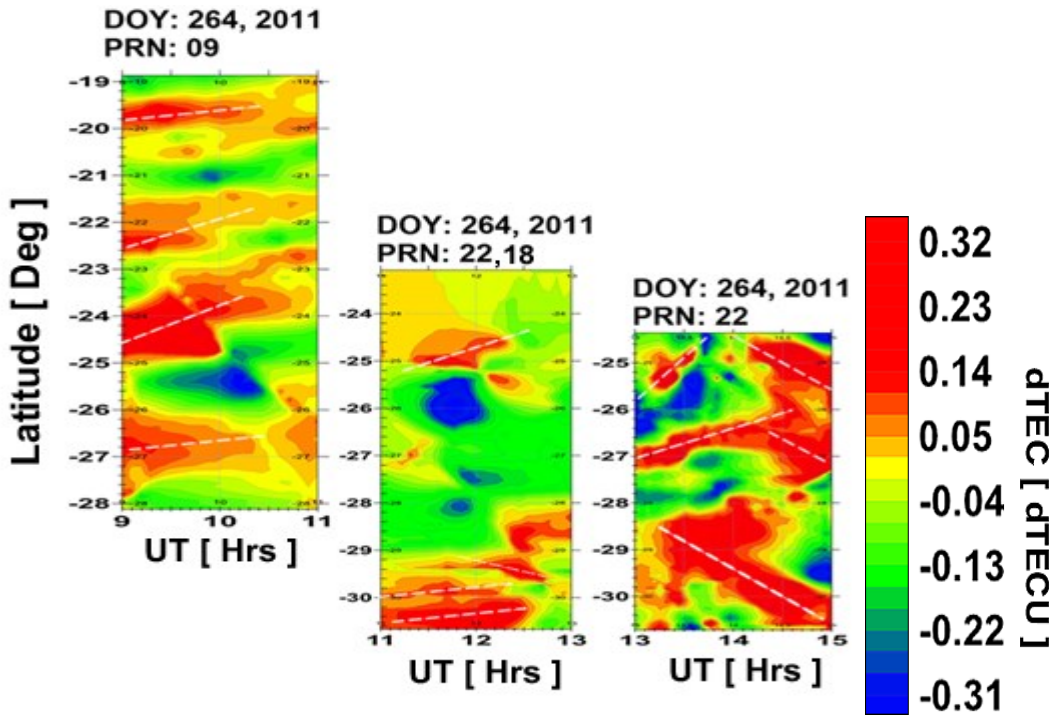
Figure 7.4d: Two-dimensional propagation maps of MSTIDs over the Equatorial and low latitude in SH of African region during daytime (0900 to ~1500 UT) on 21st September, 2011 (DOY 264).
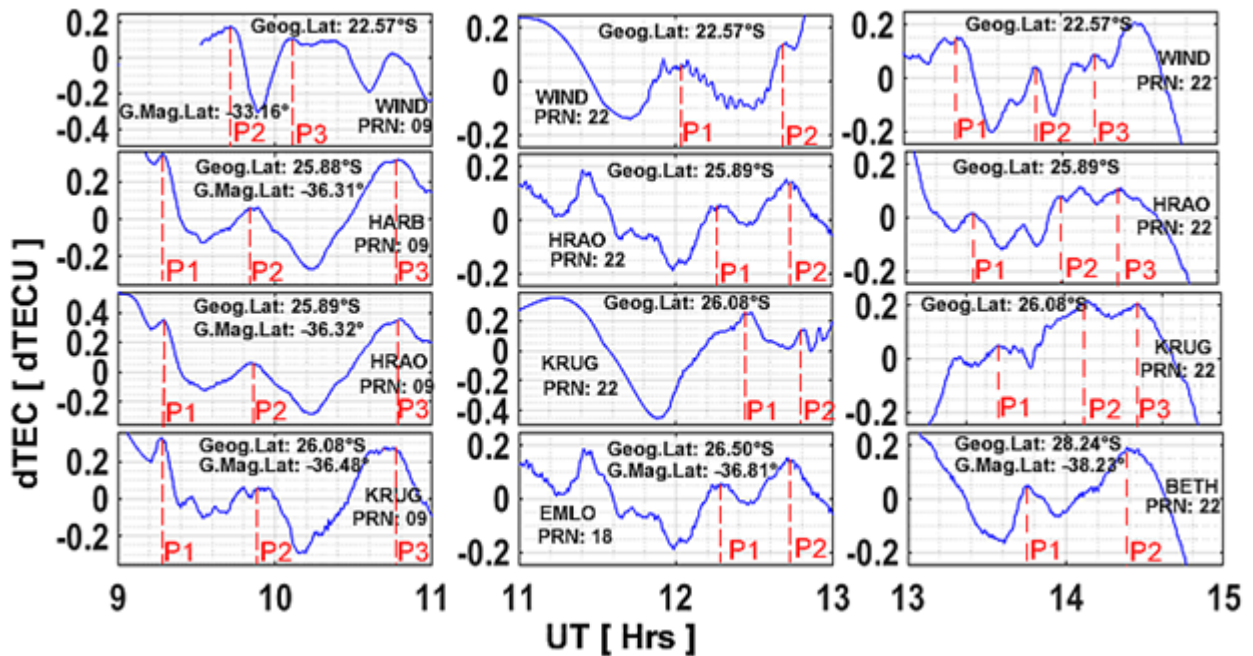
Figure 7.4e: TEC perturbations values exhibiting MSTIDs measured in the SH at different location of GPS receivers.

In this section (7.3.2), the MSTIDs are parameterized by analyzing the amplitude of dTEC as well as its peak-to-peak comparison in time to estimate the direction of propagation. There are similar

and few differences features noted during day 264 of 2011 in fig. (7.4a-b) and fig. (7.4d-e), respectively; there are more clearer structures of MSTIDs at SH than NH, most especially during 0900-1100 UT. By visually observing the peaks (P1, P2, and P3), the dTEC values measured in the NH in fig. (7.4b) shows that peak P1 seems to be travelling southward from geographic latitude 8.56°N to 0.28°N with a travel time of 1hour 30minutes (mins). The peak P2 is observed at time 12.82 UT, 13.34 UT, 13.77, 13.99, and 14.42 UT for stations ABUZ, BJKA, NAZR, BJCO, and ACRA, respectively. This implies that the disturbances travel southward from geographic latitude 11.15°N to 5.56°N with a travel time of 1hour 36mins. The peak P3 is observed at time 13.32 UT, 13.78 UT, and 14.16 UT for stations ABUZ, BJKA, and NAZR, respectively. This implies that the disturbances travel southward from geographic latitude 11.15°N to 8.56°N with a travel time of 50mins. On the contrary, in fig. (7.4e), the visual observation of peak P1 shows that the disturbances traveled towards the south-pole and eastward (south-eastward) from geographic latitude 26.08°S to 22.57°S, 26.50°S to 22.57°S, and 28.24°S to 22.57°S and from geographic longitude 17.09°E to 27.77°E, 17.09°E to 29.98°E, and 17.09°E to 28.33°E with a travel time of ~7 mins during (0900 – 1100 UT), 25 mins during (1100 – 1300 UT) and 6 mins during (1300 – 1500 UT) respectively. The same procedure was done to monitor travel direction for P2 and P3. However, the travel time for MSTIDs propagation in this current study varies. If the station is situated close to each other, then the travel time is low as in the case of fig. (7.4e). Figure (7.4b) shows that MSTIDs can propagate over a long distance (1028.36 km) as in the case of P2 (ABUZ) to P2 (ACRA), Frissell et al. (2014).

7.4 MSTIDs equatorial and low latitude characteristics

Hemisphere may be in the summer season because such a hemisphere receives more sun's rays while concurrently another hemisphere is in the winter season because the axis of that region on earth is tilted away from the Sun. Due to this fact, seasons in the NH and SH differ from each other. Hence, we analyzed the seasonal variation in the MSTID characteristics. At the NH, the year has been divided into four seasons: spring (February–April), summer (May–July), autumn (August–October), and winter (November–January). At the SH, each year has been divided into four seasons: spring (September–November), summer (December–February), autumn (March-May), and winter (June–August).

7.4.1 Local observation of MSTIDs over selected region in NH and SH of Africa

Selected GPS network stations at equatorial and low latitude regions showing the results of MSTIDs in both NH and SH. Data gaps are indicated by the white portions on the figures.
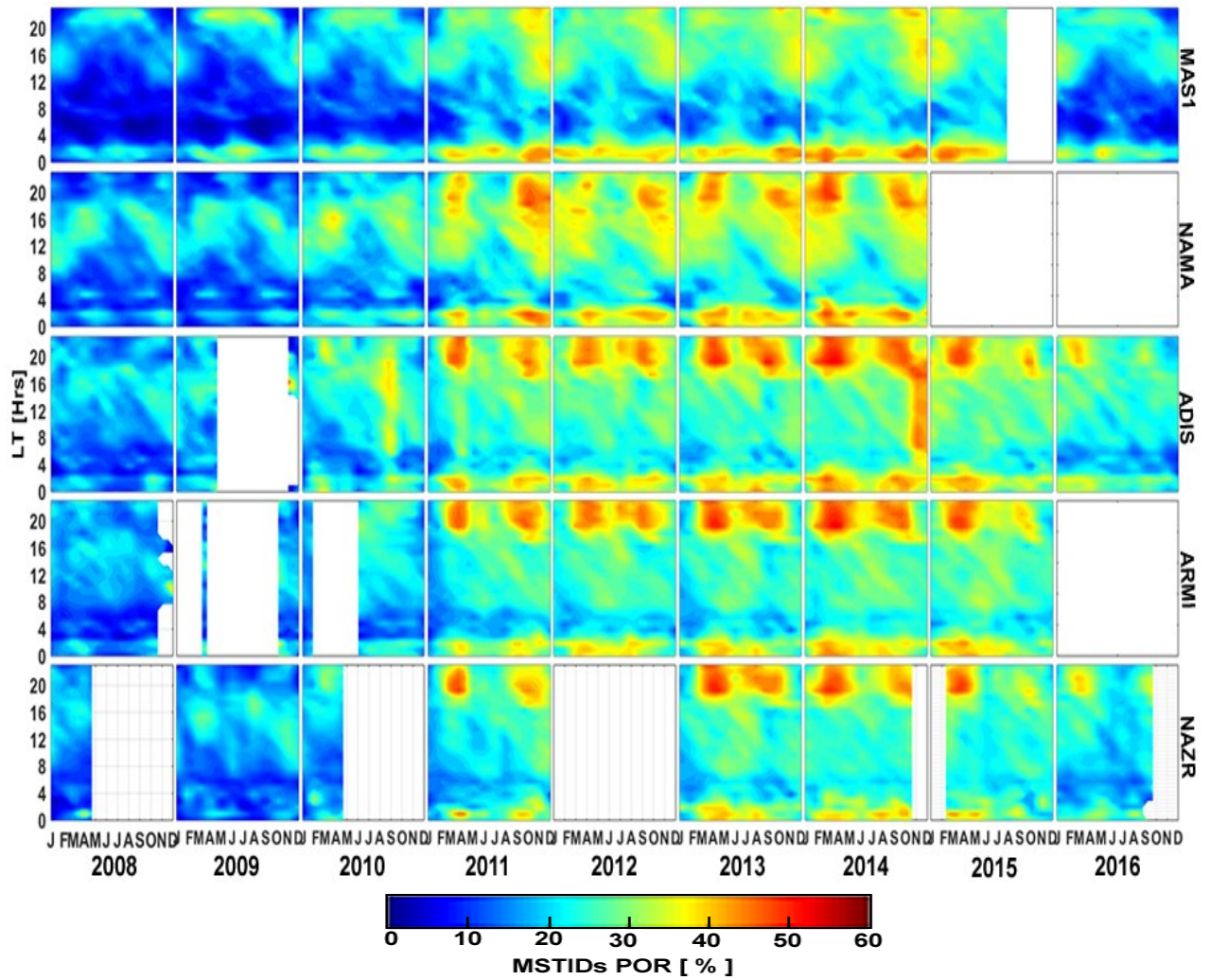
Figure 7.5a: Local diurnal and seasonal variations of MSTIDs occurrence at low latitude stations in northern hemisphere during 2008-2016.
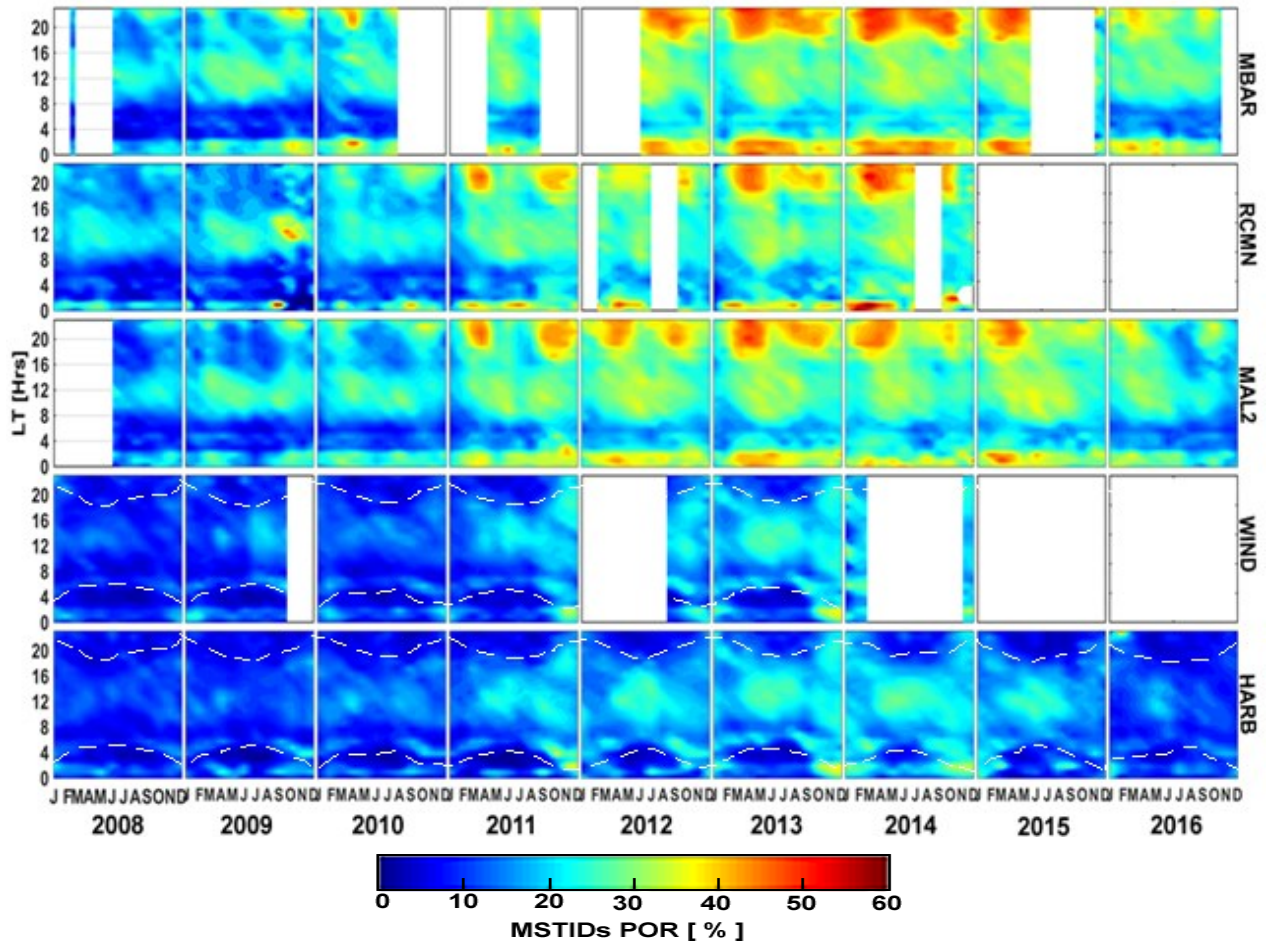
Figure 7.5b: Local diurnal and seasonal variations of MSTIDs occurrence at low latitude stations in southern hemisphere during 2008-2016. The white dashed lines represent the solar terminator

In fig.7.5 (a-b), each panel shows a similar contour structure pattern of MSTIDs event that is peculiar to its locality but with a clear different diurnal and seasonal variations of MSTIDs occurrence. It is visually clear that the MSTIDs occurrence shows a strong dependence on the season and different local times but with a major peak around the nighttime periods at both NH and SH, respectively. The major peaks of MSTIDs POR are observed in stations that are nearer to the equator in both hemispheres. At the NH, ADIS, NAZR, and ARMI exhibited a similar major peak at nighttime around 2000-0200 LT, during spring and autumn season. The occurrence rate increases with solar activities. MAS1 exhibited its major peak at nighttime around 2000-0100 LT during spring and autumn season during 2011-2015, and in summer during the solar minimum of 2008-2010 and solar ascending phase in 2016. NAMA exhibited its major peak at nighttime around 1900-0200 LT in the spring and autumn season, respectively during 2011-2014, while other major peaks are exhibited around 1500-1900 LT during 2008-2010. In the SH, WIND and HARB exhibited a low MSTIDs occurrence relative to other stations within the same hemisphere.

117

Stations like MBAR, RCMN, and MAL2 exhibited a similar major peak at nighttime around 1900-0300 LT, 2100-0100 LT, and 2000-0200 LT, respectively, during autumn and spring season. The daytime MSTIDs are fairly pronounced (minor peak) mainly around 0800-1500 LT, 0800-1300 LT, and 0800-1600 LT at stations MBAR, RCMN, and MAL2 respectively. WIND and HARB exhibited no visible MSTIDs occurrence rate at nighttime relative to other stations during 2008-2010 but shows mild daytime MSTIDs occurrence mainly around 1100-1600 LT and 0900-1600 LT during 2011-2015 respectively. There is also an indication of the solar terminator near 1700 and 1900 LT in the other seasons, most especially in stations outside the EIA zone in SH. At NH major peaks are observed at nighttime during spring (February-April) and autumn (August-October). At SH, major peaks are observed at nighttime during autumn (March-May) and spring (September -November), while the daytime is observed to be partly May month and during the winter season (June-August). Nighttime MSTIDs appears to be more dominant in POR. The result shows that MSTIDs event at different locations are not homogeneous. In subsequent sections, we analyze daytime and nighttime amplitudes and further separate them to make a statistical count of daily maximum amplitude during the day and night period.

7.4.2 Interannual and seasonal dependence of MSTIDs amplitudes at NH and SH

The time series of both daytime and nighttime amplitude of MSTIDs observations obtained from all GPS receiver stations located in both hemispheres is shown in fig. (7.6). We implemented a mathematical function (simple moving average) which estimates the average value to determine the trend of line-curve for both daytime (red line) and nighttime (black line) for better visual analysis and to observe subtle changes in the multiple scatter plots. The figure exhibited hemispheric variability of MSTIDs, and 2014 shows the maximum MSTIDs amplitude in both hemispheres. The embedded inset plot is to clearly show the trend line-curve behavior during 2008-2010 which shows that the nighttime MSTIDs are dominant during the low solar activities, and on the contrary, the daytime MSTIDs are dominant during the low solar activities at the SH.
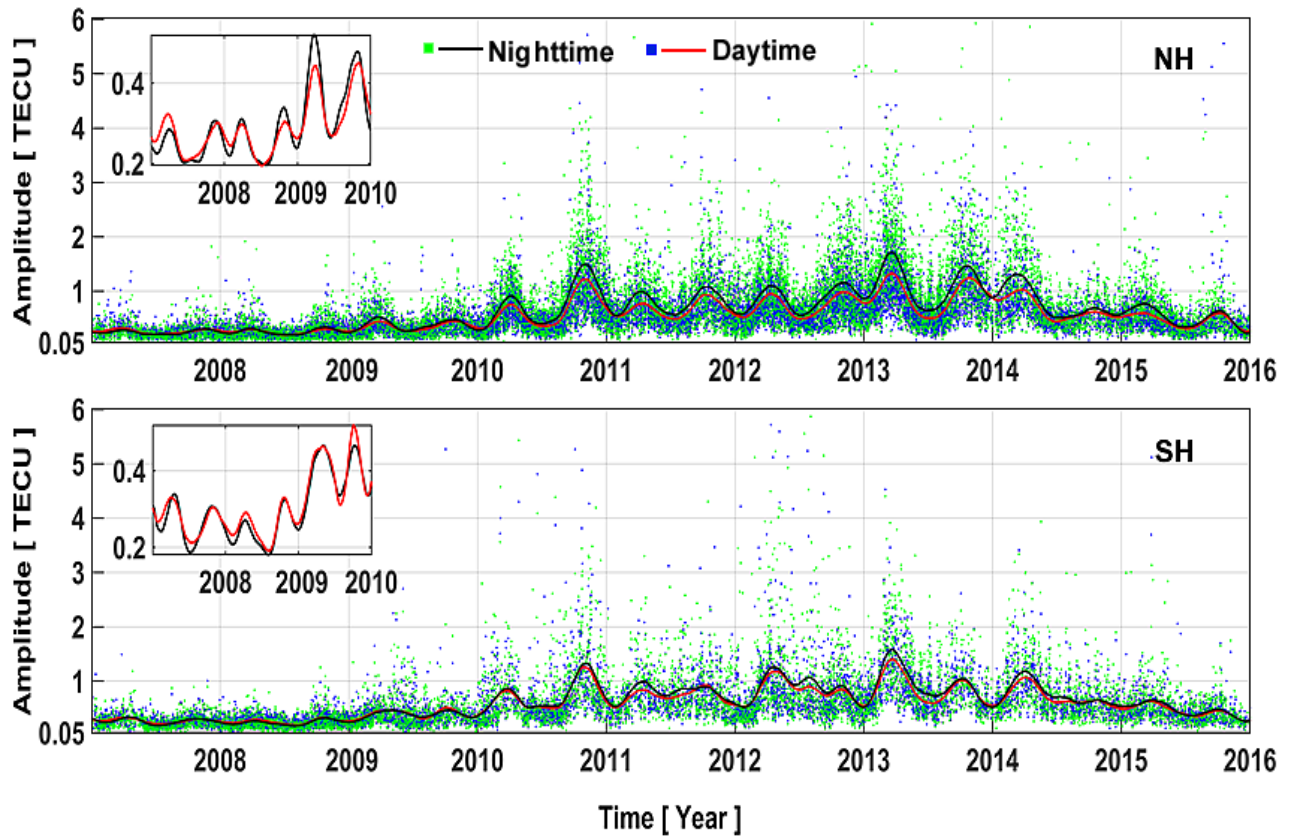
Figure 7.6 (Top panel): MSTIDs amplitude time series for both nighttime and daytime at northern hemisphere (NH). Bottom panel: MSTIDs amplitude time series during 2008-2016 for nighttime and daytime at southern hemisphere (SH). The trend curve is indicated with black and red lines for nighttime and daytime respectively.

In figure (7.6), the annual MSTIDs time series shows maximum amplitudes at NH and SH during 2011 and 2014 respectively. At the NH (top panel), the estimated mean amplitude of the major peaks (2011 and 2014) in the time series is 1.22 TECU (daytime) and 1.50 TECU (nighttime) around autumn (August-October) of 2011, and 1.32 TECU (daytime) and 1.79 TECU (nighttime) around spring (February-April) of 2014. At SH (bottom panel), the estimated mean amplitude of the major peaks is 1.25 TECU (daytime) and 1.32 TECU (nighttime) around spring (September-November) of 2011, and 1.40 TECU (daytime) and 1.58 TECU (nighttime) around autumn (March-May) of 2014. Some previous studies of MSTIDs in other regions have reported that MSTIDs do not increase with the solar activity (Bowman, 1992; Candido et al., 2008; Martinis et al., 2010) which is not the same situation in this study. MSTIDs were observed to increase with solar activity, and there is a semiannual effect of the amplitude during the nighttime and daytime in both hemispheres, irrespective of the solar activity condition. The amplitude gradually dropped during 2015-2016 due to the solar cycle approaching another solar minimum year (descending phase). In addition, the high TEC background experienced during high solar activities in autumn

and spring season could also influence the high amplitude, in that whenever the TEC background is large, the amplitude of TEC perturbation too would be high.

7.4.3 MSTIDs characteristics at NH and SH

MSTIDs propagation direction

Using the network geometry approach in subsection (4.7.4) and the same procedure in subsection (6.2.3), we formed sub-networks N1 (ARMI-ADIS-NAZR) and N2 (MBAR-RCMN-MAL2) to estimate the propagation direction and propagation direction. Each sub-network is situated at NH (N1) and SH (N2). Figure (7.7a) and (7.7b) shows the polar plot of propagation direction and phase velocity of MSTIDs.
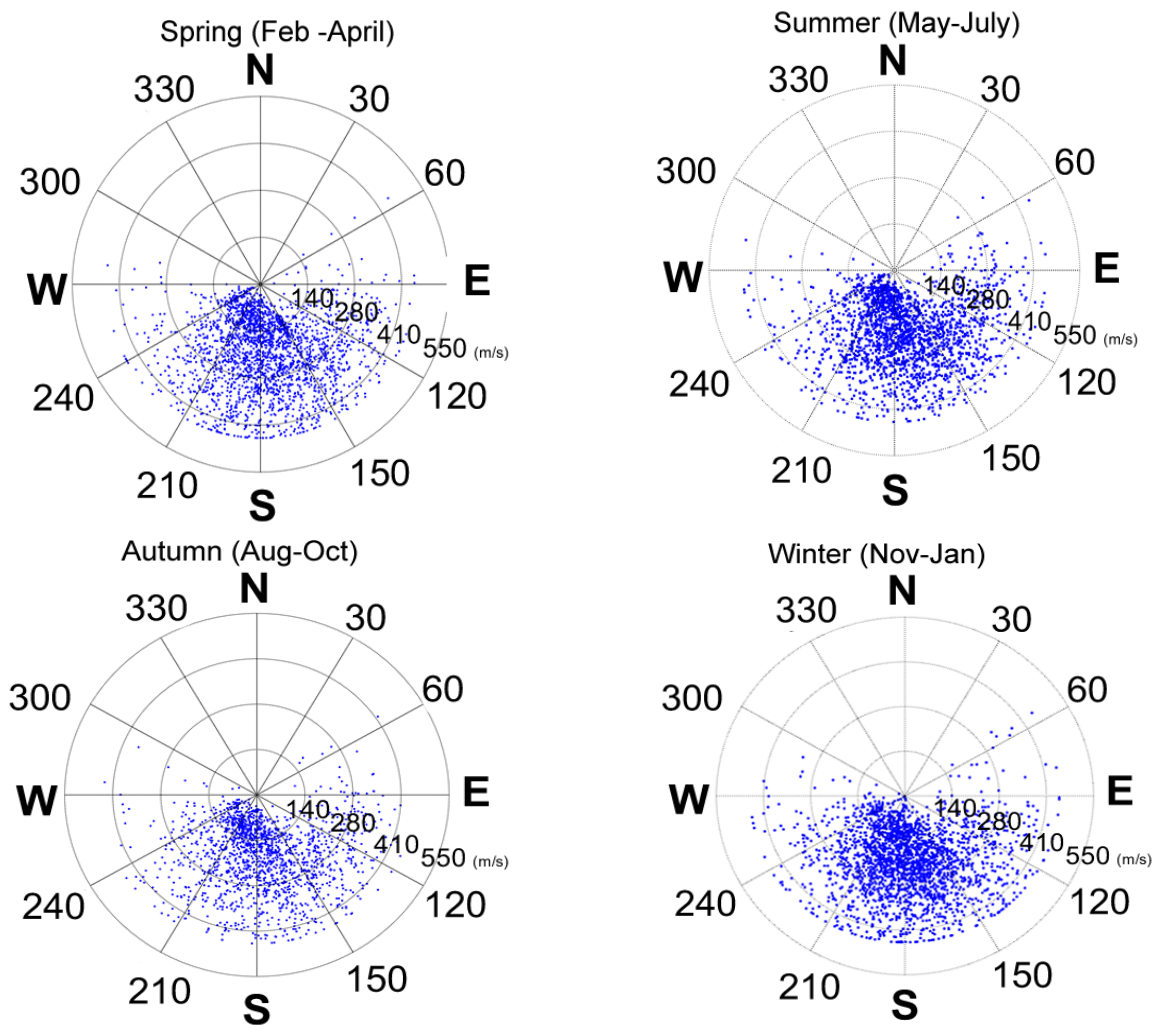
Figure 7.7a: Polar plot representing MSTIDs azimuths and phase velocities (m/s) at NH (N1) during 2008-2016. Top panel: spring and summer. Bottom panel: autumn and winter.
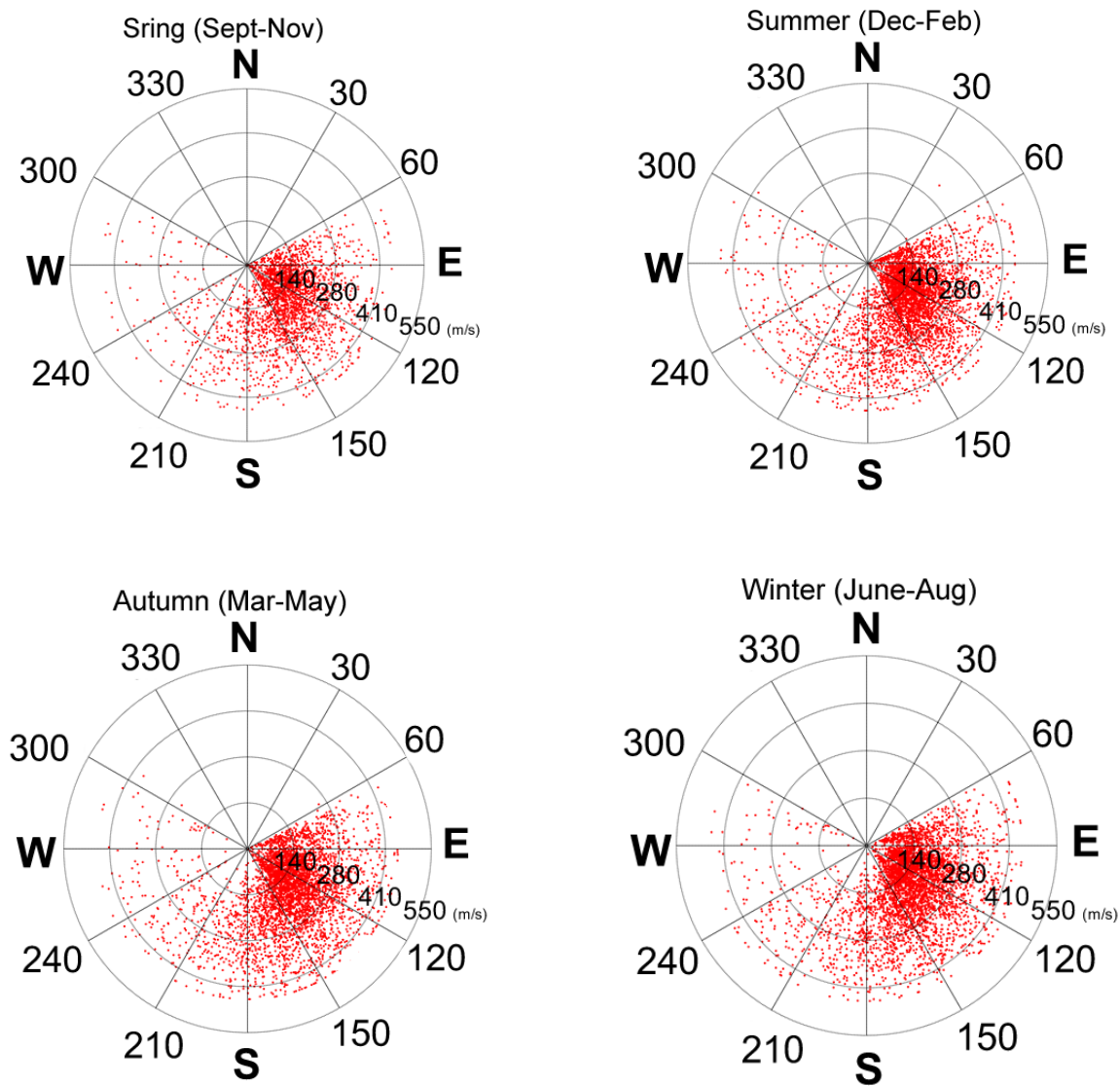
Figure 7.7b: Polar plot representing MSTIDs azimuths and phase velocities (m/s) at SH (N2) during 2008-2016. Top panel: spring and summer. Bottom panel: autumn and winter.

The figures (7.7 a-b) reveal the variability of MSTIDs propagation directions at NH and SH. Data are classified into 45° interval bins, and the occurrence rate is grouped into an hourly bin as a function of UT and the MSTID azimuth starts from 0° to 360° (azimuth measurement starts from 0° at the north and 180° at the south). In a general view, figure (7.7 a), shows that the preferred directions for MSTIDs propagation are southward (i.e. equatorward), but dominantly propagates to the southwest and southeast. We quantified the amount of disturbance that propagated in different cardinal directions (North (N), North-East (NE), East (E), South-East (SE), South (S), South-West (SW), West (W), and North-West (NW)) by estimating its percentage, but we only report the top-three cardinal direction percentage with their corresponding mean velocity (also see figure 7.7d). The MSTIDs were propagating dominantly towards the: southeast-south-southwest

121

(36.8 %, 26.0 %, and 33.6 %; ~239 m/s) in spring season, southeast-south-southwest (37.9 %, 25.5 %, and 31.6 %; ~231 m/s) in summer season, southeast-south- southwest (34.8 %, 25.7 %, and 34.9 %; ~226 m/s) in autumn season, and southeast-south-southwest (33.7 %, 28.0 %, and 34.6 %; ~242 m/s) in winter season. Furthermore, figure (7.7 b); reveal the variability of MSTIDs propagation directions at SH. The MSTIDs propagation in SH tends to be more of eastward-southeastward direction. The MSTIDs in SH were propagating dominantly towards the: east-southeast-southwest (19.0 %, 64.6 %, and 7.7 %; ~201 m/s) in spring season, east-southeast-southwest (20.0 %, 64.4 %, and 8.3 %; ~215 m/s) in summer season, east-southeast-southwest (19.4 %, 65.1 %, and 9.0 %; ~218 m/s) in autumn season and east-southeast-southwest (23.2 %, 64.5 %, and 7.8 %; ~214 m/s) in winter season. To avoid the clustering of azimuth, and for a clearer analysis of MSTIDs propagation direction, we plotted the points in fig. (7.7a-b) on a bar-chart which gives discrete cardinal directions (see fig. (7.7c)); North (N), North-East (NE), East (E), South-East (SE), South (S), South-West (SW), West (W), and North-West (NW).
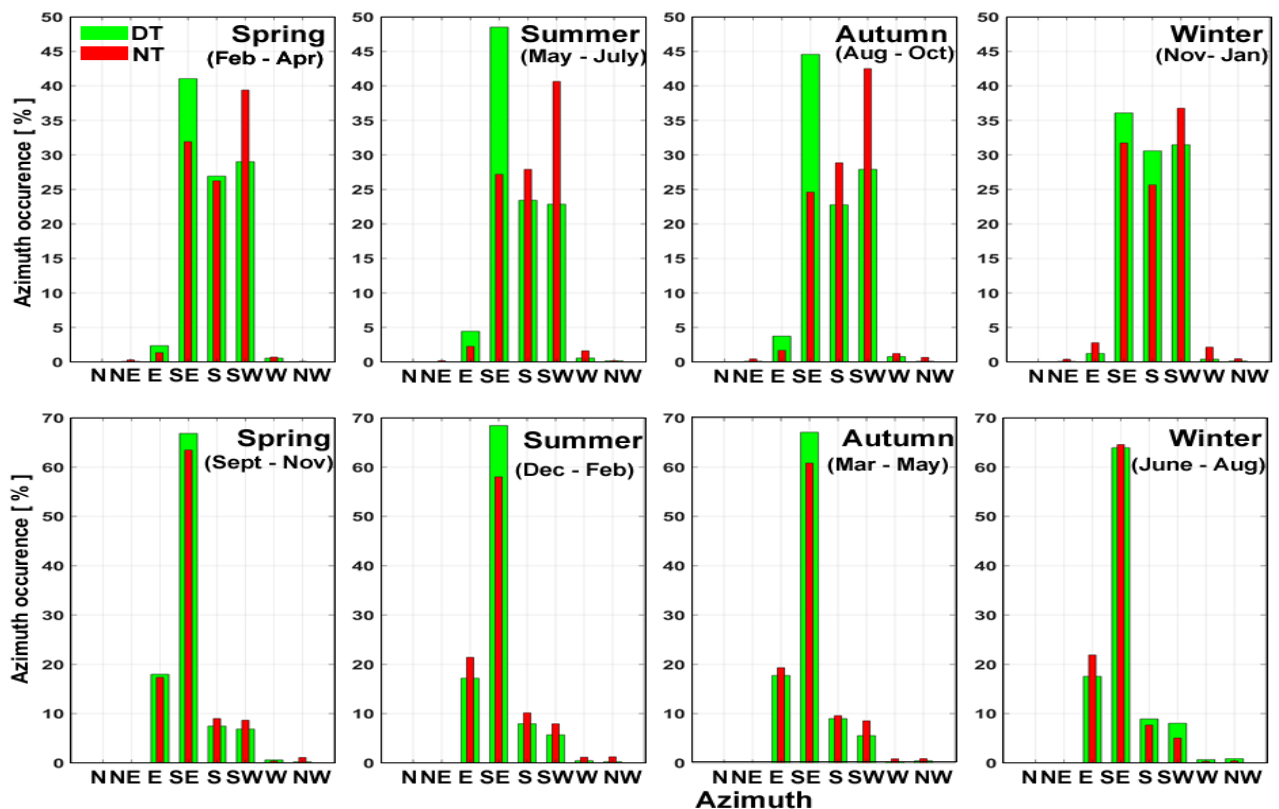
Figure 7.7c: Propagation direction of daytime (green bar) and nighttime (red bar) MSTIDs during different seasons. The upper panel is N1 at northern hemisphere and the bottom panel is N2 at southern hemisphere.

The vertical axis is the azimuth occurrence rate in percentage, while the horizontal axis is the azimuth. The figure shows that MSTIDs propagate in almost all directions but dominant in a southeast direction at daytime and southwest at nighttime in NH. At SH both daytime and nighttime MSTIDs preferably propagate towards east-southeast direction. The daytime MSTIDs exhibited the highest percentage of occurrence during the summer season, while nighttime exhibited its highest during summer and autumn season in NH. At SH, the MSTIDs exhibited a high percentage of occurrences during summer, spring, and autumn season daytime, while nighttime exhibited its high occurrence during spring, autumn, and winter season.

MSTIDs velocity dominance distribution
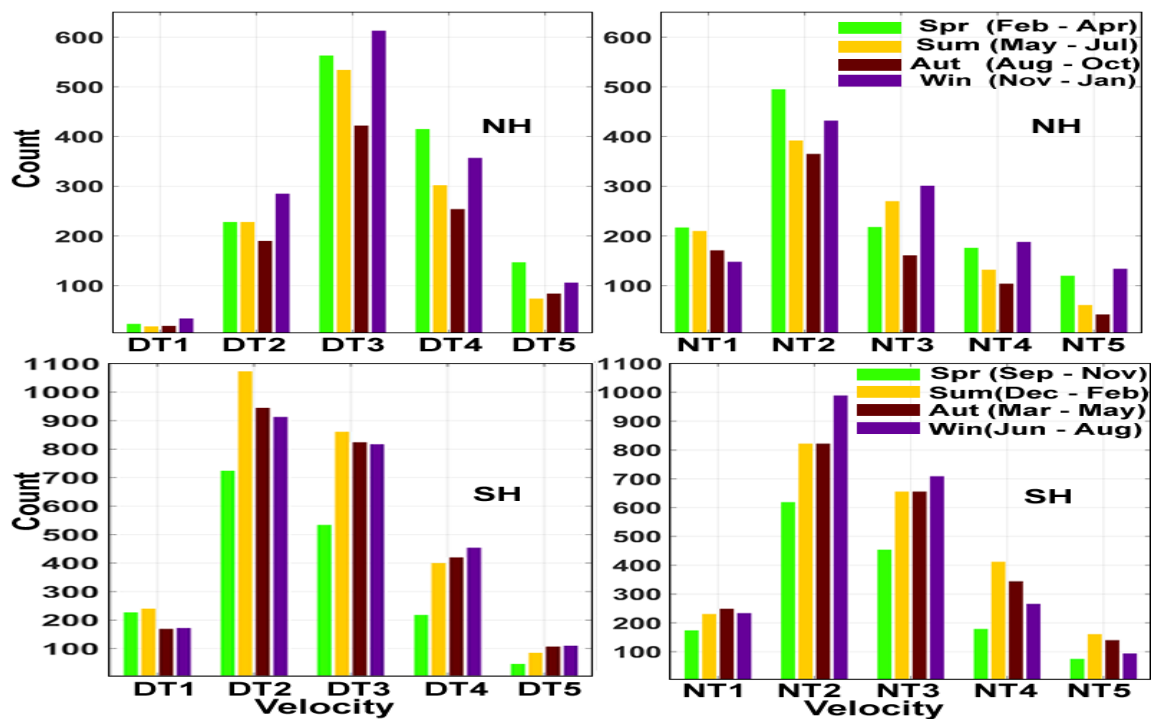
Figure 7.7d: Distribution of the phase velocity of the observed MSTIDs during the daytime (DT) and nighttime (NT) during 2008-2016. The top panel is for the northern hemisphere (NH) and the bottom panel is for southern hemisphere (SH). DT1 and NT1: 20-100 m/s, DT2 and NT2: 100-200 m/s, DT3 and NT3: 200-300 m/s, DT4 and NT4: 300-400 m/s, DT5 and NT5: 400-450 m/s

Figure (7.7d) presents the horizontal phase velocity distribution of the MSTIDs. The figure reveals seasonal variability in velocity, and also most dominant MSTIDs phase velocity is within the range of 200 to 300 m/s and, 100 to 200 m/s during the daytime and nighttime respectively in NH, while the dominant phase velocity at SH is within the range of 100 to 200 m/s for both daytime and nighttime, but the dominance is more pronounced in the daytime than nighttime.

MSTIDs wavelength dominance classification
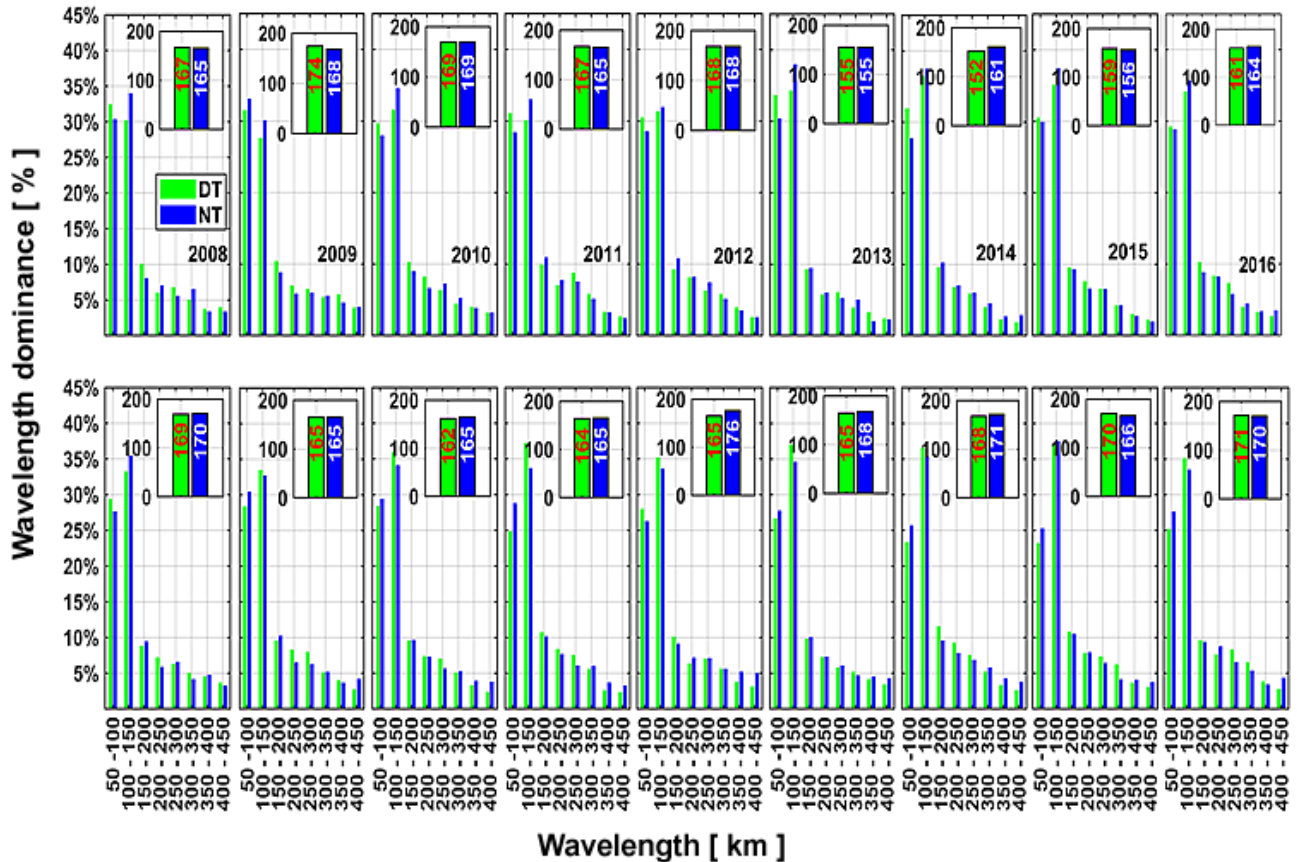
Figure 7.7e: Distribution of the observed wavelength (km) of MSTIDs events at DT and NT during 2008-2016. The upper panel is N1 at NH and the bottom panel is N2 at SH.

Figure (7.7e) displays a bar chart of the horizontal wavelength (WL) observed for MSTIDs. The minimum and maximum values of the MSTIDs wavelength in fig. (7.7e) falls within ~51 km and ~450 km respectively. The figure also indicates a strong dominance of wavelength within 100-150 km (~35 % - 38 %), 50-150 km (~24 % - 30 %), 150-200 km (~10 %), 200-350 km (5 % <WL<10 %), and 400-450 km (1 % <WL<5 %) for both daytime and nighttime. Considering the dominant wavelengths greater than 5% occurrence (i.e. > 5%), see fig. (7.7e)), we then may say that the wavelength in the current study is within 50 - 350 km. The plot of the inset bar chart in fig. (7.7e) is the wavelength average value. The daytime wavelength values at NH are higher than the nighttime values, and vice vasa for SH. The average nighttime wavelength seems higher in SH than NH, while the average daytime wavelength seems higher in NH than SH.

Table 7.1a: The mean value of MSTIDs period and wavelength in N1 at NH

Year	Period (minutes)		Wavelength (kilometre)	
	N1		**N1**	
	Daytime	**Nighttime**	**Daytime**	**Nighttime**
2008	15.00 - 42.50	13.80 – 39.20	77 - 204	77-199
2009	14.50 – 43.70	13.10 – 39.80	77 - 212	76-207
2010	15.20 – 43.50	14.60 – 41.20	76 - 200	78-198
2011	16.00 – 43.60	15.60 – 42.00	81 - 203	80-195
2012	16.70 – 44.40	16.10 – 42.60	80 - 199	81-197
2013	16.00 – 44.20	15.49 – 43.50	81 - 189	80-182
2014	16.20 – 44.10	16.10 – 44.10	82 - 183	81-188
2015	16.20 – 44.40	16.70 – 44.60	81 - 189	79-184
2016	15.90 – 43.90	15.70 – 42.50	79 - 193	80-194

Table 7.1b: The mean value of MSTIDs period and wavelength in N2 at SH

Year	Period (minutes)		Wavelength (kilometre)	
	N2		**N2**	
	Daytime	**Nighttime**	**Daytime**	**Nighttime**
2008	15.37 - 45.33	14.79 – 42.37	78 - 208	80-195
2009	15.69 – 43.87	14.24 – 41.76	80 - 201	79-199
2010	16.11 – 43.84	14.97 – 42.24	81 - 195	78-199
2011	17.19 – 44.28	15.96 – 45.66	81 - 192	80-199
2012	17.24 – 44.80	16.71 – 45.46	81 - 199	80-209
2013	17.16 – 44.76	16.08 – 44.37	82 - 201	81-200
2014	16.93 – 44.08	16.10 – 43.36	82 - 195	81-201
2015	17.14 – 44.62	15.66 – 43.80	82 - 198	81-195
2016	16.36 – 43.94	15.45 - 43.86	81 - 204	79-203

Table (7.1a) and (7.1b) contain the estimated mean periods of N1 and N2 using FFT following (Husin et al., 2011; Arikan et al., 2017) during 2008-2016. Periods estimated with less than 6 minutes were regarded as noise fluctuations and therefore eliminated (Valladares and Hei, (2012)). The period ranged between ~12 and ~58 min, and the mean period is within ~15 and ~45 mins for both N1 and N2 respectively. At both NH and SH, MSTIDs exhibited higher values of the mean period during the daytime than nighttime.

7.5 Regional distribution of MSTIDs on a spatio-temporal map over low latitude

Figure (7.8) shows the regional distribution of MSTIDs on a spatio-temporal map over the low latitude Africa region. The mean value of POR MSTIDs data from different sectors at equatorial

and low latitude were estimated and plotted. The local times (LT) were converted to UT for time uniformity, easy analysis and most importantly to observe the dominant MSTIDs event time of occurrence for each year covering geographic latitudes (GLat) ~20°N to ~20°S and geographic longitude (GLon) ~16°W to ~39°E following (Otsuka et al., 2013).
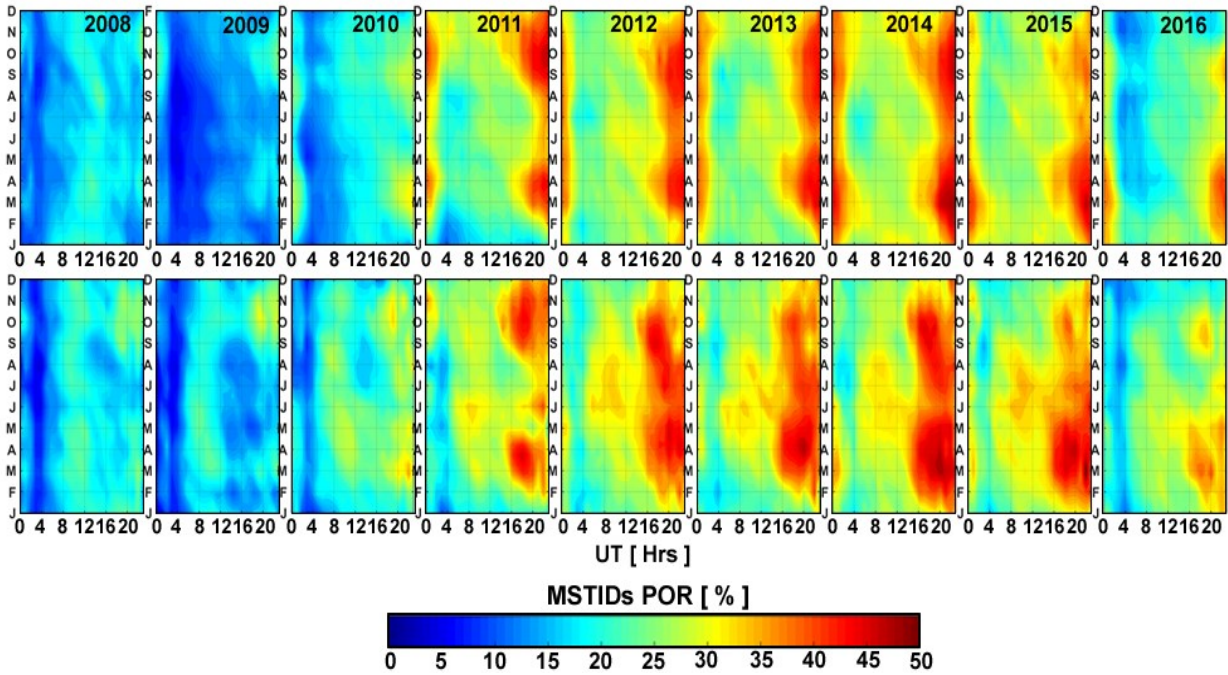
Figure 7.8: Universal time and seasonal variations in MSTIDs POR at equatorial and low latitude during 2008 – 2016. The top panel is for NH, while the bottom panel is for SH

The regional observation of MSTIDs in fig. (7.8) is similar to the local observation of MSTIDs in fig. (7.5a-b) in terms of seasonal dependency, and local time. At NH in fig. (7.8), there are mild occurrences of MSTIDs in the daytime (0800 - ~1300 UT) in summer and autumn season during 2008 - 2016. Furthermore, there is also a mild occurrence of MSTIDs in the nighttime (1800 - 0100 UT) spring, and autumn during 2008-2010 (solar minimum), but strong occurrence in the nighttime (1800 - ~0400 UT) in spring, autumn and summer during 2011-2016, with major peaks in spring and autumn. It is worth noting that the MSTIDs occurrence got extended from spring to summer during the ascending phase and solar maximum years. The density of the occurrence rate depends on the level of solar activity year. In the SH, MSTID occurrence is more pronounced in the daytime (0700 - 1200 UT) autumn and winter season during 2008-2010, 2016, and in the winter during 2011-2015. At nighttime (1900 - 0100 UT) the occurrence is high in autumn and spring during 2008-2010 (solar minimum), and in autumn, winter, and spring during 2011-2015. The distribution of the dominant occurrence of MSTIDs shows a semiannual variation with the

major primary peak in spring and winter during the nighttime (2000 - 0200 UT) in NH. At SH, the major primary peak is in autumn and spring during the nighttime (1900 - 2300 UT) and a secondary peak in winter and partly autumn during the daytime (0800-1200).

7.6   Wavelet analysis of MSTIDs over low latitude

Wavelet analysis transforms or decomposes time series into different frequencies and time components with a high resolution that matches its scale. To further analyze, and have a general view of the localized variations of the magnitude of MSTIDs and their behavior in terms of the period of occurrence, density, frequency, and the trend, which is of great interest in this study, we apply the wavelet transform method. We adopted one of the common classes of wavelet transforms; the Continuous Wavelet Transform (CWT). The CWT provides a higher resolution of periodicity in the time-space. For each hemisphere, we extracted the daily maximum of MSTIDs amplitude at daytime and nighttime, respectively during 2008-2016 and the mean value was computed which is referred to as MSTIDs-Amp (i.e. daily MSTIDs-Amp). We further examine the characterization of these non-stationary MSTIDs-Amp time series by performing wavelet analysis.

7.6.1   Continuous wavelet transform

The wavelet transform decomposes signals in terms of function $\phi_{(y, x)}$ over a dilated (parameter y) and translated (parameter x) function is called mother wavelet. The general expression for the mother wavelet is given as:

$$\Phi_{y,x}(t) = \frac{1}{\sqrt{y}} \Phi\left(\frac{t-x}{y}\right)$$
(7.3)

A CWT of a time series, $M(t)$, in respect of the selected type of mother wavelet ($\phi(t)$) is given as follows:

$$W(y,x) = \int_{-\infty}^{\infty} M(t)\Phi_{y,x}^{*}(t)dt$$
(7.4)

$$W(y,x) = \int_{-\infty}^{\infty} M(t)\frac{1}{\sqrt{y}}\Phi^{*}\left(\frac{t-x}{y}\right)dt$$
(7.5)

where x denotes the shift variable (translation), y denotes wavelet scale (dilation), and its $y > 0$, $(y)^{-1/2}$ is the energy normalization factor, ϕ^{*} is the complex conjugate of $\phi(t)$, which is the analysis wavelet function and $M(t)$ is regarded as the MSTIDs-Amp in this study. Equation (7.5) is the coefficients of the wavelet ($W(y, x)$). The equation is viewed as cross-correlation of a signal

M (*t*), which allows for the determination of a particular frequency (y values) of different "widths" or "scales" of the signal *M* (*t*) at different time positions (x values). In general, wavelet functions are built to strike a balance between the finite-length time domain and the finite-length frequency domain of the time series. However, the most frequently used type of CWT is the Morlet wavelet (i.e. Gaussian function modulated by a sine wave). High frequency precision and correct localized timing position are thus required in choosing a wavelet approach, which is why we choose the Morlet wavelet, and on the contrary, the Mexican hat wavelet approach, by comparison, has a good time position also but not so good frequency range or precision (Cazelles et al. (2008)). So, the Morlet wavelet function makes it possible to calculate the time change of frequency transients in a time series to be determined by splitting the amplitude and phase components (Bloomfield et al., 2004). Hence, the mother wavelet expresses Morlet wavelet as:

$$\Phi(t) = \frac{1}{\sqrt[4]{\pi}} e^{j\omega_o t} e^{-\frac{t^2}{2}} \tag{7.6}$$

where ω_o (frequency) and *t* (time) are both dimensionless. Morlet wavelet with ω_o of six (i.e. $\omega_o = 2/\text{pi}$) is a good choice to be considered for the extraction of a special feature as it provides a good balance between time and frequency localization (Grinsted et al., 2004). Lau et al. (1995), Grinsted et al. (2004), and Cazelles et al. (2008) provide further details about wavelet analysis. Morlet wavelet provides us the useful information about the amplitude in relation to period in terms of the month from locations reflected by the ionosphere, see fig. (7.9). The edge effects at the border of fig. (7.9) are called the cone of influence (COI). The COI (i.e. white translucent area) is the data area where edge effects distort the spectrum and the result in this area is not reliable, hence it is discarded to avoid wrong interpretation of periodic events. The white broken lines in fig. (7.9) means the 95 % confidence interval (CI) or COI boundary, and the thick black contour means the 5 % significance level against the red noise background spectrum. Figure (7.9) illustrates Wavelet transform scalogram for MSTIDs obtained after performing CWT on the structures observed during 2008 – 2016 as obtained from the mean values of daily MSTIDs maximum amplitude at daytime and nighttime (i.e. MSTIDs-Amp).
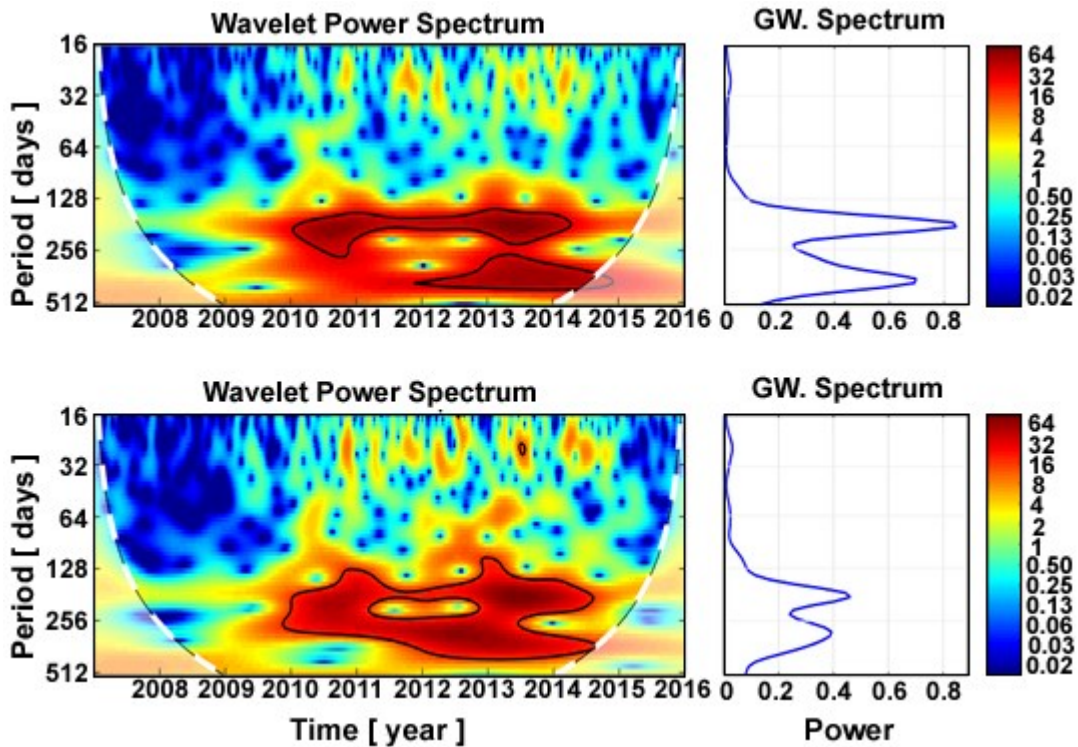
Figure 7.9: Wavelet transform scalogram for MSTIDs-Amp time series at both NH (top panel) and SH (bottom panel) during 2008-2016, each panel showing two major periodic components. The white curve dash line indicates cone of influence. The right-hand plots are the global wave spectrum (GW. Spectrum). The color bar indicates the range of wavelet power in the wavelet power spectrum, with hotter colors matching maximum wavelet power peaks.

The global wavelet spectrum (GW.Spectrum) at the right-hand in fig. (7.9) is the time average of the wavelet coefficients that is normalized, and the period (days), of the observed MSTIDs was obtained by taking the scale values at the GW.Spectrum peaks. The CWT computation was performed using Equation (7.5) as embedded in the MATLAB wavelet toolbox functions. On the right-hand plots (NH-top panel and SH-bottom panel) are the wavelet global spectra, which is an average power of the periodicity in the CWT plot. At both NH and SH, the CWT plot of the MSTID-Amp shows a strong significant periodic component between 128 and ~354 days. The NH exhibited stronger peaks at ~192 and 352 days, while the SH exhibited stronger peaks at ~192 and 320 days. The global wavelet spectrum which is an average power of the periodicity in the CWT shows two major peaks of power component with a period between 128 and ~256, and between 256 and ~352, but exhibited a higher power amplitude component with a period between 128 and ~256 days at both NH and SH, respectively. However, NH exhibited a higher magnitude of power. Both hemispheres show a strong density and statistically significant signal between 2011 - 2014 (framed by a black line).

7.7 Discussion

We have investigated statistically the dTEC variations expressed as MSTIDs using GPS receivers situated across the equatorial and low latitude of the African region in both the NH and SH, respectively. Our statistical results show a distinct variation of the MSTIDs activities. We started by discussing the results from a selected single day (21st September, 2011) study and thereafter multiple days (2008-2016) observation result of the MSTIDs time series, and characteristics are discussed. The discussion compares current result with some selected previous MSTIDs result obtain from other regions (Asia, North America, South America, Europe) around the world. Each paragraph (tied to each figure) highlights and compare MSTIDs observed features from each hemisphere at a time and compare it with other regions of the same hemisphere. The study shows MSTIDs POR variation in terms of local time, season, hemisphere, period, propagation direction, and velocity for both daytime and nighttime, respectively. Regional distribution and wavelet analysis during 2008-2016 results are presented. Our results show a level of consistency with previous studies that have deployed various instruments for MSTIDs measurements in different regions. However, some new findings relating to the African region in terms of seasonal variation, MSTIDs variation, propagation direction amongst others need reporting, and further discussion for regional comparison.

7.7.1 Observed MSTIDs at NH and SH along the Equatorial and low latitude.

The TEC wave-like structure exhibited by PRN 28 (nighttime) and PRN 14 (daytime) in figs. (7.2a), and (7.2b) on 21st September, 2011 is a typical expression of MSTID occurrence. By visual observation, the MSTID event local time (LT), and geographical longitude in both hemispheres reveals that the disturbances seems to be propagating towards the southeast from the NH, while MSTID propagate towards the equator (northward) from the SH. Perturbed temperature has been thought to be a good index to monitor the AGWs passage caused by tropospheric activities, and earlier, Fukushima et al. (2012) reported that majority of MSTIDs event in the equatorial and low latitude regions are related to tropospheric convection as its source. Hence, we may infer that the MSTIDs event in figs. (7.2a) and (7.2b) could be as a consequence of AGWs passage due to convection activities. Stations (see fig. (7.3a) and fig. (7.3b)) with the geomagnetic latitude that are around the EIA crest ±15° exhibited higher nighttime (1800-0300 LT) MSTIDs amplitude, and a higher value of standard deviation, than the daytime. This is in good agreement with the

nighttime TEC perturbation amplitude behavior result obtained by Valladares and Hei, (2012) who investigated TIDs characteristics at a low latitude in Peru. Moreover, the observed high nighttime MSTID amplitudes are due to TEC background condition associated with low latitude instabilities which we refer to as equatorial plasma bubbles (EPBs), more on nighttime MSTIDs causative mechanism is discussed later.

7.7.2 Two-dimensional observation of MSTIDs along the Equatorial and low latitude.

In fig. (7.4b) and fig. (7.4d), the daytime TEC perturbation expressed as MSTIDs are plotted, and are re-presented as MSTIDs 2-D map in fig. (7.4a) and fig. (7.4c), respectively. A careful observation of fig. (7.4b), and fig. (7.4d) shows that the TEC perturbation peaks (P1, P2, and P3) are propagating towards the south (i.e. equatorward) and south-poleward, respectively. Also notice that TEC perturbation amplitude increases as its propagation gets near the equator. Some past literature (Balthazor et al., 1997; Hernandez-Pajares et al., 2012) have shown that daytime MSTIDs propagates northward from the southern hemisphere, on the contrary, a critical observation of the peaks in fig. (7.4d) reveals a south-poleward propagation. By visual assessment, the 2-D map in fig. (7.4 a, c) exhibited a wave-like structure identified to be the daytime MSTIDs with a maximum amplitudes peak value of ~ 0.35 dTECU, and having an average MSTIDs event period between 19.5 mins and 38.70 minutes. The observed daytime MSTIDs in fig. (7.4a-d) is often thought to be caused by the passage of AGWs from meteorological processes, such as convection activities in the troposphere (Hines, 1960). Details of AGWs as a causative mechanism for day MSTIDs is detailed in section 3.1 of chapter 3 in this thesis. Now we discuss below the statistical result of the MSTIDs time series and its features.

7.7.3 Local observation, seasonal characteristics and interannual dependence of MSTIDs over NH and SH of Africa.

Figures (7.5a) and (7.5b) consist of GPS receiver stations located at the NH and SH, respectively, and they show different characteristics between daytime and nighttime MSTIDs occurrence, such as local time, seasonal, and solar activity dependence. These facts indicate that different mechanisms initiate MSTIDs occurrence at the two hemispheres during daytime and nighttime period, and at different seasons. The MSTIDs intensity gets reduced as the latitudes get farther away from the equator, most especially at the night time. At the NH in fig. (7.5a), the highest

occurrence rate of MSTIDs was observed at nighttime during spring (February–April), autumn (August–October), and mild occurrence (~33% POR) at daytime during summer (May–July). Whereas, Hernandez-Pajares et al. (2012) investigated MSTIDs event over North America region, and they reported a high MSTIDs occurrence during the daytime of winter and autumn followed by summer during nighttime at Hawaii (low latitude). Also, Chen et al. (2019) carried out a statistical analysis of MSTIDs during 2014 - 2017 at Hong Kong in Asia region, and they reported a high MSTIDs occurrence rate during the daytime of spring, autumn and winter, with the summer having highest occurrence rate at the nighttime. However, the current result of MSTIDs is similar with the result obtained by Chen et al. (2019) in terms of time of the day, but during different seasons. Comparing these three regions (African, Asian, and North American), we may say that local geophysical background situation peculiar to different region could influence the MSTIDs occurrence time period and its intensity.

At the SH in fig. (7.5b), we observed a high occurrence rate of MSTIDs at nighttime during autumn (March-May), spring (September–November), and also a high occurrence during the daytime in winter (June–August), but nighttime exhibited the highest occurrence rate. Liu et al. (2017) studied MSTIDs over South America (at SH) using Gravity Field and Ocean Circulation Explorer (GOCE) satellite measurements, and they reported a high occurrence of MSTIDs during winter. Likewise, MacDougall et al. (2011) investigated MSTIDs over three towns (Caico, Cariri and Campina Grande) in Brazilian sector during 2010 - 2011. They used a spaced transmitter known as Canadian Advanced Digital Ionosonde (CADI) to measure MSTIDs near the equator in the SH, they reported a high daytime MSTIDs occurrence during the winter. In addition, Figueiredo et al. (2018) reported a high daytime MSTIDs occurrence during the winter over Brazilian region (Brazil region (15.0°S - 30.0°S and 35°W - 55°W) in SH using GPS network for their study, and they could not notice nighttime MSTIDs. On the contrary, within the same Brazilian region, Jonah et al. (2016) reported a high daytime MSTIDs over Brazilian sector (20°S – 30°S and 45° 55°W) during the summer. Furthermore, Takahashi et al., (2018) investigated a simultaneous occurrence of EPBs and MSTIDs over low latitude South American continent during 2014 - 2015 using data from GPS (TEC), ionograms, and 630 nm all-sky airglow images, and they reported MSTIDs occurrence under a strong tropospheric convective activity, with a high occurrence rate during autumn and spring months. Our findings on daytime MSTIDs occurrence during winter months in SH are similar with results from MacDougall et al. (2011), Liu et al. (2017), and Figueiredo et al. (2018), while the nighttime agrees with Takahashi et al., (2018). Also, an interesting feature we cannot ignore is that as the stations are situated far away from the

EIA zone, the less the occurrence rate of the nighttime MSTIDs, and most especially at the SH (WIND and HARB stations). Also, at the WIND and HARB stations, solar terminator effect is well pronounced (indicated with white dash curve lines) which may be traced to be the local source of AWGs passage in those sectors (Figueiredo et al. (2018), which consequently generate the MSTIDs. Both NH and SH MSTIDs increase with increase with solar activity.

The nighttime MSTIDs occurrence has been categorized into two (Otsuka et al. 2013), based their generation processes, and conditions involved at different latitudinal sector. The first category is already discussed in the previous chapter where nighttime MSTIDs are thought to be generated via electrodynamical forces under Perkins instability condition (Otsuka et al. 2013) at the mid-latitude. The second category which indirectly enhances MSTIDs generation at the low latitude is the AGWs propagating in the F-layer bottom height. Earlier, Otsuka, (2018) reported that AGWs could be generated from convection activities around the equatorial regions and propagate upward where some of the generated waves could reach the ionosphere/thermosphere which consequently produce MSTIDs. He reported another possible source of the AGWs generation in the equatorial region to be Intertropical Convergence Zone (ITCZ) where tropospheric convection is active. During these developments of the low latitude ionospheric irregularities, MSTIDs, and equatorial plasma bubbles (EPBs) are generated under the condition of the Rayleigh–Taylor instability (RTI) which is local time, seasonal, longitudinal, and solar activity dependent. However, the linear growth rate of the RTI is low, hence a seeding mechanism such as the generated AGW is needed to increase the growth rate of the RTI (Makela et al., 2012), during this process MSTIDs could be generated which consequentially initiates EPBs (Takahashi et al., 2018). Another way is that, the AGWs could generate polarization electric fields in the E-region, which would map to the bottom side of the ionosphere, and enhance the growth rate, and lastly the AGWs could cause perturbation in the electron density background, by simply providing the initial perturbation in the layer's vertical density profile (Makela et al., 2012). These conditions may be liable at the nighttime (at low latitude) as a causative mechanism for the high amplitudes of TEC perturbations being expressed as MSTIDs.

In fig. (7.6), both NH and SH MSTIDs amplitude increases with solar activities during winter (December – January). Whereas, Martinis et al. (2010) investigated the seasonal dependence of MSTIDs over Arecibo, Puerto Rico (18.3° N, 66.7° W) in North America (at NH) using 630.0 nm air glow imaging during 2002 to 2007. They reported a relatively high MSTIDs amplitude during December - January solstice months. In the same manner, Candido et al. (2008) studied the

statistical analysis MSTIDs occurrence over Brazilian low latitudes (at SH) in South America using OI 630.0 nm emission all sky images during 1990 - 2000. They reported a high amplitude of MSTIDs in June solstice. Both authors reported that MSTIDs amplitude does not increase with solar activity. On the contrary, Fukushima et al. (2012) reported a nighttime MSTIDs event from 2002 to 2009 using a 630-nm airglow imager at Kototabang, Indonesia in Asia region (at SH), they further recorded a decrease in the MSTID occurrence rate with decreasing solar activity. Also, Oinats et al. (2016) studied MSTIDs statistical characteristics using radar datasets over East Asia (Hokkaido-F region at NH) during 2007 to 2014 and the European-Asian sector during the 2013-2014 solar maximum and found that MSTIDs amplitude increases with solar activities. The current result shows that MSTIDs amplitude increases with solar activity, and this is in good agreement with Fukushima et al. (2012) and Oinats et al. (2016). A careful observation of each year shows that the MSTIDs amplitude curve is semi-annual, this could be as a result of the inter-hemispheric coupling during the generation mechanism of MSTIDs. In both NH and SH, 2014 show a high MSTID amplitude and this could be because 2014 is a solar maximum year since we already stated that the amplitude increases with solar activities. Also, MSTIDs displayed a substantial increase in 2011 compared with 2010 and 2012, most notably during the winter in NH and spring in SH, presumably due to an ascending solar phase year. The sudden rise in the winter and spring seasons may be due to the increase in solar activity as demonstrated by an increase in sunspot numbers. The monthly average sunspot values during October, November, and December from the solar minimum (2010), ascending period (2011) and solar maximum (2012) are as follows: 33.6, 34.4, 24.5 during 2010; 125.7, 139.1, 109.3 during 2011; and 76.5, 87.6, 56.8 during 2012, respectively[7.2].

7.7.4 MSTIDs propagation direction and its characteristics

In our observation, we categorized MSTIDs propagation direction into two types based on the level of occurrence dominance. We grouped the azimuth of the MSTIDs propagation direction into daytime (DT), nighttime (NT), and seasons. We focused on the dominance propagation directions in our discussion, and propagation occurrence rate below ~ 5 % is disregarded. In the NH, the MSTIDs propagates majorly towards the southeast, south, and southwest cardinal direction (see fig. (7.7a-top panel)), but most pronounced towards the southeast (100°-168°), (mostly in summer and autumn) and southwest (190°-259°), (mostly in summer, autumn, and spring), during DT and NT, respectively (see fig. (7.7c-top panel)). Some studies have shown a

similar result up to certain level with the current NH result of propagation direction of MSTIDs. For instance, Kotake et al. (2007) reported the results of the statistical study of MSTIDs over Southern California at the North America region in NH using GPS networks during 2002. They reported the azimuth of the MSTID propagation direction during the daytime to be southeastward in equinox and in winter season, respectively, they further stated that the nighttime MSTIDs is southwestward and westward propagation in equinox and summer seasons. In addition, Hernández-Pajares et al. (2012) investigated the propagation of MSTIDs over Hawaii (low latitude), at North America in NH during different solar cycle conditions (2004 - 2011). They reported a dominance propagation of MSTID to be southeastward during the daytime in winter and autumn, while the nighttime propagates southwestward (low latitude) during summer and spring. On the other hand, Otsuka et al. (2013) in their MSTIDs study over European region in the NH during 2008 using more than 800 permanent GPS receivers reported dominance (more than ~ 43%) daytime propagation towards the south, and less than ~ 24% propagated southeastward. Comparing these results with the current study indicates variations in propagation direction. Also, this discussion reveals that propagation direction is always not homogeneous when it comes to daytime and nighttime period, and that background geophysical condition could influence MSTIDs propagation direction. The phase velocity is observed to be faster in the DT (200 – 300 m/s) than NT (100 – 200 m/s); this is in good agreement with Husin et al. (2011) and Hernández-Pajares et al. (2012). The mean velocity for all seasons in NH is about 235 m/s. These velocity values are still within the MSTIDs velocity characteristic in the NH, and hence agree with the previous study (Hernández-Pajares et al., 2012; and Chen et al., 2019). The daytime MSTIDs dominant periods are higher than the nighttime in both NH and SH (see, table (7.1a-b)), which agrees with Hernández-Pajares et al. (2012) report. The mean wavelength values (see, fig. (7.7e-upper panel), table (7.1a)) tends to decrease with increasing solar activity from ~204 km (daytime) and ~199 km (nighttime) in 2008 (solar minimum), to ~183 km (daytime) and ~188 km (nighttime) in 2014 (solar maximum) to ~193 km (daytime) and ~194 km (nighttime) in 2016 (solar descending phase). This kind of wavelength behavior in response to solar activity is similar to the wavelength result obtained by Oinats et al. (2016).

Although MSTIDs over different regions (Oceania, South American) in SH have been reported to be northeast and northwest propagation direction during daytime and nighttime, respectively, (Hernandez-Pajares et al., 2012; Jonah et al., 2016), but the MSTIDs results over SH in the current study is on the contrary. The MSTIDs propagation direction in the current study over SH is distinct from the results previously observed, the MSTIDs propagation direction is observed around the equatorial region (0.60°S - 2.99°S and 30.74°E - 40.19°E, Geomag. Lat: -10.22° to - 12.42°), and it preferentially propagating southeastward (east (~22%), southeast (~68%)) as shown in the polar plot fig. (7.7b) and fig. (7.7c-bottom panel). Both daytime and nighttime are dominantly southeastward, and next to it is the eastward direction. Our results are slightly similar with MacDougall et al. (2011) results, they used CADI to study MSTIDs in the east of Brazil region (6.0°S - 11.5°S and 35.9°E - 49.0°E) near the geomagnetic equator (~10°S) during March 2010 - February 2011. They reported a dominant propagation direction of daytime MSTIDs to be south-southeast during the investigation period. In addition, the azimuth slightly varied during night/evening -morning hours, and the velocity was dominantly in the range of 150 - 300 m/s. Also, Figueiredo et al. (2018) using GNSS data for the study of MSTIDs over the south-southeast of Brazil region (15.0°S - 30.0°S and 35°W - 55°W) during 2012 - 2016. They reported that most daytime MSTIDs preferred propagating towards north-northeast (~55%), and also exhibited the highest occurrence during the winter. They reported MSTIDs propagating towards the: (northeast, and southeast), (southeast), (northwest, northeast, and southeast), (north and northeast) in spring, summer, autumn, and winter respectively. They could not notice major nighttime MSTIDs event, except some few occasional cases, and also reported the velocity within 200 to 500 m/s. Comparison of the SH MSTIDs propagation direction results from these previous studies; MacDougall et al. (2011), Figueiredo et al. (2018), and the current study shows an indication that locations (e.g., Oceania region [geog lat: -50° to -38°]: Hernandez-Pajares et al., 2012, South American regions: [geog lat: -30° to -20°]: Jonah et al., 2016; and [geog lat: -30° to -15°]: Figueiredo et al., 2018) of different MSTIDs source could possibly influence propagation direction. Another possible reason for these different propagation directions may be an effect of wave filtering by background wind in the thermosphere (i.e. wind filtering), Figueiredo et al. (2018b). However, wind filtering influence on MSTIDs directional change still requires further investigation, which can be carried out in future studies. In addition, Liu et al. (2011) reported that the EIA crests are significant in MSTIDs propagation direction as it could inhibit the equatorward propagation direction of MSTIDs. Hence the southeastward (east-southeast) propagation of our SH MSTIDs could be a consequence of any of these reasons stated above. There is variation in season propagation occurrence during the daytime MSTIDs, and also spread into all the seasons

(summer, spring, autumn, and winter), having azimuth (see fig.7.7c - bottom panel) and phase velocity (see fig.7.7d - bottom panel) which are dominant at 100° - 168° (southeast- ~ 68%), and 200 - 300 m/s, respectively. The percentage propagation occurrence during summer and autumn is slightly higher than in other seasons during the daytime. The nighttime MSTIDs also spread into all the seasons, having azimuth and phase velocity; 55° - 100° (east- ~ 23%), and 100 - 200 m/s, respectively. However, the percentage propagation occurrence during spring and winter are slightly higher than in other seasons during nighttime. The velocity values indicate that MSTIDs travel faster during the daytime than the nighttime. The entire dominant values are within 100 - 300 m/s, and the mean velocity value for all seasons is about 212 m/s. In SH, the mean wavelength values (see, fig. (7.7e-buttom panel), table (7.1b)) seems to be different from NH values, as it seems to increase with increasing solar activity from ~208 km (daytime) and ~195 km (nighttime) in 2008, to ~195 km (daytime) and ~201 km (nighttime) in 2014 to ~204 km (daytime) and ~203 km (nighttime) in 2016.

The structure of regional distributions of MSTIDs in fig. (7.8) is similar with the local distribution of MSTIDs in fig (7.5a-b) in terms of seasonal dependency and occurrence time period which has been discussed in section (7.5). Also, the causative mechanism for daytime and nighttime MSTIDs has been thought to be AGWs, and other induced mechanism as discussed earlier in this section. The regional distributions of MSTIDs increases with solar activity in both nighttime and daytime during 2011-2015 in both NH and SH, respectively.

The MSTIDs wavelet analysis in fig (7.9) provides an information on the behavior of MSTIDs amplitude as a function of solar cycle/activity in low latitude during the study period, and most importantly the period of occurrence. The figure shows 2011 and 2014 as the most intense due to solar activity which agrees with Oluwadare et al. (2018). At both NH and SH, the wavelet power spectrum (WPS) exhibited a strong density and statistically significant signal between 2011 - 2014 (framed by a black line) at dominant periods of 128 - 256 days, and at periods of 256 - ~ 320 days during 2013 – 2014, and coinciding with these high densities is the significant power amplitude in the global wave spectrum (GWS) plot.

Chapter 8

SIMULTENEOUS OBSERVATION AND HEMISPHERIC CONJUGACY OF MSTIDs OVER AFRICAN REGION

Most of MSTIDs investigations are often carried out in a single hemisphere, without considering or observing the possibility of any effect on the conjugate hemisphere. The simultaneous occurrence of MSTIDs at different hemispheres within the same region is an indication that the causative mechanism of such event acts in both hemispheres. In this chapter, we report for the first time in the African sector the simultaneous occurrence of MSTIDs in both NH and SH, by using TEC perturbation from GPS receiver data to describe the variability of daytime MSTIDs, the geomagnetic conjugacy of the MSTID structures, and the possible mechanisms responsible for the observed event on a selected day in September, 2011. Hence, our result is a special report of a MSTID case study, and does not necessarily represent the total feature of MSTIDs, which can only be inferred by studying more such cases.

8.1 Simultaneous observation of MSTIDs in NH and SH.

MSTIDs are described as wavelike structure disturbances in the electron density and electric field, traveling in the ionosphere (Jonah et al., 2016). One of the intriguing features of the MSTID is it possibility to occur simultaneously at different hemispheres, and ability to be generated at the conjugate hemispheres by electric field mapping (Valladares et al., 2009, 2016). The daytime MSTIDs occurrences have been generally assumed to be caused by AGWs (discussed in chapter 6), while the nighttime is most often thought to be caused by electrodynamical forces such as Perkins instability (PI) for mid-latitudes investigation (Perkins, 1973; Garcia et al., 2000). The PI growth is slow and not strong enough to initiate plasma instability such as nighttime MSTIDs, but its growth rate could be enhanced through the E- and F-region electrodynamics coupling process, and polarization electric field (Figueiredo et al., 2018), (PI details are written in chapter 6). The low latitude nighttime MSTIDs mechanism is different from the mid-latitude (low latitude nighttime MSTIDs are discussed in chapter 7). At low and equatorial latitude, the ionospheric irregularities are generated under the condition of

RTI, but the RTI growth rate is slow, and hence, a seeding mechanism such as AGWs is needed which increases the growth rate of the instabilities (Makela et al., 2012). In a nutshell, the RTI describes the development of plasma instabilities around or near equatorial latitudes, while the PI describes ionospheric irregularity events at mid–latitudes. In recent times, Valladares et al. (2009) reported a simultaneous occurrence of traveling ionospheric disturbances (TID) at high, mid, and low latitudes in both NH and SH during a disturbed day of 29th - 30th October, 2003 also known as the Halloween storm at the region of North America and Caribbean. The authors reported that TID phase velocity, wavelength, and amplitude differ from hemisphere to hemisphere. They further discussed that the TIDs observed was as a consequence of AGWs passage from both auroral regions towards the geographic equator, and that and TEC perturbation converges more at the geographic equator than the geomagnetic equator. They added that the Joule heating of the neutral gas produced by the neutral-ion velocity may be responsible for the AGWs generation. In the current study, we derived the TEC perturbation (dTEC) from the background TEC wave-like structures following the procedure in section 4.7.3 in chapter 4. Hence, we report dTEC distribution expressed as MSTIDs during a quiet geomagnetic condition (kp ≤ 3) day (a non-storm day 264, 2011) in NH and SH across the African region, see fig. (8.1). The figure shows a general view of MSTIDs occurrence distribution during the daytime and nighttime across the region. The TEC perturbation is generated at two hours intervals, and the signs used to indicate TEC perturbation are colored circles having radii as a function of the dTEC amplitude. The size of the perturbation seems to increase as it propagates closer to the geographic equator. By visual assessment, the nighttime TEC perturbation amplitudes are predominant than the daytime, and most especially those within the EIA region exhibiting strong amplitude ranging between 2.6 - 3.1 dTECU. The MSTIDs characteristics were estimated for both hemispheres. The NH MSTIDs occurrence period and propagation speed are within the ranges of 21.2 mins to 32.2 mins, and 144 m/s to 361 m/s, respectively, while that of SH are within period and propagation speed are within the ranges of 15.0 mins to 30.7 mins, and 134 m/s to 328 m/s, respectively. The MSTIDs characteristics were computed following the procedures in sub-section 4.7.4 in chapter 4. Two stations were selected for the purpose of investigating conjugate MSTIDs, see figs. (8.6-8.7), while all stations were used for simultaneous observation of MSTIDs over NH and SH (see fig. 8.1).
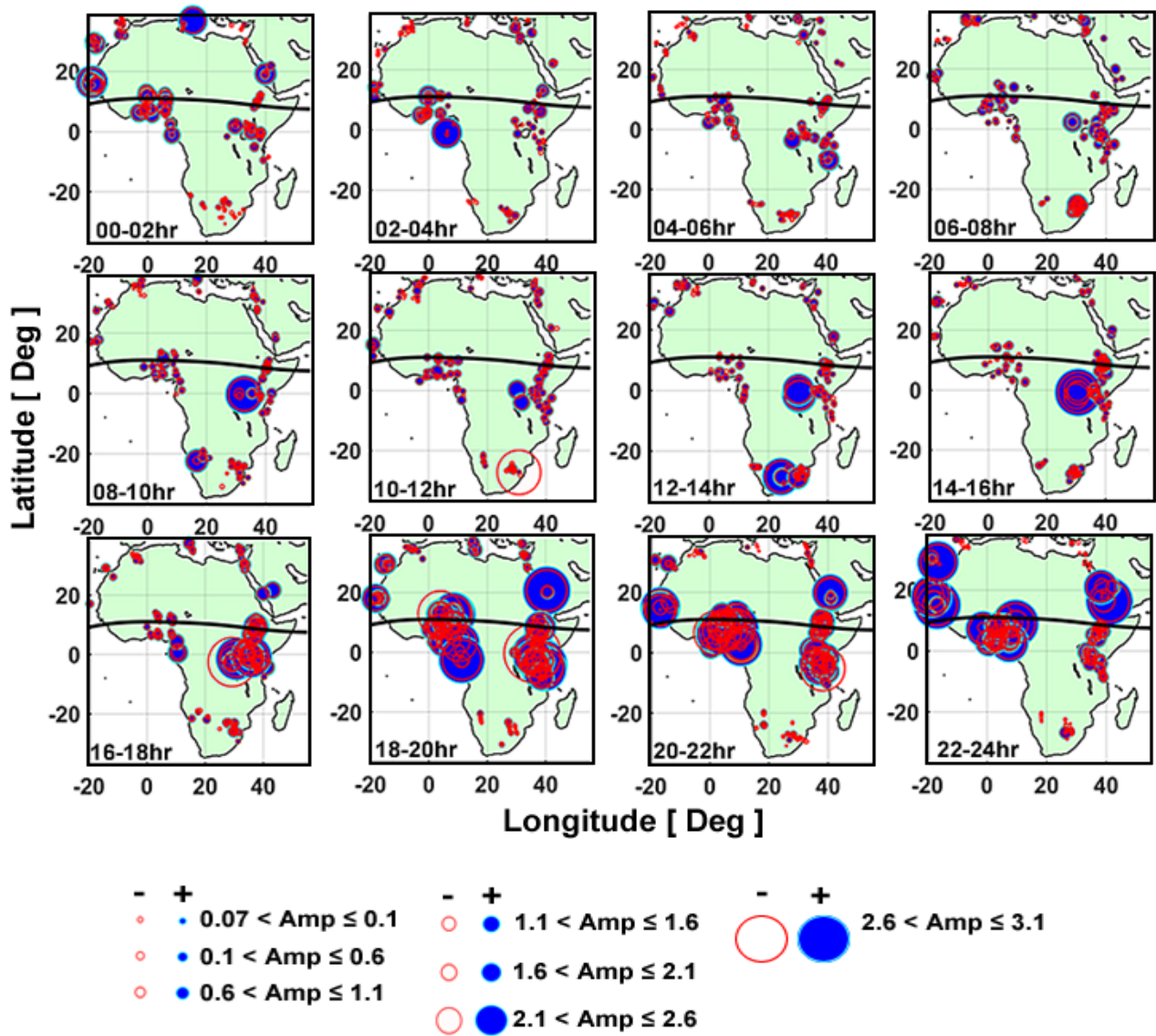
Figure 8.1: TEC perturbation (dTEC) distributions at both northern and southern hemisphere during day 264 of 2011 (21st September, 2011). The blue circles indicate the positive amplitude (Amp), while the red empty circles indicate the negative amplitude. The size of the circles indicates the variability of TEC perturbation which varies between - ~3.1 and ~ 3.1 dTECU.

The dTEC amplitude near 30º E – 42º E longitude during 0800 – 2000 UT seems higher and denser than the perturbation amplitude near 20º W – 15º E during 2000 UT - 0400 UT, this has made us to further investigate if MSTIDs has been mapped from one hemisphere to the other; hence we examined MSTIDs conjugacy. Before investigating conjugate MSTIDs, we further investigated the daytime and nighttime MSTIDs 2-D map (i.e. latitude-time), see figs. (8.5), few stations were selected for this purpose, see figure (8.2). The GPS receiver station coordinates in figs. (8.3a-b) are given in the table (1). The stations are arranged from the NH to the SH in a latitudinal value decreasing order.
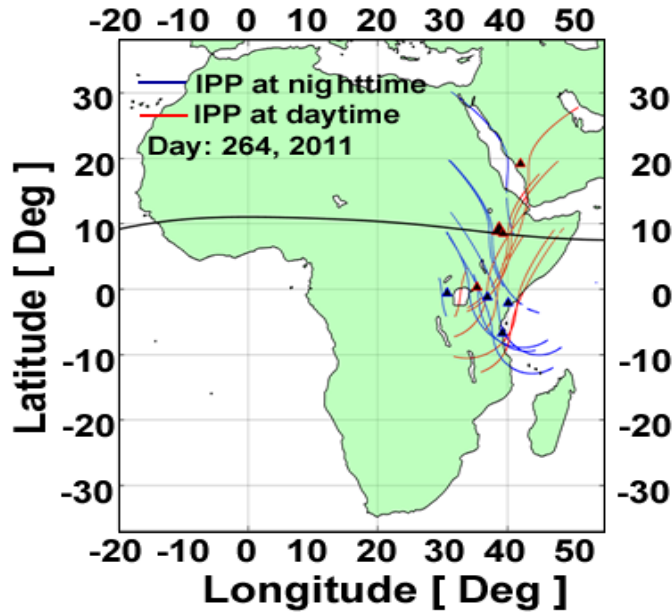
Figure 8.2: The GPS receiver locations are indicated with triangle. Red and blue triangles indicate stations in NH and SH, respectively. The red and blue curves are the IPPs from each station.

Table 8.1. GPS receiver stations showing geographical and geomagnetic coordinate values

Station name	Geographic	Geomagnetic
ADIS	9.04°N, 38.76°E	0.17°N, 110.46°E
NAZR	8.56°N, 39.29°E	0.26°S, 111.00°E
ARMI	6.06°N, 37.56°E	3.03°S, 109.29°E
MOIU	0.28°N, 35.29°E	9.17°S, 107.00°E
MBAR	0.60°S, 30.74°E	8.98°S, 102.38°E
RCMN	1.22°S, 36.89°E	8.11°S, 108.63°E
MAL2	2.99°S, 40.19°E	6.00°S, 111.98°E
TANZ	6.77°S, 39.21°E	2.13°S, 110.96°E

8.2   Two-dimensional observation of MSTIDs at NH and SH on 21st September 2011.

Figures (8.3a) and (8.3b) are the observed TEC perturbation expressed as MSTIDs during daytime and nighttime, respectively. The stations are arranged from the NH to the SH in a latitudinal value decreasing order. The figures exhibit similar TEC perturbation structures, although there is a slight phase shift in the NH and SH perturbation structures which might be

due to local time delay, or a small difference in the geographical location and different geophysical conditions in generating MSTIDs at the different hemispheres.
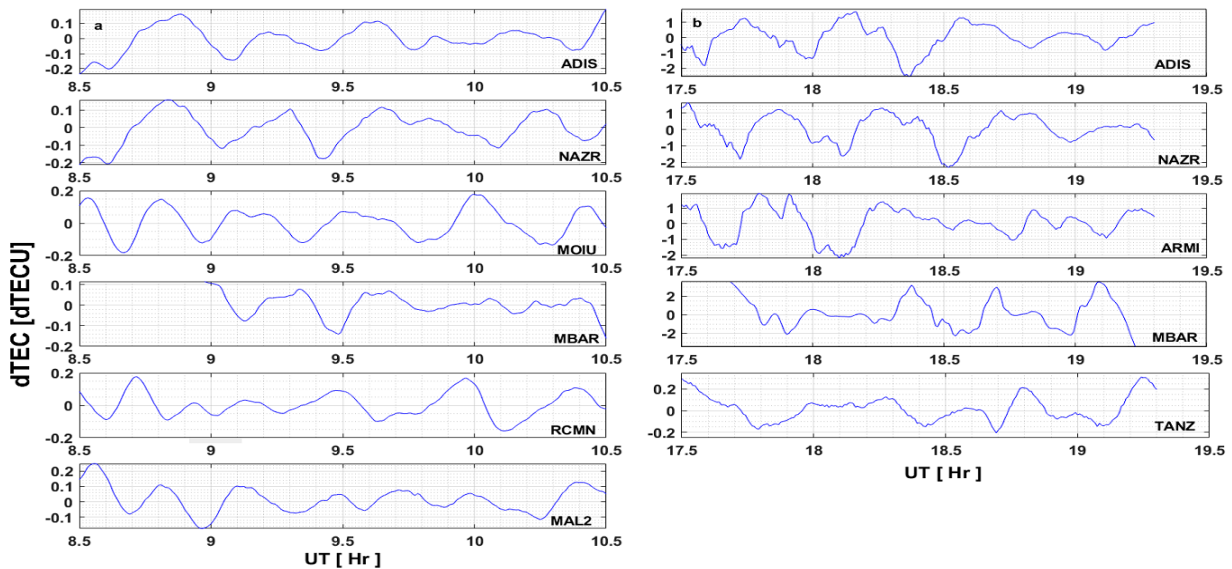
Figure 8.3: (a) TEC perturbation values derived from GPS-TEC (PRN 9) in the NH and SH during daytime in 21st September, 2011. (b) Same as (a), but for nighttime using GPS-TEC (PRN 6). The station name is written on each plot. 1 TECU = 10^{16} el /m^2.

The exhibited MSTIDs in fig. (8.3a-b) has been thought to be caused by vertical propagation of AGWs which could be due to convection activities that occur around the investigated regions. The AGWs passage evidence is exhibited in the temperature profile which shows some perturbation effects that eventually got into the ionosphere (Jonah et al., 2016). One important atmospheric parameter that exhibit the AGWs passage is the cloud top brightness temperature, and a significant phenomenon that could cause this class of perturbed temperature is the convection activities (i.e. convection cloud intensity). In previous studies, Figueiredo et al. (2018) has reported that certain category of brightness temperature (BT) value that is less than 250ºK (i.e. BT < -23.15ºC) corresponds to deep or strong convection activities. Temperature within this threshold is an important atmospheric parameter that exhibits the AGWs passage. Therefore, we infer from this report that the observed MSTIDs during the selected day is possibly generated by AGWs as a consequence of convection activities, see fig. (8.4a-b). It must be noted that getting the exact coordinate point of the temperature profile aligning with the GPS coordinate point is difficult, so we used the closest temperature profile coordinate point to the GPS coordinate point. The geographical coordinates of the temperature profile from SABER satellite in NH and SH are (7.8º N, 23.3ºE) and (4.8ºS, 20.3ºE), respectively. While that of COSMIC satellite in NH and SH are (24.4ºN, 42.1ºE) and (2.8ºS, 21.2ºE), respectively. It is noteworthy to say that the propagation

time of the perturbed temperature profile is earlier than the observation time of the MSTIDs occurrence, this is because we believe it would take up to an hour for the gravity waves to travel from the source to impact the ionosphere. Earlier studies using digisonde by Abdu et al. (2005), reported the evidence of AGWs seeding plasma bubble development at the F layer bottom-side. They further stated that the vertical propagation of AGWs seeding process takes about 1 to 2 hours before the bubble development as observed from the digisonde.
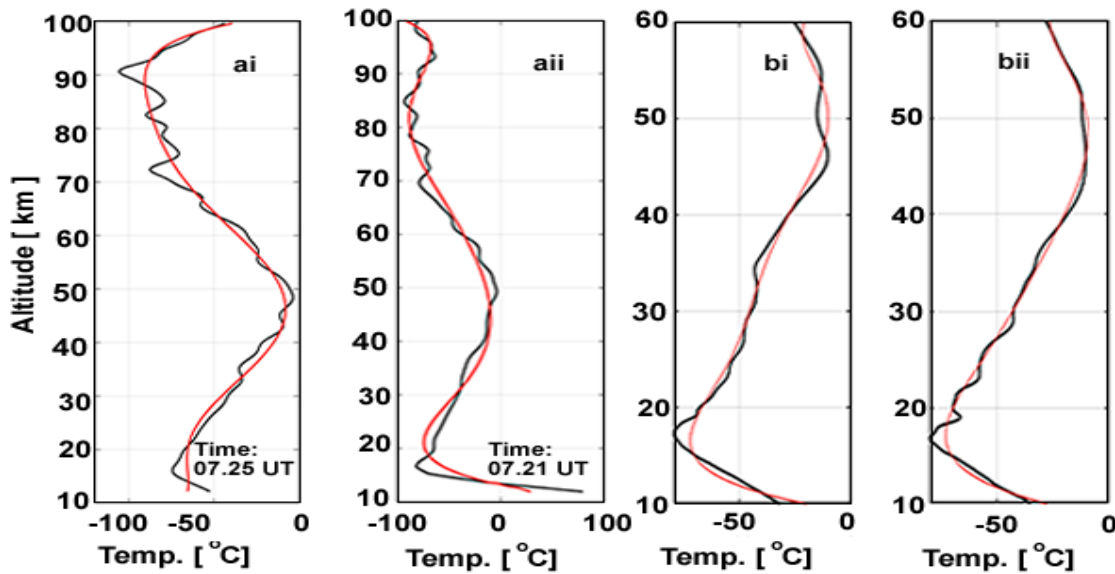
Figure 8.4: Perturbed temperature profile from satellite (black color) and its fit curve line (red color) on 21st September, 2011. Perturbed temperature profiles from SABER satellite during daytime (0800 - 1100 UT) coinciding with/near NH stations of interest is presented in (ai), while that of SH is presented in (aii). Perturbed temperature profiles from COSMIC satellite during the nighttime (1700 - 2000 UT) coinciding with/near NH stations of interest is presented in (bi), while that of SH is presented in (bii).

In the current study, the average dominant period is in the range of 15 mins to 41 mins, at both NH and SH during the daytime, and 12 mins to 33 mins at both NH and SH during nighttime. There is variability in the amplitude from one hemisphere to another during daytime and nighttime. The daytime MSTIDs average azimuth is southeastward (161°) and northeastward (68°) for NH and SH, respectively. Following the criteria for azimuth computation, as stated in chapter 4, PRN 6 exhibiting MSTIDs passage could only be observed in two GPS stations, therefore we could only compute the MSTIDs azimuth during the nighttime in NH. However, the nighttime MSTIDs preferred propagation direction is east-equatorward (165°). The 2-D map of the MSTIDs in figs. (8.3a-b) is presented in figs. (8.5).
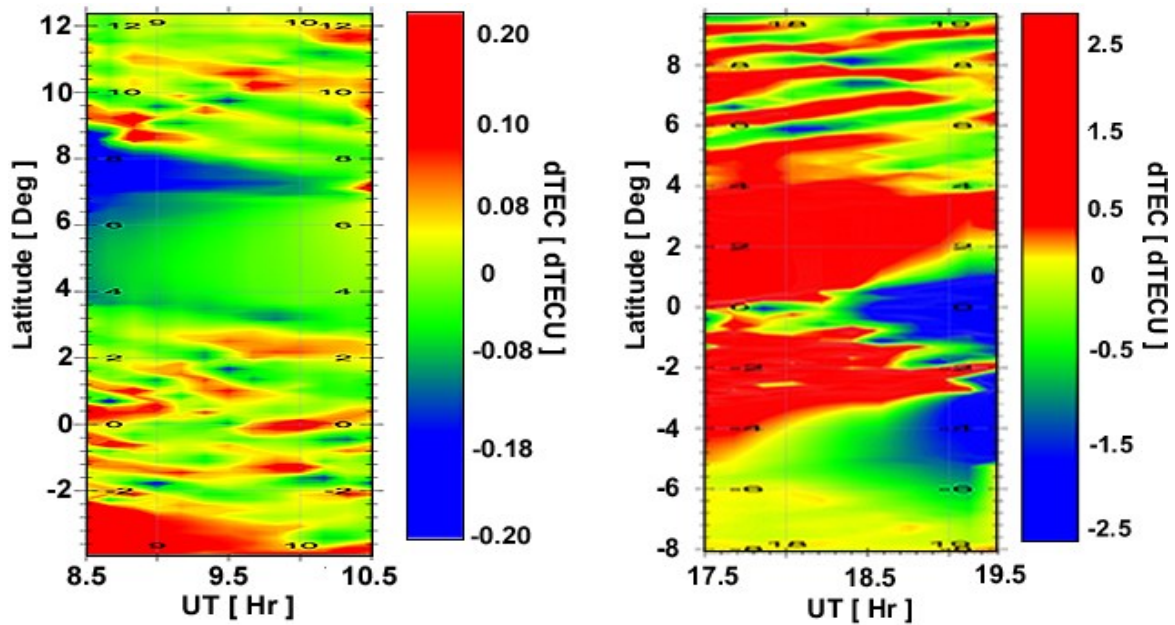
Figure 8.5: Two-dimensional propagation maps of MSTIDs over the NH and SH simultaneously on 21st September, 2011during daytime (left) and nighttime (right).

We observed variability in MSTIDs velocity: ~ 334.3 m/sec and ~ 222.3 m/sec at daytime in NH and SH, respectively, while the nighttime is ~136 m/sec in NH. Figure 8.5 shows that a slightly similar perturbation structures are observed in the different hemispheres at each time period. However, the nighttime MSTIDs exhibit a better defined MSTIDs structure and pattern than the daytime. Maxima peaks shifts towards the equator.

8.3   Observation of conjugate MSTIDs during daytime on 21st September, 2011.

One of the striking features of MSTIDs is its ability to be developed at the conjugate region through the mapping of the electric field being transported along the geomagnetic field lines (**B**) or patters from the source hemisphere to the conjugate hemisphere without any form of depletion, due to high electrical conductivity parallel to the geomagnetic field (**B**). During the transportation process, the F- region plasma is moved upward or downward by E x B drifts which consequently cause plasma density perturbation such as MSTIDs to be mirrored from one conjugate hemisphere to the opposite hemisphere (Otsuka et al., 2004). This breed of generated MSTIDs is classified as electrified MSTIDs, or electro-buoyancy waves as named by Kelley et al. (2000). Burnside et al. (1983) have studied MSTIDs morphology using incoherent scatter radar (ISR), they observed that large electric fields could originate at the opposite hemisphere and map along the magnetic field lines. Both Otsuka et al. (2004) and Shiokawa et al. (2005) in their experiment reported that

electric field aligning to the opposite hemisphere can produce conjugate reminiscence MSTIDs (i.e. mirrored MSTIDs) at opposite hemisphere during the nighttime. The former in their experiment discussed that mirrored MSTIDs at NH and SH, respectively, occurred as a consequence of ionospheric plasma movement in the direction perpendicular to the magnetic field in both hemisphere, these suggest that electric field perhaps might be associated with the development of MSTIDs at the conjugated sectors. Recently, Jonah et al. (2017) investigated conjugate daytime MSTIDs during selected daytime over the Brazilian region in the South American sector using detrended TEC derived from GPS during 2014. They further stated that MSTIDs generated in SH or NH mirrored in conjugate hemispheres, and concluded that electrified MSTIDs / electric field produced at F region could map to conjugate hemisphere. To investigate geomagnetic conjugacy of the MSTID structures of the selected day over African sector, the TEC perturbation structures (PRN 29) from Saudi-Arabia (GPS name: NAMA) were mapped to its magnetic conjugate points along the geomagnetic field lines (B) which coincides with those TEC perturbation structures (PRN 30) in Tanzania (GPS name: TANZ). This is an indication that polarization electric field (**Ep**) is a major driver in the MSTIDs generation. The polarization electric field is mapped along the **B**, and moves the F region plasma upward or downward through E x B drifts. This process causes plasma density perturbation having structures mirrored in the NH and SH. Figure (8.6) shows the TEC perturbation traces from two conjugate stations that simultaneously observed MSTIDs in opposite hemispheres on 21st September, 2011.
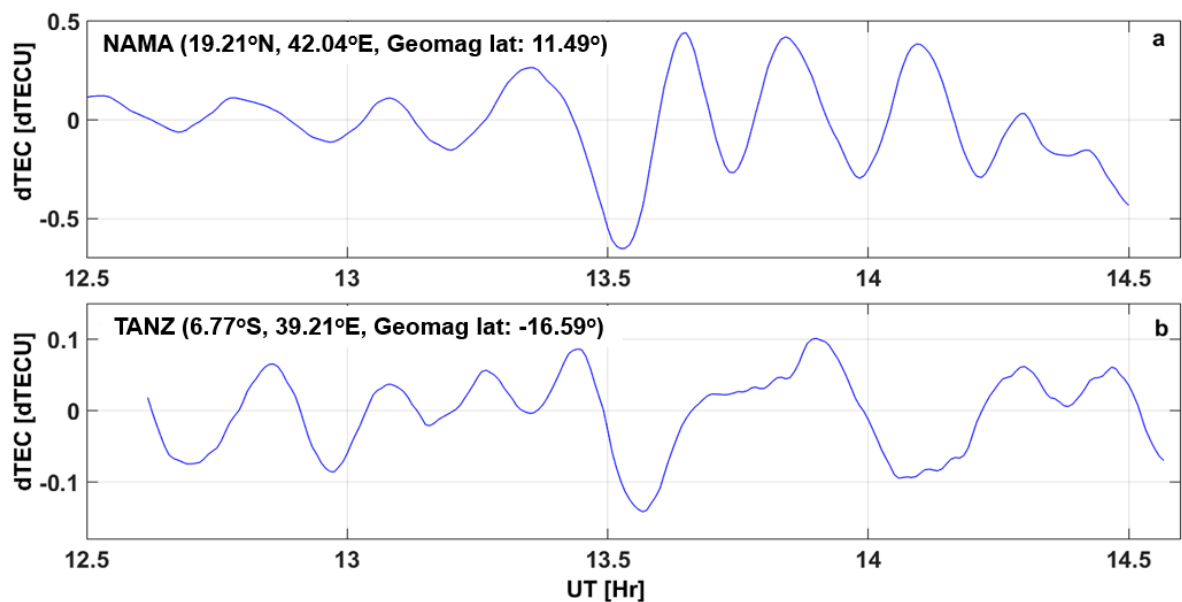
Figure 8.6: TEC perturbation values measured by NAMA GPS receiver station located at (a) Saudi-Arabia, and (b) at conjugate location is TANZ station located in Tanzania.
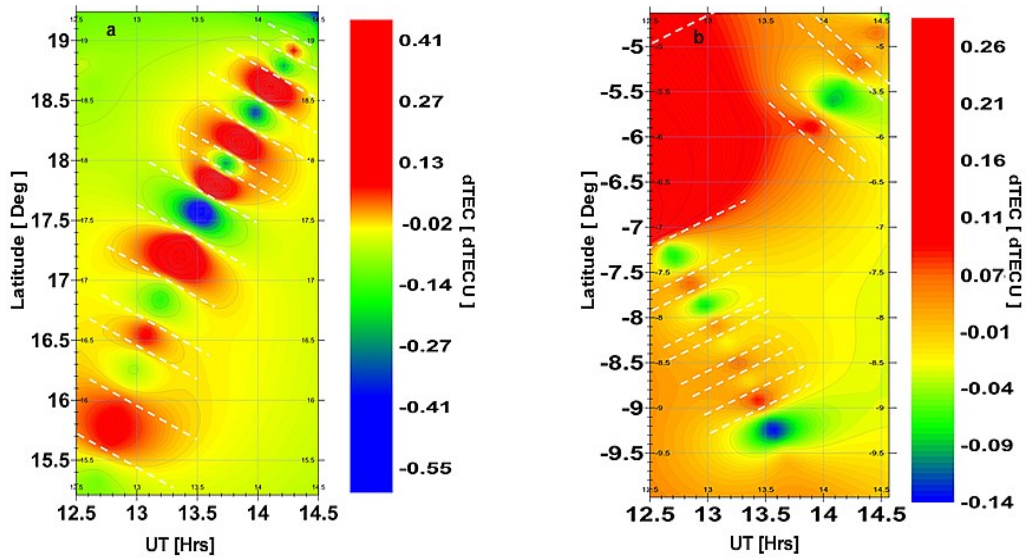
Figure 8.7: Example of MSTIDs conjugate points. (a) MSTIDs structure in NH observed at Namas (Saudi-Arabia) mapped along geomagnetic field lines to SH at Tanzania (Tanzanian)

The white dashed lines in figs. (8.7a-b) is to indicate MSTIDs amplitude peaks as it propagates. Due to the high amplitude observed in fig. (8.7a), we may say that the MSTIDs structure is mapped from NH to SH.

8.4 Discussion

Figure (8.1) shows MSTIDs distributions in both NH and SH. The figure shows certain similar features with the previous studies reported by Valladares et al. (2009) who study reported a simultaneous occurrence of traveling ionospheric disturbances (TID) at high, mid, and low latitudes in both Northern and Southern hemispheres during a disturbing day of 29th – 30th, October 2003 also known as the Halloween storm at the region of North America and the Caribbean. Our result shows a high TEC perturbation amplitude which differs from hemisphere to hemisphere. The TEC perturbations associated with MSTIDs in fig. (8.1) seem to propagate or converge near both the geographical and geomagnetic equator but seem more dominant in the vicinity of the geographical equator. The observed TEC perturbations near the geographic equator show a good agreement with the previous investigation by Valladares et al. (2009). Interestingly, the MSTIDs occurrence near the equatorial and low latitude exhibits high and dense amplitude compared to the mid-latitudes, this possibly could be due to AGWs generated by the Intertropical Convergence Zone (ITCZ) at the equatorial region where tropospheric convection is active (Otsuka, 2018). The increased perturbation amplitude during the post-sunset

146

could be a result of an enhanced vertical E x B drift due to the eastward electric field. This process is known as the pre-reversal enhancement (PRE) which consequently lifts the ionosphere to a high altitude where the growth rate of Rayleigh-Taylor (RT) instability mechanism is larger as a result of ion-neutral collusion, but before the RT mechanism begins, there must be a seeding process that initiates some perturbation processes such as AGWs, and MSTIDs (Taori et al., 2015). The daytime TEC perturbation associated with MSTIDs has been thought to be typically associated with AGWs and nighttime MSTIDs as a result of the electrodynamics process of Perkins instability in the mid-latitude (Perkins, 1973).

Figures (8.3) and (8.5) reveals the observation of MSTIDs events from the line plot and MSTIDs structures from the 2-D plot, respectively. Hence, the MSTIDs is estimated to propagate equatorward, and the propagation velocities are estimated at 334.3m/s and 222.3 m/s in the NH and SH, respectively, during the daytime. While the nighttime is estimated to be 136m/s in the NH. The MSTIDs occurrence in fig. (8.3) is suspected to be caused by AGWs as a result of convection activities, as we observed from the perturbed temperature profiles in fig. (8.4). This observation shows that MSTIDs move faster toward equator than at the NH than the SH. These values are within the range of daytime and night MSTIDs which could be caused by the preferred movement of charge/neutral particles along the geomagnetic field line. Although the nighttime MSTIDs from the NH have been thought to propagate towards the equator-southwest (Otsuka et al., 2013), but the current study nighttime MSTIDs exhibited a preferred movement towards the equator-southeast. This could be as a result of different locations of MSTIDs sources, in addition, we may also possibly say that these propagation direction differences may be as a consequence of wind filtering (Figueiredo et al., 2018b). Another important result of the present study is that both NH and SH daytime MSTIDs preferentially propagate towards the equator/eastward which agrees with the previous study (Hernandez-Pajares et al., 2012; Jonah et al., 2016). The equatorward propagation of MSTIDs estimated (sec. 8.2) and observed (fig. 8.1 and 8.5) in this study is as a result of gravity wave forcing mechanism reported by Otsuka et al. (2013): the gravity waves propagating towards the equator causes a larger neutral gas oscillation in the north-south direction, compared to the gravity waves propagating in other directions. This process leads to a larger ionospheric motion along geomagnetic field lines (**B**) which consequently make the equatorward direction a preferred propagation direction for the MSTIDs. This condition may be liable at the NH and SH, as a causative mechanism for the equatorward propagation of MSTIDs during the selected day.

Simultaneous observation of MSTIDs at NH and SH (Japanese/Australian sector) was carried out for the first time by described in (Shiokawa et al., 2005; Otsuka et al., 2004). They reported the simultaneous occurrence of nighttime MSTIDs as bands were seen at both hemispheres. Ever since that time, several investigations have been made for the study of inter-hemisphere electric field mapping. An electric field could cause plasma instability and it has been also thought to be one of the sources of MSTIDs (Saito et al., 1998a). Studies already establish it that MSTIDs occurrence is generated by AGWs passage in the ionosphere as a result of convection activities, with this known fact, the daytime electric field could be excited by gravity waves in the F-region, and this may likely be responsible for the mapping of MSTIDs at the conjugate hemisphere, this aligns with (Miller et al., 1997). An experiment about the likelihood of gravity wave-induced electric field causing daytime MSTIDs, mapped, and mirrored at the conjugate hemisphere can be found in Jonah et al. (2017). Also, an electric field has been thought to initiate plasma instability, and it is also reported to be one of the sources of MSTIDs (Saito et al., 1998a). The electric field can be transported along the geomagnetic field (**B**) lines from one hemisphere to the other without any decrease, due to high electrical conductivity parallel to the geomagnetic field (**B**). This process makes the ionospheric plasma present in both hemispheres to propagate in directions that are perpendicular to the geomagnetic field, consequently causing MSTIDs to be mirrored from one conjugate hemisphere to the opposite hemisphere (Otsuka et al., 2004). This mechanism is possibly responsible for the mirrored MSTIDs structure observed in fig. (8.7) which shows MSTIDs structure being mirrored from one hemisphere to conjugate hemisphere during the daytime. Although, the mirrored MSTIDs structure/pattern to conjugate hemisphere seems deformed or not exactly (SH) like the source structure (NH) which could be due to different magnitude of magnetic field strength at the hemispheres (Martinis et al., 2011). Despite similar perturbation structures at the conjugate hemispheres, there is still variability in amplitude at the conjugate hemisphere. This might be due to variability in TEC background conditions, in that whenever the TEC background is large, the amplitude of TEC perturbation is also large. Hence, this has in a way shown a correlation between background TEC and MSTIDs (Jonah et al., 2020). Statistical observation of the electric field through satellite observation or other instruments capable of measuring the electric field would still be needed for future investigation to ascertain, and model the possibility of mapping fields as a result of the generation of electrified MSTIDs.

Chapter 9

CONCLUSIONS AND SUGGESTIONS FOR FURTHER RESEARCH

In this thesis, we have been able to statistically study, observe, and report the occurrence of ionospheric irregularities with main focus on MSTIDs. This is the first time MSTID occurrence is being observed and reported over the Africa region. We also report the MSTIDs occurrence of possible sources, characteristics, and mechanisms responsible for the occurrence. This study covers a period of 9 years during the quiet geomagnetic condition (kp ≤ 3) in 2008 – 2016 using observation data from GPS network receivers distributed over African region, and temperature profile data obtained from the COSMIC mission and SABER for selected days. The subsequent sections of the conclusion are organized sequentially based on the order of result obtained starting from characterization of TEC using GPS over the African EIA zone, to the conclusions derived from MSTIDs study over Northern and Southern hemisphere and lastly future study.

9.1 Conclusions

9.1.1 Interannual variation of characterization of the ionospheric TEC.

A long-term time-series study of ionospheric behavior provides a proper understanding of the ionosphere under different atmospheric conditions. Generally, the equatorial and low latitude ionospheric events are considered to be dynamic in nature with characterized complex and dynamic ionospheric structures, most especially within the EIA zone when compared to the mid-latitude ionosphere. Hence, beginning a study on ionospheric behavior on a long-term basis over the equatorial and low latitude provides a good platform for the investigation of both regular and irregular behavior under different geomagnetic conditions and solar cycle activity. We examined the spatial-temporal distributions of ionospheric TEC using GPS under different geomagnetic conditions (Kp ≤ 1, and 1 > Kp ≤ 4) during 2008-2016 for the daytime and nighttime period, respectively. The ionospheric TEC varies with latitude, local time, season, solar cycle, and geomagnetic activity. Studies show a clear correlation between TEC and solar indices (solar flux F10.7 cm, SSN, and EUV irradiance). It is clearly observed that the ionospheric TEC increases with solar activities. Seasonal variability of ionospheric disturbances reveals about 76% and 24% for equinoctial and solstice months, respectively, during 2009-2016. Also, there is an ionospheric

TEC increase in 2011, and 2013–2015, with 2014 having the highest TEC amplitude attributed to solar maximum year. Solar activity dependence of ionospheric TEC within the EIA region reveals that EUV flux exhibited the strongest correlation with TEC better than SSN and solar flux F10.7 cm index, having values of 0.94, 0.85 and 0.86, respectively. There are post-sunset ionospheric TEC disturbances, which have been attributed to the plasma bubble diffusion propagating from the equator along magnetic field lines to low-latitude, and consequently generate ionospheric disturbance. Multiple observations of ionospheric disturbances, which often appear as oscillating waves, are observed. The study of these oscillating waves is suspected to be MSTIDs, and this engineered the beginning of MSTIDs study over the African region in the subsequent section.

9.1.2 Climatology of MSTIDs over Northern Mid-latitude, and Equatorial and low latitude

We present for the first time the MSTIDs occurrence over the NH and SH of the African region during solar cycle #24 (2008-2016) using the GPS network. Quiet days with Kp ≤ 3 were considered in this study. The obtained estimated TEC data in section (9.1) is filtered to select the TEC structure exhibiting wave-like features. We derive the TEC perturbations (dTEC) by subtracting the TEC time series from corresponding best fitted (TEC$_{SSA-fit}$) obtained from non-parametric models such as singular spectrum analysis (SSA) as a band-pass technique to filter out TEC perturbations associated with MSTIDs. We examined the MSTIDs occurrence rate, statistical characteristics for daytime and nighttime, the excitation mechanism, and spatial-temporal distribution.

9.1.3 MSTIDs over Northern Mid-latitude region.

MSTIDs occurrence is a local phenomenon. MSTIDs occurrence rate can be categorized into different groups based on location, and it is more frequent at northwest compared with northeast. The analysis of TEC wave-like structures and perturbed temperature profile of the selected day (7th March 2010), showed that AGWs may be responsible for the MSTIDs occurrence, and note that this single day investigation cannot be used to generalize all situations.

The daytime MSTIDs at NW and NE frequently occur around (~1200 - ~1600 LT) and (~1000 - ~1400 LT) in December solstice, respectively. The nighttime MSTIDs frequently occur around (NW: 2100 - 0200 LT) and (NE: 1900 - 0200 LT) in June solstice, and exhibited a pronounced minor peak in solar maximum year (2014) during March equinox. MSTIDs occurrence rate increase with increase in solar activity.

MSTIDs are more of solstice seasons phenomenon in both nighttime and daytime compared with equinoctial seasons. The solstice diurnal asymmetry was predominant at nighttime (daytime) in June solstice (December solstice) in comparison with equinoctial seasons. MSTIDs propagation velocity is faster during daytime compared to nighttime, except in June solstice where the propagation velocity exhibited a higher magnitude at nighttime than daytime.

The magnitude of the MSTIDs depends on solar activities. MSTIDs maximizes (minimizes) during high (low) solar activity in both nighttime and daytime. MSTIDs generally propagates equatorward (southward) for both daytime and nighttime, but dominantly propagates southwestward at nighttime.

On a regional distribution scale, MSTIDs activity exhibits a primary peak during June solstice and secondary peak during December solstice.

9.1.4 MSTIDs over the Equatorial and low latitude region

Both NH and SH are investigated and result reported. There is a potential relationship between the observed TEC wave-like structures and gravity waves. We deduce that AGW may be responsible for the excitation mechanism responsible for daytime MSTIDs occurrence of the selected days.

MSTIDs were observed majorly in daytime and nighttime, we thus present the mean values of horizontal wavelength, period, and phase velocity of 152 - 174km, 13 -45 min, 150 - 250 m/s for equatorial and low latitude in the NH, and 162 - 176 km, 15 - 44 min, 100 - 205 m/s for equatorial and low latitude in the SH.

There are occurrences of MSTIDs in every month but are dominant in certain months/season than the other. At both NH and SH, all stations (sub-sectors) exhibits different MSTIDs percentage occurrence rate as a function of local time, season, and latitude, respectively. Occurrence rate increases with increasing solar activity. At both hemispheres, occurrence peaks are exhibited at nighttime (2000 - 0200 UT, during spring and winter) and (1900 - 2300 UT, during autumn and spring) in both NH and SH, respectively.

MSTIDs propagation direction is not homogenous. At the NH, the equatorward propagation of MSTIDs prevails. In all seasons, the nighttime MSTIDs dominantly propagate southwestward with autumn having the highest prevalence percentage (43%), while daytime dominantly propagates southeastward with summer having the highest prevalence percentage (48%). At the

SH, both daytime and nighttime MSTIDs predominantly propagate southeastward having the highest prevalence percentage in summer (68%) and winter (65%) respectively, followed by nighttime eastward propagation in winter (~23%).

The regional distribution of MSTIDs exhibits a strong dependence on time period (UT) and season. At NH there are mild occurrences at daytime (0800 - ~1300 UT) in the summer and autumn season during 2008 – 2016, and but strong occurrence at nighttime (1800 - ~0400 UT) in spring, autumn and summer during 2011-2016, with major peaks in spring and autumn. The daytime occurrence rate ranges between 20% -24% during 2008-2010, and 25% - ~32% during 20011-2016, while the nighttime occurrence rate ranges between ~33% - ~50%. At SH, the daytime (0800 - ~1300 UT) MSTIDs occurrence is more pronounced than NH daytime, as it ranges between ~20% - ~30% in autumn and winter season during 2008-2010, 2016, and between ~30% - ~34% in winter during 2011-2015, but there is a strong occurrence at nighttime (1900 - 0100 UT) ranging between ~30% - ~32% in autumn and spring during 2008-2010, while ranges between 33% - ~48% in autumn, winter, and spring, respectively during 2011-2015.

The wavelength (at NH) tends to decrease and SH wavelength tends to increase, with increase in solar activity. The amplitude increases with increasing solar activity. The daytime propagation velocity values are larger than the nighttime which implies that MSTIDs propagate faster at daytime than the nighttime. The relative amplitude increases with an increase in solar activity.

9.1.5 Simultaneous and hemispheric conjugacy of observed MSTIDs

This study is an event-driven investigation. Hence, we studied a single-day event of the simultaneous distribution of MSTIDs in across the African region using TEC perturbations associated with MSTIDs derived from GPS-TEC during 21st September, 2011. Clustered and dense structures of TEC perturbation amplitude within the longitude 30ºE and 42ºE during the selected day initiate further MSTIDs conjugate study. The study reveals that MSTIDs seem to propagate or converge near both the geographical and geomagnetic equator and during the post-sunset. The convergence seems more dominant in the vicinity of the geographical equator with high and dense TEC perturbation amplitude compared to the mid-latitude. The high occurrence rate near the geographical equator has been thought to be associated with tropospheric convection, and the post-sunset high amplitude suggests contributions from the AGWs.

Considering the structure of the perturbed temperature profile due to AGWs passage in the vicinity of the stations under investigation, we may infer that the possible source of the MSTIDs is through convection activities. The daytime MSTIDs propagation direction was south-east and north-east in the NH and SH, respectively, while the preferred nighttime MSTIDs propagation direction was equator/eastward in the NH. Mirrored electrified MSTIDs during daytime are observed at the conjugate hemisphere for the first time over the African sector for a selected day. However, the mirrored MSTIDs at the SH does not reflect the exact structure at the SH, probably due to different magnitude of magnetic field strength at the hemispheres.

9.2 Further research

In this thesis, it has been presented that TEC exhibiting a wave-like structure is a possible occurrence of MSTIDs as a result of the AGWs passage. The results of selected days show that AGWs passage is possibly the cause of the development of MSTIDs activities. MSTIDs time series have been reported, which gives us a view of its occurrence time, characteristics, and causative mechanism. However, there are still several subject matter that needs more understanding, and most importantly a better approach to MSTIDs analysis. Hence, more investigation of MSTIDs is still needed.

For instance, in this thesis, we have defined MSTIDs as one of the major and frequent ionospheric irregularity phenomena that can degrade GNSS positioning accuracy. We have also presented a singular spectrum analysis (SSA) algorithm as a non-parametric method for the detection of ionospheric TEC perturbations (i.e. dTEC) and its characteristics. The SSA method was also used to extract dTEC associated with the MSTIDs. Hence, it would be interesting estimate the MSTIDs impact on precise positioning applications of GNSS, and to develop a model that can significantly improve the accuracy of GNSS real-time positioning.

Furthermore, it would be interesting to develop a model that considers the physics of ionospheric disturbances to forecast TIDs occurrence, detect ionospheric phenomena causing local disturbances of electron density, and generate geomagnetic storm indices.

This thesis only includes days with a quiet geomagnetic condition, which by implication do not include space weather activities. Compilation of event-driven study should be carried out on TID response to space weather activities using GNSS (GPS-TEC data), and Swarm satellite mission ionospheric products.

A more investigation on convention activity is required by using a space-based or/and ground-based instrument for the measurement of the vertical column profiles of temperature and humidity, and most importantly, a proper understanding of the thermodynamic conditions that must be into play to initiate convection activities needs to be studied. Also, a multi-instrument observation of AGWs/MSTIDs requires more study, as well as more study of its causative mechanism.

Finally, to study the ionospheric responses associated with geo-hazards and/or climate hazards such as earthquakes, tsunamis, cyclones should be considered. The proposed study would be to investigate ionospheric disturbance as a consequence of pre or post hazard (climate/geo-hazard), and hence establish a connection between the natural hazards, the ionospheric disturbances, and the coupling process.

REFERENCE

Abdu M A (2005) Equatorial ionosphere thermosphere system: electrodynamics and irregularities. Adv. Space Res. 35 (5), 771–787.

Abdullah M, Zain A F M, Ho Y H, Abdullah S (2009) TEC and Scintillation study of equatorial Ionosphere: A month campaign over Sipitang and Parit Raja Stations. Am. J. Eng. Appl. Sci. Malaysia 2, 44–49.

Abe O E, Otero Villamide X, Paparini C, Radicella S M, Nava B, Rodríguez-Bouza M (2017) Performance evaluation of GNSS-TEC estimation techniques at the grid point in middle and low latitudes during different geomagnetic conditions, J Geod (2017) 91:409–417 DOI 10.1007/s00190-016-0972-z.

Ackah J B, Obrou O K, Zaka Z, Mene M N, Groves K (2011) Study of Equatorial Ionospheric Scintillation and TEC characteristics at Solar minimum using GPS-SCINDA data. Sun and Geosphere: The International Journal of Research and Applications. 6(1): 27 – 30.

Adebiyi S J, Adimula I A, Oladipo O A (2016) Characterisation of GPS-TEC in the African equatorial and low latitude region and the regional evaluation of the IRI model. J. Atmos. Sol. Terr. Phys. 143–144.

Adeniyi J O, Bilitza D, Radicella S M, Willoughby A A (2003) Equatorial F2-peak parameters in the IRI model. Adv. Space Res. 31, 507–512. https://doi.org/10.1016/S0273-1177(03)00039-5.

Adewale A O, Oyeyemi E O, Adeloye A B, Ngwira C M, Athieno R (2011) Responses of equatorial F region to different geomagnetic storms observed by GPS in the African sector. J. Geophys. Res. 116, A12319.

Adewale A O, Oyeyemi E O, Cilliers P J, McKinnell L A, Adeloye A B (2012) Low solar activity variability and IRI 2007 predictability of equatorial Africa GPS TEC. Adv. Space Res. 49, 316–326.

Afraimovich E L, Boitman O N, Zhovty E I, Kalikhman A D, Pirog T.G (1999) Dynamics and anisotropy of travelling ionospheric distances as deduced from transionspheric sounding data. Radio Sci., 34, 477-487.

Afraimovich E L, Palamartchouk K S, Perevalova N P (1998) GPS radio interfereometry of travelling ionospheric disturbances. J. Atmos. Sol. Terr. Phys., 60, 1205– 1223.

Afraimovich EL, Perevalova NP, Zhivetiev IV (2008) Relative amplitude of the total electron content variations depending on geomagnetic activity. Adv Space Res 42:1231–1237.

Aggarwal M (2011) TEC variability near northern EIA crest and comparison with IRI model. Adv. Space Res. 48, 1221–1231.

Akala A O, Seemala G K, Doherty P H, Valladares C E, Carrano C S, Espinoza J, Oluyo S (2013) Comparison of equatorial GPS-TEC observations over an African station and an American station during the minimum and ascending phases of solar cycle 24. Ann. Geophys. 31, 2085–2096.

Akala A O, Doherty P H, Carrano C S, Valladares C E, Groves K M (2012) Impacts of ionospheric scintillations on GPS receivers intended for equatorial aviation applications, Radio Sci., 47, RS4007, doi:10.1029/2012RS004995, 2012.

Akala A O, Doherty P H, Valladares C E, Carrano C, Sheehan R (2011) Statistics of GPS scintillations over South America at three levels of solar activity, Radio Sci., 46, RS5018, doi:10.1029/2011RS004678.

Akala A O, Oyeyemi E O, Somoye E O, Adeloye A B, Adewale A O (2010a) Variability of foF2 in the African equatorial ionosphere, Adv. Space Res., 45, 1311–1314.

Akala A O, Adeloye A B, Somoye E O, (2010b) Ionospheric foF2 variability over the Southeast Asian sector. J. Geophys. Res. 115, A09329. https://doi.org/10.1029/2010JA015250.

Alizadeh M, Wijaya D, Hobiger T, Weber R Schuh H (2013) Ionospheric effects on microwave signals. In J. Boehm and H. Schuh, eds., Atmospheric Effects in Space Geodesy, Springer Verlag, ISBN:978-3-642-36931-5.

Alizadeh Mohamad Mahdi (2013) Multi-Dimensional modeling of the ionospheric parameters, using space geodetic techniques. Ph.D. thesis, Vienna University of Technology, Austria.

Anderson D N, Roble R G (1981) Neutral wind effects on the equatorial F-region ionosphere. J. Atmos. Sol. Terr. Phys. 43, 835–843. https://doi.org/10.1016/0021-9169(81)90061-1

Arikan F, Yarici, A (2017). Spectral investigation of traveling ionospheric disturbances: IONOLAB-FFT. Geodesy and Geodynamics. 8 (2017), 297-304. http://dx.doi.org/10.1016/j.geog.2017.05.002.

Arora B S, and Fifty-nine others (2015) Ionospheric modelling using GPS to calibrate the MWA. 1: Comparison of first order ionospheric effects between GPS models and MWA observations. Publications of the Astronomical Society of Australia (PASA) Astronomical Society of Australia 2015; published by Cambridge University Press. https://doi.org/10.1017/pasa.2015.29

Azeem I, Barlage M (2017) Atmosphere-ionosphere coupling from convectively generated gravity waves, Advances in Space Research. Pages 1931-1941, doi.org/10.1016/j.asr.2017.09.029.

Bagiya M S, Joshi H P, Iyer K N, Aggarwal M, Ravindran S, Pathan B M (2009) TEC variations during low solar activity period (2005–2007) near the Equatorial Ionospheric Anomaly Crest region in India. Ann. Geophys. 27, 1047–1057.

Bailey G J, Su Y Z, Oyama K I (2000) Yearly variations in the low latitude topside ionosphere. Ann. Geophys. 18, 789–798.

Balan N, Bailey G J (1992) Latitudinal variation of nighttime enhancements in TEC: solar and magnetic activity effects. Adv. Sci. Res. 12 (6) (6)219 – (6)222.

Balan N, Bailey G J (1995) Equatorial plasma fountain and its effects: possibility of an additional layer. J. Geophys. Res. 100, 21421–21432.

Balan N, Liu L, Le H (2018) A brief review of equatorial ionization anomaly and ionospheric irregularities. Earth and Planetary Physics, 2(4), 1–19. doi:10.26464/epp2018025.

Balan N, Otsuka Y (1998) Equinoctial asymmetries in the ionosphere and thermosphere observed by the MU radar. J. Geophys. Res. 103 (A5), 9481–9495.

Balthazor R L, Moffet R J (1997) A study of atmospheric gravity waves and travelling ionospheric disturbances at equatorial latitudes. Ann. Geophysicae 15, 1048-1056.

Behnke R (1979) F layer height bands in the nocturnal ionosphere over Arecibo. J. Geophys. Res., 84, 974–978, doi:10.1029/JA084iA03p00974.

Bhuyan P K, Borah R R (2007) TEC derived from GPS network in India and comparison with the IRI. Adv. Space Res. 39 (5), 830–840.

Bloomfield D S, McAteer R T J, Lites B W, Judge P G, Mathioudakis M, Keenan F P (2004) Wavelet phase coherence analysis: application to a Quiet-Sun magnetic element, The Astrophysical Journal, 617, 623–632.

Bolaji O S, Adeniyi, J O, Radicella S M, Doherty P H (2012) Variability of total electron content over an equatorial West African station during low solar activity. Radio Sci. (USA) 47. doi.org/ 10.1029/2011RS004812, 2012.

Bowman G G (1992) Upper-atmosphere neutral-particle density variations compared with spread-F occurrence rates at locations around the world, Ann. Geophys., 10, 676–682.

Brunner F, Gu M (1991) An improved model for the dual frequency ionospheric correction of GPS observations. Manuscripta geodaetica, Springer-Verlag, 205-214.

Budden K. (1985). The propagation of radio waves. Cambridge Univ. Press.

Burnside R G, Walker J C G, Behnke R A, Gonzales C A (1983), Polarization electric fields in the nighttime F layer at Arecibo, J. Geophys. Res., 88, 6259– 6266, doi:10.1029/JA088iA08p06259.

Campbell W H (1997) Introduction to geomagnetic fields‖, Cambridge University Press, Cambridge, UK.

Candido C M N, Pimenta A A, Bittencourt J A, Beckerguedes F (2008) Statistical analysis of the occurrence of medium-scale traveling ionospheric disturbances over Brazilian low latitudes using OI 630.0 nm emission all-sky images. Geophysical Research Letter, v. 35, n. L17105.

Cazelles B, Chavez M, Berteaux D, Ménard F, Vik J O, Jenouvrier S, Stenseth N C (2008) Wavelet analysis of ecological time series. Oecologia 2008, 156, 287–304.

Chakraborty, S.K., Hajra, R., 2007. Solar control of ambient ionization of the ionosphere near the crest of the equatorial anomaly in the Indian zone. Bull. Astron. Soc. India 35, 599–605.

Chandra K R, Srinivas V S, Sarma A D (2009) Investigation of ionospheric gradients for GAGAN application. Earth Planet Sp, 61, 633–635. https://doi.org/10.1186/BF03352939

Chapman S, Ferraro V R (1933) A new theory of magnetic storms, Terrestrial Magnetism and Atmospheric Electricity, Vol. 38, pp. 79–96. https://doi.org/10.1029/TE038i002p00079.

Chauhan V, Singh O P, Singh B (2011) Diurnal and seasonal variation of GPS-TEC during a low solar activity period as observed at a low latitude station Agra. Indian J. Radio Space Phys. 40 (1), 26–36.

Chen Guanyi, Chen Zhou, Yi Liu, Jiaqi Zhao, Qiong Tang, Xiang Wang, Zhengyu Zhao (2019) A statistical analysis of medium-scale traveling ionospheric disturbances during 2014–2017 using the Hong Kong CORS network. , Earth, Planets and Space. doi.org/10.1186/s40623-019-1031-9

Christopher T Rusell, Janet G Luhmann, Robart J Strangeway (2016) Introduction to Space physics. Cambridge University press.

Ciraolo L, Azpilicueta F, Brunini C, Meza A, Radicella S M (2006) Calibration errors on experimental slant total electron content (TEC) determined with GPS, J Geodesy (2007) 81:111–120, DOI 10.1007/s00190-006-0093-1.

Clark R M, Yeh K C, Liu C H (1971) Interaction of internal gravity waves with the ionospheric F2-layer. Journal of Atmospheric and Terrestrial physics 33, 1567–1576.

Cosgrove R B (2004) Coupling of the Perkins instability and the sporadic E layer instability derived from physical arguments. J. Geophys. Res., 109. doi:10.1029/2003JA010295.

de Abreu A J, Roberto M, Alves M A, Abalde J R, Nogueira P A B, Venkatesh K, Fagundes P R, de Jesus R, Gende M, Martin I M (2019) Effects of X2-class solar flare events on ionospheric GPS-TEC and radio waves over Brazilian sector. Adv. Space Res., 63(11), 3586-3605 DOI: 10.1016/j.asr.2019.02.020.

D'ujanga F M, Mubiru J, Twinamasiko B F, Basalirwa C, Ssenyonga T J (2012) Total electron content variations in equatorial anomaly region. Adv. Space Res. 50 (4), 441–449.

D'ujanga F M, Opio P, Twinomugisha F (2016). Variation of the total electron content with solar activity during the ascending phase of solar cycle 24 observed at Makerere University, Kampala. In: Fuller Rowell, T., Yizengaw, E., Doherty, P.H., Basu, S. (Eds.), Ionospheric Space Weather: Longitude and Hemispheric Dependences and Lower Atmosphere Forcing. John Wiley & Sons, Inc., Hoboken, NJ, USA. http://doi.org/10.1002/9781118929216.ch12.

Dach R, Hugentobler U, Fridez P, Meindl M (2007). Bernese GPS Software, Version 5.0. Astronomical Institute, University of Bern.

Davies K, Jones J E (1971) Three-dimensional observations of traveling ionospheric disturbances, J. Atmos. Terr. Phys., 33, 39-46.

Dieminger W, Hartmann G R, Leitinger R (Eds.) (1996) The Upper Atmosphere, Data Analysis and Interpretation. New York: Springer Verlag.

Ding F, Wan W, Ning B, Wang M (2007) Large-scale traveling ionospheric disturbances observed by GPS total electron content during the magnetic storm of 29–30 October 2003. J Geophys Res, doi:10.1029/2006ja012013.

Ding F, Weixing W, Guirong X, Tao Y, Guanlin Y, and Jing-Song W (2011) Climatogy of medium-scale traveling ionospheric disturbances observed by a GPS network in central China, J Geophys Res. doi: 10.1029/2011JA016545.

Ding F, Yuan H, Wan W, Reid I M, Woithe J M (2004) Occurrence characteristics of medium-scale gravity waves observed in OH and OI nightglow over Adelaide (34.5°S, 138.5°E). J Geophys Res. doi.org/10.1029/2003JD004096.

Duly T M, Chapagain N P, Makela J J (2013) Climatology of nighttime medium-scale traveling ionospheric disturbances (MSTIDs) in the Central Pacific and South American sectors. Ann Geophys 31:2229–2237, https://doi.org/10.5194/ angeo-31-2229-2013.

Essex, E.A., 1977. Equinoctial variations in the total electron content of the ionosphere at Northern and Southern Hemisphere stations. J. Atmos. Terr. Phys. 39, 645–650.

Evans J V, Holt J M, Wand R H (1983) A differential-Doppler study of traveling ionospheric disturbances from Millstone Hill, Radio Sci., 18, 435–451.

Fayose R S, Rabiu B, Oladosu O, Groves K (2012) Variation of total electron content and their effect on GNSS over Akure, Nigeria. Appl. Phys. Res. 4 (2). https://doi.org/10.5539/apr.v4n2p105.

Fedorenko Y P, Tyrnov O F, Fedorenko V N (2010) Parameters of Traveling Ionospheric Disturbances Estimated from Satellite Beacon Observations in Low Earth Orbit. doi.org/10.1134/S0016793210040109.

Fejer, B.G., 2011. Low latitude ionospheric electrodynamics. Space Sci. Rev. 158, 145–166, https://doi.org/10.1007/s11214-010-9690-7.

Fejer B G, Jensen J W, Su S Y (2008) Quiet time equatorial F region vertical plasma drift model derived from ROCSAT-1 observations. J. Geophys. Res. 113, A05304, https://doi.org/10.1029/2007JA012801.

Feltens J, Angling M, Jakowski N, Mayer C, Hoque M, Hernandez- ´Pajares, Garc´ıa-Rigo M, Orus-Perez R, Aragon-Angel A (2009) Analysis of the state-of-the-art ionosphere modelling and observation techniques. Tech. Rep. OPS-SYS-TN-0017-OPS-GN, Iss. 1/0, ESA/ESOC.

Figueiredo C, Takahashi H, Wrasse C M, Otsuka Y, Shiokawa K, Barros D (2018) Medium-scale traveling ionospheric disturbances observed by detrended total electron content maps over Brazil. J Geophys Res Space Phys 123:2215–2227. doi.org/10.1002/2017JA025021.

Figueiredo, C A O B, Takahashi H, Wrasse C M, Otsuka Y, Shiokawa K, Barros D (2018b) Investigation of nighttime MSTIDS observed by optical thermosphere imagers at low latitudes: Morphology, propagation direction, and wind filtering. Journal of Geophysical Research: Space Physics,123, 7843857.https://doi.org/10.1029/2018JA025438

Frissell N A, Baker J, Ruohoniemi J M, Gerrard A J, Miller E S, Marini J P, West M L, Bristow W A (2014) Climatology of medium-scale traveling ionospheric disturbances observed by the midlatitude blackstone superdarn radar. J. Geophys. Res. Space Phys. 119 (9), 7679–7697, URL: https://agupubs.onlinelibrary.wiley.com/doi/abs/10.1002/2014JA019870.

Fukushima D, Shiokawa K, Otsuka Y, Ogawa T (2012) Observation of equatorial nighttime medium-Scale TID in 630nm airglow images over 7 years. J Geophys Res 117: A10324. https://doi.org/10.1029/2012JA017758.

Fuller-Rowell T J (1998) ''The Thermospheric spoon": a mechanism for the semiannual density variation. J. Geophy. Res. 103, 3951–3956.

Gao Y, Liu ZZ (2002) Precise Ionosphere Modeling Using Regional GPS Network Data, Journal of Global Positioning Systems, 18-24.

Hamzah S Z M, Homam M J (2015) The correlation between total electron content variations and solar activity, Asian research publishing network (ARPN). ARPN J. Eng. Appl. Sci. 10 (20).

Garcia F J, Kelly M C, Makela J J, Huang C S (2000) Airglow observations of mesoscale low-velocity traveling ionospheric distur-bances at midlatitudes, J. Geophys. Res., 105, 18, 407-18, 415, doi:10.1029/1999JA000305.

Georges T M (1968) HF Doppler studies of traveling ionospheric disturbances, J. Atmos. Terr. Phys., 30, 735-746.

Golyandina N, Nekrutkin V, Zhigljavsky A A (2001) Analysis of time series structure: SSA and related techniques. Chapman and Hall, New York.

Grant W B, Pierce R B, Oltmans S J and Browell E V (1998) Seasonal evolution of total and gravity waves-induced laminae in ozonesonde data in the tropics and subtropics. Geophys. Res. Lett. 25, 1863-6.

Grinsted A, Moore J C, Jevrejeva S (2004) Application of the cross wavelet transform and wavelet coherence to geophysical time series, Nonlin. Processes Geophys., 11, 561–566, https://doi.org/10.5194/npg-11-561-2004.

Grocott A, Hosokawa K, Ishida T, Lester M, Milan S E, Freeman M P, Sato N, Yukimatu A S (2013) Characteristics of medium-scale traveling ionospheric disturbances observed near the Antarctic Peninsula by HF radar, J. Geophys. Res. Space Physics. doi:10.1002/jgra.50515.

Guanyi C, Chen Z, Yi L, Jiaqi Z, Qiong T, Xiang W, Zhengyu Z (2019) A statistical analysis of medium-scale traveling ionospheric disturbances during 2014–2017 using the Hong Kong CORS network. doi.org/10.1186/s40623-019-1031-9, Earth, Planets and Space.

Habarulema J B, Katamzi Z T, McKinnell L A (2013a) Estimating the propagation characteristics of large-scale traveling ionospheric disturbances using ground-based and satellite data. J. Geophys. Res. 118, 7768–7782.

Hargreaves J K (1992) The Solar-Terrestrial Environment. New York: Cambridge Univ. Press, Atmospheric and Space Science Series

Hargreaves J (1995) The Solar-Terrestrial Environment - An Introduction to Geospace - The Science of the Terrestrial Upper Atmosphere, Ionosphere, And Magnetosphere. Cambridge University Press.

Hartmann G K, Leitinger R (1984) Range errors due to ionospheric and tropospheric effects for signal frequencies above 100 MHz. Bull. G´eod., 58, 109-399.

Heisler L H (1958) Anomalies in ionosondes records due to travelling ionospheric disturbances, Austr. J. Phys. 11, 79,

Hernández-Pajares M, Juan J M, Sanz J (2006a) Medium-scale traveling ionospheric disturbances affecting GPS measurements: Spatial and temporal analysis, J. Geophys. Res., 111, A07S11, doi: 10.1029/ 2005JA011474.

Hernández-Pajares M, Juan J M, Sanz J, Aragón-Àngel A (2012) Propagation of medium scale traveling ionospheric disturbances at different latitudes and solar cycle conditions, Radio Sci., 47, RS0K05, doi:10.1029/2011RS004951.

Hines C O (1960) Internal atmospheric gravity waves at ionospheric heights. Canadian Journal of Physics, pp.1441–1481.

Hines C O, Reddy C A (1967) On the propagation of atmospheric gravity waves through regions of wind shear, Journal of Geophysical Research, Vol 72, No-3.

Ho C M, Manucci A J, Sparks L, Pi X, Lindqwister U L, Wilson B D, Iijima B A, Reyes M J (1998a) Ionospheric total electron content perturbations monitored by the GPS global network during two Northern Hemisphere winter storms, J. Geophys. Res., 103, 26409–26420.

Hocke K, Schlegel K A (1996) Review of atmospheric gravity waves and travelling ionospheric disturbance: 1982-1995. Max-Planck –Institute fur Aeronomie, Germany, Ann. Geophysicae

Hofmann-Wellenhof B, Lichtenegger H, Collins J (1993). GPS Theory and Practice. Springer, Wien New York, 2nd edn.

Hofmann-Wellenhof B, Lichtenegger H, Collins J (2001) Global Positioning System: Theory and Practice, ch. 6, pp. 97,98,102. Springer, 5th revised ed.

Holton J R (1992) An introduction to dynamic meteorology. 3.ed. Academic Press,v. 48. 551p. International Geophysics Series.

Hooke W H (1968) Ionospheric irregularities produced by internal atmo-spheric gravity waves. J. Atmos. Terr. Phys., 30, 795 – 823.

Horvath and Essex (2000) Using observations from the GPS and TOPEX satellites to investigate night-time TEC enhancement at mid-latitudes in the southern hemisphere during a low sunspot number period, Journal of Atmospheric and solar Terissterial-Physics, Vol. 62, No. 5, pp. 371-391.

Huang C S, Miller C A, and Kelley M C (1994) Basic properties and gravity wave initiation of the mid-latitude F region instability. Radio Science, 29, 395–405, doi:10.1029/93RS01669.

Huang Y N, Cheng K (1996) Solar cycle variation of equatorial ionospheric anomaly in total electron content in the Asian region. J.Geophys. Res. 101, 24513–24520.

Hunsucker R D (1982) Atmospheric gravity waves generated in the high latitude ionosphere: A review, Rev. Geophys. Space Phys., 20, 293–315. doi:10.1029/RG020i002p00293.

Hunsucker R D, Hargreaves J K (2003) The high-latitude ionosphere and its effects on radio propagation. Cambridge University Press.

Husin A, Abdullah M, Momani M A (2011) Observation of medium-scale traveling ionospheric disturbances over Peninsular Malaysia based on IPP trajectories. Radio Sci., 46, RS2018. doi:10.1029/2010RS004408.

Ikubanni and Adeniyi (2012) Dependence of F2 Layer Critical Frequency on F10.7 Solar Flux. World Journal of Engineering and Pure and Applied Science, ISSN 2249-0582.

Jacobson A R, Carlos R C, Massey R S, Wu G (1995) Observations of traveling ionospheric disturbances with a satellite-beacon radio interferometer: Seasonal and local time behavior. J. Geophys. Res, 100, 1653–1665.

Jayawardena Pinto T S, Chartier A T, Spencer P, Mitchell C N (2016). Imaging the topside ionosphere and plasmas-phere with ionospheric tomography using COSMIC GPS TEC.Journal of Geophysical Research: Space Physics,121, 817–831.https://doi.org/10.1002/2015JA021561

Jin SG, Luo OF, Park P (2008) GPS observations of the ionospheric F2-layer behavior during the 20th November 2003 geomagnetic storm over South Korea. J Geod 82(12):883–892. doi:10.1007/s00190-008-0217-x.

Jonah O F, Zhang S, Coster A J, Goncharenko L P, Erickson P J, Rideout W, de Paula E R, de Jesus R (2020) Understanding Inter-Hemispheric Traveling Ionospheric Disturbances and Their Mechanisms. Remote Sens. 12, 228.

Jonah O F, Coster A, Zhang S, Goncharenko L, Erickson P J, de Paula E R, Kherani E A (2018) TID observations and source analysis during the 2017 Memorial Day weekend geomagnetic storm over North America. Journal of Geophysical Research: Space Physics, 123, 8749–8765. https://doi.org/10.1029/2018JA025367

Jonah O F, Kherani E A, De Paula E R (2017) Investigations of conjugate MSTIDS over the Brazilian sector during daytime, J. Geophys. Res. Space Physics, 122, 9576–9587, doi:10.1002/2017JA024365.

Jonah O F, Kherani E A, De-Paula E R (2016) Observation of TEC perturbation associated with medium scale traveling ionospheric disturbance and possible seeding mechanism of atmospheric gravity wave at a Brazilian sector. J. Geophys. Res. Space Physics, 121, 2531-2546, doi:10.1002/ 2015JA022273.

Jonah Olusegun Folarin (2017) A Study of Daytime MSTIDs over Equatorial and Low Latitude Regions During Tropospheric Convection: Observations and Simulations. Ph.D. thesis, Instituto Nacional de Pesquisas Espaciais – INPE.

Kagan L M, Bakhmet'eva N V, Belikovich V V, Tolmacheva A V, Kelley M C (2002) Structure and dynamics of sporadic layers of ionization in the atmospheric E region, Radio Sci., 37(6), 1106, doi:10.1029/2001RS002534, 2002.

Karia S P, Pathak K N (2011) GPS based TEC measurements for a period of Agust 2008-December 2009 near the northern crest of Indian equatorial ionospheric anomaly region, J Earth Syst Sci (2011) 120: 851. doi:10.1007/s12040-011-0114-1, 2011.

Kelley M C, Fukao S (1991) Turbulent upwelling of the mid-latitude ionosphere: 2. Theoretical framework. J. Geophys. Res., 96, 3747–3753.

Kelley M C, Miller C A (1997) Electrodynamics of midlatitude spread F, 3. Electrohydrodynamic waves? A new look at the role of electric fields in thermospheric wave dynamics, J. Geophys. Res., 102, 11,539–11,547.

Kelley M, Makela J, Saito A, Aponte N, Sulzer M,Gonzalez S (2000). On the electrical structure of airglow depletion/height layer bands over Arecibo. Geophys. Res. Lett. 27 (18), 2837–2840.

Kelley M C (1989) The Earth's Ionosphere; Plasma Physics and Electrodynamics. International Geophysics Series vol. 43.

Kelley M C (2009) The Earth's Ionosphere; Plasma Physics and Electrodynamics. International Geophysics Series vol. 96.

Kherani A, De-Paula E, Olusegun J (2013) Observations and simulations of equinoctial asymmetry during low and high solar activities. Presentation at a Proceeding of the Thirteenth International Congress of the Brazilian Geophysical Society, Rio de Janeiro, Brazil, August 26–29.

Kherani E Alam, Mangalathayil Ali Abdu, Dave C Fritts, Eurico R de Paula (2011) The Acoustic Gravity Wave Induced Disturbances in the Equatorial Ionosphere, Aeronomy of the Earth's Atmosphere and Ionosphere, IAGA Special Sopron Book Series 2, DOI 10.1007/978-94-007-0326-1_10.

Kherani, A., De-Paula, E., Olusegun, J., 2013. Observations and simulations of equinoctial asymmetry during low and high solar activities. In: Presentation at a Proceeding of the Thirteenth International Congress of the Brazilian Geophysical Society, Rio de Janeiro, Brazil, August 26–29.

Kherani A, De-Paula E, Olusegun J (2013) Observations and simulations of equinoctial asymmetry during low and high solar activities. In: Presentation at a Proceeding of the Thirteenth International Congress of the Brazilian Geophysical Society, Rio de Janeiro, Brazil, August 26–29.

Kil H, Oh S -J, Paxton L J, Fang T W (2009) High-resolution vertical E X B drift model derived from ROCSAT-1 data. J. Geophys. Res. 114, A10314. https://doi.org/10.1029/2009JA014324.

Kil H, Paxton L J, Oh S -J (2009a) Global bubble distribution seen from ROCSAT-1 and its association with the evening pre-reversal enhancement. J. Geophys. Res. 114, A06307. https://doi.org/10.1029/2008JA013672.

Klobuchar J A, Anderson D N, Doherty P H (1991) Model studies of the latitudinal extent of the equatorial anomaly during equinoctial conditions, Radio Sci., 26, 1025–1047.

Klobuchar J A (1986) Design and characteristics of the GPS ionospheric time-delay algorithm for singlefrequency users. Procdings of the IEEE Position Location and Navigation Symposium, Las Vegas, November 4-7.

Klobuchar J A (1996) Ionospheric effects on GPS. In: Parkinson, B.W, Spilker, J.J. (Eds.), Global Positioning System: Theory and Application, vol. 1. American Institute of Aeronautics and Astronautics Inc.

Klobuchar J A, Anderson D N, Doherty P H (1991) Model studies of the latitudinal extent of the equatorial anomaly during equinoctial conditions. Radio Sci. 26, 1025–1047.

Koekkoek H S (1997) Excitation mechanisms of medium scale travelling ionospheric disturbances Eindhoven: Technische Universiteit Eindhoven DOI: 10.6100/IR491978.

Kotake N, Otsuka Y, Ogawa T, Tsugawa T, Saito A (2007) Statistical study of medium-scale traveling ionospheric disturbances observed with the GPS networks in Southern California. Earth Planets and Space 59:95–102. https://doi.org/10.1186/BF03352681.

Kotake, N, Otsuka Y, Tsugawa T, Ogawa T, Saito A (2006) Climatological study of GPS total electron content variations caused by medium-scale traveling ionospheric disturbances. Journal of Geophysical Research, v.111, n. A04306, doi: 10.1029/2005JA011418.

Kumar, Sanjay, Singh A K, Lee Jiyun (2013) Equatorial Ionospheric Anomaly (EIA) and comparison with IRI model during descending phase of solar activity (2005–2009). Adv. Space Res. 53, 724–733.

Langley R B (1993) "The GPS observables", GPS world, 4(4), 52-59.

Langley R, Fedrizzi M, Paula E, Santos M, Komjathy A (2002) Mapping the low latitude ionosphere with GPS. GPS World 13 (2), 41–46.

Lau K M, Wenig H (1995) Climate signal detection using wavelet transform: How to make a time series sing. Bull. Am. Meteorol. Soc., 76, 2391–2402.

Lee C C, Reinisch B W (2012) Variations in equatorial F2-layer parameters and comparison with IRI-2007 during a deep solar minimum. Journal Atmos. Sol. Terr. J. Atmos. Sol. Terr. Phys. 74, 217–223. https://doi.org/10.1016/j.jastp.2011.11.002.

Lee C C, Reinisch B W, Su S Y, Chen W S (2008) Quiet-time variations of F2-layer parameters at Jicamarca and comparison with IRI-2001 during solar minimum. J. Atmos. Sol. Terr. Phys. 70, 184 – 192. https://doi.org/10.1016/j.jastp.2007.10.008.

Liu Libo, Wan Weixing, Chen Yiding, Le Huijun (2011) Solar activity effects of the ionosphere: A brief review. Chinese. Sci. Bull. 56 (12), 1202–1211. https://doi.org/10.1007/s11434-010-4226-9.

Liu H, Pedatella N, Hocke K (2017). Medium-scale gravity wave activity in the bottom-side F region in tropical regions. Geophysical Research Letters, 44, 7099–7105. https://doi.org/10.1002/2017GL073855.

Liu L, Wan W, Yue X, Zhao B, Ning B, Zhang M L (2007) The dependence of plasma density in the topside ionosphere on solar activity level. Ann. Geophys 25 (6), 1337–1343.

MacDougall J, G Li, Jayachandran P T (2009a) Traveling ionospheric disturbances near London, Canada, J. Atmos. Sol. Terr. Phys., 71, 2077–2084, doi: 10.1016/j.jastp.2009.09.016.

MacDougall J, Abdu M, Batista I, Buriti R, Medeiros A, Jayachandran P, Borba G (2011) Spaced transmitter measurements of medium scale traveling ionospheric disturbances near the equator. Geophysical Research Letters, 38, L16806. https://doi.org/10.1029/ 2011GL048598.

MacDougall, J., M. Abdu, I. Batista, P. R. Fagundes, Y. Sahai, and P. T. Jayachandran (2009b), On the production of traveling ionospheric disturbances by atmospheric gravity waves, J. Atmos. Sol. Terr. Phys., 71, 2013–2016, doi: 10.1016/j.jastp.2009.09.006.

Makela J J, Otsuka Y (2012) Overview of Nighttime Ionospheric Instabilities at Low- and Mid-Latitudes: Coupling Aspects Resulting in Structuring at the Mesoscale. Space Sci Rev 168, 419–440 (2012). https://doi.org/10.1007/s11214-011-9816-6

Makela J J, Miller E S, Talaat E R (2010), Nighttime medium-scale traveling ionospheric disturbances at low geomagnetic latitudes, Geophys. Res. Lett., 37, L24104, doi:10.1029/2010GL045922.

Mannucci A J, Wilson B D, Edwards C D (1993) A new method for monitoring the earth's ionospheric total electron content using the GPS global network. Proc. ION GPS-93, Institule of Navigation, pp.1323–1332.

Mannucci A J, Wilson B D, Yuan D N, Ho C H Lindqwister U J, Runge T F (1998) A global mapping technique for GPS-derived ionospheric total electron content measurements. Radio Sci. 33, 565–582. https://doi.org/10.1029/97RS02707.

Martinis C, Baumgardner J, Wroten J, Mendillo M (2010), Seasonal dependence of MSTIDs obtained from 630.0 nm airglow imaging at Arecibo, Geophys. Res. Lett., 37, L11103, doi:10.1029/2010GL043569.

Martinis C, Baumgardner J, Wroten J, Mendillo M (2011), All-sky imaging observations of conjugate medium-scale traveling ionospheric disturbances in the American sector, J. Geophys. Res., 116, A05326, doi:10.1029/2010JA016264.

Martyn D F (1950) Cellular atmospheric waves in the ionosphere and troposphere, Proc. Roy. Soc. London A201, 216-233.

Martyn D F (1955) Theory of height and ionization density changes at the maximum of a Chapman-like region, taking account of ion production, decay, diffusion, and total drift. In Proceedings Cambridge Conference. Physical society, London, pp. 254–259.

Materassi M, Mitchell C N (2007) Wavelet analysis of GPS amplitude scintillation: A case study, Radio Sci., *42*, RS1004, doi:10.1029/2005RS003415.

Mayaud P N (1973) A hundred years series of geomagnetic data 1868 – 1978, IAGA Bull., 33, 255 pp., IUGG Publ. Off., Paris.

McNamara L F (1991) The Ionosphere: Communications, Surveillance, and Direction Finding. Orbit: A Foundation Series, Kreiger Publishing Company, Malabar, Florida.

Mendillo Michael (2020) The Dynamical Ionosphere: A Systems Approach to Ionospheric Irregularity. Chapter three (3),2020, Pages 13-20, Copyright © 2020 Elsevier Inc. All rights reserved.

Mendillo M, Baumgardner J, Nottingham D, Aarons J, Reinisch B, Scali J, Kelley M (1997) Investigations of thermosphericionospheric dynamics with 6300-A° images from the Arecibo Observatory. Journal of Geophysical Research, v. 102, p. 7331– 7343, 1997.

Miller C, Swartz W, Kelley M, Mendillo M, Nottingham D, Scali J, Reinisch B (1997) Electrodynamics of midlatitude spread F: 1. Observations of unstable, gravity wave-induced ionospheric electric fields at tropical latitudes, J. Geophys. Res., 102, 11,521–11,532, doi:10.1029/96JA03839.

Millward G H, Rishbeth H, Fuller-Rowell T J, Aylward A D, Quegan S, Moffett R J (1996) Ionospheric F2 layer seasonal and semiannual variations. J. Geophys. Res. 101, 5149.

Mimno H R (1937) The physics of the ionosphere, Rev. Mod. Phys., 9, 1-43.

Mitra S K (1946) Geomagnetic control of region F2 of the ionosphere. Nature, 158(4019), 668–669. https://doi.org/10.1038/158668a0.

Mitra A P (1974) Ionospheric Effects of Solar Flares, Astrophysics and Space Science Library. D. Reidel Publishing Company, Dordrecht Holland.

Mukherjee S, Sarkar S, Purohit P K, Gwal A K (2010) Seasonal variation of total electron content at crest of equatorial anomaly station during low solar activity conditions. Adv. Space Res. 46 (3), 291–295.

Munro G H (1950) Traveling disturbances in the ionosphere, Proc. Roy. Soc., A202, 208-223.

Ngwira C M, Seemala G K, Habarulema J B (2013) Simultaneous observations of ionospheric irregularities in the African low-latitude region. J. Atmos. Sol.-Terr. Phys. 97, 50–57. https://doi.org/10.1016/j.jastp.2013.02.014.

Norsuzila Y, Abdullah M., Ismail M., Zaharim A (2009) Model validation for total electron content (TEC) at an equatorial region Eur. J. Sci. Res. 28 (4), 642–648.

Ogawa T, Igarashi K, Aikyo K, Maeno H (1987) NNSS Satellite observations of medium-scale traveling ionospheric disturbances at southern high-latitudes. J. Geomagn. Geoelec., *39*(12), 709–721.

Oinats A V, Nishitani N, Ponomarenko P (2016) Statistical characteristics of medium-scale traveling ionospheric disturbances revealed from the Hokkaido East and Ekaterinburg HF radar data. Earth Planet and Space doi.org/10.1186/s40623-016-0390-8.

Oliver W L, Otsuka Y, Sato M, Takami T, Fukao S (1997) Aclimatology of F-region gravity wave propagation over the middle and upper atmosphere radar, J. Geophys. Res. 102, 14499–14512.

Oluwadare T S, Thai C N, Akala A O, Heise S, Alizadeh, M, Schuh H (2018) Characterization of GPS-TEC over African equatorial ionization anomaly (EIA) region during 2009–2016. Advances in Space Research. doi.org/10.1016/j.asr.2018.08.044.

Olwendo O J, Baki P, Mito C, Doherty P (2012) Characterization of ionospheric GPS total electron content (GPS-TEC) in low latitude zone over the Kenya region during a very low solar activity phase. J. Atmos. Solar-Terr. Phys. 84- 85, 52–61.

Opio S, D'ujanga F M, Ssenyonga T J (2015) Latitudinal variation of ionosphere in the Africa sector using GPS TEC data. Adv. Space Res. 55, 1640–1650.

Oron S, D'ujanga, F M, Ssenyonga T J (2013) Ionospheric TEC variations during the ascending solar activity phase at an equatorial station, Uganda. Indian Journal of Radio & Space Physics Vol 42, February 2013, pp 7-17.

Oryema B, Jurua E, D'ujanga F M, Ssebiyonga N (2015) Investigation of TEC variations over the magnetic equatorial and equatorial anomaly regions of the African sector. Adv. Space Res. 56, 1939–1950.

Otsuka Y (2018) Review of the generation mechanisms of post-midnight irregularities in the equatorial and low-latitude ionosphere. Prog Earth Planet Sci 5, 57. https://doi.org/10.1186/s40645-018-0212-7

Otsuka Y, Onoma F, Shiokawa K, Ogawa T, Yamamoto M, Fukao S (2007) Simultaneous observations of nighttime medium-scale traveling ionospheric disturbances and E region field-aligned irregularities at mid-latitude. J. Geophys. Res., 112, A06317, doi:10.1029/2005JA011548.

Otsuka Y, Suzuki K, Nakagawa S, Nishioka M, Shiokawa K, Tsugawa T (2013) GPS observations of medium-scale traveling ionospheric disturbances over Europe, Ann. Geophys., 31, 163–172.

Otsuka Y, Shiokawa K, Ogawa K, Wilkinson P (2004), Geomagnetic conjugate observations of medium-scale traveling ionospheric disturbances at midlatitude using all-sky airglow imagers, Geophys. Res. Lett., 31, L15803, doi:10.1029/2004GL020262.

Otsuka Y, Kotake N, Shiokawa K, Ogawa T, Tsugawa T, Saito A (2011) Aeronomy of the Earth's atmosphere and ionosphere. In Statistical Study of Medium-Scale Traveling Ionospheric Disturbances Observed with a GPS Receiver Network in Japan (pp. 291–299). Dordrecht, Netherlands: Springer. 978-94-007-0326-1.

Ouattara F, Fleury R (2011) Variability of CODG TEC and IRI 2001 total electron content (TEC) during IHY campaign period (21 March to 16 April 2008) at Niamey under different geomagnetic activity conditions. Sci. Res. Essays 6 (17), 3609–3622.

Park J, Lühr H, Nishioka M, Kwak Y -S (2015). Plasma density undulations correlated with thermospheric neutral mass density in the daytime low-latitude to midlatitude topside ionosphere. Journal of Geophysical Research: Space Physics, 120, 6669–6678. https://doi.org/ 10.1002/2015JA021525.

Paulino I, Medeiros A F, Vadas S L, Wrasse C M, Takahashi H, Buriti R A (2016) Periodic waves in the lower thermosphere observed by OI 630 nm airglow images. Annales Geophysicae, 34(2), 293–301. https://doi.org/10.5194/angeo-34-293-2016.

Perkins F (1973) Spread F and ionospheric currents. J. Geophys. Res., 78, 218 – 226, doi: 10.1029/JA078i001p00218.

Pratap Misra, Per Enge (2006) Global Positioning Systems: Signals, Measurements and Performance, second ed. Ganga-Jamuna Press, Lincoln, Massachusetts.

Radicella S M, Adeniyi J O (1999) Equatorial ionospheric electron density below the F2 peak. Radio Sci. 34, 1153–1163. https://doi.org/10.1029/ 1999RS900071.

Rajaram, G., Rastogi, R.G., 1977. Equatorial electron densities seasonal and solar cycle changes. J. Atmos. Terr. Phys. 39, 1175–1182. https://doi.org/10.1016/0021-9169(77)90026-5.

Rajesh P K, Liu J Y, Lin C H, Chen A B, Hsu R R, Chen C H, Huba J D (2016), Space-based imaging of nighttime medium-scale traveling ionospheric disturbances using FORMOSAT-2/ISUAL 630.0 nm airglow observations. Geophys. Res. Space Physics, 121,4769–4781, doi:10.1002/2015JA022334.

Richmond A D (1978) Gravity wave generation, propagation, and dissipation in the thermosphere, J. Geophys. Res., 83, 4131.

Rishbeth H, Garriott O K (1969) Introduction to Ionospheric Physics. Academic Press.

Rishbeth H, Lyon A J, Peart M (1963) Diffusion in the equatorial F layer. J. Geophys. Res., 68(9), 2559–2569. https://doi.org/10.1029/JZ068i009p02559.

Rui Jin, Shuanggen Jin, Guiping Feng (2012) M_DCB: Matlab code for estimating GNSS satellite and receiver differential code biases, GPS Solut (2012) 16:541–548, DOI 10.1007/s10291-012-0279-3.

Saito A, Iyemori T, Blomb erg L G, Yamamoto M, Takeda M (1998a) Conjugate observations of the mid-latitude electric field fluctua-tions with the MU radar and the Freja satellite, J. Atmos. Sol. Terr. Phys.,60(1), 129–140, doi:10.1016/S1364-6826(97)00094-1.

Samuel H F (1974) A Theory of Medium-Scale Traveling Ionospheric Disturbances. Journal of Geophysical Research vol. 79, No. 34.

Schaer S (1999) Mapping and predicting the Earth's ionosphere using the Global Positioning System. Ph.D. thesis, Bern University, Switzerland.

Schunk R W, Nagy A F (2000) Ionospheres-Physics, Plasma physics and Chemistry. Atmospheric and Space science series, Cambridge University Press Cambridge, U.K, doi.org/10.1017/CBO9780511551772.

Scotto C (1995) Sporadic-E layer and meteorological activity, Published by INGV, Istituto Nazionale di Geofisica e Vulcanologia - ISSN: 2037-416X, 21–24. https://doi.org/10.4401/ag-4129.

Seemala G K (2011) GPS-TEC Analysis Application Read Me. Institute for Scientific Research, Boston College, USA.

Seemala G K, Valladares C E (2011) Statistics of total electron content depletions observed over the South American continent for the year 2008. Radio Sci. 46, RS5019. https://doi.org/10.1029/2011RS004722.

Shiokawa K, Otsuka Y, Tsugawa T, Ogawa T, Saito A, Ohshima K, Kubota M, Maruyama T, Nakamura T, Yamamoto M, Wilkinson P (2005), Geomagnetic conjugate observation of night-time medium-scale and large-scale traveling ionospheric disturbances: FRONT3 campaign, J. Geophys. Res., 110, A05303, doi:10.1029/2004JA010845.

Singh S, Johnson FS, Power RA (1997) Gravity wave seeding of equatorial plasma bubbles. J Geophys Res 102(A4):7399–7410, doi: 0148-0227/97/96JA03998509.00.

Sivakandan M, Chakrabarty D, Ramkumar T K, Guharay A, Taori A, Parihar N (2019).
Evidence for deep ingression of the midlatitude MSTID into as low as ~3.5° magnetic latitude. Journal of Geophysical Research: Space Physics, 124, 749–764. https://doi.org/10.1029/ 2018JA026103

Somsikov V M (1995) On mechanisms for the formation of atmospheric irregularities in the solar terminator region, J. Atmos. Terr. Phys., 57(1), 75– 83.

Takahashi H, Wrasse C M, Figueiredo C A O B (2018) Equatorial plasma bubble seeding by MSTIDs in the ionosphere. Prog Earth Planet Sci 5, 32 (2018). https://doi.org/10.1186/s40645-018-0189-2

Taori A, Parihar N, Ghodpage R, Dashora N, Sripathi S, Kherani EA, Patil PT (2015) Probing the possible trigger mechanisms of an equatorial plasma bubble event based on multistation optical data. J Geophys Res Space Phys 120. https://doi.org/10.1002/2015JA021541.

Tariku, Y A (2015) TEC prediction performance of the IRI-2012 model over Ethiopia during the rising phase of solar cycle 24 (2009–2011). Earth Planet Sp 67, 140 (2015). https://doi.org/10.1186/s40623-015-0312-1.

Teunissen P, Kleusberg A (1998) GPS for Geodesy, Springer, 187-229.

Thome G D (1964) Incoherent scatter observations of traveling ionospheric disturbance. J. Geophys. Res. 69, 4047 – 4049.

Tinsley B A, Brown G M, Scherrer P H (1989) Solar variability influences on weather and climate: possible connections thorough cosmic rays' fluxes and storm intensification, J. Geophys. Res., Vol. 94, pp. 14783–14792.

Titheridge J E, Buonsanto M J (1983) Annual variations in the electron content and height of the F layer in the Northern and Southern Hemispheres, related to neutral composition. J. Atmos. Terr. Phys. 45, 683–696.

Todorova S (2008) Combination of space geodetic techniques for global mapping of the ionosphere. Ph.D. thesis, Vienna University of Technology, Austria.

Torr M R, Torr D G (1973), The seasonal behavior of the F2-layer of the ionosphere, J. Atmos. Terr. Phys., 35, 2237–2251.

Tsuda T (2014) Characteristics of atmospheric gravity waves observed using the MU (Middle and Upper atmosphere) radar and GPS (Global Positioning System) radio occultation. Proc Jpn Acad Ser B Phys Biol Sci.;90 (1):12–27. doi:10.2183/pjab.90.12.

Tsugawa T, Otsuka Y, Coster A J, Saito A (2007) Medium-scale traveling ionospheric disturbances detected with dense and wide TEC maps over North America. Geophys. Res. Lett., 34, L22101, doi:10.1029/2007GL031663.

Tsunoda R T, Cosgrove R B (2001) Coupled electrodynamics in the nighttime midlatitude ionosphere, Geophys. Res. Lett., 28, 4171–4174, doi:10.1029/2001GL013245.

Tucker A, Fanin B. (1968) Analysis of ionospheric contributions to the Doppler shift of CW signals from artificial ssatellites. J. Geophys. Res., 73, 4325-4334.

Unglaub C, Jacobi Ch, Schmidtke G, Nikutowski B., and Brunner, R (2012) EUV-TEC proxy to describe ionospheric variability using satellite-borne solar EUV measurements, Adv. Radio Sci., 10, 259–263, doi:10.5194/ars-10-259.

Vadas S L (2007) Horizontal and vertical propagation and dissipation of gravity waves in the thermosphere from lower atmospheric and thermospheric sources. J. Geophys. Res. 112, A06305. https://doi.org/10.1029/2006JA011845.

Valladares C E, Hei M A (2012) Measurement of the characteristics of TID susing small and regional networks of GPS receivers during the campaign of 17-30 July of 2008. International Journal of Geophysics, 2012, 1–14, 2012.

Valladares C E, Villalobos J, Hei M A, Sheehan R, Basu Su, MacKenzie E, Doherty P H, Rios V H (2009) Simultaneous observation of traveling ionospheric disturbances in the Northern and Southern Hemispheres. Annales Geophysicae, vol. 27, no. 4, pp. 1501–1508.

Valladares C E, Sheehan R (2016), Observations of conjugate MSTIDs using networks of GPS receivers in the American sector, Radio Sci., 51, 1470–1488, doi:10.1002/2016RS005967.

Vigeesh G, Jackiewicz J, Steiner O (2017) Internal Gravity Waves in the Magnetized Solar Atmosphere. I. Magnetic Field Effects. The Astrophysical Journal, 835:148 (12pp).

Waldock J A, Jones T B (1986) HF Doppler observations of medium-scale traveling ionospheric disturbance at mid-latitudes, J. Atmos.Terr. Phys., 48, 245-260.

Walt M (1994) Introduction to Geomagnetically Trapped Radiation. Cambridge, Atmospheric and Space science series.

Wang L Alexander J (2009) Gravity wave activity during stratospheric sudden warming in the 2007-2008 Northern Hemisphere winter. J. Geophys. Res., 114, doi:10.1029/2009JD011867.

Wang M, Ding F, Wan W (2007) Monitoring global traveling ionospheric disturbances using the worldwide GPS network during the October 2003 storms. Earth Planet Space. doi.org/10.1186/BF03352702.

Warnant R (1998) Detection of irregularities in the total Electron content using GPS measurements - Application to a mid-latitude station. Acta Geod. Geo1'h. Hung., Vol. 33(1), 1'1'. 121-128, 1998.

Warnant R, Pottiaux E (2000) The increase of the ionospheric activity as measured by GPS. Earth Planets Space, 52, 1055–1060.

Wu C C, Fryb C D, Liuc J Y, Lioud K, Tseng C L (2004) Annual TEC variation in the equatorial anomaly region during the solar minimum: September 1996–August 1997. J. Atmos. Terr. Phys. 66, 199–207.

Yeh K C, Liu C H (1969) Theory of Ionospheric Waves, Department of Electrical Engineering, University of Illinois at Urbana-Champaign Urbana. Illinois, Academic Press New York and London

Yokoyama T, Hysell D L (2010) A new midlatitude ionosphere electrodynamics coupling model (MIECO): Latitudinal dependence and propagation of medium-scale traveling ionospheric disturbances. Geophys. Res. Lett., 37, L08105, doi:10.1029/2010GL042598.

Yokoyama T, Yamamoto M, Otsuka Y, Nishioka M, Tsugawa T, Watanabe S, Pfaff RF (2011) On post-midnight low-latitude ionospheric irregularities during solar minimum: 1. Equatorial Atmosphere Radar and GPS-TEC observations in Indonesia. J Geophys Res 116: A11325. https://doi.org/10.1029/2011JA016797.

Zhao B, Wan W, Liu L, Ren Z (2009) Characteristics of the ionospheric total electron content of the equatorial ionization anomaly in the Asian-Australian region during 1996–2004. Ann. Geophys. 27, 3861–3873.

Zoundi, C., Ouattara, F., Fleury, R., Amory-Mazaudier, C., Duchesne, L. P., 2012. Seasonal TEC variability in West Africa equatorial anomaly region. Eur. J. Sci. Res. 77 (3), 303–313.